Universitat Politècnica de
Catalunya
Barcelona, Spain

European Laboratory for
Particle Physics Geneva,
Switzerland

PhD Thesis

Redundancy of the LHC Machine Protection Systems in Case of Magnet Failures

Andrés Gómez Alonso

CERN-THESIS-2009-023
17/04/2009

Thesis Director	Dr. Francisco Calviño (UPC, Barcelona)
Thesis Supervisor	Dr. Rüdiger Schmidt (CERN, Geneva)

April 17, 2009

A Kiko, Inma y Javier

Resumen

El Gran Colisionador de Hadrones (LHC) construido en el CERN, el Laboratorio Europeo para la Física de Partículas, es el acelerador de partículas ms energético que se haya construido. Acelerará haces de protones de alta intensidad hasta una energía nominal de 7 TeV en un anillo de 27 km de largo. La energía almacenada en los imanes del LHC alcanza unos 10 GJ y cada uno de los haces de protones almacena unos 360 MJ a energía nominal. La descarga accidental de esa energía de forma incontrolada tendría graves consecuencias para los equipos que componen el acelerador. Los Sistemas de Protección del LHC han sido diseñados para proteger el acelerador de tal descarga incontrolada de energía. Proporcionan monitorización constante de los equipos críticos (imanes, criogenia, sistema de vacío, etc.); monitorización constante de la posición y pérdidas del haz; un sistema de descarga del haz muy fiable; y un sistema de interlock ultra-rápido y muy fiable para transmitir las señales críticas. Los Sistemas de Protección deben asegurar también una disponibilidad óptima de los haces.

Los fallos de los imanes producen los efectos más rápidos en el haz y son los más críticos para la protección del LHC. Sen han considerado quenches (pérdida de la superconductividad) y fallos de los convertidores de potencia (fallos de alimentación). Estos fallos producen una caída de la corriente en el imán (y por tanto en el campo magnético). La caída de corriente después de un quench ha sido modelizada con una gausiana en base a estudios previos. La caída de corriente tras un fallo de alimentación se ha considerado exponencial.

Para evaluar los efectos de los fallos de imanes en el haz, se ha realizado tracking de partículas con campo magnético variable utilizando MADX. Los fallos de dipolos producen una distorsión de la órbita cerrada que puede ser estudiada analíticamente. Las pérdidas producidas por fallos de dipolos son generalmente localizadas. Los fallos de los cuadrupolos generan cambios en la óptica de acelerador que se traducen en una desfocalización o desplazamiento transversal del haz. El cruce de resonancias no lineales debido al cambio en la óptica puede generar pérdidas de hasta un 10% del haz. Las pérdidas producidas por los cuadrupolos pueden estar distribuidas en muchos puntos del acelerador. Los fallos más rápidos generalmente producen pérdidas más distribuidas.

La distribución de las pérdidas primarias en los colimadores se puede describir con una función de tipo exponencial que permite una rápida caracterización del impacto a partir de los parámetros de la función. Los impactos generados por fallos de dipolos o cuadrupolos no presentan diferencias significativas, y en ambos casos los fallos más rápidos producen impactos más anchos. El parámetro de impacto medio para los casos estudiados se sitúa entre 5 μm y 1 mm. La cantidad de pérdidas que alcanza los elementos superconductores tras dispersarse en un colimador es mayor para impactos primarios en colimadores fuera o al final de las inserciones de colimación, y pueden alcanzar hasta 10% de la intensidad del haz a 450 GeV y 1% a 7 TeV.

En el LHC, los fallos de los dipolos D1 en IR1 e IR5 producen las pérdidas más rpidas, tanto a 450 GeV como a 7 TeV, alcanzando los niveles de daño en menos de 3 ms. Otros fallos de imanes no superconductores podrían generar daños al cabo de unos 10 ms, y quenches en los dipolos superconductores unos 15 ms después del inicio de la caída de corriente. Los monitores de pérdidas (BLMs) generan la señal de extracción del haz a tiempo para todos los fallos estudiados. En combinación con los sistemas de protección de quench (QPS), el controlador del interlock de alimentación (PIC) y los monitores de variaciones rápidas de corriente (FMCMs), la protección del LHC est asegurada de forma redundante para la mayoría de los fallos estudiados. Un monitor rápido de corriente del haz aseguraría tal redundancia en todos los casos estudiados.

Abstract

The Large Hadron Collider (LHC) built at CERN, the European Laboratory for Particle Physics will accelerate high intensity proton beams up to an energy of 7 TeV per proton. The energy stored in the LHC magnets reaches about 10 GJ and each of the proton beams stores about 360 MJ at nominal collision energy. Accidental release of this energy in an uncontrolled way would lead to serious damage of the accelerator equipment. The LHC Machine Protection Systems are designed to protect the accelerator against such uncontrolled release of the stored energy. They provide constant monitoring of critical equipment, constant monitoring of the beam position and losses, a very reliable Beam Dump System and fast, very reliable interlock systems to transmit protection critical signals. While protecting the accelerator in case of failure, the Machine Protection Systems must also ensure maximum operational availability of the LHC beams.

Magnet failures produce the fastest effects on the beam and are most critical with respect to machine protection. Quenches (loss of magnet superconductivity) and failures of the power converters (powering failures) have been considered. These failures produce a current decay in the magnet and the corresponding decay in the magnetic field. The current decay after a quench has been modeled by a Gaussian curve based on previous studies. The current decay generated by powering failures has been considered exponential.

In order to evaluate the effects of magnet failures on the beam, particle tracking with variable magnetic fields has been done using the MADX program. Dipole failures produce a closed orbit distortion that can be easily determined analytically. Losses produced by dipole failures are generally localized. Quadrupole failures lead to beta beating and tune shift, which in the transverse plane translate into either defocusing or displacement of the beam. The crossing of non-linear resonances induced by the tune shift can generate losses of up to 10% of the beam intensity, and beam losses induced by quadrupole failures may be distributed over many locations.

The transverse distribution of the primary losses at the collimators can be described by a function of exponential nature, allowing a fast characterization of the impact from the parameters of the function. Dipole and quadrupole failures lead to primary impacts that are not significantly different in shape or size, and in both cases faster failures produce broader impacts. The average impact parameter for the cases studied ranges from less than 5 μm to about 1 mm. The amount of losses reaching the superconducting elements from particles scattered after a primary impact is greater for impacts at collimators outside or at the end of the cleaning insertions. It may reach up to 10% of the beam intensity at 450 GeV and 1% at 7 TeV and in most cases, it decreases with increasing impact parameter of the primary impact.

With circulating beam at LHC, powering failures of the D1 dipoles at IR1 and IR5 produce the fastest losses both at 450 GeV and 7 TeV, reaching the damage level in less than 3 ms in both cases. Other failures of normal conducting magnets could produce damage after about 10 ms and quenches in the main superconducting dipoles may lead to damage about 15 ms after the current decay starts. Redundancy is ensured when, for a given failure, at least two independent protection systems react on time. The Beam Loss Monitors are able to request a beam dump in time for every failure case considered. In combination with the Quench Protection System, the Powering Interlock Controller and the Fast Magnet Current change Monitors most failure cases are redundantly protected. Only quenches of some superconducting dipoles are not redundantly protected with these systems, but redundancy can be ensured by additional systems, such as a Fast Beam Current Monitor.

Acknowledgements

This thesis represents the culmination of a difficult learning period at CERN, and it certainly would not have been successfully achieved without the help and support of my colleagues, friends and family, to whom I wish to express my most sincere gratitude.

First of all, I would like to thank Sinziana: had she not been at my side, this thesis would not have been written. Many thanks to Mme. Armand-Gerson, for her wise advice and competence, and to Michel and Arnaud Dejean, as well as Claire Laurent, for their unorthodox but effective help in the most difficult moments of the last year.

I am very grateful to all my colleagues at CERN who devoted part of their very valuable time to clarify my doubts and to answer my many questions. In particluar, many thanks to Markus and Ben, from CO, to Massimo, Andrea, Thys, Thomas, Chiara, Alex and Ricardo, from ABP, to Verena and Jörg, from OP, Hughes from PO and Reiner from QPS.

I would especially like to thank my supervisor at CERN, Rüdiger Schmidt, for his availability, the many opportunities that he offered to me and his many useful suggestions. I particularly appreciated the freedom to carry out my work as well as his support of my own ideas and research direction. During the last three years, I very much valued working under his supervision.

I would like to express my gratitude to Erik Heijne, for his understanding, time and discussions. And also to my two reporters, Jörg and Bernhard, for their time and useful suggestions. Many thanks to Laura, for her invaluable help with administrative issues, and to Paco for the opportunity to carry out this work within the UPC doctorate program.

I cannot forget all my colleagues from the MI team, in particular Bruno, for the great atmosphere in the section. It is not possible to list here all the moments I feel grateful for, but there are many that I will not forget. You can't imagine how important you all have been.

Again, I have to stress my gratitude to Rüdiger. Thank you very much for your understanding and acceptance of my personal decisions in all circumstances. Many thanks also for helping me to learn to value my work. Technical knowledge may fade away with time, but this is something that will remain.

Many thanks to Nathalie, Stephan and Sri Sri, for the wonderful hints and tools to deal with my life and for helping me to come back to the present when I most needed it.

Un grand merci à Arnaud, Markus et Arthur pour leur aide et soutien. Raph, Antoine, Jérém, Florian, Antoine, Sophie et tous les autres, merci pour votre spontaneité et tout ce que j'ai pu apprendre avec vous.

To Raquel, Montse, Alex, Iván, Juan, Elena, Andrea, Corina, Claudia, Lelde, Bala, Dorotha, Muriel and all my friends in Geneva and Vaud. Thank you so much for your support (and patience). It would have been very difficult to go till the end without you.

Por último, mi más profundo agradecimiento para Javier e Inma. Por vuestro apoyo incondicional y sufrimiento compartido, gracias.

Contents

Introduction **1**

1 Basics of Accelerator Physics **5**
1.1 Motion of charged particles in electromagnetic fields . . . 5
1.1.1 The Lorentz Force . . . 5
1.1.2 Magnetic field and charged particle motion . . . 5
1.2 Transverse Linear Beam Optics . . . 6
1.2.1 Coordinate system . . . 6
1.2.2 Linear equations of motion . . . 7
1.2.3 Transfer matrix . . . 8
1.2.4 Dispersion function . . . 9
1.3 Twiss Functions and Phase-Space Ellipse . . . 9
1.3.1 Hill's equation . . . 9
1.3.2 Twiss functions . . . 10
1.3.3 Phase-space ellipse . . . 10
1.3.4 Normalized coordinates . . . 11
1.3.5 Twiss parameters and transfer matrices . . . 11
1.3.6 Emittance and beam size . . . 12
1.3.7 Tune and optical resonances . . . 12
1.4 Effect of linear perturbations . . . 13
1.4.1 Dipolar errors . . . 13
1.4.2 Quadrupolar errors . . . 14
1.5 Luminosity . . . 15

2 The LHC and the LHC Machine Protection Systems **17**
2.1 The LHC layout and main magnets . . . 17
2.1.1 The LHC layout . . . 17
2.1.2 The LHC main magnets . . . 21
2.2 The powering scheme for the LHC magnets . . . 24
2.2.1 Powering subsectors . . . 25
2.2.2 Main circuits . . . 25
2.3 The collimation system and its layout . . . 26
2.3.1 Structure of the LHC collimation system . . . 27
2.3.2 Layout of the LHC collimators . . . 28
2.4 Naming conventions for the LHC elements and circuits . . . 28
2.5 The LHC operation . . . 30
2.5.1 The LHC operating cycle . . . 30
2.5.2 Beam losses in the LHC . . . 31

2.6 The LHC Machine Protection Systems . . . 37
2.6.1 Strategies for protection of the LHC . . . 38
2.6.2 Architecture of the interlock systems for machine protection . . . 40
2.6.3 Components of the Machine Protection Systems . . . 41
2.6.4 Summary and timing considerations of the Machine Protection Systems . . . 47
2.6.5 Redundancy of the Machine Protection Systems . . . 47

3 Tracking simulations with magnet failures in the LHC 51
3.1 The thin lens approximation for tracking simulations . . . 51
3.2 Tracking tools for the LHC . . . 52
3.2.1 MAD-X . . . 52
3.2.2 Sixtrack . . . 52
3.3 The LHC Model . . . 52
3.3.1 Tracking with aperture limitations . . . 54
3.3.2 Tracking with variable magnetic fields . . . 54
3.4 Transverse particle distribution . . . 56

4 Magnet failures and their effects on the beam 59
4.1 Types of magnet failures and modeling of the current decay . . . 59
4.1.1 Current decay in case of powering failures . . . 59
4.1.2 Current decay in case of quenches . . . 61
4.2 Effects of magnet failures on the beam . . . 63
4.2.1 Critical magnet failures in the LHC . . . 64
4.2.2 Dipole failures . . . 65
4.2.3 Quadrupole failures . . . 72

5 Distribution of the lost particles at the LHC collimators 91
5.1 Impact distributions for representative failure cases . . . 92
5.1.1 Dipole failures . . . 92
5.1.2 Quadrupole failures . . . 95
5.2 Simple fit applicable to every impact distribution . . . 95
5.3 Evaluation of the impact distribution . . . 97
5.4 Influence of the speed of the failure on the width of the impact distribution . . . 99

6 Post-impact tracking and secondary losses 101
6.1 Settings for the benchmark simulations . . . 101
6.2 Results . . . 103
6.2.1 Absorption efficiency of the collimation system as a function of the collimator that is hit first . . . 103
6.2.2 Absorption efficiency of the collimation system as a function of the impact parameter . . . 105
6.2.3 Longitudinal distribution of the secondary losses . . . 106
6.3 A method to estimate the quench time constant after a primary impact at a given collimator . . . 107

7 Critical magnet failures at LHC and redundancy of the Machine Protection Systems 109
7.1 Simulated failure scenarios . . . 109

7.2 Evaluation of the BLM thresholds based on the time evolution of the losses for the most critical failures . . . 111
7.3 Evaluated quantities for each failure . . . 112
7.4 Results . . . 113
7.4.1 Quenches at the main superconducting dipoles in the arcs . . . 113
7.4.2 Quenches at the main superconducting quadrupoles in the arcs . . . 114
7.4.3 Quenches at the inner triplets . . . 114
7.4.4 Powering failures of normal conducting quadrupoles in IR3 and IR7 at 450 GeV 114
7.4.5 Failures at the most critical superconducting dipoles in the insertions . . . 115
7.4.6 Most critical normal conducting dipoles in the insertions . . . 115
7.4.7 Summary . . . 115
7.5 Evaluation of the redundancy of the LHC Machine Protection Systems . . . 116

Conclusion **119**

References **122**

A Lists of collimators **129**

B Simulated electrical circuits and failures **133**

C Adaptation of the method of the moments for the calculation of A_f, σ and τ **137**

D Additional figures for secondary losses **139**

E Simulation output data **143**

Introduction

The Large Hadron Collider (LHC) [1] at CERN (The European Laboratory for Particle Physics) is one of the largest and most complex machines ever built. The LHC has been conceived and designed within the last 25 years and represents the cutting edge of accelerator technology, colliding protons with a center of mass energy of 14 TeV. Built in the existing underground tunnel of LEP, the LHC ring extends along 26.7 km between between the Swiss city of Geneva and the Jura mountain range, in France (figure 1). The commissioning of all the elements and circuits of the machine was completed during summer 2008. The first injection tests with beam were fulfilled successfully in August 2008 and circulating beam was obtained in September 2008.

Figure 1: Aerial view of CERN and its accelerator complex. The largest circle corresponds to the LHC ring, with a diameter of about 8.5 km.

The LHC is set to answer some of the fundamental questions in elementary particle physics, colliding particles with an energy high enough to reveal the inner workings of the quantum world. The motivation for the construction of more and more energetic accelerators lies firstly on de Broglie's relation $\lambda = h/p$, which relates the momentum (p) of a particle to its quantum-mechanical wavelength (λ). h is the Planck constant, equal to 6.626×10^{34} Js. In order to explore smaller structures, more and more energetic particles are needed. Higher energy is also needed for the discovery of more massive short-lived particles, according to Einstein's relationship $E = mc^2$.

One of the main goals of the LHC experiments in proton-proton collisions is the discovery and study of the Higgs boson. The existence of this boson would be a strong indication of the Higgs field, which has been postulated to explain the mass differences between different particles. The stronger the interaction between a particle and the Higgs field, the higher the particle mass.

The LHC has been also designed to collide heavy nuclei (primarily Pb). Fully stripped Pb ions

will be accelerated and collided at an energy of about 1150 TeV (7 TeV per charge). These ion collisions are expected to cause phase transitions from nuclear matter into a quark-gluon plasma as might have existed 10^{-6} s after the Big Bang.

Around the four interaction points of the LHC beams, four detectors have been built to obtain the information from the collision events. ATLAS [2] and CMS [3] are general purpose detectors optimized to detect any new particle generated in the collisions. The existence of the Higgs boson in the energy range of LHC is expected to be revealed or discarded from the data obtained in these two experiments. LHCb [4] is a more specific experiment devoted to the study of the asymmetry between matter and antimatter in the universe. ALICE [5] is designed for the study of the quark-gluon plasma that will be generated in the ion collisions.

The discovery potential of High Energy Physics experiments is given both by the center-of-mass energy of the colliding particles and by the event rate at the interaction points. The LHC extends the frontiers of these two quantities with respect to previous accelerators.

1. *Center of mass energy*: In an accelerator, the center of mass energy is related to the beam energy (or particle momentum). The beam energy at the LHC exceeds the values achieved by previous accelerators by a factor of 7 with the use of highly advanced superconducting magnets (figure 2). These magnets bend the charged particle beams into a circle and provide the focusing strength to keep the beam confined inside the accelerator, and to squeeze it transversely in the interaction points.

2. *Event rate*: The event rate in a collider experiment is given by the luminosity at the collision points. Luminosity is a function of the beam intensity and its transverse size at the interaction point. At LHC it reaches a design value of 10^{34} $\mathrm{cm}^{-2}\mathrm{s}^{-1}$. Luminosity is closely related to the transverse energy density of the colliding beams. At nominal operation, the LHC will contain proton beams with a total stored energy of about 360 MJ per beam (3×10^{14} protons at 7 TeV). This extends present achievements at TEVATRON (USA) and HERA (Germany) by about a factor 200 in terms of stored energy, and by a factor of 1000 in terms of transverse energy density.

Colliding particles at such high energy makes very high demands on machine operation and protection. The superconducting LHC magnets are kept at a temperature of only around two degrees above absolute zero and there is a high chance of particle impacts causing a magnet to quench, where the magnet becomes normal conducting and has to be switched off before it destroys itself. Losing as little as 10^{-8} of the beam intensity into the superconducting magnets may lead to a quench. A loss of 10^{-4} of the beam intensity into any part of the machine may cause damage, such as breaking the machine vacuum, which in the best case results in costly repairs and weeks of downtime. In a worst case, the destruction of one or more dipole magnets would mean many weeks of repairs to return the machine to operation.

Due to the unprecedented sensitivity of the machine to beam losses, and the high cost of failure, both financially and in terms of inefficiency, a complex Machine Protection System is envisaged, following and diagnosing the operation of the CERN high energy accelerators and ensuring their safe operation. The need of reliable protection systems has been confirmed after the event of the 19^{th} September 2008 during the powering tests to high current, in which a perforation of the helium vessel led to serious damage in several magnets. In this case the perforation was induced by an electric arc generated in a faulty connection, but a beam deflected from its trajectory during operation could also damage the helium vessel leading to similar consequences.

In order to properly set up the Machine Protection Systems and to evaluate the degree of protection of the LHC against an accidentally deflected beam, knowledge and understanding of the

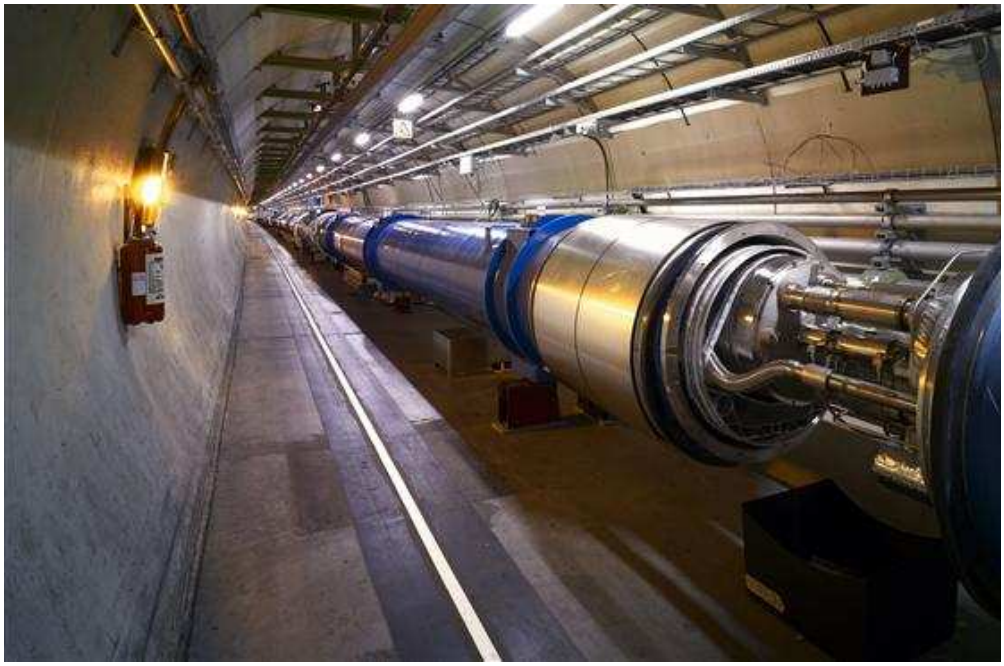

Figure 2: LHC superconducting dipoles during installation.

effects of magnet failures on the beam is needed. The first studies of these effects and their time constant, based on analytical calculations, were carried out in 2001 [6]. In the coming years the interest on the time constants of magnet failures grew and further simulation studies were made on the most critical dipole failures at LHC [7], [8]. Due to the short time constant of magnet failures at the LHC injection lines, concern rose about Machine Protection during the injection process and careful studies were published on this subject [9].

This thesis continues the work done in this direction, focused on the LHC operation with protons. It is oriented toward the understanding of the effects of magnet failures on circulating beams, particularly the effects of quadrupole failures. Numerical tools are used in order to study the behavior of the beam during magnet failure scenarios that have the potential to lead to fast equipment damage. From this understanding an evaluation of the redundancy of the Machine Protection Systems against losses that could lead to damage is done.

Outline:

Chapter 1 presents the basic concepts of Accelerator Physics, necessary to understand the simulation results presented in following chapters. These include the motion of charged particles in an accelerator, linear transverse beam optics and the effects of magnetic field perturbations.

Chapter 2 presents the LHC and the LHC Machine Protection Systems. Being the outcome of a documentary research, it is intended as a reference. It depicts the context of the failure scenarios and explains the LHC and the Machine Protection Systems sufficiently in detail to make of this thesis work an stand-alone document.

In chapter 3 the numerical tools used for the simulations are introduced. The procedures to track the particle trajectories with a variable magnetic field are presented, as well as the LHC numerical model.

Chapter 4 focuses on the magnet failures and their effect on the beam. The phenomena that

may lead to a change in the current of the circuits are presented, followed by a detailed study of the effects of the failures of dipole and quadrupole magnets. This chapter provides basically qualitative understanding about the behavior of the beam in case of magnet failures of different nature. It presents the time-evolution patterns of failure induced losses and defines quantities to quickly assess the criticality of a failure.

In chapter 5 the transverse distribution of failure-induced losses at the collimators is studied. The shape and width of this distribution is compared with the beam-size and related to the speed of the failure. A fit function that allows to estimate the concentration of primary losses at a given collimator as a function of time is proposed.

Chapter 6 presents a study on the particles scattered back into the beam from a primary impact on a collimator. The amount and distribution of secondary losses are evaluated as a function of the impact parameter and the collimator that is hit first. A method to estimate the time at which a quench will be generated is also presented.

In chapter 7 a summary of the most critical magnet failures at LHC with respect to their effects on the beam is made. The quantities defined in the previous chapters are derived for each failure case and the redundancy of the Machine Protection Systems is assessed.

Chapter 1

Basics of Accelerator Physics

This chapter describes the basic concepts of Accelerator Physics, focusing in linear beam dynamics and introducing perturbation theory, key for the understanding of the content of this thesis. A more complete picture and the derivation of the formulas presented in this chapter can be found in [10], [11] and [12].

1.1 Motion of charged particles in electromagnetic fields

1.1.1 The Lorentz Force

Charged particles are accelerated and directed using electromagnetic fields. The Lorentz force that acts on a particle with charge q is given by

$$F = q \cdot \left(\vec{E} + \vec{v} \times \vec{B}\right) \tag{1.1}$$

Only the electrical field can be used to increase the energy of the particle, while the magnetic field is used to act on the particle trajectory. Indeed, in high energy accelerators $v \approx c$ and electrical and magnetic fields having the same effect on the particle relate as

$$\left|\vec{E}\right| = c\left|\vec{B}\right| \tag{1.2}$$

A magnetic field of $1T$ would have the same effect as an electric field of $3 \cdot 10^8 V/m$, which is technically not feasible. Therefore, high energy particle accelerators use only magnetic fields for the guidance of the beam.

1.1.2 Magnetic field and charged particle motion

The motion of particles in the vicinity of the nominal trajectory is described in a Cartesian coordinate system whose origin moves with the nominal trajectory of the beam. The axis along the beam trajectory is labelled s, while x and y represent the horizontal and vertical axis respectively, as illustrated in figure 1.1. For simplicity, we will assume that the particles move parallel to the s-direction and that the longitudinal component of the magnetic field is equal to zero. For a particle moving in the horizontal plane, the Lorentz force and the centrifugal force are equal, leading to

$$\frac{1}{R(x,y,s)} = \frac{e}{p} B_y(x,y,s) \tag{1.3}$$

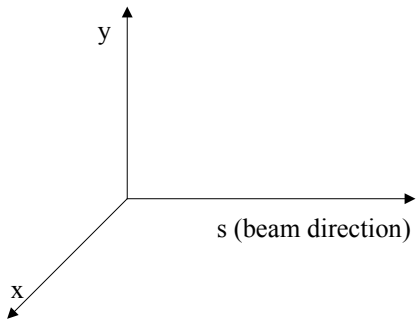

Figure 1.1: Coordinate system to describe the motion of particles in the vicinity of the nominal trajectory.

where p is the moment of the particle and R the radius of curvature of the trajectory. An analogous relation applies for a particle moving in the vertical plane. Expanding the magnetic field in the vicinity of the beam and multiplying by e/p we obtain

$$\begin{aligned} \frac{e}{p}B_y(x) &= B_{y0} + \frac{e}{p}\frac{dB_y}{dx}x + \frac{1}{2!}\frac{e}{p}\frac{d^2B_y}{dx^2}x^2 + \frac{1}{3!}\frac{e}{p}\frac{d^3B_y}{dx^3}x^3 + \cdots \\ &= \frac{1}{R} + kx + \frac{1}{2!}mx^2 + \frac{1}{3!}ox^3 + \cdots \end{aligned} \tag{1.4}$$

As illustrated by equation 1.4, the magnetic field can be depicted as a sum of multipolar elements, represented by each term of the right hand side of the equation. The main multipolar terms and their effect on the beam are represented in table 1.1.

Multipole	Parameter	Effect on the beam
Dipole	$1/R$	Bending
Quadrupole	k	Focusing
Sextupole	m	Chromaticity correction
Octupole	o	field error compensation

Table 1.1: Main multipolar terms and their effect on the beam.

1.2 Transverse Linear Beam Optics

1.2.1 Coordinate system

In order to study the motion of the particles in the accelerator we define a *reference orbit*, which represents the ideal trajectory of a particle that passes through the axis of symmetry of each of the accelerator elements. The reference orbit is determined by the structure of the machine. The motion of each individual particle is studied in a reference system that moves along this reference orbit with the nominal momentum p_0 and constant energy, as represented in figure 1.2.

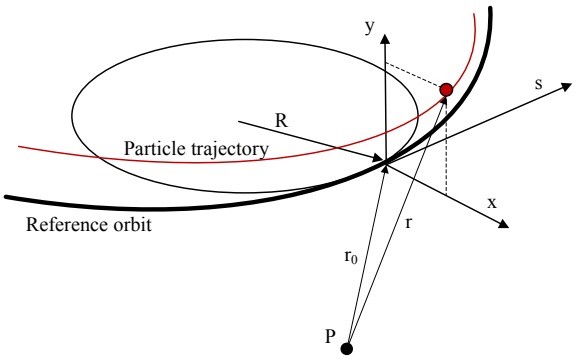

Figure 1.2: Reference orbit, r_0, and particle trajectory, r. R represents the bending radius of the reference orbit at a given point.

1.2.2 Linear equations of motion

Assuming that the longitudinal component of the magnetic field is zero ($B_s = 0$), the general equation of motion

$$\frac{d\vec{p}}{dt} = \frac{d}{dt}(m_0\gamma\vec{v}) = \vec{F} = q \cdot \left(\vec{E} + \vec{v} \times \vec{B}\right) \tag{1.5}$$

written with respect to the reference orbit yields

$$\begin{aligned} x'' - \left(1 + \frac{x}{R}\right)\frac{1}{R} &= -\frac{v}{\dot{s}}\frac{e}{p}B_y\left(1 + \frac{x}{R}\right) \\ y'' &= \frac{v}{\dot{s}}\frac{e}{p}B_x\left(1 + \frac{x}{R}\right) \end{aligned} \tag{1.6}$$

where we have expressed the velocity of the particle as a function of the velocity of the reference system

$$v = \dot{s}\left(1 + \frac{x}{R}\right) \tag{1.7}$$

Expressing the momentum of the particle as a function of the reference momentum, $p = p_0 + \Delta p$, with $\Delta p << p_0$ and keeping only the linear terms of the magnetic field[1]

$$\frac{e}{p_0}B_y = \frac{1}{R} - kx \qquad\qquad \frac{e}{p_0}B_x = -ky \tag{1.8}$$

we obtain

$$\begin{aligned} x'' - \left(1 + \frac{x}{R}\right)\frac{1}{R} &= -\left(1 + \frac{x}{R}\right)^2\left(\frac{1}{R} - kx\right)(1 - \delta) \\ y'' &= -\left(1 + \frac{x}{R}\right)^2 ky\,(1 - \delta) \end{aligned} \tag{1.9}$$

[1]The sign of the quadrupole strength is arbitrary. We choose $k < 0$ for focusing quadrupoles.

where we have noted $\delta = \Delta p/p_0$. After some algebraic manipulations, neglecting higher order terms of x, y and δ, we finally obtain the linear equations of motion for a particle travelling through the magnetic structure of an accelerator:

$$x''(s) + \left(\frac{1}{R^2(s)} - k(s)\right) x(s) = \frac{1}{R(s)}\delta$$
$$y''(s) + k(s)y(s) = 0 \tag{1.10}$$

Note that the horizontal and vertical planes are uncoupled in the linear equations of motion. Therefore we can consider them separately. In the following calculations we will refer to the horizontal plane unless indicated otherwise.

1.2.3 Transfer matrix

In a single plane, the trajectory of a particle at a given position s in the ring is determined by its phase space coordinates:

$$\boldsymbol{X}(s) = \begin{pmatrix} x(s) \\ x'(s) \end{pmatrix} \tag{1.11}$$

Assuming particles of nominal momentum ($\delta = 0$) the equation of motion inside a quadrupole magnet takes the form of a simple harmonic oscillation

$$x''(s) - kx(s) = 0 \tag{1.12}$$

whose solution can be written in matrix formalism:

$$\boldsymbol{X}(s) = \boldsymbol{M}\boldsymbol{X}_0 \tag{1.13}$$

with $\boldsymbol{X}_0 = \boldsymbol{X}(0)$ and

$$\boldsymbol{M} = \begin{cases} \begin{pmatrix} \cos\left(\sqrt{|k|}s\right) & \frac{1}{\sqrt{|k|}}\sin\left(\sqrt{|k|}s\right) \\ -\sqrt{|k|}s\sin\left(\sqrt{|k|}s\right) & \cos\left(\sqrt{|k|}s\right) \end{pmatrix} & \text{if } k < 0 \text{ (focusing)} \\ \begin{pmatrix} 1 & s \\ 0 & 1 \end{pmatrix} & \text{if } k = 0 \text{ (drift space)} \\ \begin{pmatrix} \cosh\left(\sqrt{k}s\right) & \frac{1}{\sqrt{k}}\sinh\left(\sqrt{k}s\right) \\ \sqrt{k}s\sinh\left(\sqrt{k}s\right) & \cosh\left(\sqrt{k}s\right) \end{pmatrix} & \text{if } k > 0 \text{ (defocusing)} \end{cases} \tag{1.14}$$

$\boldsymbol{M}$ is called the *transfer matrix* of the quadrupole. For a dipole with bending radius R the transfer matrix is given by

$$\boldsymbol{M}_{dipole} = \begin{pmatrix} \cos\frac{s}{R} & R\sin\frac{s}{R} \\ -\frac{1}{R}\sin\frac{s}{R} & \cos\frac{s}{R} \end{pmatrix} \tag{1.15}$$

All transfer matrices in linear beam optics have a determinant equal to 1.

1.2.4 Dispersion function

Let's consider now the case where $\delta \neq 0$. From 1.10 we see that the momentum difference has only an influence if $1/R \neq 0$. Therefore, we consider only the case of bending magnets and 1.10 becomes

$$x''(s) + \frac{1}{R^2(s)}x(s) = \frac{1}{R(s)}\delta \tag{1.16}$$

The dispersion function, $D(s)$, is the solution to 1.16 when $\delta = 1$. Solving for a dipole magnet, we obtain the transfer relationship for the dispersion function

$$\begin{pmatrix} D(s) \\ D'(s) \\ 1 \end{pmatrix} = \begin{pmatrix} \cos\frac{s}{R} & R\sin\frac{s}{R} & R\left(1-\cos\frac{s}{R}\right) \\ -\frac{1}{R}\sin\frac{s}{R} & \cos\frac{s}{R} & \sin\frac{s}{R} \\ 0 & 0 & 1 \end{pmatrix} \cdot \begin{pmatrix} D_0 \\ D'_0 \\ 1 \end{pmatrix} \tag{1.17}$$

For a particle with a momentum offset of δ, we can write

$$x(s) = x_{\delta=0}(s) + \delta D(s) \tag{1.18}$$

Therefore, the matrix formalism for off-momentum particles applies with

$$\boldsymbol{X}(s) = \begin{pmatrix} x(s) \\ x'(s) \\ \delta \end{pmatrix} \tag{1.19}$$

The transfer matrix for dipoles corresponds to the transfer matrix in 1.17. For a quadrupole with two-dimensional transfer matrix $\boldsymbol{M} = (m_{ij})$ we shall use

$$\boldsymbol{M} = \begin{pmatrix} m_{11} & m_{12} & 0 \\ m_{21} & m_{22} & 0 \\ 0 & 0 & 1 \end{pmatrix} \tag{1.20}$$

1.3 Twiss Functions and Phase-Space Ellipse

The previous section explains the physics for the motion of a single particle. In this section, we present the tools to understand the properties of a beam of many particles in circular accelerators.

1.3.1 Hill's equation

Assuming $\delta = 0$, the trajectory $x(s)$ through a magnet lattice is given by Hill's equation

$$x''(s) - K(s)x(s) = 0 \tag{1.21}$$

The focusing function $K(s) = 1/R(s) - k(s)$ is periodic: $K(s+L) = K(s)$. $x(s)$ describes an oscillation around the reference orbit denoted *betatron oscillation*, whose amplitude and phase depend on the position s. Solving 1.21 we can write the trajectory function in the form

$$x(s) = \sqrt{\epsilon\beta(s)}\cos\left[\Psi(s) + \phi\right] \tag{1.22}$$

with

$$\Psi(s) = \int_0^s \frac{d\sigma}{\beta(\sigma)} \tag{1.23}$$

Ψ is referred to as the *betatron phase*.

1.3.2 Twiss functions

In 1.22, $\sqrt{\epsilon\beta(s)}$ represents the amplitude of the trajectory oscillations at a given point. ϵ is the *emittance*, a beam property that is constant through the lattice. $\beta(s)$ is called the *beta function* and depends on the longitudinal position in the accelerator. It is periodic with the same period as $K(s)$. From $\beta(s)$ we define

$$\alpha(s) \equiv -\frac{\beta'(s)}{2} \qquad\qquad \gamma(s) \equiv \frac{1+\alpha^2(s)}{\beta(s)} \tag{1.24}$$

β, α, γ and Ψ are the so called twiss functions, defined for every point in the accelerator. When 1.21 does not have an oscillating solution for $x(s)$ we talk about unstable optics and the twiss functions are not defined. Therefore, the quadrupole strenghts $k(s)$ in an accelerator have to be set such that a stable solution of Hill's equation exists.

1.3.3 Phase-space ellipse

From 1.22 we obtain the expression for the trajectory slope

$$x'(s) = -\frac{\epsilon}{\beta(s)}\left[\alpha\cos(\Psi(s)+\phi) + \sin(\Psi(s)+\phi)\right] \tag{1.25}$$

which combined with 1.22 leads to the phase-space relationship

$$\gamma(s)x^2(s) + 2\alpha(s)x(s)x'(s) + \beta(s)x'^2(s) = \epsilon \tag{1.26}$$

This is the equation of an ellipse, whose area in phase space is equal to $\pi\epsilon$. According to *Liouville's theorem*, this area is constant through the magnet sequence when only conservative forces act on the particles. Figure 1.3 shows the phase space ellipse and how it relates to the twiss parameters.

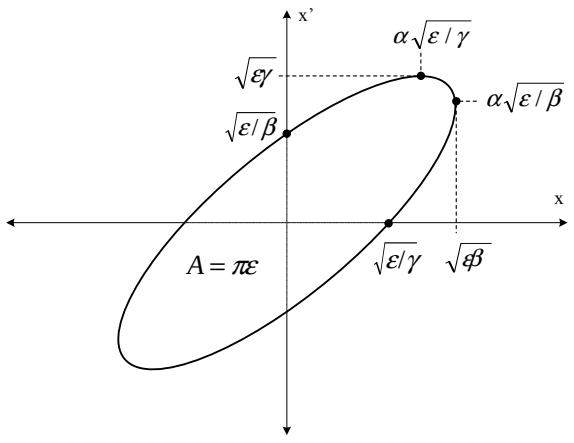

Figure 1.3: Phase-space ellipse in the $x - x'$ plane for a particle trajectory.

For proper operation, the transverse phase-space distribution of the particles must be injected within the phase-space ellipse defined by the twiss functions of the machine (matched distribution), and centered with respect to the closed orbit at the injection location. Otherwise, the distribution rotates and the beam size or beam position oscillates with time as shown in figure 1.4.

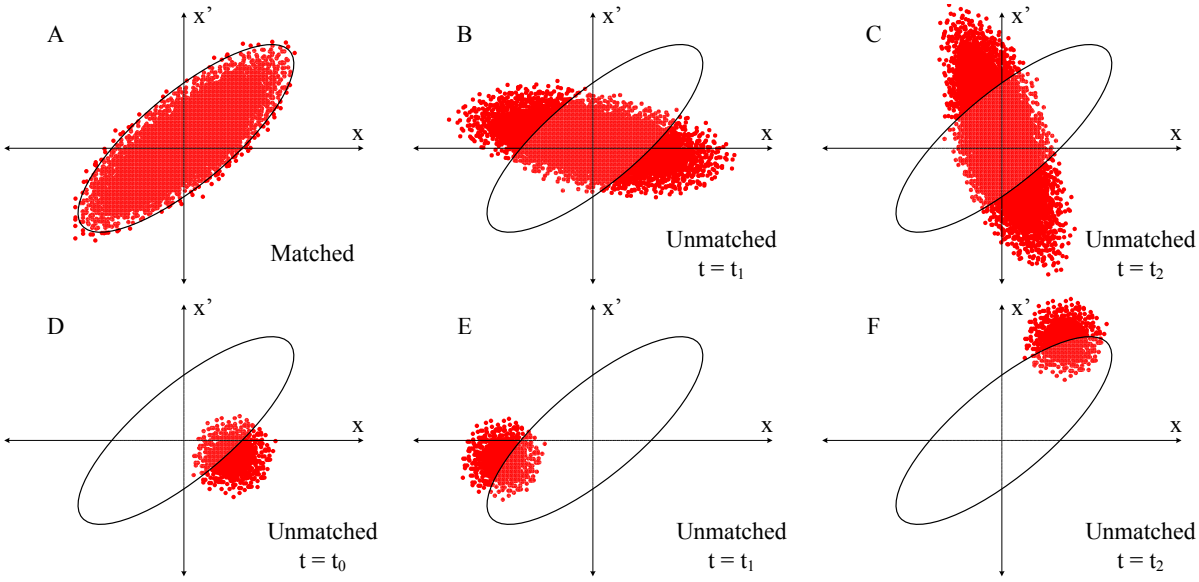

Figure 1.4: Matched and unmatched phase-space distributions in the horizontal plane. If the particle distribution does not fit inside the phase-space ellipse at a given location, the distribution is not constant over time and oscillatory phenomena are observed. A shows a matched distribution. B and C show unmatched centered distributions. D, E and F show distributions that are not centered with respect to closed orbit.

1.3.4 Normalized coordinates

In some cases it is useful to transform the phase-space ellipse into a circle. In this case, the particle trajectory is described by the normalized coordinates, $\widetilde{x} - \widetilde{x'}$, which relate to $x - x'$:

$$\begin{pmatrix} \widetilde{x} \\ \widetilde{x'} \end{pmatrix} = \begin{pmatrix} \frac{1}{\sqrt{\beta}} & 0 \\ \frac{\alpha}{\sqrt{\beta}} & \sqrt{\beta} \end{pmatrix} \cdot \begin{pmatrix} x \\ x' \end{pmatrix} \tag{1.27}$$

1.3.5 Twiss parameters and transfer matrices

From 1.22 and 1.25 we can derive the relationship between the particle trajectory at different points in the machine and the twiss parameters at these locations. Writing this in matrix form we find the transfer relationship expressed in equation 1.13. Setting $\beta(0) = \beta_0$ and $\alpha(0) = \alpha_0$ we can write the transfer matrix $\boldsymbol{M}$ as a function of the twiss functions from the previous equations:

$$\boldsymbol{M}_{s_0 \to s} = \begin{pmatrix} \sqrt{\frac{\beta}{\beta_0}} \left(\cos(\Delta\Psi) + \alpha_0 \sin(\Delta\Psi)\right) & \sqrt{\beta\beta_0} \sin(\Delta\Psi) \\ \frac{1}{\sqrt{\beta\beta_0}} \left((\alpha - \alpha_0)\cos(\Delta\Psi) - (1 + \alpha\alpha_0)\sin(\Delta\Psi)\right) & \sqrt{\frac{\beta_0}{\beta}} \left(\cos(\Delta\Psi) - \alpha \sin(\Delta\Psi)\right) \end{pmatrix} \tag{1.28}$$

1.3.6 Emittance and beam size

In the previous section, we have defined the emittance ϵ for a single trajectory. In general, the transverse distribution of particles in the whole beam can be described by a Gaussian distribution. This approximation is very accurate in the case of electron beams [11]. For proton beams an assumed Gaussian distribution may not be as accurate as for an electron beam, but is generally a good approximation. The standard deviation σ of this Gaussian distribution is referred to as the transverse beam size. From the beam size, we define the *beam emittance* as:

$$\epsilon_{beam} \equiv \frac{\sigma^2(s)}{\beta(s)} \tag{1.29}$$

Thus, once ϵ_{beam} is known, we can easily infer the size of the beam at a given location s:

$$\sigma(s) = \sqrt{\epsilon_{beam}\beta(s)} \tag{1.30}$$

The transverse emittance is defined for the horizontal and vertical planes. In some cases it is interesting to know the beam size in a different plane (the plane of a skew collimator, for instance). If the angular offset of the skew plane with respect to the horizontal one is θ, the beam size in this plane is given by

$$\sigma^2(s) = \sigma_x^2(s)cos^2(\theta) + \sigma_y^2(s)sin^2(\theta) \tag{1.31}$$

1.3.7 Tune and optical resonances

The tune Q is defined as the number of betatron oscillations that a particle undergoes in one complete revolution around the accelerator. The tunes in the horizontal and vertical planes are not necessarily equal.

$$Q \equiv \frac{\Psi(s+L) - \Psi(s)}{2\pi} = \frac{1}{2\pi}\oint \frac{ds}{\beta(s)} \tag{1.32}$$

Optical resonances occur due to the inevitable fact that the magnetic field in a real accelerator is full of small imperfections. The actual magnetic field at a given position can be written as $\vec{B}(s) = \vec{B}_{design}(s) + \Delta\vec{B}$. $\vec{B}_{design}$ is the desired magnetic field. $\Delta\vec{B}$ accounts for the field errors, and can be decomposed in its multipolar components as well.

For particular values of Q, the effects of these imperfections can add-up over consecutive revolutions, leading to a progressive increase of the amplitude of the particle oscillations. This happens if, for every turn, the error field seen by a particle kicks it in the same direction with respect to the reference orbit. Since multipolar fields of order n present an n-fold transverse symmetry, a tune such that $nQ = p$ $(p, n \in \mathbb{N})$ means that every turn, the n-polar error fields in the accelerator will kick a particle in the same direction with respect to its ideal trajectory. This yields the resonance condition in a single plane. Rather than for a single value of Q, resonances happen for a range around this value, known as the stop band-width, which depends on the strength of the error field. For the two planes, the *resonance condition* writes

$$mQ_x + nQ_y = p, \qquad m, n, p \in \mathbb{Z} \tag{1.33}$$

The sum $|m| + |n|$ is called the order of the resonance. Resonances of first and second order are *linear resonances*. If $m \neq 0$ and $n \neq 0$ we have coupled resonances. Two cases of coupled resonances are of particular interest:

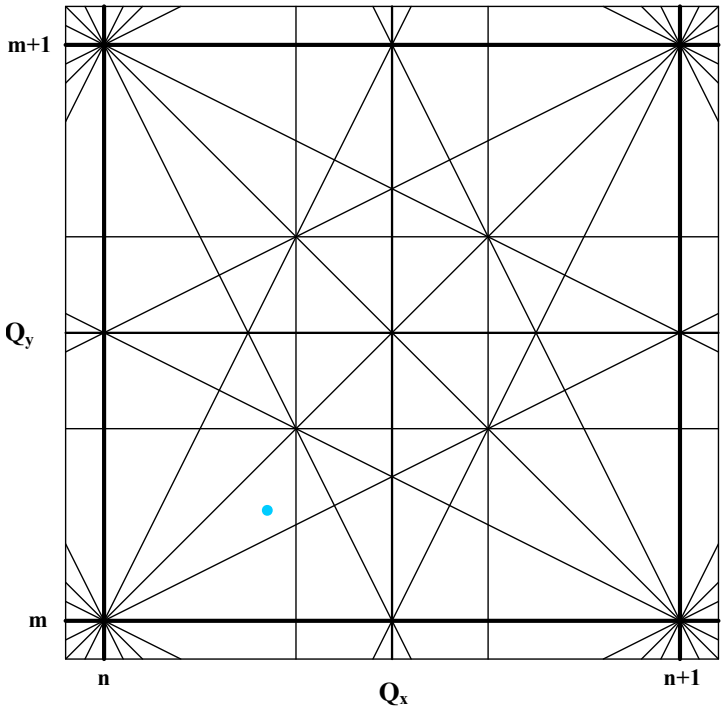

Figure 1.5: Resonance diagram up to 3rd order. The blue spot locates a possible choice for the working point.

- *Linear difference coupling resonance*: $Q_x - Q_y = p$, $p \in \mathbb{Z}$. In this case the sum of the emittances in each plane remains constant and there is no beam instability. Instead, a transfer of oscillation amplitudes between both planes takes place

- *Linear sum coupling resonance*: $Q_x + Q_y = p$, $p \in \mathbb{Z}$. The difference of the emittances in each plane remains constant and, depending on the tunes and coupling coefficient, the beam can become instable.

Figure 1.5 shows a graphic representation of the resonance conditions up to third order. The working point of the machine has to be chosen far from the resonance lines in the diagram, particularly from those corresponding to integer and half integer resonances, since the strength of the resonances quickly decreases with its order.

1.4 Effect of linear perturbations

The dipolar and quadrupolar components of the error magnetic field are called linear perturbations. These are particularly relevant, since not only they can lead to resonances as discussed in the previous section but they also affect the orbit and betatron functions of the machine.

1.4.1 Dipolar errors

A dipolar error in a single magnet is usually described as a localized kick θ_{err}. The effect of a localized single error kick in a the closed orbit is depicted in figure 1.6. The phase space ellipse referred to the closed orbit does not change, and the emittance of the particle remains constant.

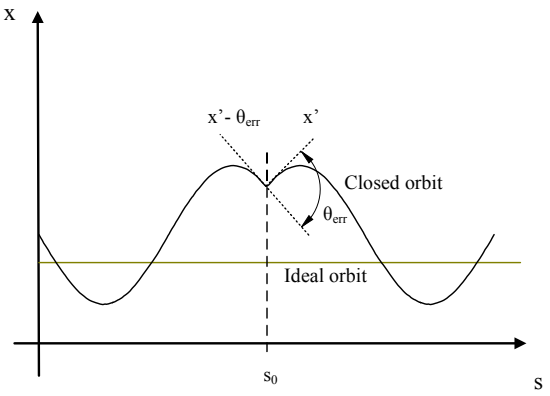

Figure 1.6: Effect of a single kick on the closed orbit.

In reality, many small error kicks are statistically distributed along the machine. Due to these kicks, the particles do not undergo their betatronic oscillations with respect to the reference orbit. Instead, they do so with respect to a stable trajectory, defined by the optics of the machine and the distributed dipolar errors. This trajectory is defined as the *closed orbit*, and it is expressed by its transverse coordinate as a function of s:

$$x_{co}(s) = \frac{\sqrt{\beta(s)}}{2\sin\pi Q} \oint P(\sigma)\sqrt{\beta(\sigma)}\cos\left(\Psi(s) - \Psi(\sigma) + \pi Q\right) d\sigma \tag{1.34}$$

where $P(\sigma)$ represents the error kick as a function of the longitudinal coordinate.

If at a given time a finite number of localized error kicks appears[2] the closed orbit at every point in the machine is displaced by:

$$\Delta x_{co}(s) = \frac{\sqrt{\beta(s)}}{2\sin\pi Q} \sum_i \theta_i \sqrt{\beta(s_i)}\cos\left(\Psi(s) - \Psi(s_i) + \pi Q\right) \tag{1.35}$$

where θ_i is the kick angle due to the field error at location s_i. $\beta(s_i)$ and $\Psi(s_i)$ are the betatron amplitude and betatron phase at the location of the error while $\beta(s)$ and $\Psi(s)$ refer to the values at any point in the lattice.

1.4.2 Quadrupolar errors

A quadrupolar error is represented by a change in the quadrupole strength, Δk. Quadrupolar errors affect the optics of the machine, producing a change in the tune and in the beta function. These changes are referred to as *tune shift* and *beta beating*. In case of failure of a finite number of magnets and supposing $\Delta k << k$ for each failing magnet, the tune shift and beta beating write:

[2]This can be due to different circumstances that will be discussed in detail in chapter 4

$$\Delta Q = \frac{1}{4\pi} \sum_i \Delta k_i l_i \beta(s_i) \tag{1.36}$$

$$\frac{\Delta\beta(s)}{\beta(s)} = -\frac{1}{2\pi \sin(2\pi Q)} \sum_i \Delta k_i l_i \beta(s_i) \cos\left(2(\Psi(s) - \Psi(s_i)) + 2\pi Q\right) \tag{1.37}$$

Where l_i is the length of the i^{th} failing quadrupole. The quadrupolar errors affect the focusing function $K(s)$. If they are large enough, equation 1.21 does not have a real solution and there is no stable beam. In the case that the errors appear at a given time, the optics quickly becomes instable leading to a loss of the whole beam.

1.5 Luminosity

In colliders, accelerators whose main purpose is to produce particle collisions for High Energy Physics, it is of interest to obtain the highest possible rate of collisions. When two bunched beams moving in opposite directions intersect, only a fraction of the particles will collide. The rate of interactions of a given type at the collision point is given by the product of the interaction cross-section and the *luminosity*. Luminosity is defined by the accelerator optics and beam intensity:

$$L = \frac{N^2 \cdot f \cdot n_b}{4\pi \cdot \sigma_x^* \sigma_y^*} \tag{1.38}$$

N is the number of particles in each bunch, f the revolution frequency, given by the length of the machine, n_b is the number of bunches in the beam and σ_x^*, σ_y^* the horizontal and vertical beam sizes at the collision point.

Chapter 2

The LHC and the LHC Machine Protection Systems

This chapter introduces the layout of the LHC and its nominal operation cycle. The state of the art of simulation studies on beam losses in the LHC is presented and the Machine Protection Systems are described focusing on the reaction times of the different subsystems.

2.1 The LHC layout and main magnets

In the LHC, two vacuum chambers contain the two beams circulating in opposite directions. In the major part of the storage ring the horizontal distance between the two beams is 194 mm. In the four experimental areas, the vacuum chambers merge allowing the two LHC beams to cross in the interaction point, thus generating the $p-p$ collisions. The different LHC elements are disposed around the vacuum chambers at different locations in order to control the beam, accelerate the particles or measure the different beam parameters necessary for a smooth and safe operation.

2.1.1 The LHC layout

The LHC accelerator ring is divided into eight *sectors*, each confined by two *interaction points*[1] (IPs). At both sides of each IP there is a long straight section, named *insertion region*, which connects to the *arc* of the adjacent sector (figure 2.1).

2.1.1.1 The LHC arcs

The arcs are formed by consecutive FODO cells (figure 2.2), which contain six main dipole magnets, two main quadrupoles and a set of less powerful magnets with up to 10 poles. These are used for orbit correction, betatron tune control and compensation of chromaticity and other higher order phenomena. All the magnets in the arc are superconducting.

At each end of the arcs, before the insertions, lie the *dispersion suppressors* (DS), two FODO cells with missing dipoles. Their main role is to reduce the dispersion arising in the arc and generated by the strong dipoles in the insertions.

[1] Altough physical interactions are meant to occur only in four of these points -IP1, IP2, IP5 and IP8-, all of them are referred to as interaction points.

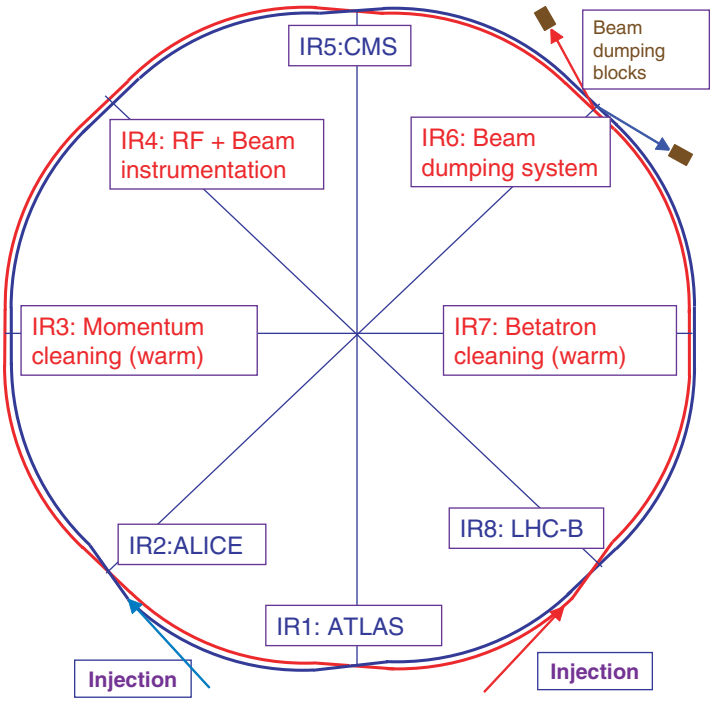

Figure 2.1: Schematic layout of the LHC. Beam1 circulates clockwise, beam 2 circulates counter-clockwise.

2.1.1.2 The LHC insertions

The insertion regions contain equipment which is specific of each IP. The four experimental insertions have a similar layout whose main function is to prepare the beams for collision. In addition, IR2 and IR8 (insertions for the ALICE and LHCb experiments respectively) host the injection kickers and septum magnets, as well as the connection of the vacuum chamber to the injection lines.

Figure 2.3 shows a longitudinal view of the layout of the right side of IR1. Q1, Q2 and Q3, referred to as *inner triplets*, are strong superconducting quadrupoles that squeeze the beam to achieve a very small transverse size at the collision point. D1 and D2 are the dipoles that control the crossing of the two beams and separate them after the collision. IR5, the experimental insertion for the CMS detector, has a similar layout.

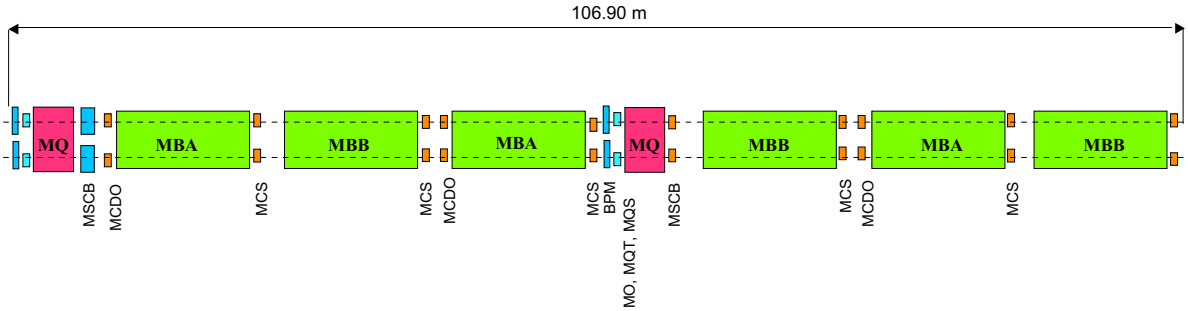

Figure 2.2: Schematic layout of an LHC arc FODO cell [1].

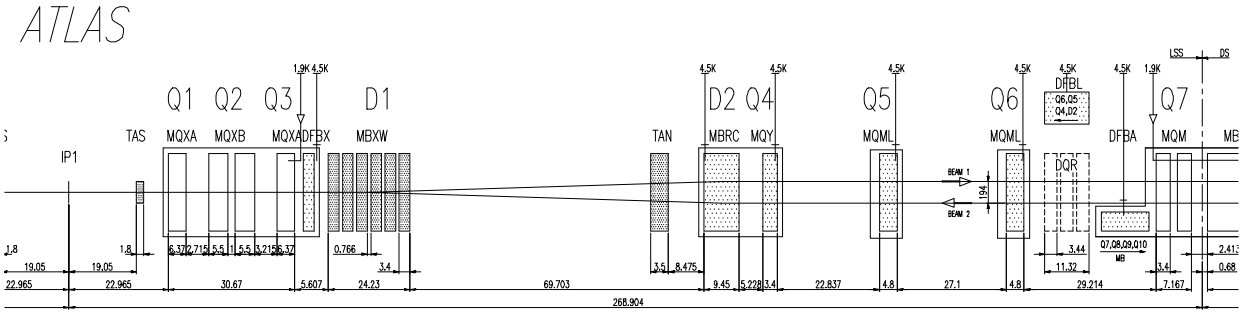

Figure 2.3: Schematic longitudinal layout of the insertion region right to IP1 [1].

The layout of IR2 is represented in figure 2.4. The main elements described above are present, with in this case a superconducting magnet for D1. Injection kickers are located between Q4 and Q5, and injection septa between Q5 and Q6. The collimators TDI and TCDD between D1 and D2 protect the equipment against possible faulty injections. Besides, the ALICE experiment contains a strong dipole for spectrometry and normal conducting compensating dipoles are placed close to the experiment (MBXWT and MBWMD). IR8 has a similar layout.

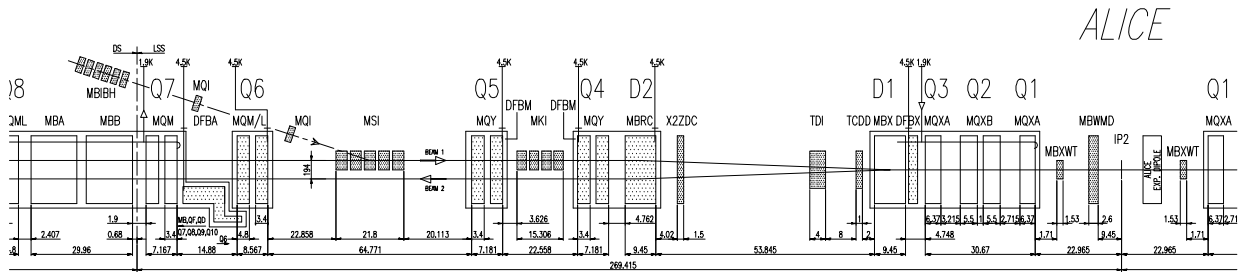

Figure 2.4: Schematic longitudinal layout of the insertion region left to IP2 [1].

The superconducting accelerating cavities of the LHC are located in IR4 (*RF insertion*). To leave enough space for the accelerating cavities, the two beams need a larger horizontal separation than nominal, which is achieved with two superconducting dipoles (D3 and D4). The layout of IR4 is depicted in figure 2.5.

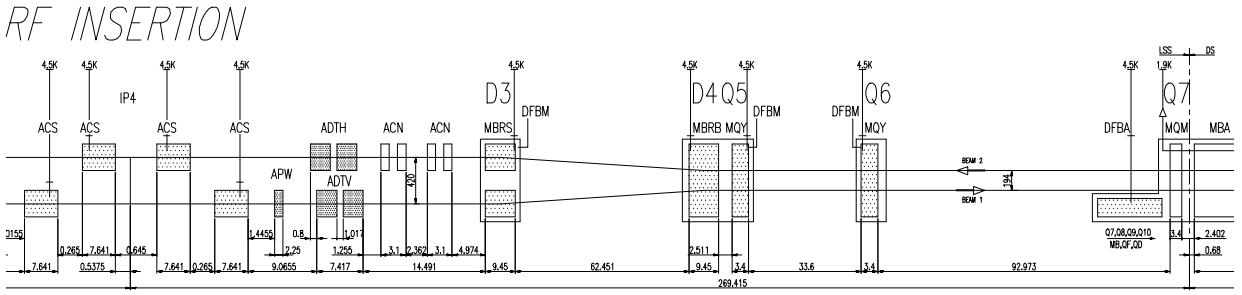

Figure 2.5: Schematic longitudinal layout of the insertion region right from IP4 [1].

IR3 and IR7 are referred to as the *cleaning insertions* and they are reserved for the collimation of particles with high momentum offset or transverse amplitude deviations. Due to the collimation

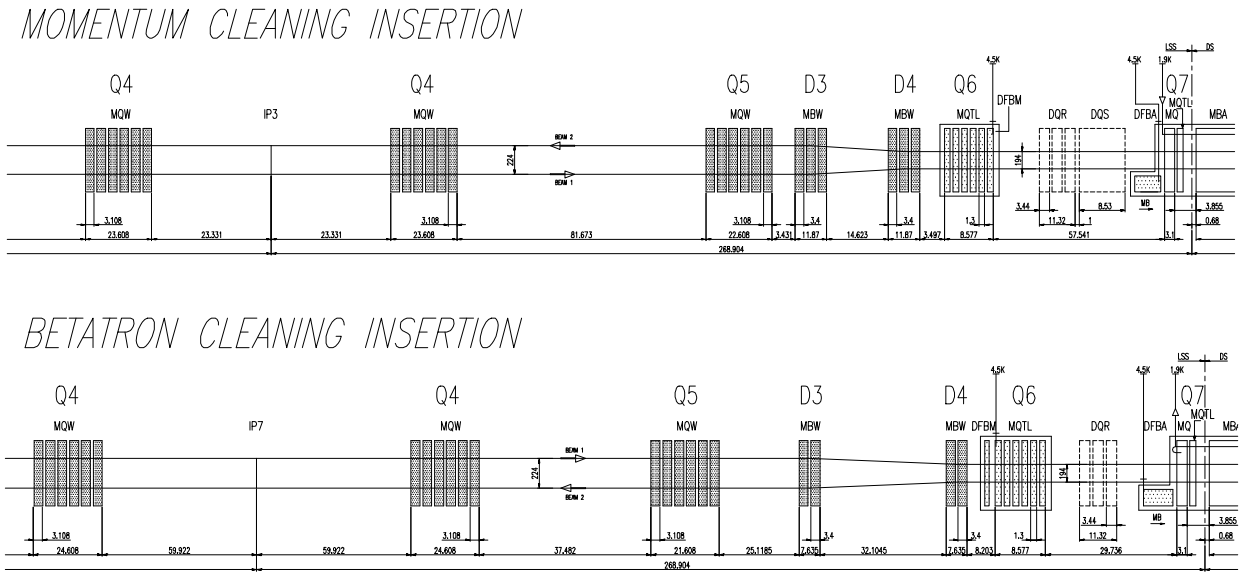

Figure 2.6: Schematic longitudinal layout of the right side of the cleaning insertions IR3 and IR7. [1].

process, many scattered particles are expected to deposit part of their energy in the magnets at these regions. Therefore, maintaining the cryogenic temperature required for superconducting magnets in the cleaning insertions is a difficult task, and normal conducting magnets are used in order to avoid quenches.

IR3 is the *momentum cleaning insertion*. The optics in this region have been designed to provide a high dispersion function so that a set of collimators adequately located can intercept and absorb particles with a high momentum offset. IR7 is named the *betatron cleaning insertion* and it is reserved for the collimation of the particles with high betatron amplitudes. In this region, the beam undergoes large betatron oscillations. Collimators located in the points where the beam is larger intercept the particles with amplitudes larger than about six times the beam size. The layout of the cleaning insertions is represented in figure 2.6. The layout of the collimators in these regions will be presented later in this chapter.

IR6 houses the beam dump systems for both beams. Kicker magnets are located between Q4 and Q5, before the IP, and further in the extraction line. The extraction septa are located around IP6 for both beams (figure 2.7). To protect against possible faulty extractions, the TCDQ collimator is located in front of the Q4 magnet and the TCDS absorber in front of the septum magnet.

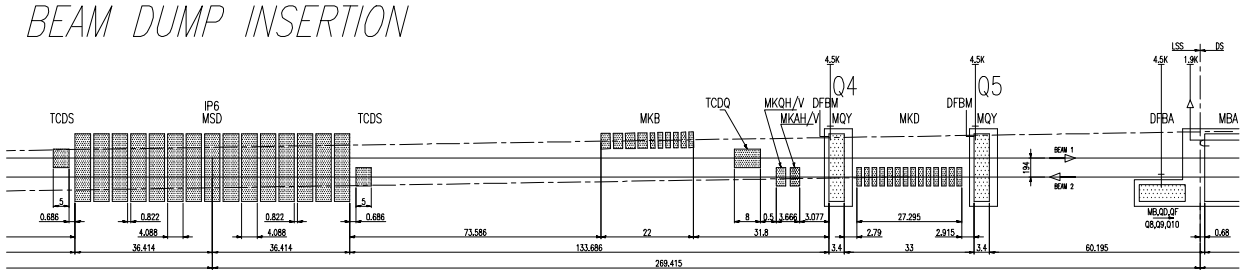

Figure 2.7: Schematic longitudinal layout of the insertion region right from IP6 [1].

2.1.2 The LHC main magnets

This section gives an overview of the main magnets of the LHC. Only the magnets that are needed for a proper understanding of the following chapters are treated below. A detailed presentation of all the magnets in LHC can be found in [1].

There are 9594 magnets along the LHC ring from which about 2900 have the potential, in case of faliure, to produce significant losses within hundreds of milliseconds or less. Their failures are of particular relevance to machine protection. Table 2.1 lists the different types of magnets in the LHC that have been considered for failure studies.

In order to reach the high magnetic fields required to operate beams at an energy of 7 TeV, superconducting technology is needed in most of the magnets. The coils are made of Nb-Ti cables that need to be cooled down to a temperature of 1.9 K to reach superconductivity under the nominal operating conditions of the LHC [13]. In some magnets requiring less magnetic field the nominal operating temperature is of 4.5 K.

2.1.2.1 Magnets in the arc

Each of the eight LHC arcs contains 154 main dipole magnets, 49 main quadrupole magnets as well as a higher number of smaller dipoles for orbit correction and higher order multipole magnets [14]. The most important characteristics of the main dipoles and quadrupoles are listed in table 2.2.

The superconducting coils are winded inside an iron and steel cold mass, which provides a very stable mechanical support against the strong electromagnetic forces that the coils stand during operation. The cold mass contains also other built-in equipment, such as heat exchange tubes, magnet bus bars, instrumentation wires and spool-piece correction magnets. Insulation layers

Magnet Name	Type[a]	Description	B_{nom} / g_{nom} [b]	Number[c]
MB	SC	Main dipole (arc)	8.33 T	1232
MBRB/C/S	SC	Separation dipoles D2, D3, D4 (IRs)	3.8 T	14
MBW	NC	D3 and D4 in IR3 and IR7	1.42 T	20
MBX	SC	Separation dipole D1 (IR2, IR8)	3.8 T	4
MBXW	NC	Separation dipole D1 (IR1, IR5)	1.28 T	24
MBWMD	NC	Compensator for ALICE spectrometer	1.35 T	1
MBXWH	NC	Compensator for LHCb spectrometer	1.24 T	1
MBXWT	NC	Compensator for ALICE	1.68 T	2
MBXWS	NC	Compensator for LHCb	1.1 T	2
MCBxx	SC/NC	Orbit correctors (arc/IRs)	1.1 - 3.6 T	1
MKD	NC	Dump extraction kicker	0.25 T	30
MKI	NC	Injection kicker	1.2 T	8
MSDA/B/C	NC	Dump extraction septa	0.8 - 1.2 T	30
MSIA/B	NC	Injection septa	0.8 - 1.7 T	10
MQ	SC	Main quadrupole (arc)	223 T/m	392
MQWA/B	NC	Q4 and Q5 in IR3 and IR7	30 - 35 T/m	48
MQXA/B	NC	Inner triplet quadrupoles (Q1, Q2, Q3)	205 T/m	48

Table 2.1: Magnets that have the potential to produce a relevant amount of fast beam losses in case of failure.
a: NC for normal conducting, SC for superconducting.
b: Nominal field for dipoles, nominal gradient for quadrupoles. Given for nominal operation at 7 TeV
c: Number of magnet modules, not necessary equal to the number of functional magnets (i.e. D1, D2, Q4, etc.) For instance, each D1 in IR1 and IR5 is formed by six MBXW modules (see figure 2.3)

Parameter	MB	MQ
Magnetic length (m)	14.3	3.1
Nominal temperature (K)	1.9	1.9
Inductance (mH)	102	5.6
Nominal current (A)	11850	11870
Nominal field (T)	8.33	-
Nominal gradient (T/m)	-	223
Bending angle (mrad)	5.099	-
Stored energy (kJ)	7162	789

Table 2.2: Some important characteristics of the main dipole and quadrupole in the arcs. The values are given for nominal operation at 7 TeV.

surround the cold mass in vacuum to reduce heat exchange. The cold mass, the insulation layers and the vacuum vessel form the *cryostat*, which is the basic unit of the LHC physical layout in the arcs. An arc quadrupole cryostat is shown in figure 2.8.

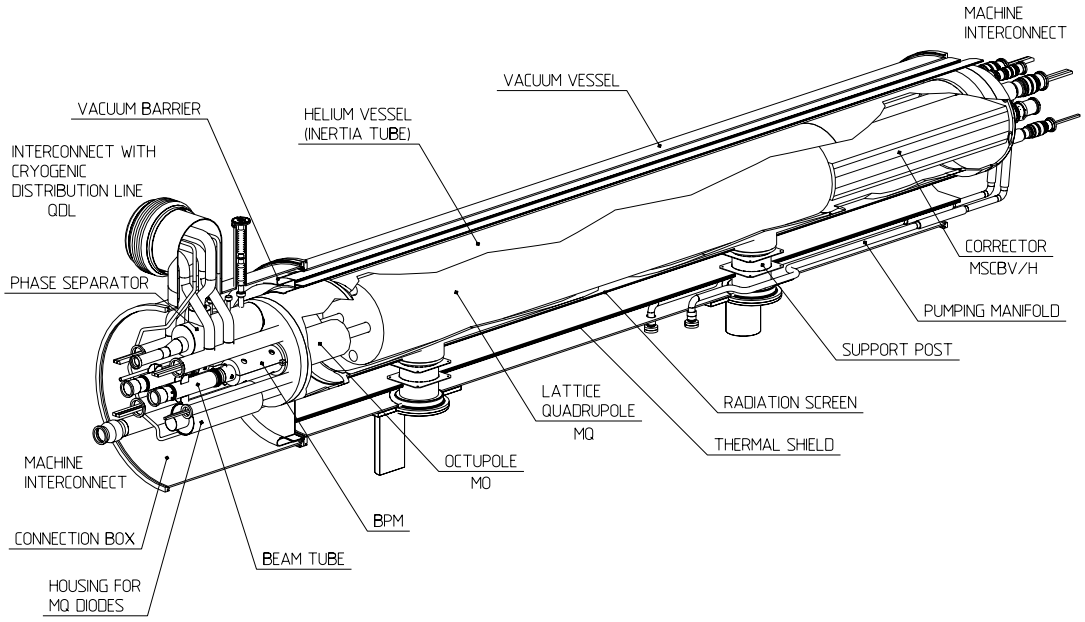

Figure 2.8: Cryostat for a superconducting quadrupole in the arc [1].

Smaller magnets are embedded in the main dipole and quadrupole cryoassemblies, as shown in figure 2.8. These include:

- Dipoles for orbit correction.
- Quadrupoles for coupling compensation and optics matching.
- Sextupoles for chromaticity compensation.
- Octupoles and decapoles for correction of other non linear effects and compensation of multipolar errors.

Although the cryostats in the arcs share the same structure, many of them are adapted to their particular location. A detailed list of the different types of magnets and cryostats is beyond the scope of this work and can be found in [1].

2.1.2.2 Magnets in the insertions

The number of different types of magnets in the insertions is greater than in the arcs, since they are adapted to the particular optical solutions required around each IP. Each superconducting magnet in the insertions is installed in a cryostat, very much like the main magnets in the arcs described above. Besides, in some regions, debris from the experimental collisions or protons scattered out of the beam by collimators lose most of their energy in the accelerator elements, depositing an unacceptable heat load into superconducting magnets in these areas. For this reason some of the magnets in the insertions are normal conducting.

The types and roles of the magnets in the insertion are listed below. Not all of these magnets are installed in all the insertions.

- *Separation dipoles* (D1, D2, D3, D4): Their role is to adapt the trajectory of the beams to the requirements of the IRs or to control the crossing of the two beams in the interaction points. D1 in IR1 and IR5 as well as D3 and D4 in IR3 and IR7 are normal conducting; the other magnets are superconducting.

- *Compensator dipoles*: Normal conducting magnets to compensate for the effect on the beam of the experimental spectrometers from the ALICE and LHCb detectors.

- *Inner triplets* (Q1, Q2A, Q2B, Q3): Four associated superconducting quadrupoles very close to the experimental areas. Their role is to squeeze the beams in the interaction points to achieve high luminosity for collisions. Therefore, they are installed only in the experimental insertions (IR1, IR2, IR5 and IR8).

- *Matching and trim quadrupoles* (Q4 to Q7): Used to match the optics between the insertion regions and the arcs. All are superconducting except Q4 and Q5 in IR3 and IR7.

- *Orbit correctors, trim quadrupoles and multipole packages*: Associated to the matching quadrupoles and inner triplets. Apart from 16 warm orbit correctors in IR3 and IR7, they are built-in inside the quadrupole cryostats.

- *Kickers and septa*: Fast magnetic elements used for injection, in IR2 and IR8 and for the extraction of the beam in the dump region in IR6.

Table 2.3 shows the most relevant characteristics of the main dipoles in the insertions. Table 2.4 presents a similar list for the inner triplets and warm matching quadrupoles in the insertions. The data are given for each physical magnet (coil). In some cases, particularly for normal conducting magnets, each functional magnetic unit is made up of several magnets lined up and connected in series:

- D1 in IR1 and IR5 consists of six MBXW magnets.

- D3 and D4 are made up of three MBW magnets in IR7 and two MBW magnets in IR3.

- Q4 and Q5 in IR3 and IR7 are made of five MQWA magnets and one MQWB magnet each.

Parameter	MBX	MBXW	MBRC	MBRS	MBRB	MBW
Magnetic length (m)	9.45	3.40	9.45	9.45	9.45	3.40
Nominal temperature (K)	1.9	293	4.5	4.5	4.5	293
Coil inductance (mH)	25.8	145	51.6	25.8	51.6	180
Coil resistance (mΩ)	-	60	-	-	-	55
Nominal current (A)	5800	750	6000	5520	5520	720
Nominal field (T)	3.8	1.3	3.8	3.5	3.5	1.4
Bending angle (mrad)	1.54	0.19	1.54	1.42	1.42	0.21
Stored energy (kJ)	434	40	929	786	786	47
Coils in cryostat	1	-	1	2	1	-

Table 2.3: Some parameters of dipole magnets in the insertions. Orbit correctors are not listed. The values are given for nominal operation at 7 TeV.

Parameter	MQXA	MQXB	MQWA	MQWB
Magnetic length (m)	6.37	5.50	3.11	3.11
Nominal temperature (K)	1.9	1.9	293	293
Coil inductance (mH)	90	19	28	28
Coil resistance (mΩ)	-	-	37	37
Nominal current (A)	6450	10630	710	600
Nominal gradient (T/m)	205	205	35	30
Stored energy (kJ)	1887	1073	7	5
Coils in cryostat	1	1	-	-

Table 2.4: Some parameters of the inner triplets and warm quadrupoles in the insertions. The values are given for nominal operation at 7 TeV.

2.2 The powering scheme for the LHC magnets

The high number of magnets, the high currents in the coils and the necessity of very stable magnetic fields represent demanding constraints for the electrical equipment needed to power the magnets. Most magnets fulfilling the same role with respect to the optics of the LHC are connected in series in the same circuit, if they are located in the same sector or insertion region. Some magnets, particularly in the insertions, need to be individually powered to provide flexibility during operation. In total, the LHC uses 1612 different electrical circuits of superconducting and normal conducting magnets.

The different superconducting coils in the same circuit are connected in series via superconducting bus bars located inside the cryostats. The connection of the superconducting circuits to the power converters is done via especially designed distribution feed boxes (DFBs) that allow the passage of the current from normal conducting cables at room temperature to the superconducting bus bars in the cryostats at 4.5 K [15].

Besides, the energy stored in the superconducting circuits is very high (see tables 2.2, 2.3 and 2.4). This represents a potential danger for the magnets if this energy were dissipated inside the cryostats. Protection mechanisms are set up in order to extract this energy if a quench (loss of superconductivity) is detected. The current is redirected towards discharge resistors that dissipate the stored energy safely [16], [17]. The detection of the quench and the extraction of the energy stored in the circuits is ensured by the Quench Protection Systems (QPS) [18], presented later in this chapter.

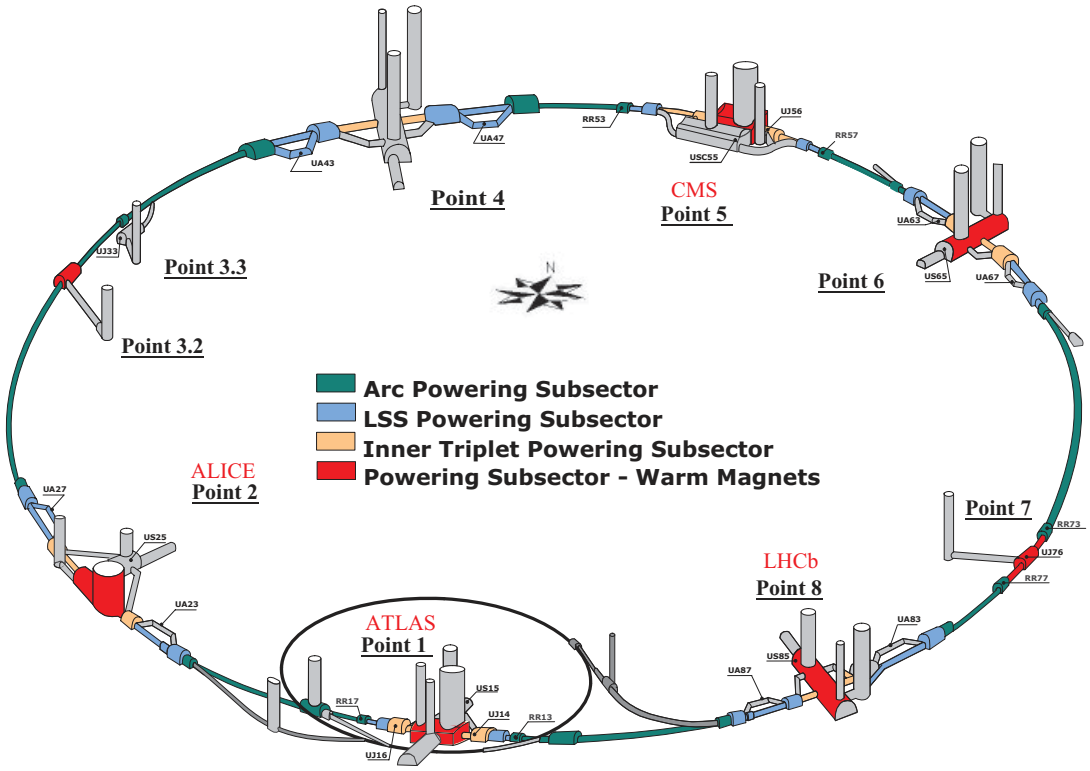

Figure 2.9: Distribution of the different powering subsectors in the LHC ring.

2.2.1 Powering subsectors

In order to reduce the energies stored in the electrical circuits and allow easier installation, testing and commissioning, the electrical circuits in the LHC are divided into 28 independent powering subsectors:

- 8 arc powering subsectors with all the powering equipment related to the magnets in the arc cryostats.
- 8 powering subsectors for all the superconducting magnets close to the experimental insertions (inner triplets and superconducting D1).
- 12 powering subsectors for the rest of the superconducting magnets in the insertion regions.
- 7 powering subsectors for the normal conducting magnets.

The distribution of the powering subsectors listed above along the LHC ring is represented in figure 2.9.

2.2.2 Main circuits

Many of the magnets presented in the previous section are not individually powered. Table 2.5 lists the characteristics of some important circuits containing more than one magnet. The rest of the magnets presented in the previous section are individually powered. In most cases, the powering of the coils is common for both beams (the coils corresponding to beam 1 and beam 2 are connected in series within the same circuit).

Circuit	Location	Magnet type	Number of magnets	Description
RB	Arcs	MB	154	Main dipoles
RQF	Arcs	MQ	47/51	Main quadrupoles (focusing)
RQD	Arcs	MQ	47/51	Main quadrupoles (defocusing)
RQX	IR1/2/5/8	MQXA/B	4	Inner triplets
RD1	IR1/5	MBXW	12	Warm separation dipoles
RD34	IR3/7	MBW	12/8	Warm separation dipoles
RQ4/5	IR3/7	MQWA/B	12	Warm matching quadrupoles

Table 2.5: Some important circuits with more than one magnet connected in series.

The main dipole circuit in the arcs (RB) contains all the 154 main bending magnets connected in series and covers the whole arc. There are eight RB circuits in the LHC, one per sector, storing 1.22 GJ each. Two circuits per sector connect the main quadrupoles in the arc, one for the focusing quadrupoles (RQF) and one for the defocusing ones (RQD). Depending on the sector, these circuits count either 47 or 51 magnets each. The interconnection of the magnets in the arcs is shown in figure 2.10.

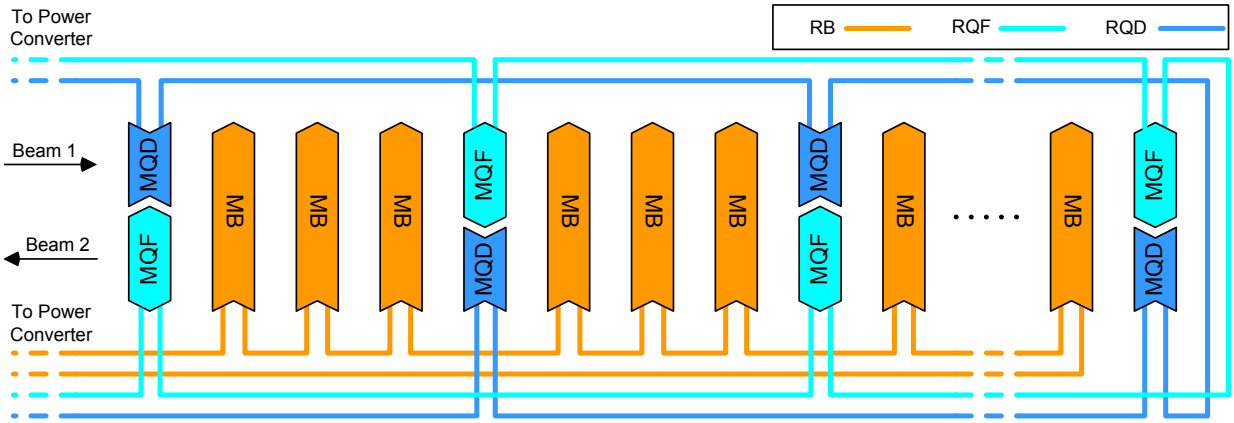

Figure 2.10: Powering of the main dipoles and quadrupoles in the arcs. Note the alternate connection of focusing and defocusing quadrupoles, with magnets for both beams connected in the same circuit.

For the inner triplets, a scheme with three nested power converters was chosen [19] in order to optimize the powering. The quench protection and energy extraction is common to all of the triplet quadrupoles.

The normal conducting circuits RD1 (in IR1 and IR5), RD34, RQ4 and RQ5 (in IR3 and IR7) contain normal conducting magnets that are simply connected in series. The particularity of these circuits is that they include the corresponding magnets at both sides of the interaction point, unlike superconducting circuits.

2.3 The collimation system and its layout

Each of the LHC beams will contain an energy of more than 350 MJ with a transverse energy density of about 1 GJ/mm^2 [20]. This high energy concentration makes the LHC beams very destructive. Besides, it has been estimated that a fraction of about 10^{-7} of the beam is sufficient to generate a quench in the superconducting magnets [21]. An efficient collimation system is therefore

mandatory for LHC operation and intensive research has been carried out beyond the state of the art of previous collimation systems.

2.3.1 Structure of the LHC collimation system

The main goal of the collimation system in the LHC is efficient cleaning of the beam halo during operation in order to avoid quenches. In addition, the collimators reduce the halo-induced noise in the experiments and provide passive protection of other LHC elements in case of accidental beam losses.

Beam cleaning in circular machines is usually performed using blocks of carefully chosen materials that are mechanically brought close to the beam. The particles with high amplitudes are absorbed by the block, which is commonly called *jaw*. The distance between the edge of the jaw and the center of the beam is the collimator *half gap* or *half opening*. The majority of the collimators in LHC are made of two parallel jaws that limit the aperture at both sides of the beam. Figure 2.11 shows an LHC carbon-carbon collimator jaw. The jaws are movable for most of the LHC collimators in order to adapt their position to the local beam parameters during operation.

Figure 2.11: Carbon collimator jaw used in LHC collimators.

In the LHC, three collimation stages reduce beam losses in the cold aperture under quench level [22]. Primary collimators intercept the lost primary protons, generating a secondary halo of scattered particles. Most of this secondary halo is absorbed in the secondary collimators. The small fraction of the particles that escapes the secondary collimators form a tertiary halo that can be lost in most of the cold aperture without producing quenches. In critical locations needing additional protection tertiary collimators and absorbers are used to intercept the tertiary halo. The phase advances and orientation of the collimators are optimized to achieve the best possible coverage in both horizontal and vertical phase-space planes. More than 99.9% of the halo particles should be captured in the cleaning insertions [22].

Table 2.6 lists the main characteristics of the primary and secondary collimators installed in the LHC.

	Primary (TCP)	Secondary (TCSG)
Length (m)	0.6	1.0
Material of jaws	C-C	C-C
Width of jaw (mm)	80	80
Depth of jaw (mm)	25	25
Minimum gap (mm)	$\leq$ 0.5 mm	$\leq$ 0.5 mm
Maximum gap (mm)	$\geq$ 60 mm	$\geq$ 60 mm

Table 2.6: Characteristics of the LHC primary (TCP) and secondary (TCSG) collimators.

2.3.2 Layout of the LHC collimators

The requirements imposed by the operation of LHC on the collimator materials and design are very restrictive [23] and there is not a single solution that can fulfill all of them. Particularly, materials robust enough to resist the LHC potential load of losses would introduce performance limitations during peak luminosity operation. Therefore, a phased approach for the installation and operation of the collimators has been adopted:

- *Phase 1*: Optimized for robustness, it includes a two-stage cleaning in IR3 and IR7 with carbon collimators, tertiary collimators at the experimental insertions and special collimators for injection protection. The layout of phase 1 collimators is presented below.
- *Phase 2*: Hybrid collimators with reduced robustness but compatible with the nominal LHC performance. Used only once the beam is stable and the losses and accident risk reduced.
- *Phase 3 and 4*: Some additional collimators will be needed if the LHC exceeds the nominal design luminosity after several years of operation. Besides, if the cleaning efficiency is not sufficient with phase 1 and 2 collimators, space has been allocated for the installation of extra collimators.

In this work, only phase 1 collimators are considered and all the references to the collimation system in the following are limited to phase 1 only. A list of the phase 1 collimators and their parameters is given in appendix A. Most of the LHC collimators are installed in the cleaning insertions IR3 and IR7. Figure 2.12 illustrates the layout of the collimation system in IR7.

2.4 Naming conventions for the LHC elements and circuits

In the following chapters, we will refer to circuits, magnets and collimators in the LHC extensively. For individual magnets, the naming convention adopted for LHC is based on the type of magnet, the position of the functional magnet from the IP, called *cell*, and the position of the physical magnet within the cell as follows: *magnet_type.position_in_cell cell*. The position of the magnet in the cell is given by a letter (A, B, C, etc.) only if there are several magnets in the cell. The cell itself is determined by its order and side from the interaction point. For instance, the first magnet left to IP2 (Q1) is named MQXA.1L2 and the second magnet in the Q4 right to IR3 is named MQWA.B4R3.

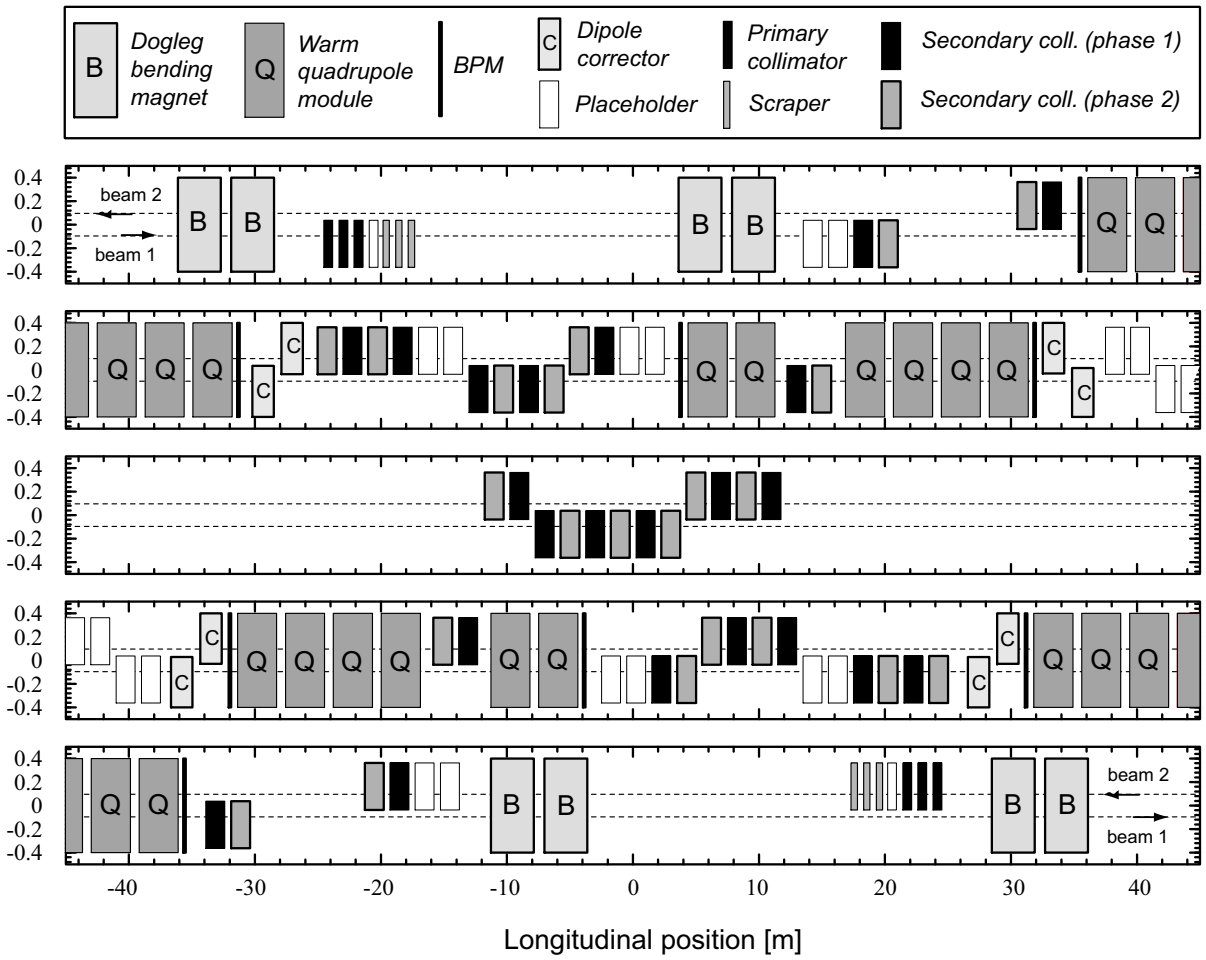

Figure 2.12: Layout of the collimators in IR7 [1].

The same convention applies for the collimators, except that the beam is also specified: *collimator_type.position_in_cell cell.beam*. Thus, TCSG.6R7.B1 refers to the secondary collimator for beam one, in the sixth cell right from IP7.

For the circuits, the convention is as follows:

- *Arc powering subsectors*: for the main dipole and quadrupole circuits, *circuit_type.A sector*. Example: RQF.A12 for the circuit containing the focusing main quadrupoles in sector 1-2, RB.A56 for the circuit with the main dipoles in sector 5-6.

- *Powering subsectors in the insertions*: *circuit_type cell_number.side ip_number*. When the circuit covers both sides it is indicated with both L and R after the cell number. Examples: RD34.LR3 for the circuit powering the separation dipoles both left and right of IP3; RD1.L2 for the circuit powering the D1 left to IP2.

2.5 The LHC operation

2.5.1 The LHC operating cycle

The operation of the LHC aims to maximize the collision time in optimal luminosity conditions and follows a well defined cycle (physics fill). This operation cycle is illustrated in figure 2.13. A physics fill is divided in different phases: injection, ramping, squeezing and physics.

The LHC beams are produced in the CERN accelerator complex. Before injection into the LHC, they are accelerated in the SPS up to 450 GeV, an energy that corresponds to a magnetic field in the LHC dipoles of about 0.54 T [24]. During the injection phase, 12 batches of either 216 or 288 bunches each are injected from SPS into each of the LHC beams. The total injection process lasts about 15 min and the two beams are kept separated in the collision points.

Once the two beams have been injected and are circulating in the LHC at 450 GeV, the field on the LHC dipole magnets is ramped up to 8.33 T corresponding to a particle energy of 7 TeV. The ramping takes about 28 min.

The beams are then prepared for collision: the transverse size in the interaction points is reduced (squeezing) and then the both beams are directed into the interaction point . This optical squeezing and crossing of the beams lasts for 5 to 10 min. Data are then acquired in the physics run for several hours.

At the end of the fill or after the detection of a failure, the beams are extracted in the beam dump region where they deposit their energy into specially designed absorbers. The magnets are then ramped down to a level slightly below the field required for injection, and just before the following injection sequence the field is set to the injection value.

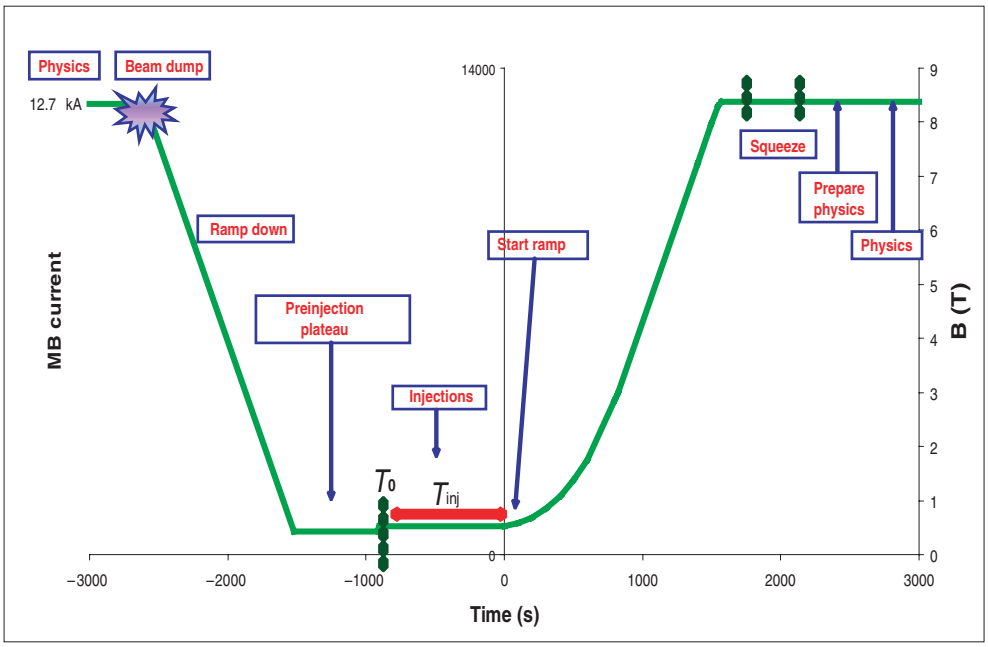

Figure 2.13: LHC operation cycle, showing the different phases of operation and energies [25].

Table 2.7 shows the main beam parameters for design injection and collision optics in the LHC. In the following, when referring to *injection optics* or *collision optics*, we mean the corresponding phase of the nominal LHC cycle, with the parameters listed in table 2.7.

		Injection	Collision
Beam Data			
Proton energy	[GeV]	450	7000
Relativistic gamma		479.6	7461
Number of particles per bunch		1.15×10^{11}	
Number of bunches		2808	
Transverse normalized emittance	[μm rad]	3.5	3.75
Circulating beam current	[A]	0.584	
Stored energy per beam	[MJ]	23.3	362
Peak Luminosity Related Data			
RMS beam size at IP1 and IP5	[μm]	375.2	16.7
RMS beam size at IP2 and IP8	[μm]	279.6	70.9
Peak luminosity at IP1 and IP5	[$\mathrm{cm}^{-2}\mathrm{s}^{-1}$]	-	1.0×10^{34}
Luminosity lifetime	[hours]	-	14.9

Table 2.7: LHC beam parameters with nominal injection and collision optics. From [1].

2.5.2 Beam losses in the LHC

A particle moving in a circular accelerator has a stable movement only if its betatron amplitude is within a certain distance to the core of the beam. The amplitude limit for this stability is called the dynamic aperture and is an important parameter of the optics of the machine [12]. Particles with amplitudes larger than the dynamic aperture are eventually lost. Besides, different phenomena make the particles drift away from the beam core. These include space charge effects, scattering of particles with other circulating particles or with residual gas molecules and beam-beam effects at the collision points [26]. As a consequence, a small fraction of the beam is constantly being lost. These losses are unavoidable and define the need of collimators for LHC. They are usually referred to as *steady losses*.

Besides, failures during operation may induce extraordinary amounts of losses known as *accidental losses*.

2.5.2.1 Steady losses and beam lifetime

The time after which the number of particles in the beam is reduced by a factor of $1/e$ due to steady losses is called the *beam lifetime* (τ). The number of particles left in the beam at a given time is therefore given by the expression:

$$N(t) = N_0 e^{-\frac{t}{\tau}} \tag{2.1}$$

The beam lifetime at LHC for nominal operation with colliding beams has been estimated to about 18 hours at 7 TeV [1], which corresponds to steady losses of about $3{\times}10^9$ p/s.

The beam lifetime during nominal injection and ramping conditions is shorter, and still shorter lifetimes can be acceptable for short periods of time. In order to limit the beam losses in superconducting magnets, the LHC will be the first accelerator requiring collimation through its entire operation cycle. Table 2.8 shows the minimum acceptable lifetimes at LHC depending on the mode of operation as well as the heat load deposited in the collimators.

Mode	T [s]	τ [h]	R_{loss} [p/s]	P_{loss} [kw]
Injection	continuous	1.0	0.8×10^{11}	6
	10	0.1	8.6×10^{11}	63
Ramp	1	0.006	1.6×10^{13}	1200
Top energy	continuous	1.0	0.8×10^{11}	97
	10	0.2	4.3×10^{11}	487

Table 2.8: Specified minimum beam lifetimes τ, their duration T, the proton loss rate R_{loss} and maximum power deposition P_{loss} in the cleaning insertion. From [1].

2.5.2.2 Accidental beam losses

During the operation of the LHC, equipment failures, operation mistakes or phenomena such as quenches may generate accidental beam losses. The accidental beam losses expected in LHC can be due to the following causes:

- *Beam deflection or defocusing*: Due to a change in the magnetic field or in the momentum of the particles, the beam can be deflected or defocused, leading to an increase of the losses.
- *Debunching*: Due to a loss of synchronization in the RF systems, the bunched structure of the beam can be affected. A debunched beam would lead to losses when extracted from the machine in the dump region [27].
- *Aperture reduction*: A total of 476 different objects can reduce or completely close the beam aperture at LHC [28]. These include collimators, vacuum valves, roman pots, injection and matching screens, RF and safety stoppers and alignment mirrors [28].
- *Beam scattering*: In case of a vacuum leak, the pressure in the vacuum chamber will locally rise. This will lead to abnormal losses due to scattering of the protons with the gas molecules [29]. Some movable objects such as wire scanners can also produce scattering of the circulating beam and generate localized losses.

Figure 2.14 represents all the possible operational failures that could lead to beam losses in the LHC.

Type of failure	Speed of losses	Cause of losses	Localization of losses
Change in magnetic field	Ultra fast to slow	Beam deflection / defocusing	Local / distributed
Change in momentum[a]	Fast	Beam deflection / defocusing	Local
Loss of vacuum	Slow	Scattering	Local
Movable object	Fast to slow	Aperture reduction	Local

Table 2.9: Different types of possible failures during operation of the LHC. Values from [30], [27], [6], [29] and [28].
a: Refers to a change in the momentum of protons caused by a failure of the RF systems. Different processes take place and the data in the table are only illustrative. See [6] for a more detailed study.

Speed of losses

Accidental beam losses can occur in a single turn, over multiple turns in a short time (less than 1 s) or during a longer timescale. The time constant of the losses is an important parameter: it

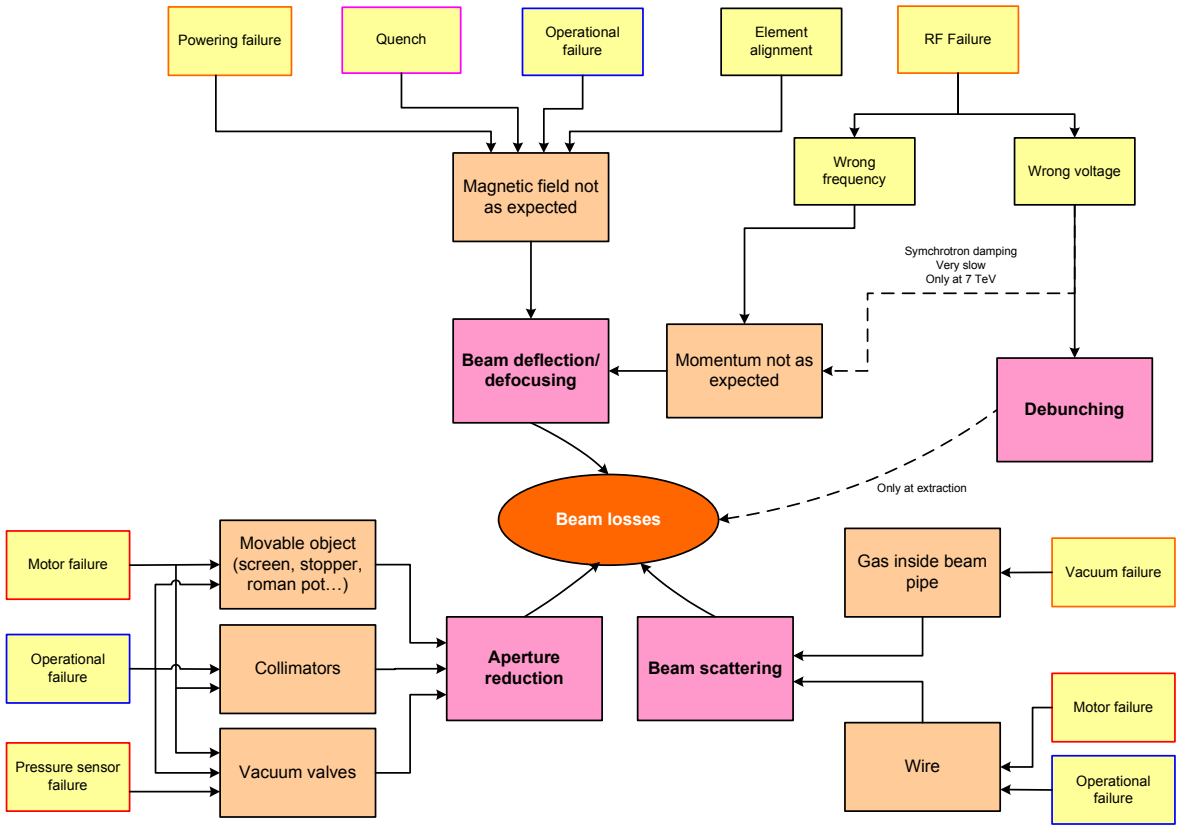

Figure 2.14: Possible failures during the operation of LHC that may lead to accidental beam losses.

determines the maximum affordable reaction time to protect the LHC elements from damage or quench. The time constants of the different failures have been estimated in [6] and [30] and are summarized in table 2.9. According to their time constant, beam losses have been classified in [31]:

- *Ultra-fast losses*: Significant beam losses develop in one turn or less. Ultra-fast losses can be produced by failures at beam injection, at beam extraction or during operation of dedicated kicker magnets [7], [27].
- *Very fast losses*: Losses develop in less than 5 ms (∼60 turns). Failures in some particular magnets in LHC can produce losses in this timescale during nominal operation [8], [30].
- *Fast losses*: Losses appear in less than 1 s (11236 turns). Most operational failures are likely to produce losses within this timescale.
- *Slow losses*: Losses develop in times larger than 1 s. Failure of low strength multipole compensator magnets, vacuum leaks and unexpected movements of slow-moving objects into the beam generate slow losses.

The above classification has been established for practical reasons, since it is not conceivable to consider all possible failure cases individually. Particularly, some accidental very slow losses can be assimilated to steady losses and be still acceptable for operation under some conditions. Similarly, some normal operating conditions can lead to high losses during a short time that would not be acceptable for continuous operation. Table 2.10 lists a set of various situations with different beam lifetimes likely to occur during operation of the LHC at 7 TeV.

Scenario	Beam Lifetime	Losses	Lost beam power (1 beam)	Comments
Optimum operating conditions	100 hr	Low steady	1 kW	Operation after some years of experience and possible upgrade of the collimation system
Acceptable operating conditions	10 hr	Normal steady	10 kW	Expected during early operation
Particular operating conditions	12 min	High steady	500 kW	Change of optics, tuning, setting of collimators aperture, etc. Operation possible only for a short time (∼10 min). Important power deposition in collimators
Standard equipment failure	1 s	Slow	330 MW	The beam has to be dumped rapidly
Fast equipment failure	15 turns	Very fast	Several 100 GW	Detection of failure and dump as fast as possible
Failure at injection or beam dump	1 turn	Ultra fast	∼TW	Potential equipment damage. Passive protection relies on collimators

Table 2.10: Beam lifetimes and losses for different operation scenarios. Adapted from [31].

2.5.2.3 Energy stored in the LHC, consequences of accidental beam losses in LHC and risk of equipment damage

The energy stored in LHC exceeds the energy stored in previous accelerators by orders of magnitude [25]. Both the energy stored in the electrical circuits and the energy stored in the proton beams have the potential to produce severe equipment damage (table 2.11).

Each LHC dipole stores more than 7 MJ during operation at nominal current (see table 2.2). The magnetic energy stored in all of the LHC magnets is about 10 GJ, equivalent to the content of about 230 kg of gasoline [32]. This energy is sufficient to heat up and melt nearly 15 tons of copper.

Energy stored in magnet system	10	GJ
Energy stored in one main dipole circuit	1.1	GJ
Energy stored in one beam	362	MJ
Beam power averaged over the length of a fill (10 hr), both beams	20	kW
Beam power averaged over one turn, one beam	3.9	TW
World Net Electricity Generation (2002)	1.7	TW
Energy to heat and melt one kg of copper from 2 K	700	kJ

Table 2.11: Energy stored in the LHC magnets and beams. From [25].

The 7 TeV proton energy at LHC will be a factor seven higher than the highest proton energy achieved so far (1 TeV at TEVATRON). The energy stored in the beams during nominal operation (362 MJ for each beam), is larger by a factor of 200 due to the very high beam intensity (see figure 2.15). Due to the small transverse dimensions of the beam, the energy density is a factor of 1000 higher than for other accelerators such as SPS, TEVATRON or HERA. This energy density is the most relevant parameter for beam induced equipment damage. Table 2.12 summarizes the intensities of the LHC beams and the estimated quench and damage levels for different modes of

operation.

Intensity of one 'pilot' bunch	5×10^{9} protons
Nominal bunch intensity	1.1×10^{11} protons
Nominal beam intensity	2808 bunches, 3×10^{14} protons
Nominal batch from SPS (at 450 GeV)	216/288 bunches, 3×10^{13} protons
Intensity below damage level for fast losses at 450 GeV	$\approx$ 1-2$\times10^{12}$ protons
Intensity below damage level for fast losses at 7 TeV	$\approx$ 1-2$\times10^{10}$ protons
Intensity below quench level for fast losses at 450 GeV	$\approx$ some 10^{9} protons
Intensity below quench level for fast losses at 7 TeV	$\approx$ some 10^{6} protons

Table 2.12: Bunch intensities, quench and damage levels for the LHC. From [25].

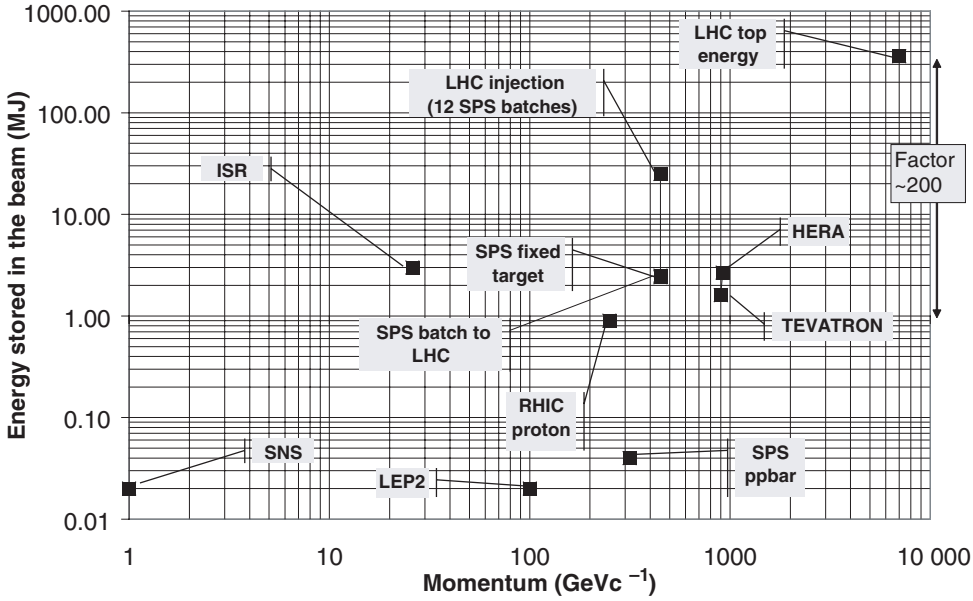

Figure 2.15: Comparison of the energy stored in the beams of different accelerators. From [25].

Release of even a small fraction this energy into the LHC elements may have serious consequences for the accelerator equipment. Beam impact into solid materials produces particle cascades due to nuclear and electromagnetic interactions. The local energy deposition and temperature increase depend on the material and on the number, energy and spatial distribution of the impacting particles. The energy deposition is calculated with simulation tools such as FLUKA [33]. The temperature increase can be estimated using the temperature-dependent heat capacity of the material, but in case of very intense and energetic beams, complex phenomena such as a localized change of state of the material or thermal shock waves take place. In this case other programs such as ANSYS® and BIG-2 [34] have to be used.

A dedicated experiment was carried out to cross-check the validity of FLUKA simulations in case of beam impact into different materials [35]. The 450 GeV beam extracted from SPS was directed into a specially designed high-Z target in order to generate damage in a controlled way (see figure 2.16). The beam intensities were chosen above the damage levels of the target: 2×10^{12}

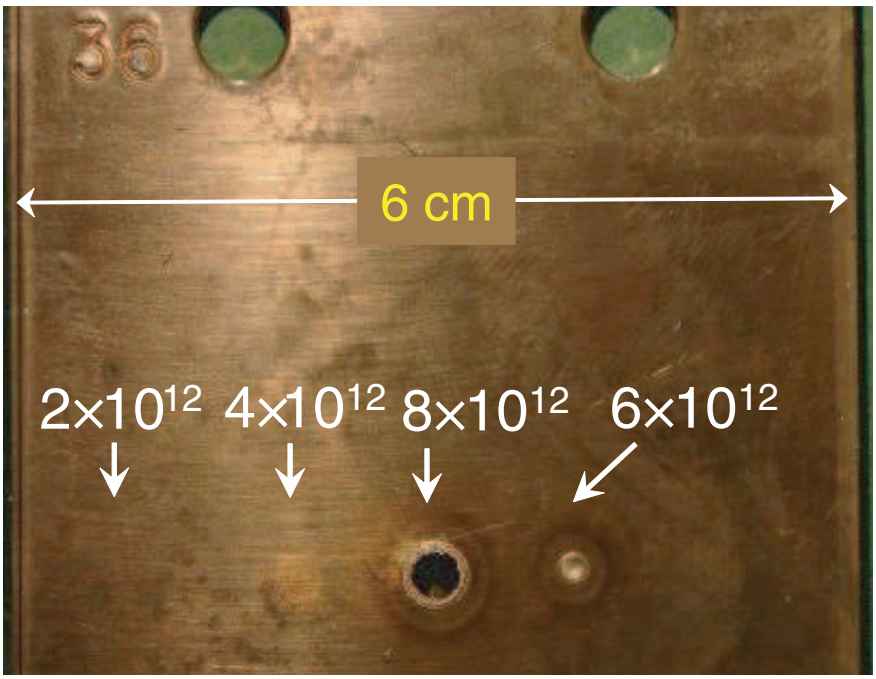

Figure 2.16: Damage of a copper plate by 450 GeV proton beams with different intensities. From [35].

to 8×10^{12} with and r.m.s. transverse size of about 1 mm. Simulations were in good agreement with the experimental results.

Quench:

A quench happens when superconducting materials return to a normal conducting state due to an increase in temperature, magnetic field or current in the coil [36]. A quench is a localized phenomenon: it builds up at a precise location in the superconducting cable and propagates thereafter. Before the propagation, the resistive part of the Nb-Ti cable is concentrated in a very small volume, and the electrical energy stored in the circuit starts dissipating in it. Without protection mechanisms, a quench in most of the LHC superconducting magnets quickly leads to damage of the coil strands. Figure 2.17 shows an unprotected dipole coil after a quench.

The temperature increase in the superconducting coils due to accidental beam losses is very likely to generate quenches, which are expected during the LHC operation. Estimates point out that a fraction as small as 10^{-8} - 10^{-7} of the LHC beam at 7 TeV can quench the LHC superconducting magnets [21]. Collimators ensure that the energy deposited in the magnets by steady losses does not reach this limit. This is not the case for accidental losses, and quenches are expected to be the fastest undesired consequence of an increase of beam losses.

Damage in the collimators:

Damage of the collimators can be caused by melting of the jaws or by the deformation of jaws and/or metallic support due to thermo-mechanical stress waves. Both effects occur in case of fast deposition of a highly concentrated heat load in case of beam impact.

Tests of carbon collimator robustness have also been performed at CERN [37]. The experimental setup reproduced the impact that the collimator would receive in case of a faulty injection (450 GeV and five full intensity batches at different offsets). The collimator jaw did not show any particular

Figure 2.17: Damage of a dipole coil after a quench during tests. The 7 MJ stored in the magnet were released in one point of the coil due to an interturn short-circuit (production imperfection).

damage. However, the metallic support showed a permanent deformation of ∼300 μm induced by the thermo-mechanical shock. Tests were carried out again with a support material with a higher elastic limit and no damage was observed. Besides, the subsequent simulation studies revealed a transient deformation of the collimator jaw of up to 1.4 mm at its center about 12 ms after the impact [38].

So far, studies on the interaction of high energy beams with different materials suggest that the LHC carbon collimators are robust enough to withstand a worst case beam impact and protect the rest of the LHC elements at 450 GeV [37], [39]. However, they would be seriously damaged in case of severe accidental losses at 7 TeV [39], [40]. As an example, a direct impact of the full intensity 7 TeV LHC beam would drill a hole between 30 m and 40 m long in copper and between 10 m and 15 m long in carbon [40].

Damage in other elements:

The effects of the beam in other elements is of the same nature as those presented for collimators, with the additional drawback that the majority of the LHC elements have not been designed to absorb a large amount of beam losses. Figure 2.18 shows the consequences of a beam impact in the vacuum chamber after a high intensity faulty extraction from the SPS in 2004.

However, direct beam impact in elements other than collimators is extremely unlikely. Losses in other elements are scattered protons and shower particles from previous impact in the collimators and are rather disperse, not being a threat for direct material damage.

2.6 The LHC Machine Protection Systems

As discussed in the previous sections, the operation of LHC involves large stored energies. In a worst case hypothetical scenario, the uncontrolled release of this energy could lead to the destruction of

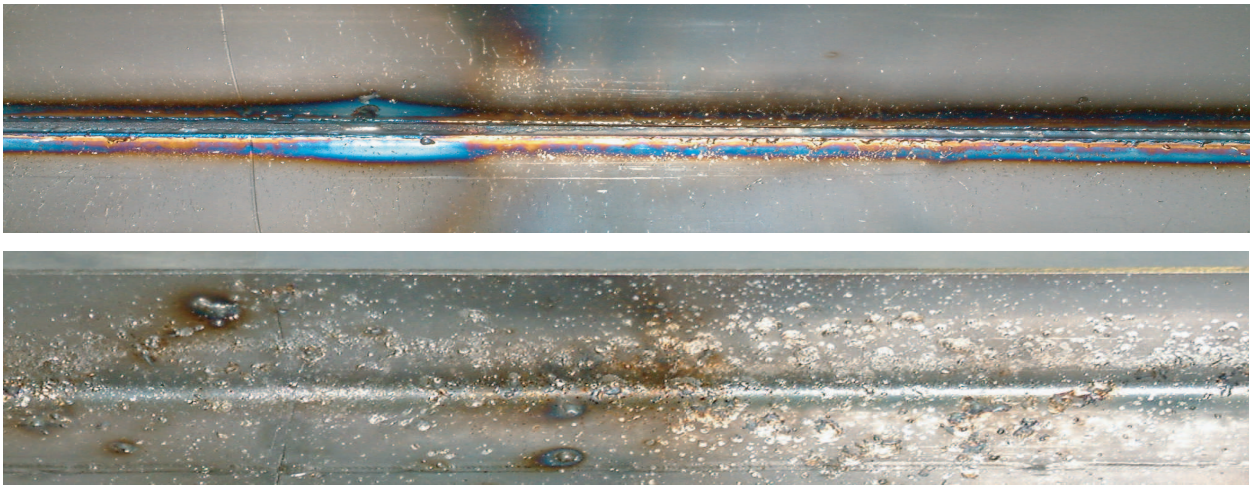

Figure 2.18: Consequences of an uncontrolled impact of a high intensity 450 GeV beam on the vacuum chamber. Groove due to removed material about 1 m long in the beam impact side (top) and droplets of projected molten material in the opposite side of the vacuum chamber (bottom).

most of the LHC magnets. A certain number of spare LHC magnets has been produced, but the cost of a replacement is high and the machine operation would have to be stopped for many weeks. If the percentage of damaged magnets is too high, they would not be replaced due to economical reasons and the LHC project would be over.

This ability to self-destruct puts the whole LHC at stake and reliable protection of the accelerator has to be ensured. The Machine Protection Systems (MPS) comprise the necessary measurement, protection and control devices to efficiently fulfill this task.

2.6.1 Strategies for protection of the LHC

In order to ensure the protection of the LHC, the Machine Protection Systems rely on interlock systems that allow operation only if the system is sufficiently functional or circulating beams do not represent a danger for machine equipment. Besides, the number of false alarms has to be reduced in order to optimize the time for physics in each cycle and to allow for optics tuning and beam commissioning.

The protection mechanisms and procedures are different depending on the part of the operating cycle. Three scenarios are of particular relevance: before injection, during operation with nominal circulating beam and during beam commissioning and optics tuning.

2.6.1.1 Protection mechanisms before injection

Safe beam transfer and injection from the SPS into the LHC relies on correct settings of all magnet currents both in the transfer lines and in the LHC. The energy of the beam in the SPS must be set to 450 GeV and no movable element must be intercepting the beam.

The SPS extraction interlock systems allow extraction only when all the elements downstream the extraction kickers have the correct settings. The LHC injection interlock system allows injection only when the LHC ring is ready for the beam, the injection elements have correct settings and the elements at the end of the transfer lines are ready. Besides, operational procedures have been defined for safe injection [41]. Stable circulating beam is the best proof that the system is fully operational. Therefore, full intensity beam is allowed only when below-damage intensity beam is

already circulating. Injection without pilot or low intensity circulating beam is allowed only with intensities below the damage level.

Machine Protection during the injection process is beyond the scope of this work and has been studied in detail in [9].

2.6.1.2 Protection mechanisms during operation with nominal circulating beam

Various protection strategies have been adopted in order to cover all the expected failure cases, which may produce losses at any speed. The combination of these strategies ensures that whatever the speed of the losses the LHC is protected.

Protection of the LHC with circulating beam implies active protection (detection of the failure and extraction of the beam before damage thresholds are reached) as well as passive protection (reliability of equipment and collimators). Concretely, the different strategies are [25]:

1. Definition of the aperture by the collimator jaws, with Beam Loss Monitors (BLMs) close to the collimators.

2. Early detection of failures within the equipment that acts on the beams to generate a beam dump request before the beam is affected.

3. Active monitoring of the beam with fast and reliable beam instrumentation, to detect abnormal beam conditions and generate a beam dump request within a very short time, down to a single machine turn.

4. Reliable transmission of a beam dump request to the beam dumping system by a distributed interlock system. For all interlocks, an active signal is required for operation, and the absence of the signal is considered as a beam dump request or injection inhibit.

5. Reliable operation of the beam dumping system on receipt of a dump request or internal fault detection, to safely extract the beams into the external dump blocks.

6. Passive protection by beam absorbers and collimators for specific failure cases.

7. Redundancy in the protection system such that failures may be detected by more than just one single system.

8. Very high safety and reliability standards that are applied in the design of the core protection systems, in general done in hardware.

Not all of these strategies are efficient to protect against all possible failures. For failures producing ultra-fast losses, there is no time to detect the failure and extract the beam. Effective protection is based on dedicated collimators and absorbers, and on the extremely high reliability of the equipment that could lead to these losses. Very fast losses can be detected by the BLMs in the aperture limitations, but the time constant of the losses may be too short to allow the protection systems to react before quench or even damage are reached [8], [30]. Hardware monitoring equipment has been installed in the magnets that can lead to very fast losses in order to detect critical failures before the losses start happening [42]. For failures leading to fast and slow losses, all the protection mechanisms react in parallel in order to provide optimum protection (see figure 2.19).

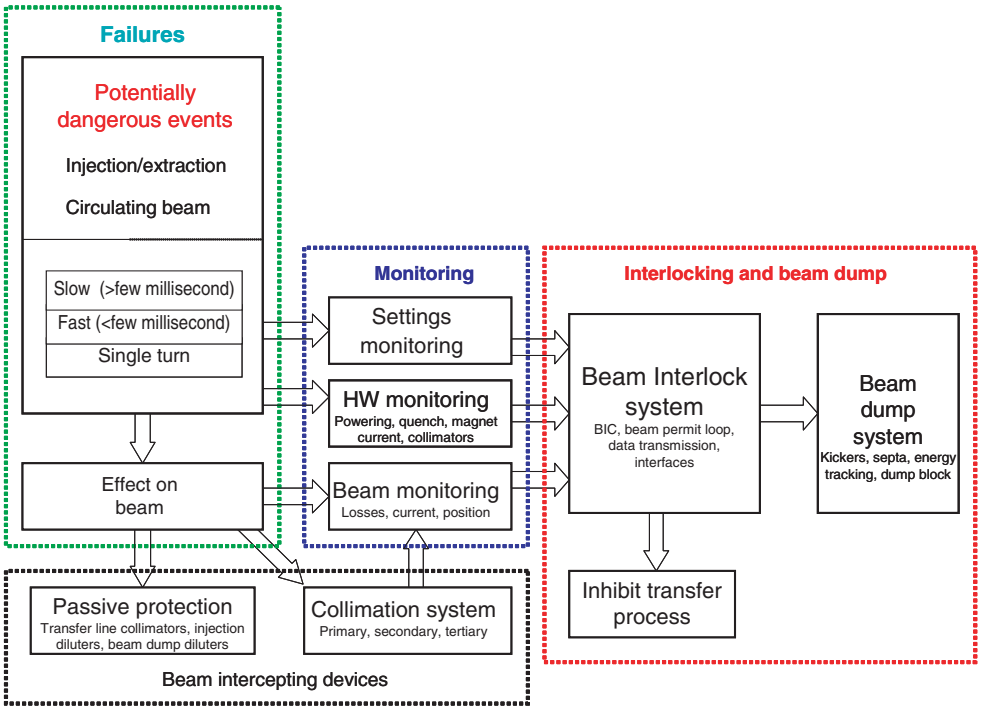

Figure 2.19: The functional blocks of the LHC machine protection system [25].

2.6.2 Architecture of the interlock systems for machine protection

Three independent interlock systems regulate the powering an operation of the LHC [43]:

- The *Powering Interlock System for superconducting magnets* [44] provides protection against uncontrolled release of the energy stored in the superconducting magnets and circuits. Its core, the *Powering Interlock Controller (PIC)*, receives input from different hardware diagnostics systems (quench detection, cryogenics, powering) and allows powering only if the conditions are safe.

- The *Powering Interlock System for normal conducting magnets* [45] provides protection against overheating of the normal conducting magnets. The *Warm Magnet Interlock Controller (WIC)* receives inputs from temperature sensors and from the power converters for normal conducting circuits.

- The *Beam Interlock System* [46], [47] regulates the presence of beams in the LHC ring. 17 *Beam Interlock Controllers (BIC)* receive information from all the systems required for operation of the LHC and allows beam presence only if the conditions are safe. If a problem is detected with circulating beams, the BIC ensures that a beam dump is requested in order to extract the beams safely.

Since adequate powering of all LHC magnets is required for operation with beam, the PIC and the WIC are important devices providing input to the BIC. All the information relative to powering and protection of the magnets is transferred to the BIC via the PIC or the WIC, thus reducing the number of BIC input channels.

2.6.3 Components of the Machine Protection Systems

When a failure happens in LHC, most of the active protection mechanisms start reacting (some mechanisms will react only for given types of failures). In order to assess the redundancy of the protection systems at different timescales, an understanding of the basic functionality and architecture of the beam related components of the Machine Protection Systems is needed.

2.6.3.1 The Quench Protection Systems

Experience in other existing superconducting accelerators shows that quenches cannot be avoided. The Quench Protection Systems (QPS) provide reliable protection of the magnets in case of quench through the following mechanisms:

1. *Detection of the quench* [48]: This is done via redundant[2] electronic systems based on the real-time measurement of the resistive part of the circuit impedance. The triggering of the quench detectors requests switching off the converter and triggers the protection mechanism.

2. *Even distribution of the magnet energy in the whole coil*: In order to avoid a high concentration of dissipated energy in the quenching point, the entire coil of the magnet is forced to quench. This is achieved by firing resistive heaters that are installed along the superconducting coils. When a magnet is forced to quench, the average temperature of the coil increases by some Kelvin, while the maximum temperature in the hot spot increases up to 300 K.

3. *Deviation of the current out of the quenched coil*: In superconducting circuits with more than one magnet, superconducting bypass diodes are installed in parallel with each magnet [49]. As the resistance in the quenched coil rises, a voltage drop develops across the coils. When this voltage exceeds the conduction threshold of the diode ($\sim$5 V) the current is transferred to the later protecting the coil from further heating. After firing the quench heaters, the current in the magnet decays following a half–Gaussian curve with $\sigma = 200$ ms.

4. *Extraction of the energy of the circuit* [16]: If the quenching magnet is connected in series with other magnets, the energy in the whole circuit needs to be extracted. The time constant of the circuit for a natural current decay is several hours due to the large inductance and very small resistance of the superconducting circuits. After a quench, discharge resistors are connected in series with the magnets in order to reduce the time constant to about 100 s.

2.6.3.2 The Powering Interlock System for superconducting magnets

This Powering Interlock System manages all the critical functions for protection of the superconducting magnets and circuits. It is based on a distributed system of 36 industrial PLCs, each allocated to the protection of one powering subsector (two PLCs for each arc subsector) [44], [50].

Hardwired signals will be exchanged via interlock current loops between the power converters, the QPS and the Powering Interlock Controller (PIC). These signals include power permit, quench signals, energy extraction requests and failures of power converters. The three systems are connected in the same current loop and even in case of failure of the controller the basic protection

[2] See section 2.6.5 for a definition of different types of redundancy

mechanisms are still guaranteed. Other systems such as Cryogenics and the Auxiliary Protection Systems (emergency stops and the LHC Uninterrupted Power System) also provide input to the PIC.

In case of failure, the PIC reacts differently with different types of circuits. Circuits are first classified according to their protection requirements. For the main dipole and quadrupole circuits, as well as for the inner triplets, a failure in one of the magnets implies the powering off of the whole powering subsector. This is not the case for magnets storing smaller amounts of energy. With respect to the operation with beam, circuits are classified according to their impact on the beam. In order to optimize operation, a beam dump request is not generated by the PIC for powering failures of auxiliary magnets such as orbit correctors or multipolar compensators.

2.6.3.3 The Powering Interlock System for normal conducting magnets

Normal conducting circuits are protected with a separate Powering Interlock System [45]. In this case, the temperature of the magnets is controlled to avoid overheating and subsequent damage of the normal conducting magnets.

Thermoswitches are installed in each warm magnet, linked via a current loop to the the Warm Interlock Controller (WIC), which is also linked to the the power converters through another current loop. The thermoswitches open the interlock loop when the temperature of the coils is above threshold sending a signal to the WIC. The WIC generates a beam dump request that is then transferred to the Beam Interlock System, and switches off the power converters after a delay of 2 s. In case a power converter fails, a fast processor within the WIC is dedicated for fast generation and transmission of the beam dump request (within 2 μs).

2.6.3.4 The Fast Magnet Current Change Monitors

Failures in the powering of the magnets will be detected in the power converters and a beam dump request will by generated by the PIC or the WIC. However, it cannot be guaranteed that the failure detection time within the converter is fast enough to ensure that the beam is dumped before significant losses develop. The failure detection and transmission timescale is in the order of several milliseconds [51], while the most critical powering failures may lead to damage in the collimators within only 2-3 ms. Therefore, additional monitoring devices are needed in some circuits.

The Fast Current Change Monitors (FMCMs) [42] measure the changes in the magnet current and trigger a beam dump request when significant fast changes are detected. These devices are based on measurement and reliable processing of the voltage signal across the magnets. They do not trigger on slow current changes, such as those due to ramping during normal operation, and their reaction time is below 60 μs.

According to preliminary studies ([8], [30]), ten FMCMs have been installed in the circuits for the normal conducting separation dipoles in IR1, IR3, IR5 and IR7, for the normal conducting quadrupoles in IR3 and IR7 and for the compensator dipoles for the ALICE spectrometer in IR2, which are also normal conducting. Additional FMCMs may be installed in the future.

2.6.3.5 Other elements for hardware monitoring and diagnostics

The QPS, the powering interlock systems and the FMCMs are protection-specific systems that ensure that magnet-related failures do not have serious consequences. Failures of other devices may also lead to significant beam losses (see figure 2.14) or introduce an unacceptable risk for the operation of the LHC. Most of the hardware that is required for the LHC operation integrates a

monitoring of its own settings, and generates a beam dump request if they are not correct. The hardware-related systems able to generate a beam dump request are:

- *Experimental devices*: The position of the movable detectors is checked, as well as the powering of the experimental magnets.
- *Collimation systems*: The position and temperature are controlled.
- *Other movable devices:* Screen, mirrors and movable vacuum devices (valves, RF stoppers and access safety blocks) have to be in their "OUT" position.
- *RF System*: Correct values of the RF frequency and voltage are required.
- *Access system*: During operation, no access is allowed to the LHC tunnel (the opening of one of the access doors generates a beam dump).

2.6.3.6 The Beam Loss Monitors

Monitoring of the losses around an accelerator is usually used for beam diagnostics, control of the aperture and post-mortem analysis of failure scenarios among others. In superconducting accelerators, machine protection is the main role of the Beam Loss Monitors (BLMs) [52], [53]. Every situation of beam-related risk for LHC equipment involves an amount of losses larger than expected, which is detected by the BLMs. If beam losses above a given threshold are detected, the beam should be dumped quickly. Therefore, the BLMs in the LHC are a very important part of the Machine Protection Systems. The beam loss monitoring system must be able to fulfill the following roles (ordered by priority):

- Protection of the LHC equipment against damage.
- Dumping of the beam before the quench level is reached in a magnet (when possible).
- Diagnostics and performance optimization for the accelerator.

Protection against equipment damage is a BLM functionality of highest priority. For this reason, the LHC BLMs have been designed to be reliable and fast-reacting in the locations where critical losses are expected.

The acquisition system is based on a current to frequency conversion. It samples the readings of the monitors every 40 μs and transmits it to the surface electronics, which calculates the integrated loss values for periods between 80 μs and 100 s. These values are then compared to a table of threshold values.

The system consists of about 4000 BLMs, most of them nitrogen filled ionization chambers ($\sim$3500 units), combined with secondary emission monitors ($\sim$500 units) to achieve a large measurement range where needed (see below). There are four families of BLMs with different purposes and characteristics:

- *BLMC*: They are installed after the collimators in the cleaning insertions, where most accidental losses are expected to happen first. BLMCs will control the steady losses in the cleaning insertions and detect transient losses due to beam manipulations, unclean dumps or magnet powering failures. The time resolution is as high as half a turn ($\sim$ 40 μs) and their dynamic range takes into account the loss enhancement by the collimators.
- *BLMS*: They are located in particular aperture limits or in critical positions. They will detect losses from the collision products and localized transient losses. Their time resolution is also half a turn.

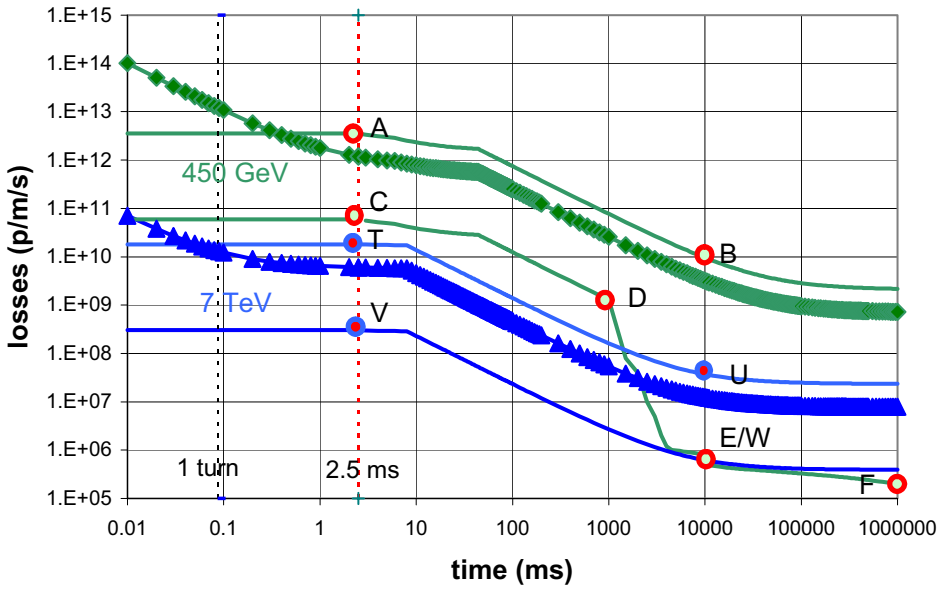

Figure 2.20: Dynamic ranges of the BLMAs and BLMSs for operation at 450 GeV and 7 TeV. The boundaries of the ranges are given by the continuous lines (the circles labelled A, B, C, etc. are reference values for the BLM system). The data series correspond to the readings at the estimated quench levels. From [53].

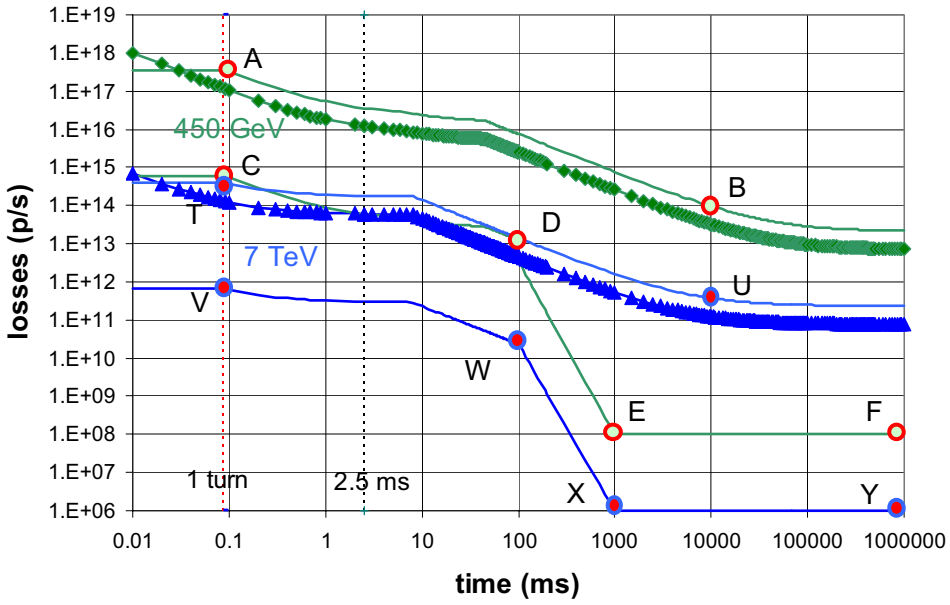

Figure 2.21: Dynamic range of the BLMCs for operation at 450 GeV and 7 TeV. The boundaries of the ranges are given by the continuous lines (the circles labelled A, B, C, etc. are reference values for the BLM system). The data series correspond to the readings at the estimated quench levels, scaled according to the loss enhancement due to collimators. From [53].

- *BLMA*: They are located in the quadrupoles in the arc. They are used to control the losses in the arc (usually slow) and their role is less critical to machine protection. Their time resolution is one turn.
- *BLMB*: Installed after the primary collimators. Used for dedicated beam studies on a bunch scale, they will have no relevant role for machine protection.

The BLMCs and the BLMSs are critical for machine protection and they need to be fully operational to for LHC operation. The BLMAs are less critical and operation under certain conditions can be allowed without fully operational BLMAs.

The BLMs measure a quantity that is proportional to the incident flux of energy on either the vacuum chamber or a collimator. Good precision and resolution are ensured within their *dynamic range*: a range of loss rates that depends on the energy and the integration time (time constant of the losses). The high end of the dynamic range has been set to three times the quench level and its low end to 5% of the quench level. The need for accurate loss measurements with pilot beam or to properly position the collimators implies a reduced low end for long integration times. Figures 2.20 and 2.21 show the dynamic ranges for the BLMA, BLMS and BLMC families.

2.6.3.7 Other elements for beam monitoring and diagnostics

Other beam monitoring devices ([54]) provide input to the Machine Protection Systems :

- *Beam Current Monitors*: The LHC will be equipped with a dual set of both DC and fast beam current transformers. Particularly, the Fast Beam Current Monitor (FBCM) will measure the LHC beam lifetime for protection purposes.
- *Beam Position Monitors (BPMs)*: 516 beam position monitors per ring are installed in the LHC, all measuring in both horizontal and vertical planes. Their role is essential for closed orbit adjustment and control [55] and they can detect fast changes in the closed orbit. The use of the global BPM data for Machine Protection has been considered but has not been implemented so far. However, it is not excluded for further upgrades of the LHC [56]. Some localized BPMs in IR6 control the maximum orbit excursion in the dump region. For a clean dump, the closed orbit offset in IR6 must be kept below 4 mm. These BPMs generate a beam dump request if the closed orbit offset exceeds 3 mm.

2.6.3.8 Safe Machine Parameters System

The Safe Machine Parameters System (SMP) is responsible for the transmission of critical information concerning the operation of the machine. This information is sent through the CERN General Machine Timing network, which ensures reliable communication. A dedicated Safe Beam Flag signal indicates whether the energy stored in the beam is below damage. Information about the beam energy, beam intensity, beam presence and mode of operation is transmitted as well [57].

2.6.3.9 The Beam Interlock System

The Beam Interlock System (BIS) is the backbone of the Machine Protection Systems at LHC [46], [58]. It collects the interlock signals from all the systems discussed above (users) and generates a beam permit signal that allows operation with beam. The beam permit signal is needed at injection to ensure that all the LHC systems are ready for beam. With circulating beams, absence of the beam permit signal triggers a fast dump of the beam. The Beam Interlock System provides one beam permit signal for each beam.

The priority of the BIS is to guarantee safe operation of the LHC. It also should avoid unnecessary dump signals and provide a tool for diagnostics and monitoring of the system, particularly after a beam dump (post-mortem analysis). The safety critical part of the interlock electronics consists in simple, reliable logic. FPGA[3] based electronics provide monitoring of all inputs and outputs with a time resolution of about 1 μs.

In total, 17 Beam Interlock Controllers (BIC) will be installed in LHC, one at each side of every IP. The controllers are interconnected by signal loops. There is one signal loop per beam, each made up of two optical fibers for redundancy. In order to minimize the transmission time to the beam dumping system, the beam permit signal travels clockwise in one of the fibers and counter-clockwise in the other. The presence of a 10 MHz square signal in the loops indicates beam permit; if one of the controllers receives a beam dump request from a user, it opens the loop to remove the beam permit. When the two controllers in IR6 detect the loss of the signal, they instantaneously send hardware signals to fire the extraction kickers of the Beam Dump System.

The BIS has been developed to be fast and reliable. The response time of the BIC (time between the reception of the beam dump request and generation of the dump trigger varies between 20 and 120 μs, depending on the location of the failing equipment generating the dump request. The mean time between failures that prevent correct transmission of the beam dump request has been evaluated between 1000 and 10000 years.

2.6.3.10 The Beam Dumping Systems

The Beam Dumping Systems are responsible for quickly and safely disposing of the beams when operation must be interrupted for any reason [1], [25]. There is one system for each beam.

When the beam dump request is received, fifteen fast kickers with a rise time of 3 μs deflect the beam by 280 μrad in the horizontal plane. Then, the beam is deviated by 2.4 mrad in the vertical plane by fifteen septum magnets. Further downstream, diluter kickers are used to reduce the energy density in the dump block by distributing the impact along a spiral transverse trajectory. A 700 m extraction line allows an increase of the beam size from 0.2 to 1.5 mm and a further spread of the bunches. The dump blocks are the only elements in the LHC capable of safely absorbing the energy of the beams. For nominal beam parameters the maximum temperature in the block is expected to be about 750°C.

The beam has a particle free abort gap of 3 μs length to allow for the rise time of the kicker magnets. In order to have a clean extraction the number of particles in the abort gap have to be kept under the level at which quenches might be provoked. Besides, to ensure a proper extraction of the beam, the following conditions have to be met:

- At least 14 of the 15 kicker magnets have to be operational.
- The beam dump kicker has to be synchronized with the 3 μs of the beam abort gap.
- The field of the extraction and dilution magnets must track the beam energy.
- The closed orbit offset in the dump insertion must be under 4 mm.

The reaction time of the Beam Dumping Systems is limited by the need of synchronization of the kicker magnets. It can take up to one turn to ensure correct synchronization. In addition, an extra turn is needed to effectively extract the beam. Therefore, a complete extraction of the beams can't be ensured in less than 180 μs.

[3] *Field Programmable Gate Array*, a powerful, versatile type of microprocessor

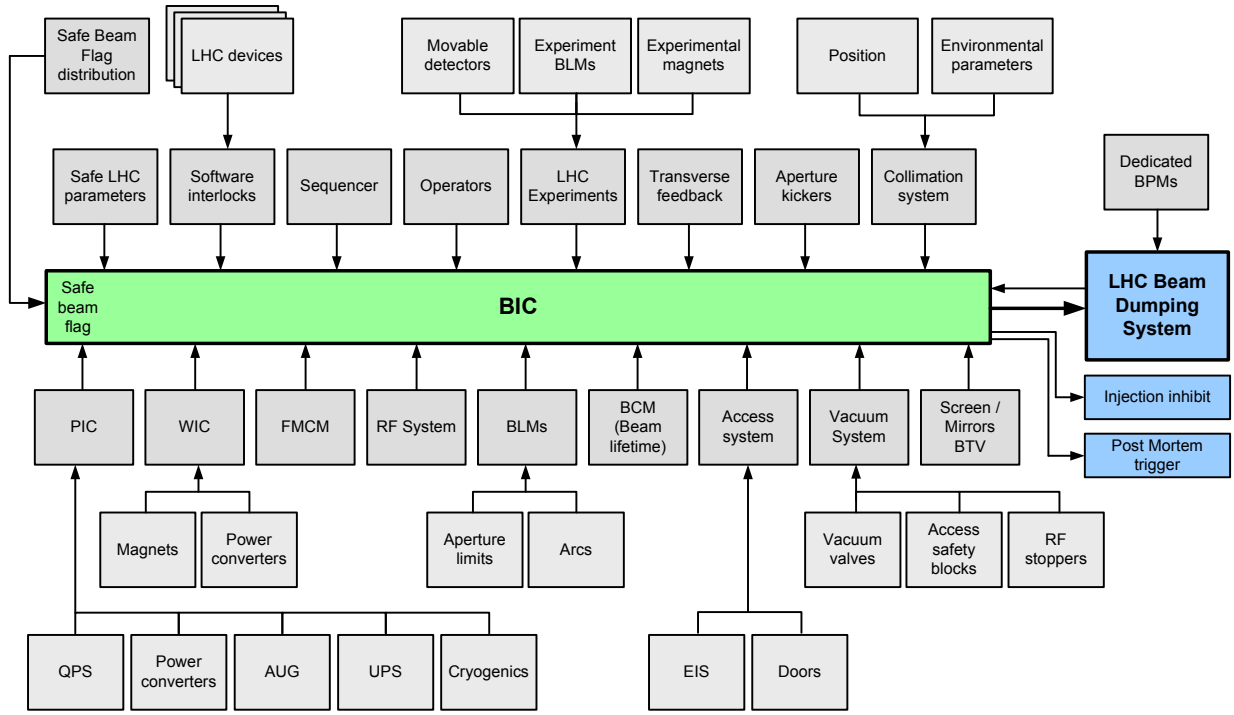

Figure 2.22: Structure and components of the Machine Protection Systems. The arrows represent the main signals transmitted between the different subsystems. Courtesy of R. Schmidt.

2.6.4 Summary and timing considerations of the Machine Protection Systems

Figure 2.22 summarizes all the components of the Machine Protection Systems and their relationship. From all the BIC users, some are maskable if the energy stored in the beam is below damage level (safe beam flag). This allows more flexible operation during beam commissioning with low intensity beam.

The time-response of the MPS is an important parameter to assess the level of protection against failures with different time constants. Table 2.13 summarizes the ranges of response times of the machine protection subsystems.

The total time performance of the MPS is limited by the transmission speed of the dump request within the BIS and the time needed by the Beam Dumping System to synchronize the extraction and effectively dump the beam, in total 200-300 μs, as illustrated in figure 2.23. In most of the cases, the greatest delay is introduced by the detection of the failure within the BIC users. It is important to note that the elements measuring the effects on the beam (BLMs and beam current monitor) may be the latest systems to react in spite of their fast response time. This is because for most failures the effects on the beam appear slowly [30], [6] and hardware monitoring devices react first.

2.6.5 Redundancy of the Machine Protection Systems

The Machine Protection Systems are of vital importance for the LHC. The reliability of the LHC MPS has been evaluated between SIL3 and SIL4[4], with a mean time between failures estimated above 2000 years [60]. Redundancy significantly contributes to this high reliability [60]. Besides,

[4]Safety Integrity Level (SIL) is defined as a relative level of risk-reduction provided by a safety function [59]

System	Approximate fastest response time	Cause of dump request
Fast Magnet Current Change Monitor	60 μs	Fast current change in magnets
Beam Loss Monitoring System	80 μs	Beam losses outside tolerances
Fast Beam Current Monitor	$>$ 1 ms	Beam lifetime too small
Powering Interlock Controller	100 μs - 10 ms	Problem in magnet circuits
Quench Protection Systems	15 ms - 250 ms	Quench in SC magnet
Vacuum System	10 - 100 ms	Gas or valve in vacuum chamber
Experiment movable devices	10 - 100 ms	Unsafe position
Collimation system	10 - 100 ms	Unsafe position or temperature
Safe LHC Parameters	100 ms	Inconsistent parameters
Beam diagnosis invasive elements	100 ms	Unsafe position
Experiment magnets	10 - 100 ms	Powering failure
Warm Magnet Interlock Controller	10 - 100 ms	Problem in NC magnet circuits
Access System	100 ms	Controlled access violation
CERN Control Room (operators)	1 - 10 s	Operator decision
Beam Dumping System	$<$ 180 μs	
Beam Interlock System	20 - 120 μs	

Table 2.13: Fastest reaction times of the main subsystems of the Machine Protection Systems. Adapted from [46].

redundancy ensures that the dump of the beam is triggered by the fastest system for every given failure case.

Redundancy can be defined in the following ways:

- *Design redundancy*: the system itself is designed in a redundant way (an output may be generated as the logical combination of various devices measuring the same quantity, various cards with the same functionality are connected in parallel, transmission lines are doubled, etc.). This type of redundancy is essential to achieve high reliability.
- *Intrinsic measurement redundancy*: distributed systems with a large number of measuring devices may produce reliable readings even if not every single device is operational. These systems collect information that is different but correlated (hence redundant) in order to achieve a more accurate picture of the measured phenomenon. This redundancy ensures that their overall functionality does not depend on a single device. The BLMs in the arcs, for example, or the detectors for the LHC experiments are intrinsically redundant.

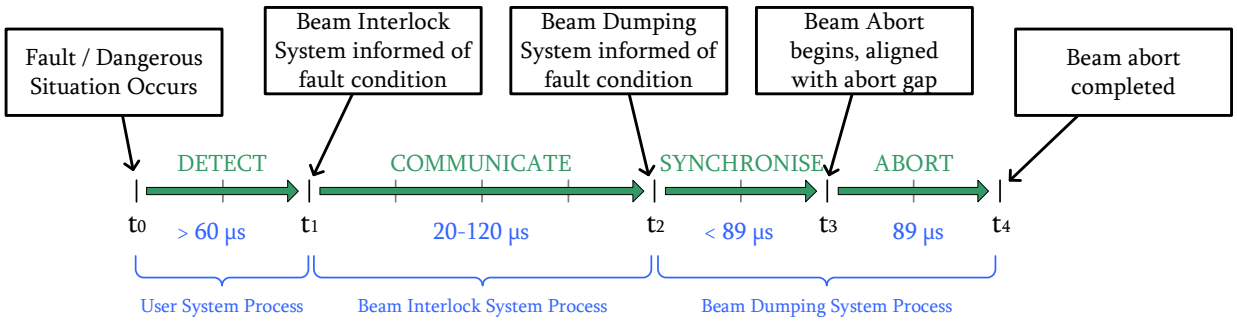

Figure 2.23: Succession of events after a failure and response times of the Machine Protection Systems. Courtesy of B. Todd.

- *Inter-system redundancy*: various systems with different architectures measuring the same phenomenon or different consequences of the same phenomenon provide inter-system redundancy. The CMS and ATLAS detectors are redundant in this sense, in their separate search for the Higgs boson. Another example is provided by the QPS and the BLMs in case of quench of a magnet, since both will detect the problem though different means. This type of redundancy provides optimization of the measurement with respect to time: the most adapted system will respond first.

These three types of redundancy are all present in the MPS. All the safety critical systems have been designed redundantly at different levels. Some systems as the BLMs are intrinsically redundant and the association of various protection subsystems at different levels provides inter-system redundancy to the machine protection architecture depicted in figure 2.22.

Chapter 3

Tracking simulations with magnet failures in the LHC

The main part of this work is the study of the effects of magnet failures on the LHC beams. For this purpose, it is necessary to understand the behavior of the circulating protons when the field of a magnet changes due to a failure. Tracking simulations with variable magnetic fields have been used to obtain relevant data. In this chapter, the tools, models and methods for the simulations are presented.

3.1 The thin lens approximation for tracking simulations

Numerical methods or algorithms that allow to reproduce the trajectory of a particle along a given element lattice are referred to as *tracking* tools. They are used extensively for studies of complex phenomena in Accelerator Physics where an analytical approach is not possible.

These methods generally use the *thin lens approximation* [11], which consists in modeling long magnetic elements as drifts and localized kicks in the same way as glass lenses are modeled in classical optics. This approximation saves a great amount of computing time providing accurate results.

Figure 3.1 represents the principle of the thin lens approximation. Every magnetic element is replaced by one or more slices separated by drift spaces. In most cases one slice per element is enough, although more slices may be needed for long elements in regions of high gradient of the twiss functions. The kick of a given slice is applied to the particle coordinates using a transfer matrix $\boldsymbol{M}_{slice}$ (see 1.2.3). The particle coordinates at the next slice are calculated using the transfer matrix of the drift space between the two slices $\boldsymbol{M}_{drift}$. The transfer matrix of each slice is calculated based on the element nature and length. Other elements than magnets, such as RF cavities, can also be modeled as thin lenses [61].

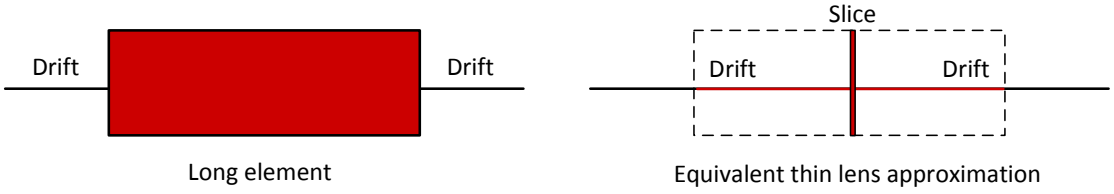

Figure 3.1: Principle of the thin lens approximation.

3.2 Tracking tools for the LHC

Modeling the LHC, a complex machine with more than 10000 elements, is not straightforward. An numerical model (see section 3.3) is provided by the Accelerator Physics group at CERN and tracking in the LHC must be done with software that is compatible with this model [62]. Two main tracking tools are used at CERN for LHC-related studies: MAD-X [63] and Sixtrack [64].

3.2.1 MAD-X

Optics studies at CERN are usually done using the Methodic Accelerator Design software (MAD), a tool for charged-particle optics in alternating-gradient accelerators and beam lines. It can handle very large and very small accelerators and solves various problems on such machines. MAD-X is its latest release.

MAD-X has a modular architecture and provides a flexible user interface. Its main purpose is to perform optics calculations, and it is not a dedicated tracking tool. However, it provides a tracking module that, combined with the flexibility of the software core, is convenient for tracking with arbitrarily variable magnetic fields.

In addition, MAD-X allows assignment of both alignment and field errors, matching of modified optics, orbit correction and aperture calculations, among other functionalities of less interest for this work. For the simulation studies presented hereby, the tracking module was modified in order to allow recording of particles lost in the aperture. This functionality is now part of the official version.

3.2.2 Sixtrack

Unlike MAD-X, Sixtrack is optimized for fast tracking. The code works with the full six-dimensional vector of coordinates and takes into account magnet non-linearities to very high orders. This code is being used for most LHC tracking simulations and includes well developed linear and non-linear error models.

Colltrack [65], a recent extension of Sixtrack, includes realistic treatment for collimators. When a particle hits a collimator, it will probably be scattered back into the beam with different coordinates and energy. Most tracking programs (including MAD-X) do not take this fact into account and consider particles hitting the aperture as instantly lost. Colltrack provides a thin lens model for collimators, where Monte Carlo routines are used to simulate the particle interactions within the collimator jaw. Scattered particles are still tracked downstream of the collimators. Colltrack has been extensively used for collimation studies. However, it does not allow tracking with an arbitrarily changing magnetic field.

3.3 The LHC Model

The LHC model for tracking simulations and optics studies is provided as a MAD-X sequence. It includes all the magnetic elements, collimators and other aperture limitations, RF cavities and beam instrumentation elements. A thin lens model is also provided for tracking studies.

The parameters for each element are given for each mode of operation (optics). Only the nominal collision (7 TeV) and injection (450 GeV) optics have been considered for the studies hereafter. Details on the optics can be found in [1].

3.3.0.1 The aperture model

The mechanical limit imposed by the physical size of accelerator elements is called the aperture [1]. Normally, it corresponds to the size of the beam pipe, although for elements such as collimators, it is the half-gap which defines the available aperture. The aperture is given as a function of the beam size (σ) at each location, typically in "number of sigmas", sigma referring to the beam size as defined in chapter 1.

Every element in the LHC sequence is assigned an aperture. The collimators receive special treatment, as they are movable devices whose settings depend on the mode of operation. Their aperture is not part of the LHC model and it has been set according to the latest collimation optimization studies [66].

The tightest aperture limitations for the LHC (excluding collimators) are given in table 3.1. Note that the beam size with injection optics is about a factor of four larger than with collision optics. Therefore, the aperture margin for most of the accelerator elements is greater for collision optics. Exceptions are collimators, which adapt their half-gap to the beam size, and particular locations such as the inner triplets with very high β at collision optics.

		450 GeV		7 TeV	
		SC	NC	SC	NC
Beam 1	Horizontal	6.8	7.9	28	8.9
	Vertical	7.7	7.8	8.3	8.4
Beam 2	Horizontal	6.7	7.7	28	8.1
	Vertical	7.6	7.6	8.7	8.7

Table 3.1: Aperture limitations in the LHC excluding the collimation system, in sigmas [67].

3.3.0.2 Machine imperfections

During manufacturing and installation, alignment and multipolar field errors are minimized to an acceptable level, but they cannot be avoided completely. Both alignment and field errors can be included in the LHC model.

Alignment errors imply that each element is not centered around the ideal particle trajectory (tenths of millimeter for the LHC magnets). This has important implications in the case of quadrupoles, since they apply an error kick proportional to their misalignment (see section 1.4.1). Orbit correction is needed in order to keep the closed orbit within acceptable limits (rms offset less than 1 mm and peak offset less than 4 mm).

Multipolar field errors are the unwanted components of the real field produced by each magnet. They add up to the design field and introduce non-linearities in the optics of the machine. Statistical distributions of multipolar errors based on real measurements at the LHC magnets can be generated and integrated with the MAD-X model. The multipolar errors considered are in the order of 10^{-4} in gradient [68], [69].

Simulating with a model including imperfections implies a recalculation of the optics and closed orbit after the errors have been added to the ideal model. For the tracking simulations presented hereafter, the following procedure has been used to obtain a realistic model including machine imperfections:

[1] For non-linear beam dynamics the *dynamic aperture* is also defined. It corresponds to the amplitude limit of stable particle movement and it's influence is negligible for the study of fast beam perturbations.

1. Loading of the ideal LHC model (version 6.500).
2. Addition of multipolar and alignment errors. The alignment errors have not been added directly to the magnets. A simpler approach yielding an equivalent result consists in introducing random measurement uncertainties in the BPMs [70]. The distorted orbit is generated by the orbit correction algorithm and can be better adapted to the LHC beam specifications (maximum rms offset of 1 mm, maximum peak offset of 4 mm).
3. Application of the orbit correction algorithm.
4. Application of the optics matching algorithms. The tune and betatron functions are recalculated taking into account the new closed orbit and the multipolar errors added to the ideal model. For this purpose, strength values different from zero are assignetd to multipole correctors.
5. Centering the movable collimators on the new closed orbit.

3.3.1 Tracking with aperture limitations

Aperture limitations must be considered to evaluate losses from tracking simulations. Comparing the amplitude of the particle with the aperture of each element while tracking is time consuming and the design of many speed-optimized codes leaves aperture restrictions aside.

In MAD-X, every thin element has a defined aperture. The tracking module compares it to the amplitude of every particle reaching the element. If the amplitude is higher than the available aperture, the particle is lost (not tracked any further) and its coordinates at the impact location are recorded. This method uses two significant approximations:

- The coordinates of the lost particles are projected on the equivalent thin lens. This yields a two dimensional matrix at the location of the slice. In the vast majority of cases the associated error ($\Delta x = x'\Delta s$) is negligible and in case of need the impact on the actual surface of the beam pipe or element can be easily reconstructed.
- The elements are considered as black absorbers. A particle that hits the aperture is considered lost and not tracked any further. Particularly, this approximation is not valid for the collimators, where most particles hitting the collimator aperture are scattered back into the beam and may circulate for several turns before being effectively lost. It is however of interest to record the primary impact in the collimators, which can be used as an input for other software for energy deposition studies or further tracking [71].

When using Colltrack, a different approach is necessary. Apart from the collimators, that are given a very particular treatment, aperture restrictions are not considered by the tracking code itself. Post processing is necessary to compare the particle amplitudes at every turn with the available aperture, which yields realistic loss patterns around the LHC ring [22].

3.3.2 Tracking with variable magnetic fields

Tracking with variable magnetic fields is possible using the thin lens tracking module of MAD-X. The procedure is heavy and slow, but yields good results. The failure generates a change in the magnetic field, modeled as a time-dependent field error that is applied to the failing magnet or magnets before tracking. This error definition cannot be implemented inside the tracking module and the module has to be entered and exited every turn [72]. This requires a set of macros and

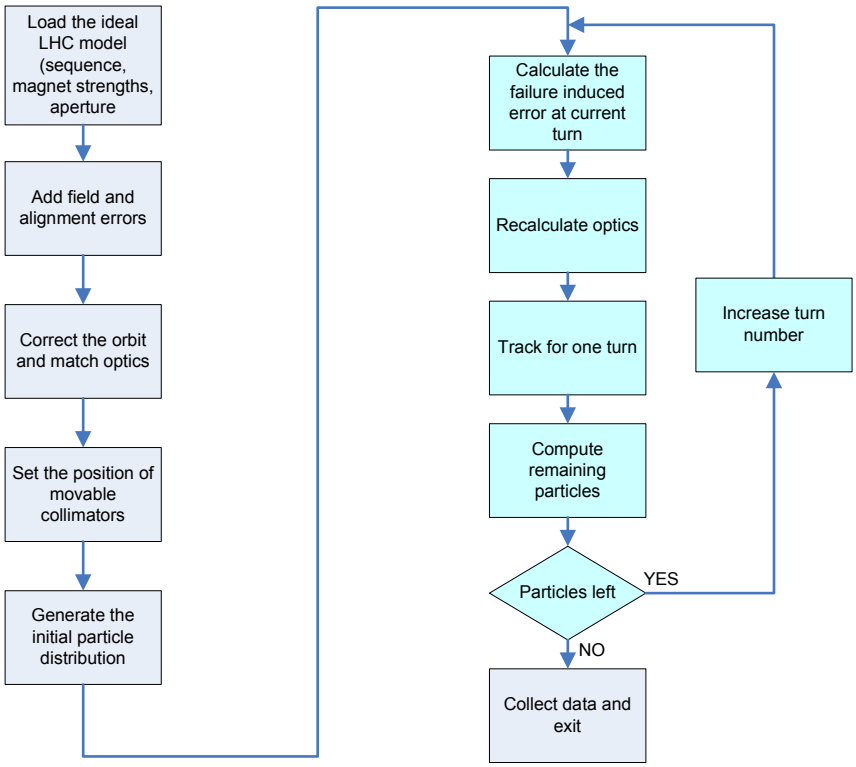

Figure 3.2: Algorithm used in MAD-X to track with a variable magnetic field. Only the light blue blocks are part of the specific algorithm for variable magnetic fields.

procedures to keep the coherence of the tracking, as well as some modifications of the original code for consistent recording of various parameters of interest. The procedure is illustrated in figure 3.2 and includes a loop with the following steps:

1. *Calculating the change in the field at the current turn*: The field difference is defined as a function of the turn for each failure (see section 4.1.1). For the first turn the error is equal to zero and it starts increasing from the turn corresponding to the beginning of the failure. The recalculated error is then applied to the failing magnets.

2. *Recalculating the optics*: after the field difference has been applied, the optics of the machine has changed and the new optics has to be recalculated. This allows recording of the twiss parameters or the orbit offset at given locations as the failure develops. If the failure is such that at one point the optics of the machine becomes unstable, the twiss parameters are not available but tracking is still possible until all particles are lost.

3. *Tracking for one turn*: The particles are tracked for one turn only. The tracking module has to be restarted every new turn and exited when the tracking is finished. This is necessary in order to set a different magnetic field in the failing magnets. The data corresponding to the tracking are stored in memory.

4. *Computing the remaining particles*: The tracking module needs a list of particles with their initial coordinates. For the first turn, a random particle distribution is generated (see section 3.4). For each following turn, a new list has to be generated with the

coordinates for each particle at the end of the previous turn. Particles that were lost in the previous turn are excluded from the list. Dichotomy is used in the algorithm in order to optimize computing time.

When all the particles have been lost, the data from the tracking are collected and combined in easily readable text files using post processing scripts.

3.4 Transverse particle distribution

Before the tracking, it is necessary to specify the initial coordinates of each particle. A Gaussian particle distribution both in the horizontal an vertical planes has been assumed. It is important to note that this is a simplistic approximation for a collimated proton beam. Most probably, the LHC beam profile will not be Gaussian, but in the absence of measurement data, a Gaussian distribution is a good, practical choice to perform simulation studies.

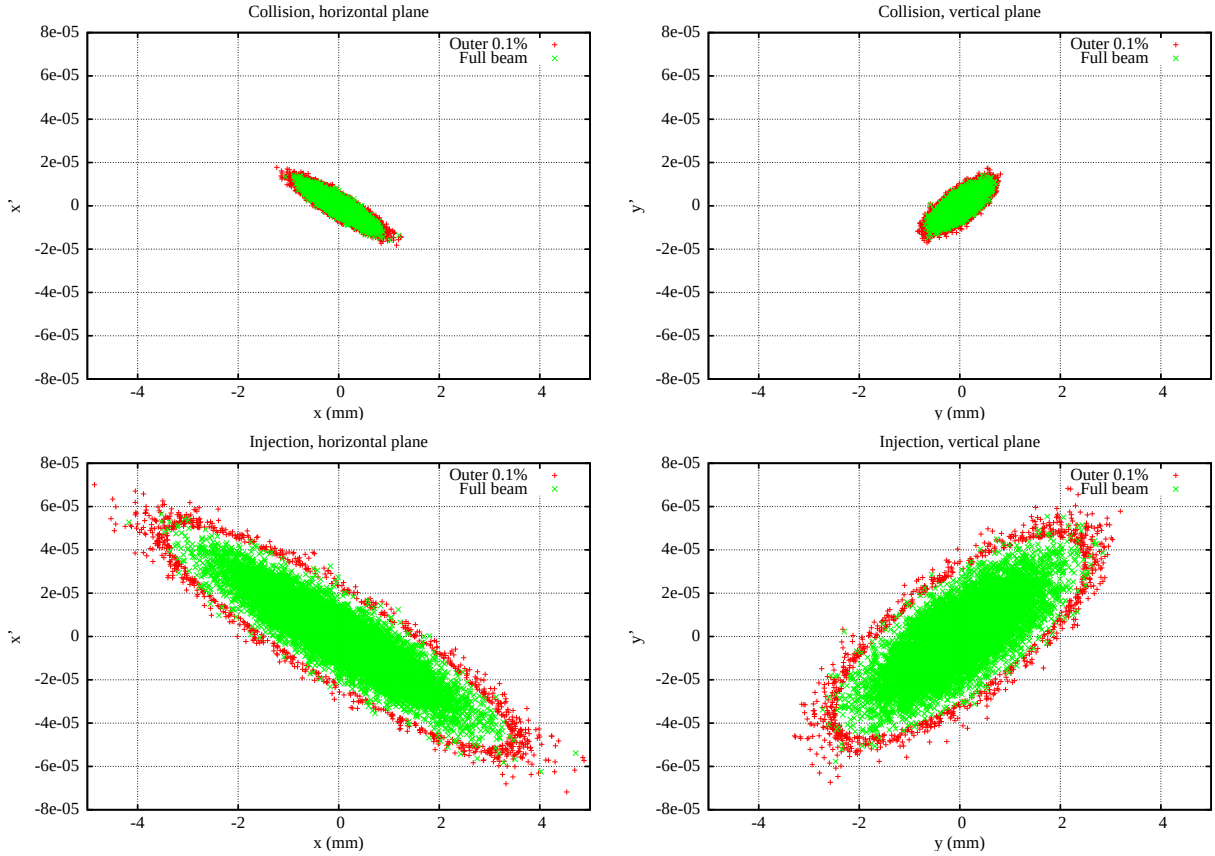

Figure 3.3: Phase space distributions at the location of TCP.C6L7.B1.

The particle distribution is generated at the start of the ring and is matched to the optics of the machine at this location. Particle coordinates are generated in the normalized phase-space using the internal MAD-X random number generator. The twiss parameters at the start of the ring are then used to obtain the particle coordinates in the real phase-space using equation 1.27 and ensuring a matched distribution.

The number of particles that can be simulated in a reasonable time within the computing resource limits available is limited to values between 10^4 and 10^5, depending on the time constant of

the failure and number of recording locations. As discussed in chapter 2, the estimated quench limit at 7 TeV can be reached if about 5×10^{-8} of the nominal beam intensity reaches the superconducting elements.

In order to obtain a good resolution for the very first losses, two particle distributions have been tracked for each failure case: a full Gaussian beam distribution and a Gaussian tail distribution with only the outer 0.1% of the beam. The phase-space distributions of beam 1 at the primary collimator TCP.C6L7.B1 in the horizontal plane both for injection and collision are shown in figure 3.3. Thus, the obtained resolution for the first lost particles reaches 10^{-7} for 10000 simulated particles, which yields acceptable statistics for the first beam losses produced by the failure. The full distribution is useful to obtain a better understanding of the evolution of the losses in case of failure. In reality, however, the fast dumping of the beam will avoid such a complete loss of the beam in the collimators[2].

Unless specified otherwise, all the tracking simulations presented in the following chapters have been run with 5×10^4 particles, which gives a resolution for the losses in the collimator of 2×10^{-5} for the whole particle distribution and 2×10^{-8} for the tail distribution.

[2]This does not apply in the case of single-turn failures, which are not discussed in this thesis.

Chapter 4

Magnet failures and their effects on the beam

When a magnet undergoes a failure, the current in the circuit changes. The time constant of the current change depends on the circuit parameters and type of failure. Neglecting saturation effects and eddy currents, the magnetic field follows the current change and the strength of the magnetic element varies. This assumption is slightly pessimistic, since in reality the variation of the magnetic field is slower than the change in the current. This change in the magnetic field induces a change in the optics of the machine, and the beam is affected.

4.1 Types of magnet failures and modeling of the current decay

Two types of failures can induce a decay in the magnet current: quenches and powering failures. The decay of the current follows different shapes for each case. In the main dipole and quadrupole circuits, a quench in one magnet is also followed by a current decay in the whole circuit due to the energy extraction mechanism.

4.1.1 Current decay in case of powering failures

Powering failure is a general term to denote any process that disturbs the adequate powering of one or several magnets, usually a failure of the power converter itself or a power-off request from the Powering Interlock Controller due to a failure somewhere else. The failure leads to a voltage different than nominal in the power converter (*failure voltage*) and the current in the circuit starts changing. The power converter can detect most failures internally, and in the vast majority of cases the failure voltage will be set to zero (*fast power abort*). However, it is not excluded that the failure voltage has a different value and in some cases failure voltages that are not zero produce the fastest current changes.

Magnet circuits can be modeled as simple RL circuits. The natural time constant of the circuit, $\tau = L/R$, determines the speed of the decay for a given failure voltage. In case of failure, the current in the circuit follows an exponential change given by:

$$i(t) = I_{nom}\left(e^{-\frac{t}{\tau}} + \frac{V_{fail}}{V_{nom}}\left(1 - e^{-\frac{t}{\tau}}\right)\right) \tag{4.1}$$

where I_{nom} and V_{nom} are the nominal current and voltage for the given mode of operation, and V_{fail} the failure voltage.

The time constant for superconducting main circuits in LHC ranges from ∼10 s for individually powered magnets up to more than 4 hours for the main dipole circuits. This is orders of magnitude slower than the reaction time of the PIC (about 10 ms) and powering failures in the LHC superconducting circuits do not lead to fast losses, except in very few particular cases.

A more elaborate approximation of the current decay takes into account the passive filter at the output of the power converter. A schematic of the output stage of a typical power converter for the normal conducting LHC circuits is presented in figure 4.1 [73].

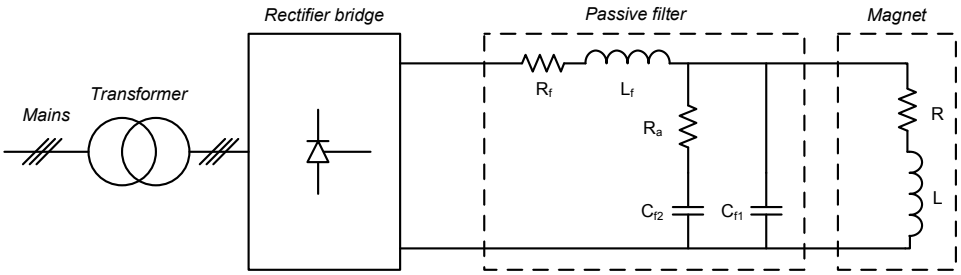

Figure 4.1: Output stage of a power converter

The filter has been modeled using MATLAB® as a voltage-current transfer function. The corresponding Bode diagram is shown in figure 4.2 for the particular case of the circuit RD1.LR1. The filter attenuates high frequencies and introduces an oscillating behavior in the current decay. It adds a damping of the current changes at short timescales (various milliseconds), in which the most critical multiturn failures at LHC lead to a complete loss of the beam.

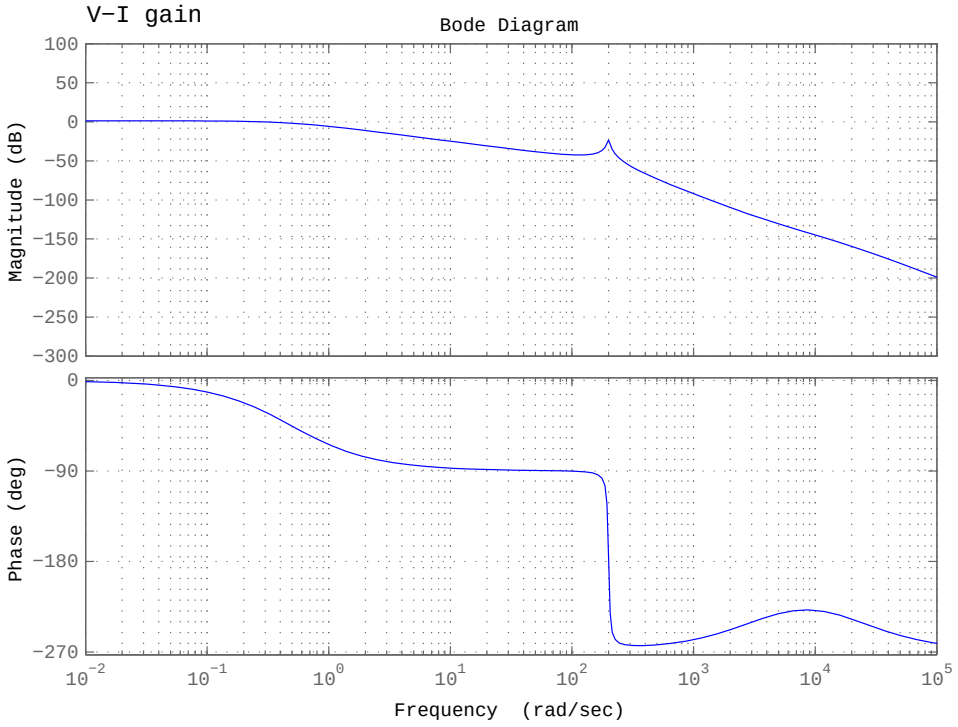

Figure 4.2: Bode diagram for the output filter of the power converter for RD1.LR1.

At the time of this study, measurements were possible only on very few LHC circuits. In order to validate the model for the simulations, measurements were taken in one of the available LHC circuits and one SPS circuit with a power converter of the same type. Figures 4.3 and 4.4 show the comparison of the measurements with the analytical formula and the results obtained from simulations of the filter model (see table B-1 in appendix B for the values of the circuit and filter parameters). The results show that for large timescales the simple analytical approach and the simulated curve yield similar results, not necessarily close to the actual measurements. Also, the model of the output stage greatly underestimates the filter damping factor for the oscillations. This implies that for short time intervals, the analytical approach yields more accurate results than the simulation that include the output filter. The differences between simulated and measured data are significantly different in both simulated circuits (see below), with better accuracy for the SPS circuit. This suggests that these differences are most probably due to the uncertainty on the circuit and filter parameters, since for the SPS circuits these parameters are known more accurately.

Following this study, the analytical approach (equation 4.1) was chosen to define the current change in the tracking simulations:

- It is simpler than the model including the output filter of the power converter.
- It yields more accurate results for shorter timescales, which are more relevant for the losses in most cases. Besides, the exponential decay is faster than the real one at small timescales, providing a worst case scenario for fast failures.
- An analytical formula can be integrated directly in MAD-X, resulting in faster simulations.

This approach is still quite approximate and the associated uncertainty must be taken into account when analyzing the results of the tracking. Particularly, in the case of RBXWSH.L8, the current change is about 30 % too pessimistic after 4 ms and for the SPS converter, ∼30% too optimistic after 10 ms.

4.1.2 Current decay in case of quenches

The origin and causes of quenches have been briefly discussed in section 2.5.2.3. The resistive transition of the coils induced by the QPS heaters combined with the fast abort of the power converter leads to a decay of the current in the circuit that follows approximately a half-Gaussian curve.

The approximation of the current decay is based on previous studies, since the majority of the failure simulations were conducted before measured LHC quench data were available. A half-Gaussian curve with σ=200 ms has been suggested as approximate current decay [36]. Figure 4.5 shows the evolution of the current in RD2.L5 with this approach, the same curve shifted by an appropriate time and the measured data. The actual Gaussian decay takes place only when the whole magnet is quenched and the power converter is switched off. The duration of the linear part depends on the particular quench case and is not expected to be less than 30 ms due to the response time of the QPS and the PIC. The slope of the linear part remains small, and depends on how the quench develops.

The analytical approach (centered Gaussian) was chosen to define the current change in the tracking simulations during quench failures. It is a simple approach providing a worst case scenario but it is, however, too pessimistic. To compensate for the linear smooth decay, an offset may be added to the time constant of the losses once statistical quench data are available from the LHC commissioning and operation. This will allow to better adapt the study to each particular quench case. If the measured data are too different from the considered curve, new studies may be needed for the most critical magnets.

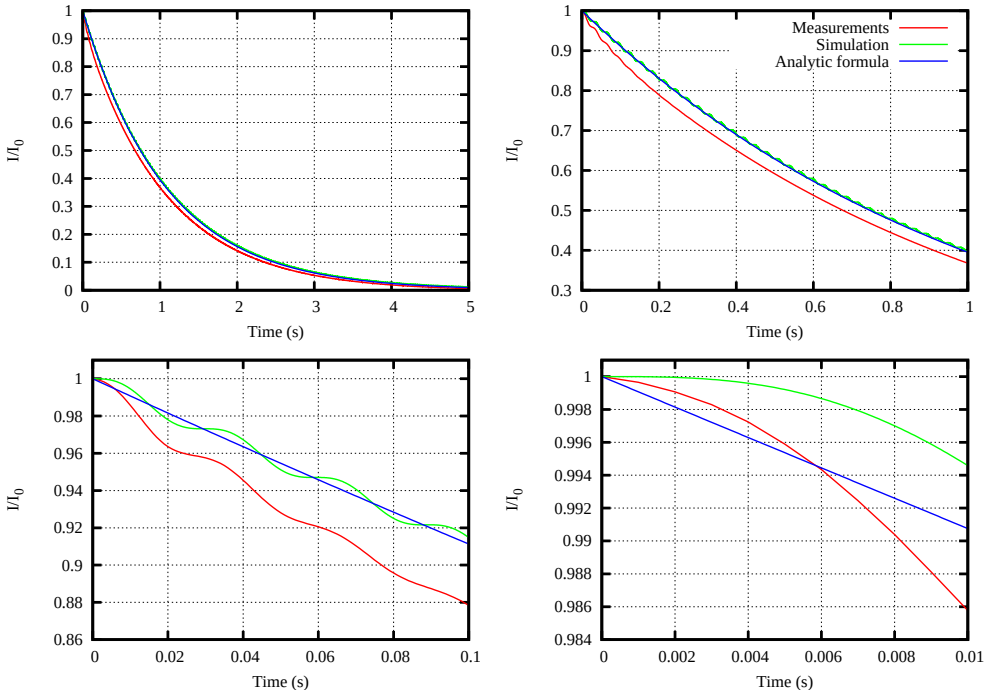

Figure 4.3: Current decay of an SPS power converter at different timescales. Comparison of the measured data, the simulated data and the analytical formula.

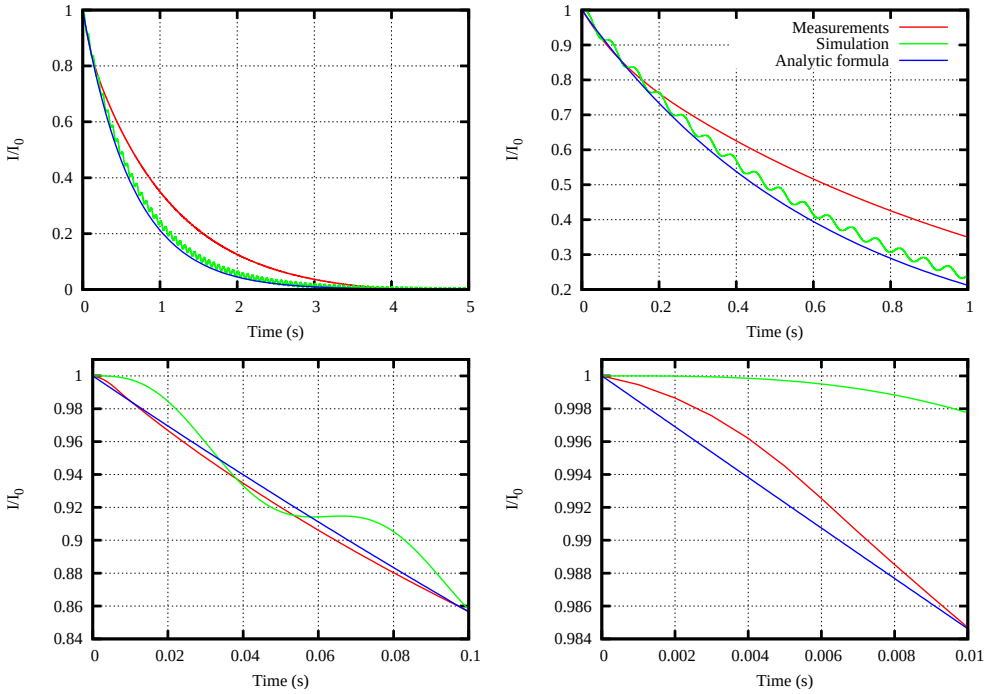

Figure 4.4: Current decay of the LHC power converter for RBXWSH.L8 at different timescales. Comparison of the measured data, the simulated data and the analytical formula.

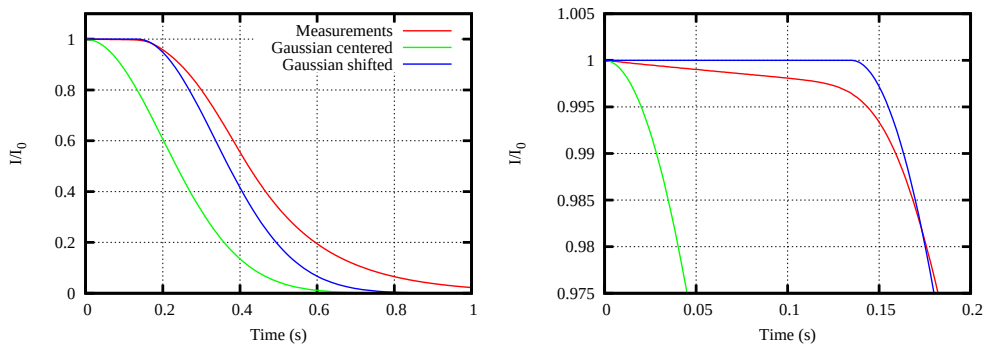

Figure 4.5: Current decay for a quench in RD2.L5. The measured data show a small linear drop until the whole magnet is quenched and then follow a Gaussian decay. The characteristics of the linear drop depend on the evolution of the quench in each particular case and on the reaction time of the QPS. In this particular case, the analytical approach with $\sigma = 200$ ms yields a decay that is slightly faster than the measured one.

4.2 Effects of magnet failures on the beam

When the magnetic field of a given magnet changes the beam is subsequently affected. From the machine protection point of view, mostly failures leading to a fast loss of a relevant fraction of the beam are of interest. Failures of multipoles of order higher than quadrupoles have too small an influence on the beam dynamics at short timescales to produce such losses and are not considered in this study. Failures of dipoles and quadrupoles are of concern for machine protection, and fast losses after such failures happen mainly (though not only) due to linear effects in the beam optics.

For machine protection, beam losses are the most significant quantity to record in case of magnet failure. The evolution of the losses with time depends on how the beam is affected by the failure. It is important to understand this evolution thoroughly in order to assess the redundancy of the protection systems. We distinguish four different time parameters with respect to the appearance of losses:

- *Loss time-constant (τ_1)*: The time from the start of the failure until all the beam is lost. Not to be confused with the time constant of the failure, which corresponds to the current decay. The loss time constant is a global quantity for the accelerator, not given for any particular location.

- *Loss threshold time (τ_f)*: The time until a fraction f of the beam is lost. The loss threshold time can be defined with respect to any fraction of the beam. Determining the loss threshold times for different lost fractions of the beam is of interest to evaluate losses that do not follow a constant evolution. The threshold time to the detection threshold is the time available to the hardware monitoring systems to request a beam dump before the beam is significantly affected. The threshold times to quench and damage levels correspond to the time available to the LHC protection systems to dump the beam safely. The loss threshold times can be defined with respect to the whole accelerator (global loss threshold times) as well as to a given particular location, provided it receives enough losses (local loss threshold times). In the following we implicitly refer to the global threshold times unless indicated otherwise.

- *Relative loss threshold time (τ_f/τ_1)*: It is often interesting to relate the different threshold times to the time constant of the losses to assess the relative time distribution of the losses. Relative loss threshold times close to one indicate that the related losses happen in a short time relative to the loss time constant of the failure scenario. Smaller values indicate that

there is a significant time gap between the loss of the corresponding fraction and the loss of the whole beam.

- *Loss rate*: The number of particles lost per turn (dN_t) or unit time (dN/dt). The loss rate relates to the time margin for the BLM system to dump the beam. Low loss rates leave a good margin between the moment when the detection threshold is reached, and the reaching of quench or damage thresholds. If the loss rate is too high, the first losses are detected by the BLMs but the quench or damage thresholds can be reached before the beam is dumped on request of the BLM system, due to the transmission time of the electronic signals. The loss rate can be defined as a global or local magnitude.

4.2.1 Critical magnet failures in the LHC

A complete overview of all dipole and quadrupole failures possible at LHC using an approximate analytical approach has been made [30]. In this preliminary study, only linear effects have been considered and the worst case combinations of betatron amplitude and phase between failing magnets and aperture restrictions have been used. Table 4.1 presents a summary of the study showing the magnets producing the fastest failures. The criterion to evaluate the speed of the losses was the time needed until the losses due to linear effects reached 1.15×10^{11} particles (bunch intensity). Dipole failures generally produce greater losses faster than quadrupole failures. Many quadrupole failures do not produce significant losses due to linear effects, and in most cases these losses appear with large loss time constants (greater than 100 ms). However, changes in optics induced by quadrupole failures also produce losses due to linear or non-linear resonances which have not been taken into account in previous studies.

450 GeV		7 TeV	
Magnet	Failure	Magnet	Failure
MBW	ΔV_{max}	MBXW	ΔV_{max}
MBXW	ΔV_{max}	MBW	ΔV_{max}
MCBWH/V	ΔV_{max}	MBX	Quench
MBXWT	ΔV_{max}	MCBWH/V	ΔV_{max}
MQWA	ΔV_{max}	MBXWT	ΔV_{max}
MBRB	ΔV_{max}	MB	Quench
MBX	ΔV_{max}	MBRC	Quench
MB	Quench	MQXA/B	Quench
MBRB	Quench	MBRB	Quench
MCBWH/V	$V_{fail} = 0V$	MBRS	Quench

Table 4.1: Top ten critical magnets and failures at 450 GeV and 7 TeV. ΔV_{max} stands for the failures that set V_{fail} so that the difference with V_0 is the greatest possible. Summary of an analytical study taking into account linear effects only [30].

In the following sections, we present the consequences of magnet failures as if the beam were not dumped. During operation at high intensity, the beam will be dumped much before the effects presented below are observed. However, it is not excluded that the whole beam gets lost when operating at low intensity (safe beam, probe beam or pilot bunch).

4.2.2 Dipole failures

Dipole failures have an impact on the closed orbit, leaving the twiss functions basically unchanged. The change in closed orbit due to a kick applied by a number of failing dipoles is given by equation 1.35. As the failure develops, the error kick of the magnets in the affected circuit increases leading to a growing distortion of the closed orbit. For a set of dipoles connected in series, we can express the evolution of the kick as a function of the current in the circuit and obtain the expression for the change in the closed orbit:

$$\Delta x_{co}(s) = \frac{\sqrt{\beta(s)}}{2\sin\pi Q}\left(\frac{i(t)}{I_0} - 1\right)\sum_i \theta_i\sqrt{\beta(s_i)}\cos\left(\Psi(s) - \Psi(s_i) + \pi Q\right) \tag{4.2}$$

where θ_i represents the nominal kick of each magnet, $i(t)$ the current in the circuit at a given time and I_0 the current in the circuit in the absence of failure. In phase-space, this change in the closed orbit translates into a displacement of the phase-space ellipse with respect to the original closed orbit offset. The shape or size of the phase space ellipse is not affected by dipole failures.

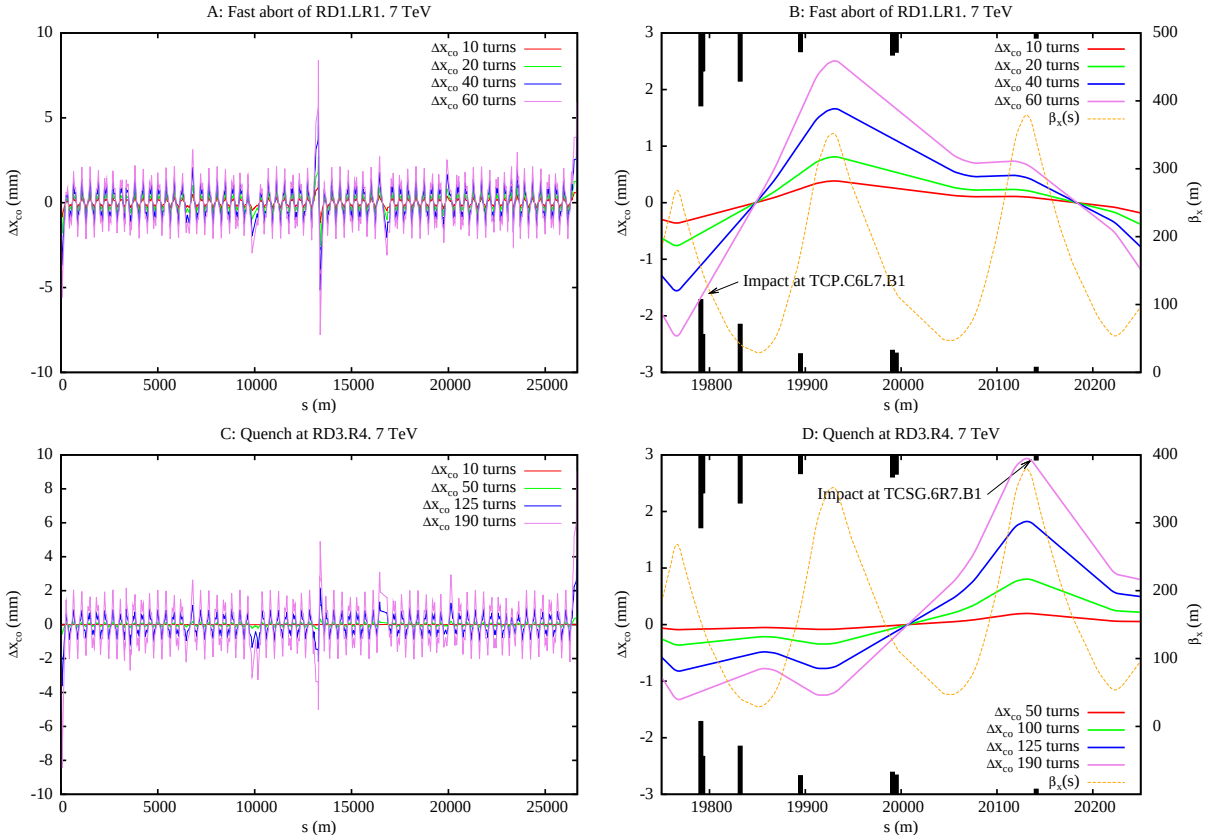

Figure 4.6: Evolution of the horizontal closed orbit distortion with time after a fast abort in RD1.LR1 (top) and a quench in RD3.L4 (bottom), with collision optics. The figures in the left show the closed orbit in all the ring; in the right a more detailed picture at IR7, where the horizontal aperture restrictions of the collimators is shown. For the failure of RD1.LR1 the main impact happens at TCP.C6L7.B1 after about 60 turns while if RD3.L4 fails, the impact happens in TCSG.6R7.B1 after about 190 turns.

For multiturn failures, this change in the closed orbit happens gradually and the losses will not necessarily appear in the aperture restrictions directly downstream from the failing magnets, as one might expect. Instead, the locations of the primary losses are determined by the betatron amplitude

at the aperture restrictions in the whole ring as well as the betatron phase difference between the failing magnets and these aperture restrictions. Figure 4.6 shows the simulated evolution of the closed orbit distortion due to a failure in RD1.LR1 as a function of time. From this graph, it is clear that the phase difference between each collimator and the failing magnets has a much bigger influence on the location of the primary impact than the actual aperture of the collimators. In both cases, the maximum distortions in the LHC ring occur in the inner triplets at IR1 and IR5, due to the high betatron amplitude at these locations. No direct losses are recorded at the inner triplets since the aperture budget is also larger (the width of the vacuum chamber is about 50 mm).

4.2.2.1 Previous studies on dipole failures

Some detailed studies on dipole failures in LHC have already been presented in [8], where an estimation of the time constant of losses produced by failures in the D1 dipoles in IR1 and IR5 is made. Other failure cases and an analysis of the beam behavior in case of dipole failures are given in [7]. The main conclusions of these studies are:

- The movement of single particles follows closely the closed orbit. The evolution of the transverse particle distribution during the failure can be estimated analytically.
- When collimators intercept the beam and the first accidental losses are recorded, an analytical approach is no longer possible to evaluate the transverse particle distribution or the loss rate. Tracking simulations are needed in these cases.
- When the beam starts touching a collimator the particle distribution is truncated at the edge of the collimator. The shape and peak amplitude of the whole distribution are also affected in every location of the ring.

Some considerations on the longitudinal distribution of these particles on different collimators have been made for a few failure cases, but no general conclusion has been drawn. The transverse distribution of the lost particles in the collimators after a failure has not been studied yet.

4.2.2.2 Closed orbit distortion and evolution of the transverse beam profile

Although the nature of the closed orbit distortion is simple and can be described accurately using equation 1.35, it is of interest to present some simulation results to ascertain the relationship between the evolution of the closed orbit distortion and the appearance of losses, as well as to study the influence of the time constant of the failure on these relationships. Table 4.2 lists the circuits and failures simulated to characterize the effects of dipole failures on the beam.

Circuit	Number of magnets	V_{nom} (V)	V_{fail} (V)	Mode	Failure case
RD1.LR1	12	633	0	Collision	Fast power abort
RD3.R4	2	5.5	0	Collision	Quench
RD1.LR1	12	40.9	695	Injection	Powering (worst case)
MB.A25R1	1[a]	12.8	0	Collision	Linear decay (none)

Table 4.2: Circuits and failures simulated to characterize the effects of dipole failures on the beam. For convenience, MB.A25R1 has been used to simulate linear current decays with different time constants which do not correspond to any particular failure case.
a: The corresponding circuit (RD.A12) contains 154 magnets, but only the current of the single magnet MB.A25R1 was changed.

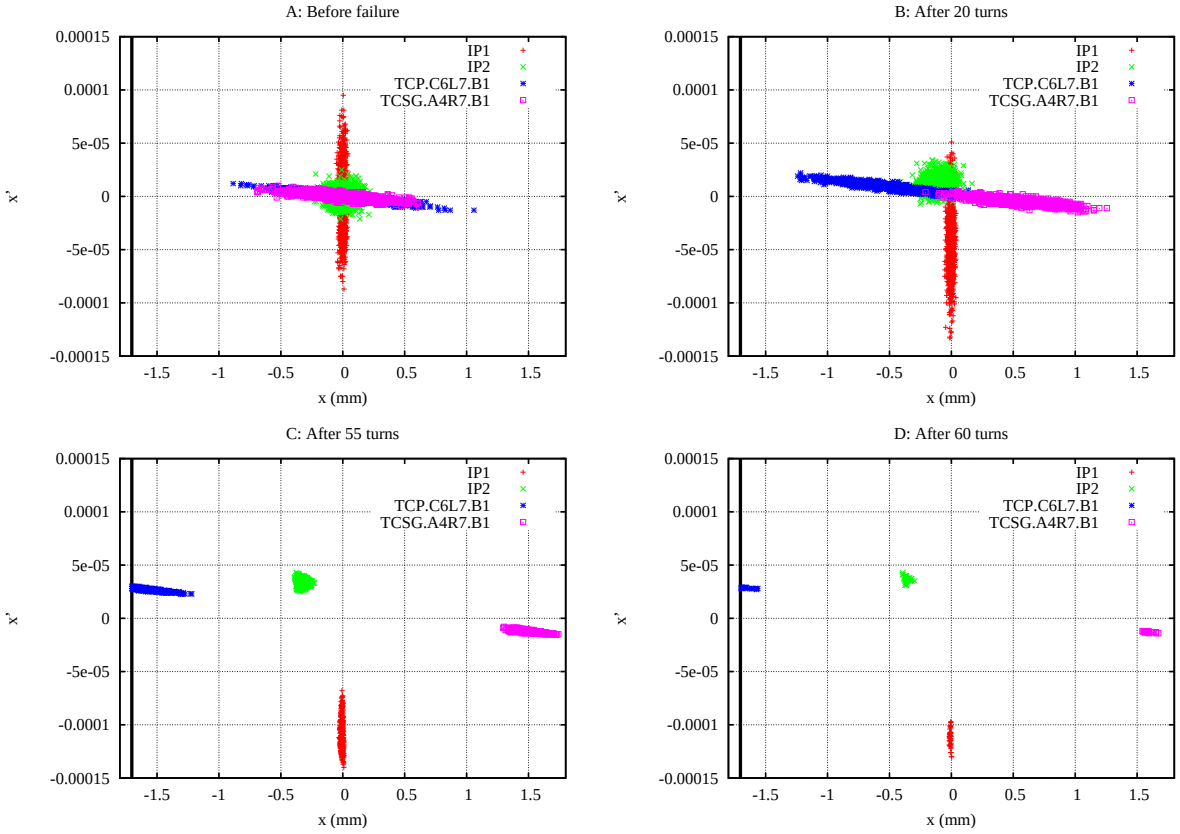

Figure 4.7: Evolution of the phase space particle distribution at different locations of the LHC after a fast abort of RD1.LR1 at 7 TeV. The vertical line at the left represents the horizontal aperture of TCP.C6L7.B1. Not surprisingly, the corresponding beam distribution is cut beyond this limit.

Figure 4.7 represents the evolution of the horizontal phase-space distribution of the beam after a fast abort of RD1.LR1 when operating at 7 TeV. The distribution is given for four locations: two collimators and two interaction points. The betatron amplitudes in the collimators (see appendix A) are more than a factor 10 larger than in the interaction points, therefore the change in the closed orbit is also much larger. It is worth to note that in IP1 the position of the beam is unchanged, and only its angle changes. This is due to the symmetric location of the failing magnets with respect to IP1.

Figure 4.8 and 4.9 show the evolution with time of the transverse particle distribution in the horizontal plane. The distribution follows the closed orbit change as the failure develops and its shape remains unchanged until the first significant losses start. Then, the profile at the location of the impact (TCP.C6L7.B1) becomes asymmetrical due to the losses. This asymmetry is less pronounced in the other locations because of the statistical redistribution of the particles due to their betatron oscillations. At IP1 the beam transverse shape remains basically unchanged and only the intensity decreases with the losses.

Figure 4.10 (A) represents a comparison between the closed orbit displacement and the average offset of the transverse beam distribution. The transverse distribution clearly moves with the closed orbit as expected. The RMS closed orbit offset $\langle x_{co} \rangle$ along the whole ring is also represented. Its initial value is due to the closed bumps in the experimental regions. $\langle x_{co} \rangle$ does not change significantly until turn 20 since this particular failure case initially makes the closed bump in IR1 smaller, compensating for the change in closed orbit in the rest of the machine.

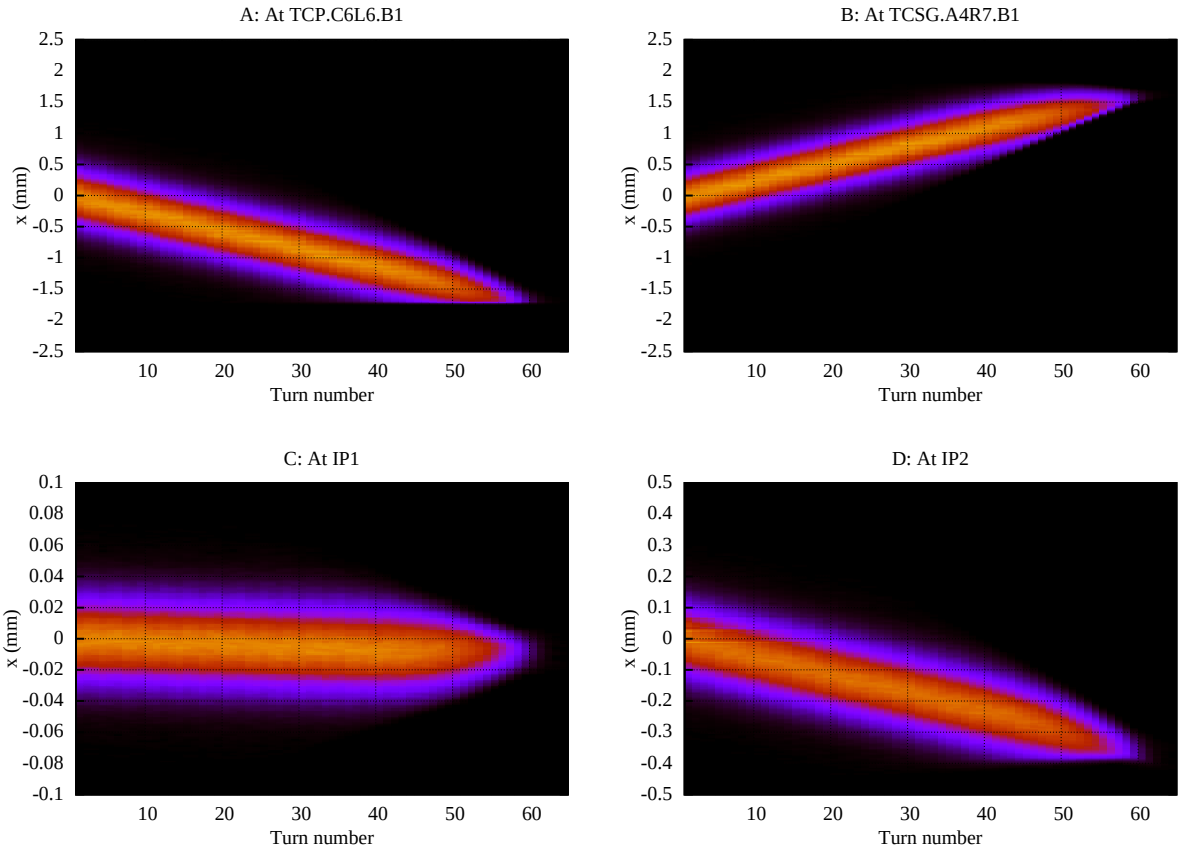

Figure 4.8: Evolution of the transverse particle distribution at different locations of the LHC after a fast abort of RD1.LR1 at 7 TeV. The color scale represents the particle density from black/blue (lower) to yellow (higher).

Figure 4.10 (B) shows the evolution of the beam size at different locations, compared with the fraction of particles remaining in the beam. The curves are close to each other, showing that the relative changes in beam intensity and beam size due to the progressive scrapping of the beam by the collimator follow a similar evolution.

4.2.2.3 Evolution of the losses

The evolution of the losses is represented in figure 4.11. For dipole failures the losses are generally very localized. For a fast abort in RD1.LR1 at 7 TeV, more than 99% of the losses occur at TCP.C6L7.B1 and the losses are distributed in five collimators only. Generally, the most affected collimator is hit first, although this is not necessarily the case: for a worst case powering failure in RD1.LR1 at injection, losses appear first at TCP.C6L7.B1 although TCSG.6R7.B1 is the most affected collimator. In this case the losses are distributed only in three collimators and TCSG.6R7.B1 receives about 90% of the total amount of losses.

4.2.2.4 Influence of the time constant of the failure

The time constant of the failure has an influence on the way the beam is affected. A very fast error kick (single turn) deflects the whole beam suddenly and the phase-space distribution becomes unmatched, behaving as a single particle. The beam as a whole undergoes betatron oscillations and

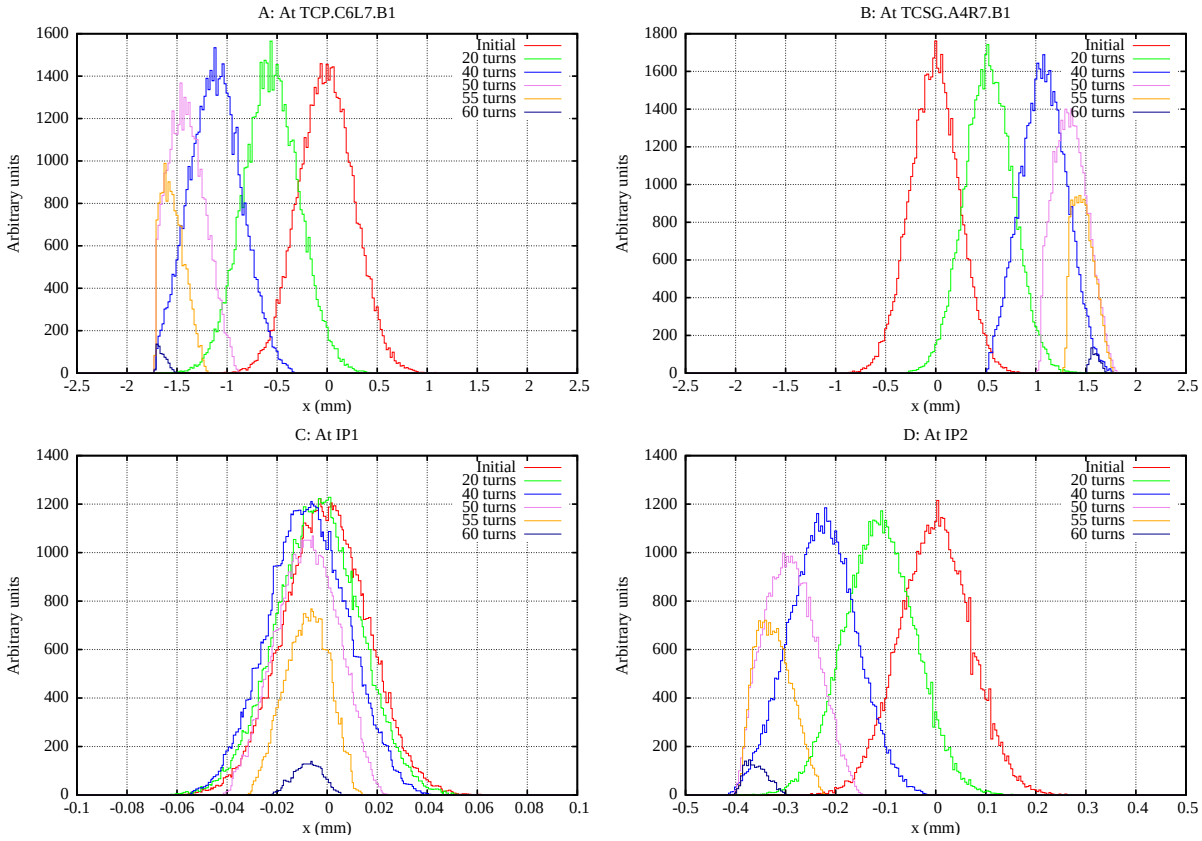

Figure 4.9: Transverse beam distribution at different times and locations after a fast abort of RD1.LR1 at 7 TeV.

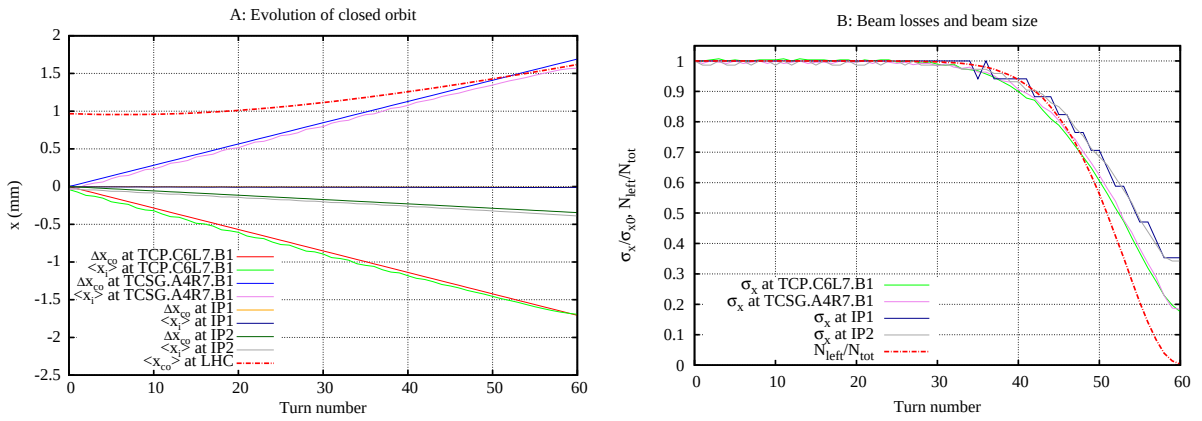

Figure 4.10: Evolution of closed orbit, beam intensity and beam size at different times and locations after a fast abort of RD1.LR1 at 7 TeV.

no closed orbit settles down (as in figure 1.4 D, E and F). For very slow dipolar errors, the change in the closed orbit can be considered adiabatic and all the particles remain in the phase-space ellipse during the failure. Very fast dipole failures lead to changes sitting somewhere in between these two extreme cases, although all the effects observed so far during LHC dipole failures indicate a behavior of the beam that is mostly adiabatic (the fastest LHC magnet failure[1] leads to a complete

[1]Excluding failures of the injection and extraction magnets

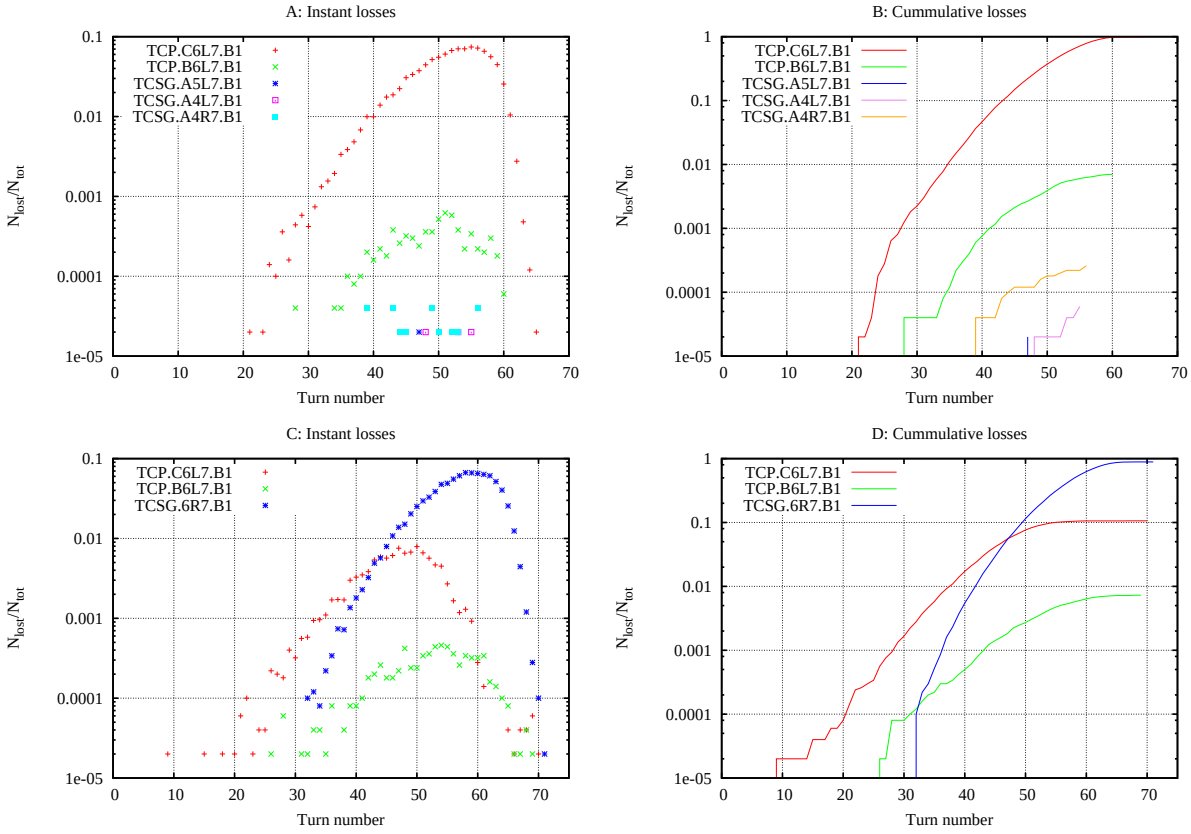

Figure 4.11: Evolution of the losses at different collimators after a fast abort of RD1.LR1 at 7 TeV (top) and a worst case powering failure ($V_{fail} = V_{max}$) at 450 GeV (bottom). The plots in the left represent the loss rate per turn. In the right the cumulated losses at each collimator are shown.

loss of the beam in not less than 60 turns).

A set of simulations of failures of MB.A25R1 using linear current decays with different slopes[2] has been done to evaluate the effects of the failure time constant on the evolution of the losses. The values of the slopes of the current decays have been chosen arbitrarily in order to yield loss time constants ranging from about 10 to 2000 turns. Each simulation has been done with 10000 particles.

The evolution of the losses at the most affected collimators is shown in figure 4.12. For the shortest loss time constant ($\tau_1 \approx 10$ turns) the position of the collimators with respect to the failing magnet is important, as evidenced by the appearance of losses in the collimators in IR6, which do not receive losses for longer time constants. The number of collimators affected by direct beam impact is also higher. This is due to a non-adiabatic change in the closed orbit from one turn to the next so that it intercepts various collimators at different locations. The closest collimators downstream from the failing magnets will intercept most particles. For slower failures, the changes are adiabatic and the beam starts hitting the collimators in IR7 first, where the beam is lost progressively, and the closed orbit offset does not reach the aperture of the collimators in IR6.

The appearance of losses in collimators other than those at IR7 is a good way to estimate the adiabatic nature of the effects on the beam at different timescales. From figure 4.12 we can infer that for failures leading to a complete loss of the beam in more than 100 turns, the change can be considered adiabatic (only collimators at IR7 are affected). The change is strongly non-adiabatic

[2]These current decays are artificial and do not correspond to any particular failure case

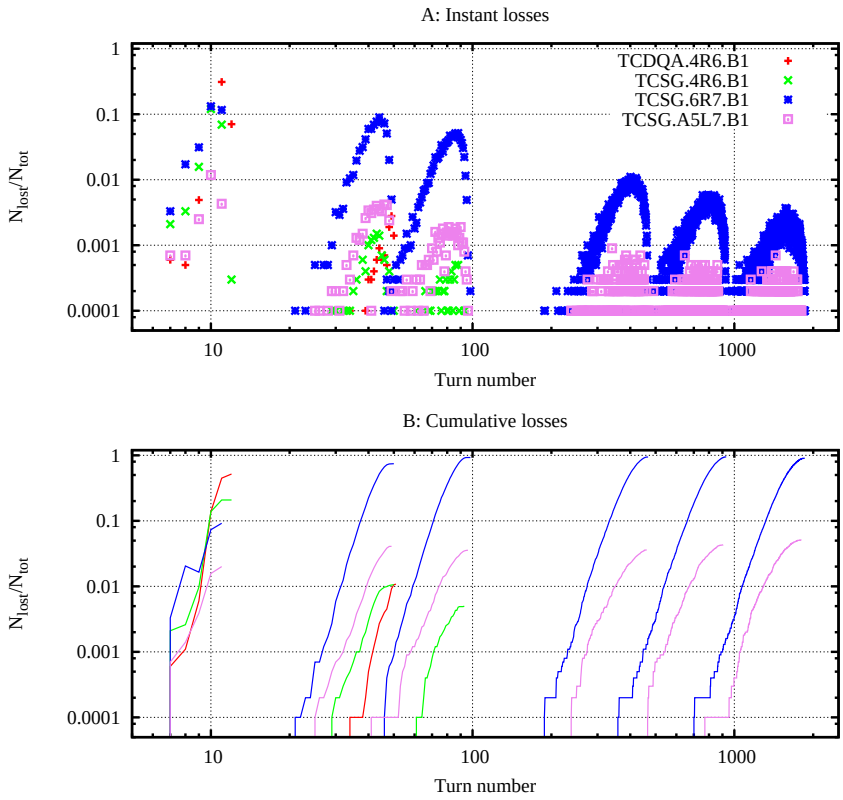

Figure 4.12: Evolution of the losses at different collimators for changes of the MB.A25R1 dipolar magnetic field with different time constants. Each simulation yields to a set of data (red, green, blue, purple) with a given loss time constant. The plot at the top represents the instant losses, the corresponding cumulated losses are represented at the bottom. 10000 particles were tracked for each case.

only for a failure leading to a loss of the beam in about 10 turns, confirming that for multiturn failures at LHC the changes can be considered adiabatic.

Figure 4.13 shows the relationship between the loss rate and the loss threshold times for the various current decays. The loss rate shows an inversely proportional relationship to the loss time constant. Threshold times evaluated at different fractions of the beam evolve in a similar way. This proportionality is expected from equation 4.2 and the simulated linear current decay. The decaying curves in figure 4.13 B indicate that for slower failures the losses are more distributed in time (losses happen in a larger time span).

4.2.2.5 Effects of the machine imperfections on the time constant of the losses

The existence of a closed orbit offset and multipolar field errors has an influence on the time constant of the losses produced by dipole failures. Because the closed orbit as well as the set of errors are unknown, this influence introduces an uncertainty on the simulation results obtained with an ideal LHC model or a different error set.

Simulations have been performed using 60 sets of statistically distributed multipolar and alignment errors with different seeds. 10000 particles were tracked for each case, both for the whole and tail distribution (see figure 3.3). The loss threshold times for different fractions of the beam and maximum loss rates have been recorded. The resulting data are summarized in figure 4.14. The loss threshold times and rates with different error sets are distributed around the loss threshold

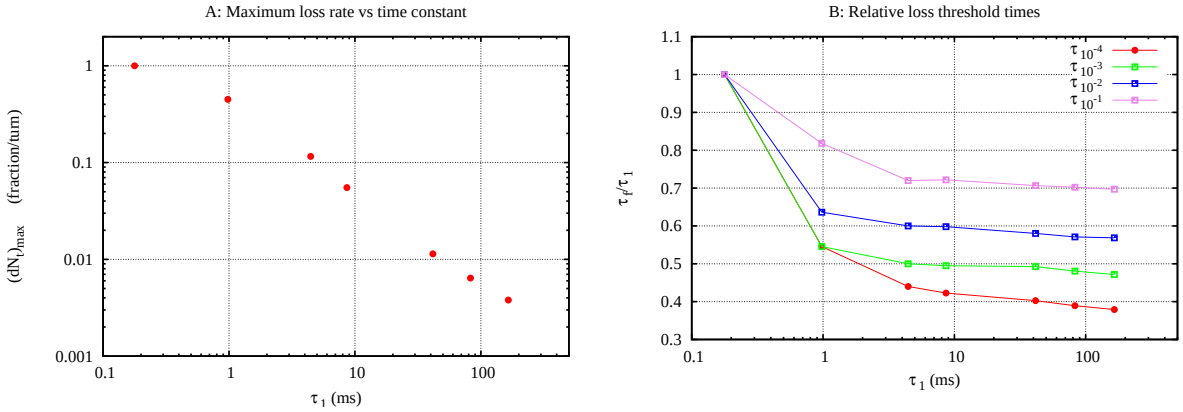

Figure 4.13: Relationship between the loss rate and loss threshold times for current decays with different time constants. The simulations were done with 10000 particles.

time and rate with an ideal model. The uncertainty associated to the machine imperfections is about ±0.5 ms (5-6 turns), or 10% of the loss time constant for the loss threshold times, and about 5% for the loss rate with respect to the ideal model.

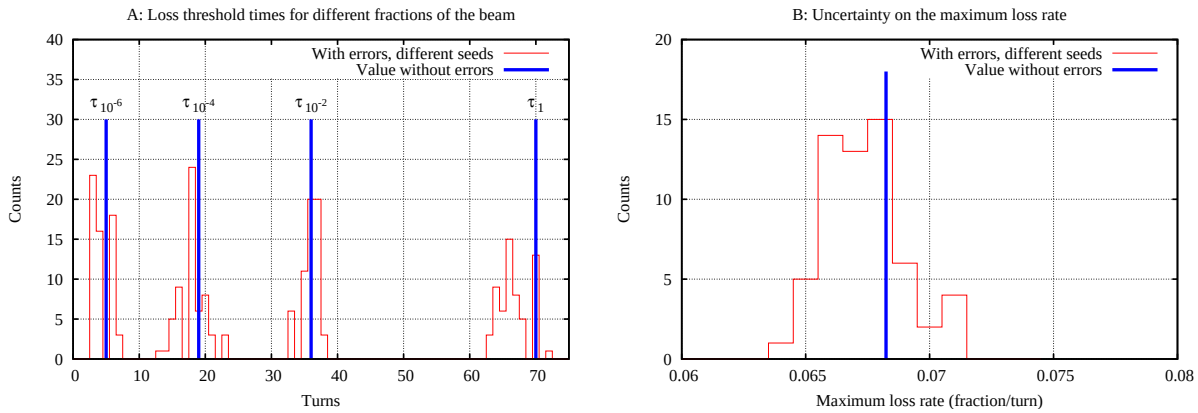

Figure 4.14: Influence of the machine imperfections on the loss threshold times for various fractions of the beam (left) and on the maximum loss rates (right). Worst case powering failure at RD1.LR1, injection.

4.2.3 Quadrupole failures

Contrary to dipole failures, studies on the effects of quadrupole failures on the beam and losses have not been published yet. In this section we present the effects of quadrupole failures on the beam, their evolution with time and their impact on the appearance of losses in the LHC ring. In this text, quadrupoles are classified as focusing or defocusing referring to the horizontal plane.

When quadrupole failures develop, the optics of the machine undergoes significant changes. The twiss functions change and the closed orbit may be affected too. The changes in the betatron tune and amplitude due to an error on a number of failing quadrupoles are given by equations 1.36 and 1.37. For a set of quadrupoles connected in series, the evolution of the beta beating and tune shift can be expressed as

$$\Delta Q = \frac{1}{4\pi}\left(\frac{i(t)}{I_0} - 1\right)\sum_i k_i l_1 \beta(s_i) \tag{4.3}$$

$$\frac{\Delta\beta(s)}{\beta(s)} = -\frac{1}{2\pi\sin(2\pi Q)}\left(\frac{i(t)}{I_0} - 1\right)\sum_i k_i l_i \beta(s_i)\cos\left(2(\Psi(s) - \Psi(s_i)) + 2\pi Q\right) \tag{4.4}$$

where k_i represents the strength of each quadrupole before the failure, $i(t)$ the current in the circuit at a given time and I_0 the current in the circuit in the absence of failure.

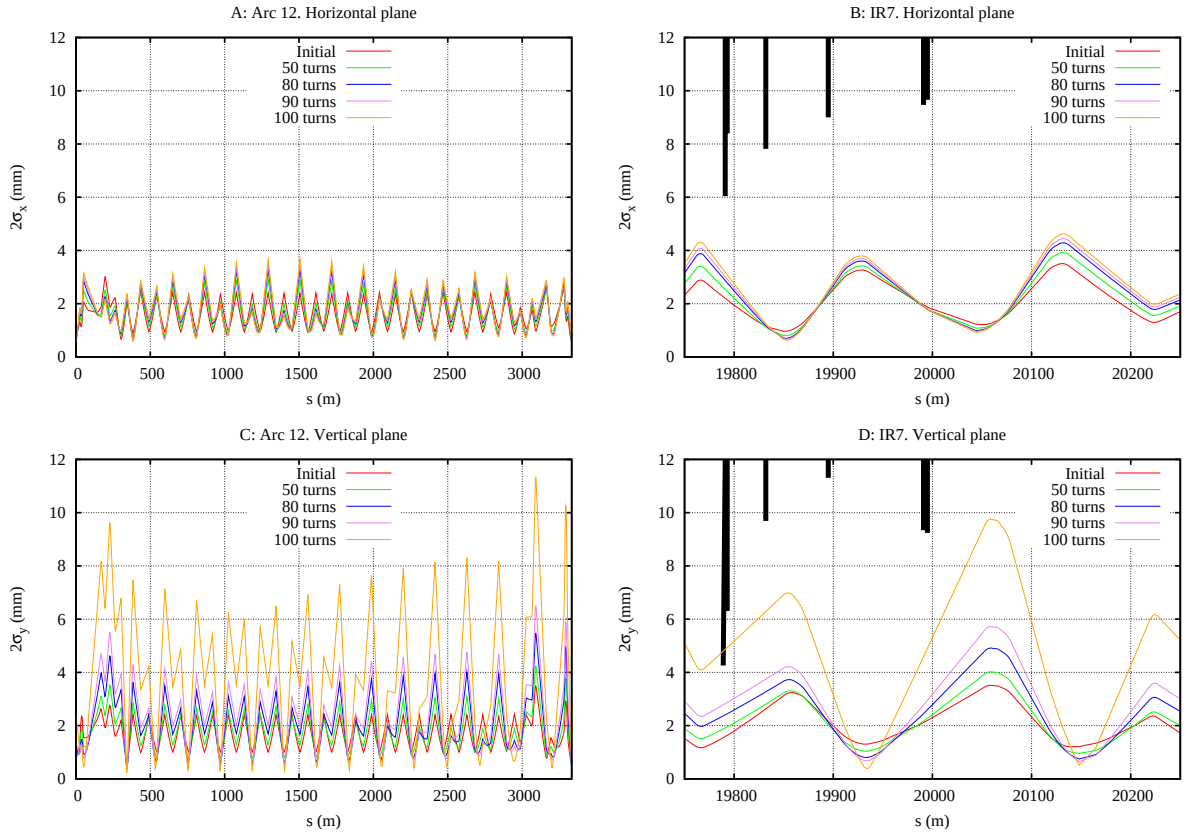

Figure 4.15: Beam size at different times after a failure in RQ4.LR7 at injection ($V_{fail} = V_{max}$), which leads to an increase of the strength of the magnets ($V_{fail} > V_{nom}$). The beam size is shown for the whole LHC ring (left) and in a more detailed view at IR7 (right). The beam size is given at 2σ.

The lattice of quadrupoles in a synchrotron is arranged to have an overall focusing effect on the beam. The role of quadrupoles is to ensure the transverse confinement of the particles and the main expected consequence of a quadrupole failure is a progressive defocusing of the beam. However, other phenomena take place as the twiss functions evolve due to the failrue. Detailed studies are needed for a good understanding of the perturbations induced in the beam, and for the quantitative assessment of the evolution of the optics parameters and subsequent losses. Equations 4.3 and 4.4 are interdependent and the analytical approach using these two equations is very approximate when the changes are large, in particular when the tune reaches a value close to a linear resonance. Simulations are needed to characterize the effects of quadrupole failures on the beam and, as in the case of dipole failures, tracking is required to study the appearance of losses.

Figure 4.15 shows the evolution of the beam size at different times after the start of the current change due to a failure in RQ4.LR7 with injection optics. RQ4.LR7 contains a set of both focusing

and defocusing quadrupoles. The change in the beam size is presented at the horizontal and vertical planes. It has been derived from the betatron amplitude and takes into account only linear effects. The beam size increases with time and after 100 turns the core of the beam in the vertical plane is already closer than 2σ to the aperture at TCP.D6L7. Note also that the greatest change happens just before the beam is lost (between 90 and 100 turns, figure 4.15 D), indicating a sudden expansion of the beam size.

4.2.3.1 Changes in the twiss functions and in the transverse beam distribution

Quadrupole failures lead to the changes in the tune and betatron amplitude described in equations 4.3 and 4.4. The increase in betatron amplitude, which leads to an increase in the transverse size of the beam is of more relevance for the losses. However, this increase of the betatron amplitude is driven mainly by the term $1/2\pi \sin(2\pi Q)$ in equation 4.4, hence by the change of the tune. The change of the betatron amplitude translates into a stretch or shrink of the transverse phase-space ellipse, while the change in the tune induces a rotation of the whole ellipse.

We can make a distinction between two types of circuits with respect to the quadrupoles that they interconnect: circuits with focusing (or defocusing) quadrupoles only, and circuits with both focusing and defocusing quadrupoles[3]. In order to characterize the effects on the beam of quadrupole failures, we consider both increasing and decreasing current at injection, and decreasing current only at collision. Because most of the magnets are powered close to their maximum current when operating at 7 TeV, the worst case scenario at 7 TeV corresponds to current decays. The circuits, modes of operation and current changes used in these simulations are listed in table 4.3.

Circuit	Focusing magnets	Defocusing magnets	V_{nom} (V)	V_{fail} (V)	Mode	Failure case (τ_1 in turns)	Case
RQ4.LR7	15	15	21.8	495	Injection	Powering (150)	1
			21.8	0	Injection	Powering (10000)	2
			340	-	Collision	Linear decay (250)	3
			340	-	Collision	Linear increase[a] (120)	4
RQ5.LR7	15	15	23.1	495	Injection	Powering (230)	5
			23.1	43.2	Injection	Powering (3900)	6
			23.1	0	Injection	Powering (4800)	7
			345	-	Collision	Linear decay (130)	8
			345	-	Collision	Linear increase[a] (150)	9
RQD.A12	0	47	14.2	-	Collision	Linear decay (120)	10
			14.2	-	Collision	Linear decay (250)	11
RQF.A12	47	0	13.4	-	Collision	Linear decay (120)	12

Table 4.3: Circuits and failures simulated to characterize the effects of quadrupole failures on the beam. For convenience, some of the simulated decays (linear decays) do not correspond to any real failure. The last column assigns a number to each case for later reference in the chapter.
a: Simulated with a current increase at collision in order to have a coherent comparison of the tune change for different current evolutions, starting from the same working point (figure 4.23).

[3]There are also some skew quadrupoles, though they do not produce fast losses [30].

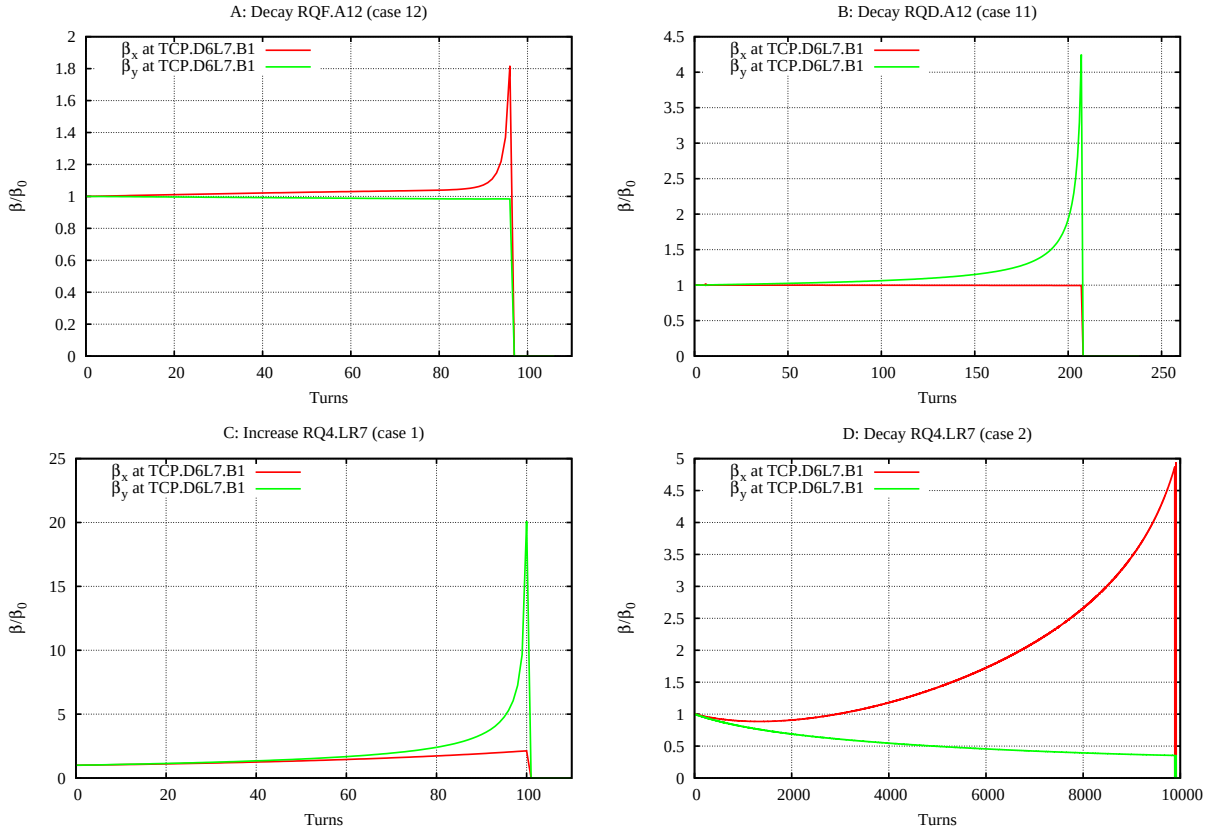

Figure 4.16: Change in the betatron amplitudes for different cases.

The relative change in the betatron amplitude for representative cases is shown in figure 4.16. The final drop in the curves indicates that the strength of the failing magnets has reached a value with which no stable optics are possible and after this point the remaining particles are lost quickly. The corresponding changes in the tunes are represented in 4.17. In this case when no stable optics exist (linear resonance crossings), no points are represented. In some cases (4.17 A and B) the resonance is crossed and some stable points are represented after the crossing. However, the remaining particle have reached amplitudes larger than the dynamic aperture and are quickly lost even if the new optics are stable.

These plots show that the change of the tune follows the change in the current for most of the time while the failure develops (linear or exponential in these cases). For circuits with focusing (or defocusing) quadrupoles only, the factor $(i(t)/I_0 - 1)$ does not play a very significant role in the change in the beta function. Instead, this change is mostly governed by the evolution of the tune itself. The beam size expands suddenly when the tune reaches an integer or half-integer value (linear resonances, figures 4.16 and 4.17 A, B and C). This sudden increase in the betatron amplitude has a slight but noticeable influence in the evolution of the tune itself.

For circuits with both focusing and defocusing quadrupoles, the tune changes more slowly since the effect of the field error in the focusing magnets compensates the effect in the defocusing magnets and viceversa ($\sum_i k_i l_i \beta(s_i)$ in equation 4.4 is smaller than in the case of purely focusing or defocusing circuits due to the quadrupole strengths of different signs). For failures in these circuits, the factor $(i(t)/I_0 - 1)$ has a much bigger influence in the change of the betatron amplitude and the beam may be lost before any linear resonance condition is met (table 4.3, case 2).

Another interesting fact is that for current decays in circuits with focusing or defocusing

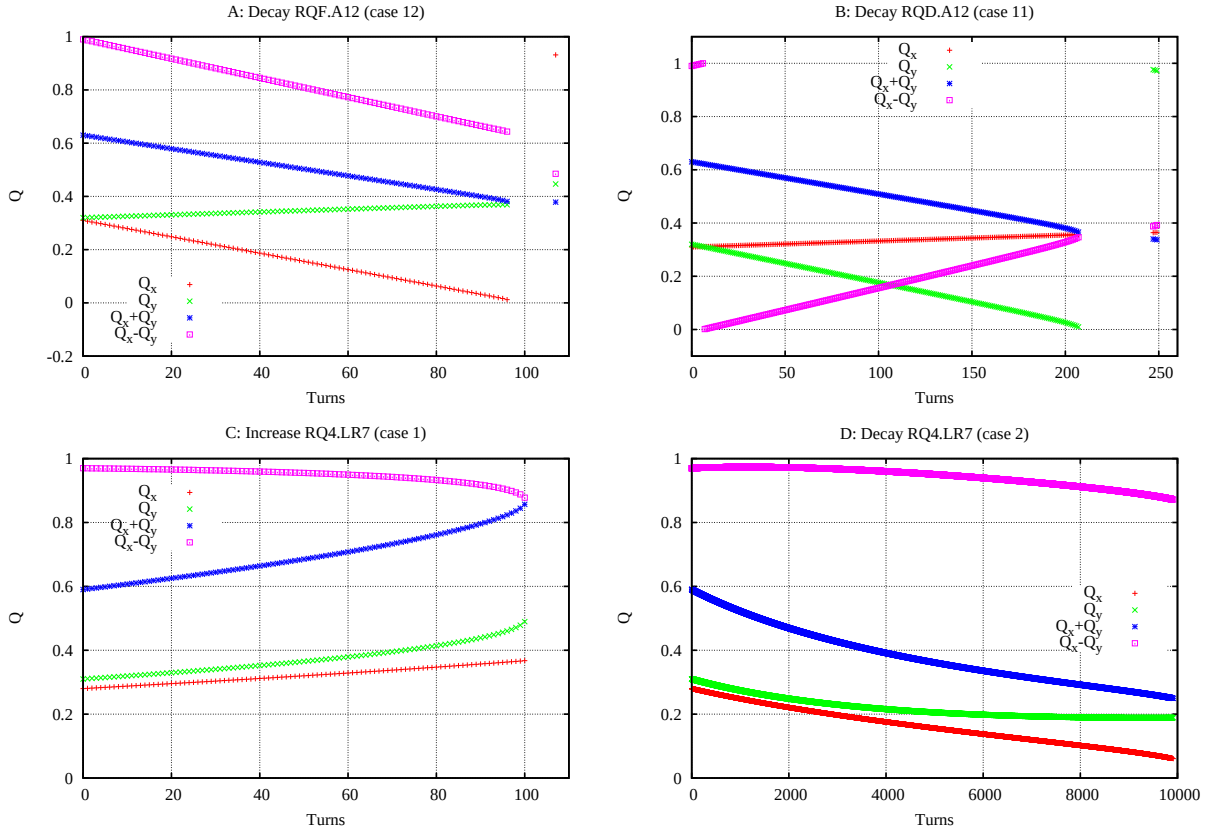

Figure 4.17: Change in the tunes for different cases. The sum and difference of the tunes in each plane are also represented to evaluate possible coupling resonance crossings.

quadrupoles only, the expansion of the beam size happens in the focusing plane while the betatron amplitude in the defocusing plane remains basically unchanged. This can be explained with equation 4.3 comparing the values of the betatron amplitudes at the focusing and defocusing quadrupoles (for the LHC arc main quadrupoles $\beta_{QF} \approx 180$ m, $\beta_{QD} \approx 30$ m). The change in the tune at the focusing plane is faster and reaches a linear resonance condition first. For failures in circuits containing both focusing and defocusing quadrupoles, the tunes in both planes change at rates

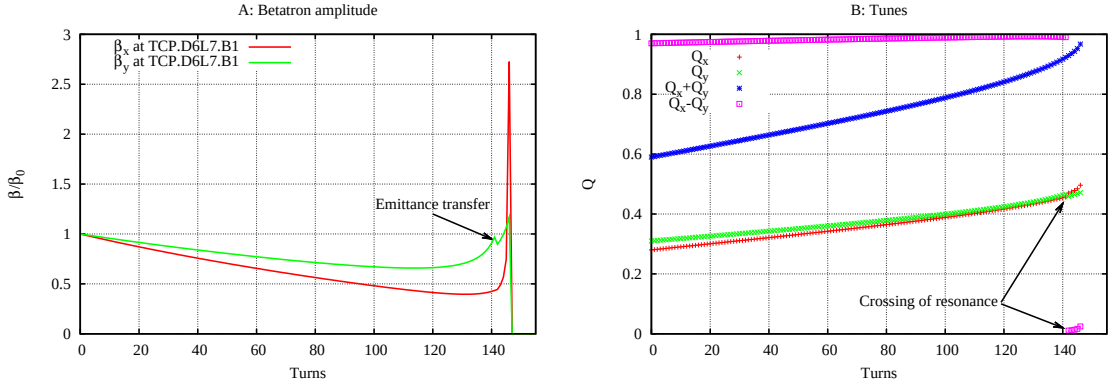

Figure 4.18: Evolution of the betatron amplitude and tunes after a current increase in RQ5.LR7 (case 5). The crossing of the difference coupling resonance is clearly visible after 140 turns.

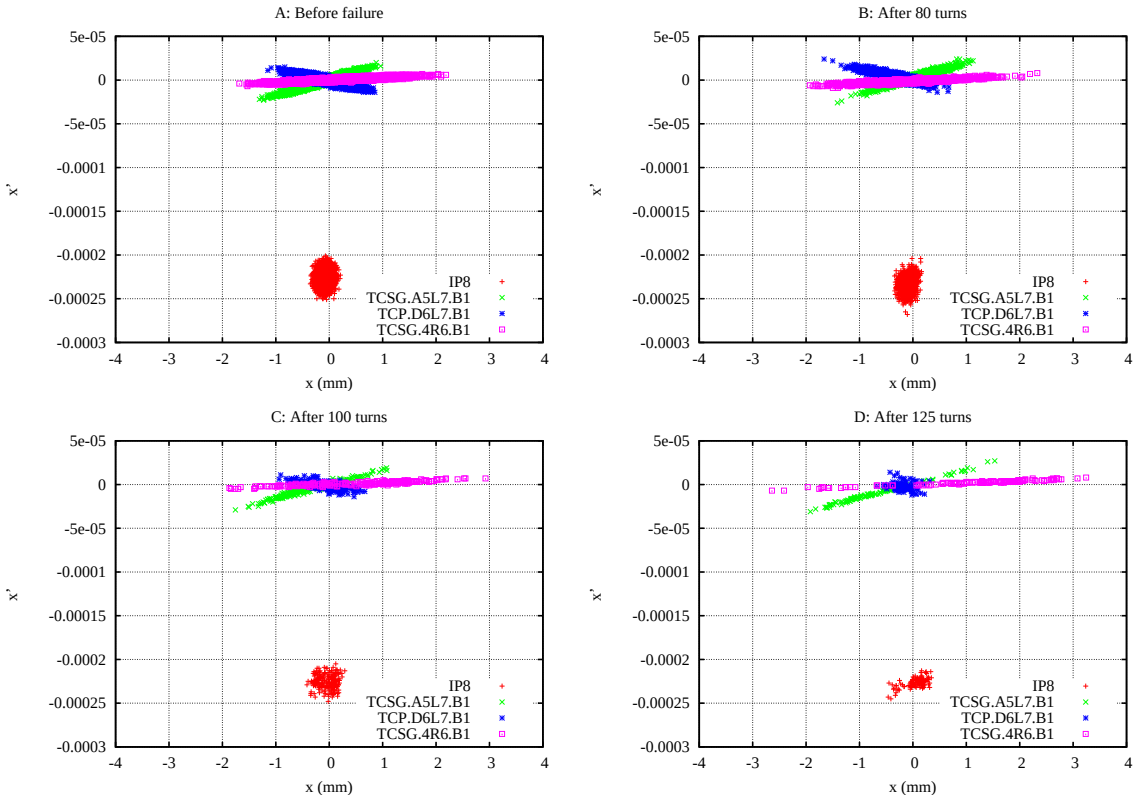

Figure 4.19: Horizontal phase space diagram for a current decay in RQD.A12 at 7 TeV (case 10).

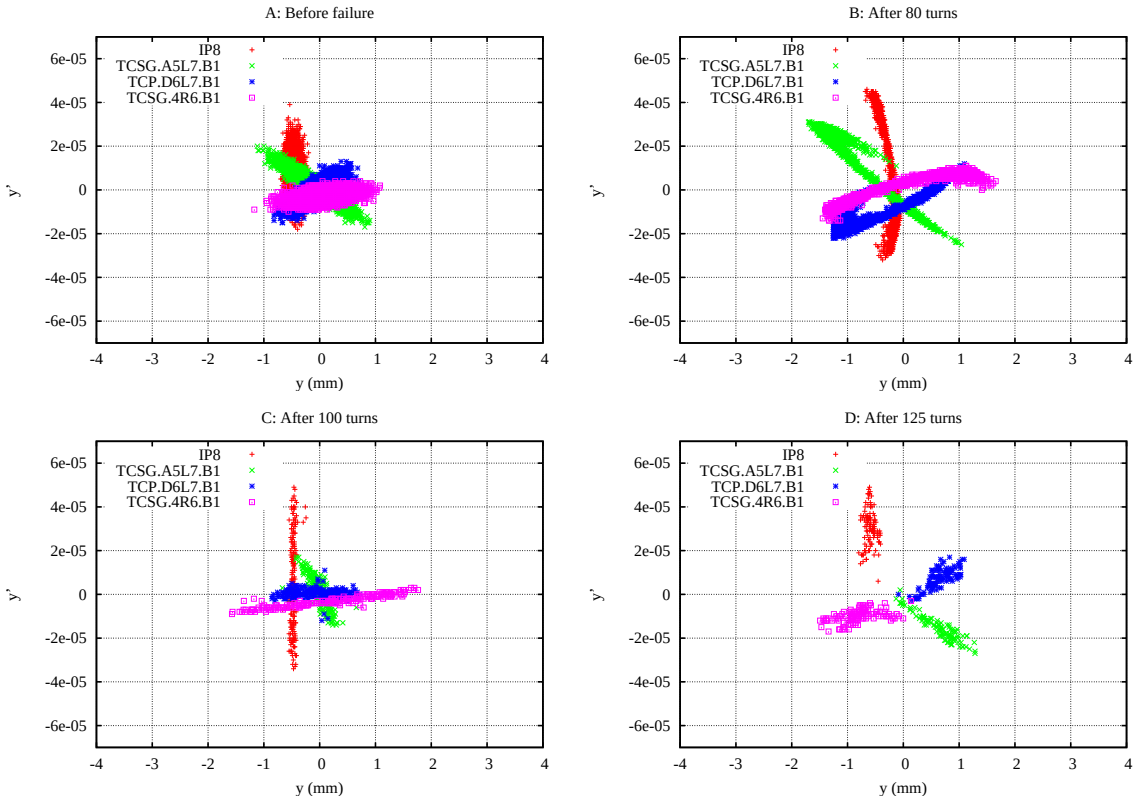

Figure 4.20: Vertical phase space diagram for a current decay in RQD.A12 at 7 TeV (case 10).

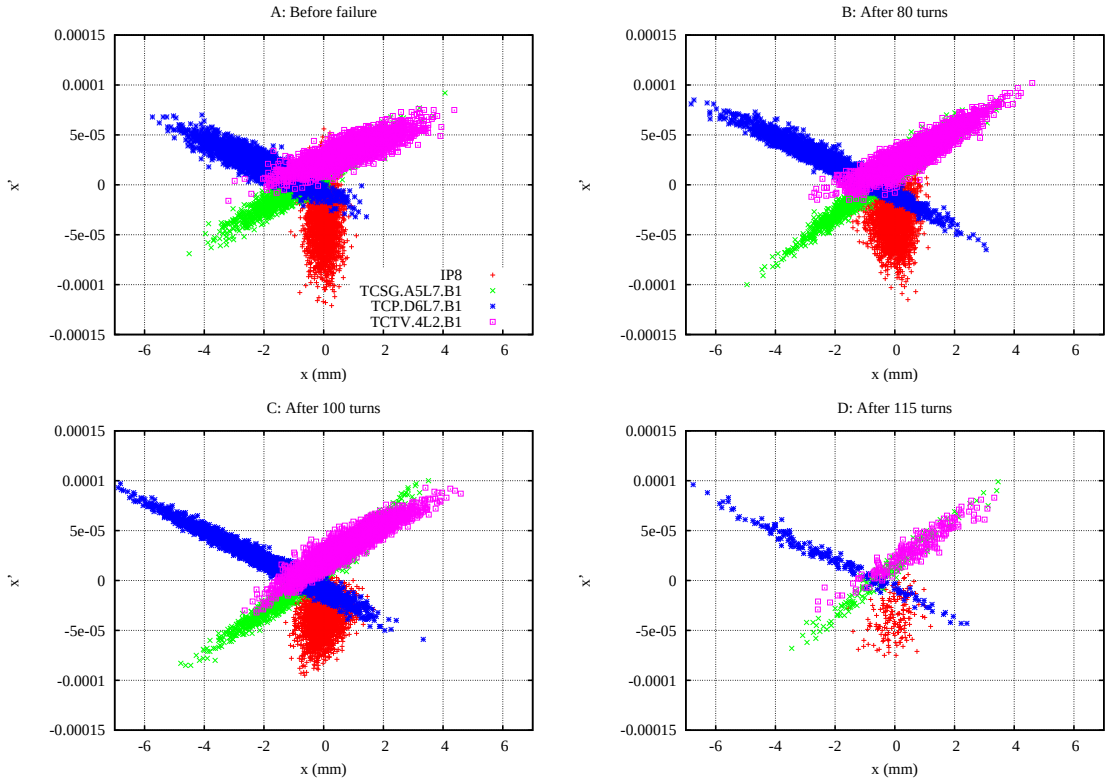

Figure 4.21: Horizontal phase space diagram for a current increase in RQ4.LR7 at 450 GeV (case 1).

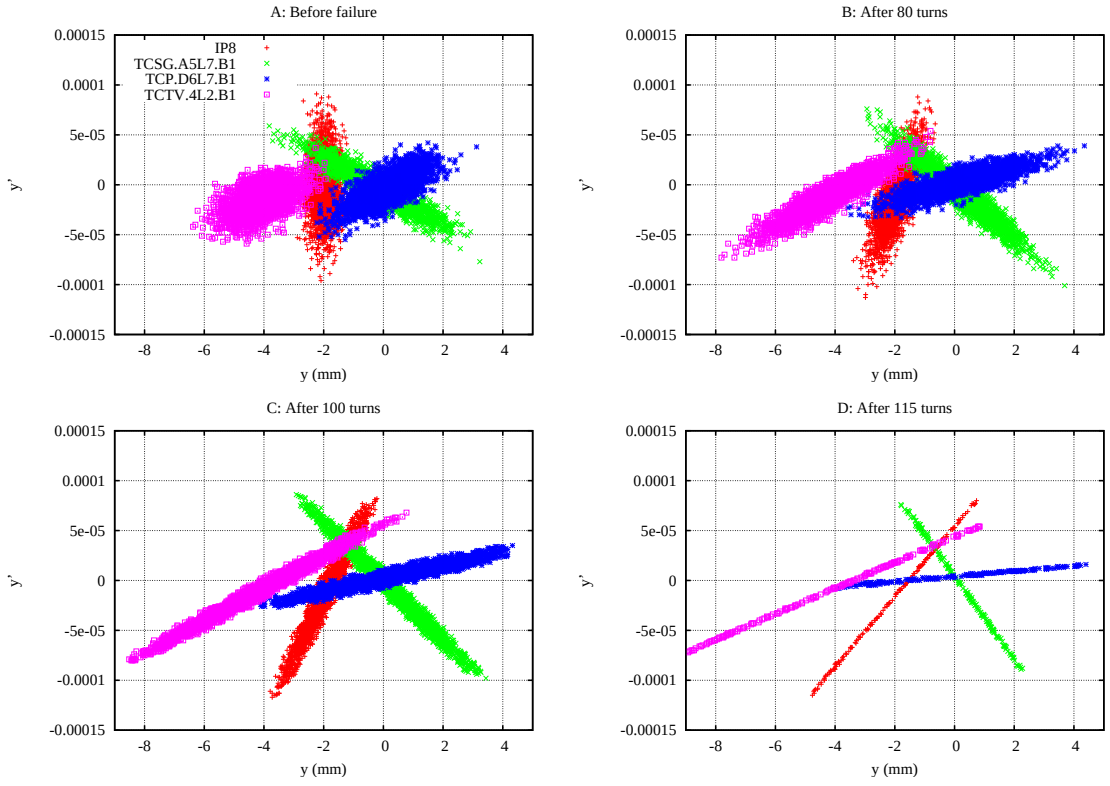

Figure 4.22: Vertical phase space diagram for a current increase in RQ4.LR7 at 450 GeV (case 1).

that are related to the betatron amplitudes in the focusing in and defocusing quadrupoles. For the LHC circuits presented here the betatron amplitudes in the focusing and defocusing quadrupoles are very close and the change in the beam size can be seen in both planes. However, the beam size expansion happens mostly in one of the two planes because the linear resonance is reached in this plane first. The direction of the change in the tunes, the initial tunes in each plane and slight differences in the betatron functions in the focusing and defocusing quadrupoles have an influence on the plane which sees the biggest beam size increase. In some cases these general considerations do not apply. For example, for a current decay in RQ4.LR7 (case 2, figure 4.16 D) the beam is lost due to the direct influence of the current change on the beam size, before any linear resonant state is reached. In this case the change in current required to lose the beam is higher and the change in the beam size more gradual.

If the working point gets closer to a difference resonance, an emittance transfer occurs [74]. This happens for a current increase in RQ5.LR7 (case 5, figure 4.18). The values of the optics functions in each plane are swapped and the beam size eventually expands in the horizontal plane.

Figures 4.19 and 4.20 show the phase space distributions for a fast current decay in RQD.A12 in the horizontal and vertical planes. The phase space diagram in the horizontal plane, where magnets in RQD.A12 are defocusing, shows an increase in the beam size and a a progressive decrease in the intensity, but the shape of the phase-space distribution does not undergo significant changes. In the vertical plane, where failing magnets are focusing, this is not the case. Together with an increase in the beam size, the shape of the distribution is distorted after 80 turns, before the intensity changes significantly. After that, the intensity of the beam drops and after 125 turns, shortly before all the beam is lost, the distributions move away from the center of the vacuum chamber. The following points explain the phase space behavior of the particles:

1. The effects in the horizontal (defocusing) plane are less pronounced. This can be explained by the smaller betatron amplitude at the defocusing quadrupoles, as discussed above.

2. The distortion of the phase-space distribution in the vertical plane is due to the change in the tune, which induces the crossing of several resonant states.

3. The drift of the distributions away from the center of the ideal orbit in the vertical plane can be explained by the unmatching of the beam during the crossing of an integer resonance. After the crossing the beam oscillates in the vertical plane (figure 4.24 D) and the phase space distribution is not centered after 125 turns.

Figures 4.21 and 4.22 show the same plots for a powering failure at RQ4.LR7. In this case, the circuit includes both focusing and defocusing quadrupoles. The change in the horizontal distribution is noticeable, but most of the effects of the failure appear in the vertical plane, in spite of the symmetry of the quadrupoles in the circuit with respect to both planes. The following points explain this behavior:

1. The vertical tune approaches a half-integer value while the horizontal tune does not cross any significant resonance.

2. The stretched shape of the distributions after 115 turns in the vertical plane are due to this second order resonance. The particles with higher amplitudes are lost quickly, and only those closer to the center of the phase-space distribution remain on the orbit.

From the preceding figures, it is clear that the most important parameter to evaluate the effects of quadrupole failures on the beam is the change in the tune. Figure 4.23 summarizes the change in the tunes for current changes in various circuits. For most cases, third order resonances are crossed and the beam is lost when the tune reaches a linear resonance. For cases 3 and 8, no resonance is crossed and the beam is lost because of the direct increase in the betatron amplitude. For cases 11 and 12 the integer resonances are crossed just before the beam is lost and some points with stable optics appear in the resonance diagram at (0.37,0.97) and (0.92,0.44).

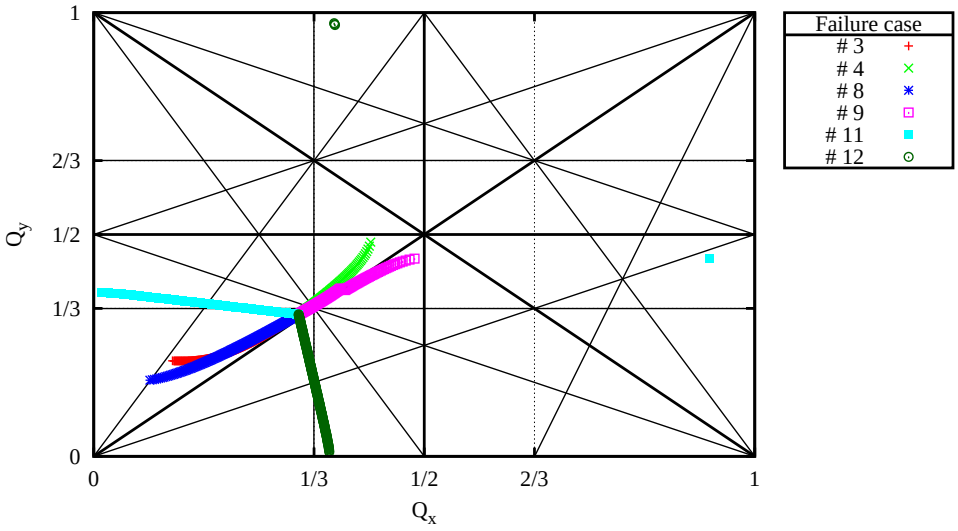

Figure 4.23: Tune diagram for different failure cases at 7 TeV, each producing a change in the working point in a different direction. Only one failure has been chosen for each direction of change of the working point.

During a quadrupole failure, the profile of the beam can evolve in different ways. The defocusing of the beam after a certain time can be seen in some cases while in other cases, different phenomena lead to a loss of the beam before the defocusing can be seen. Figure 4.24 shows the evolution of the transverse profile in both planes for two different failure cases. Typically, a purely quadrupolar failure modifies the beam as shown in figure 4.24 A: as the current changes, the beam is defocused in one plane and is not significantly affected in the other, apart from the decrease of the number of particles and very slight transverse oscillations of the average of the distribution in the horizontal plane. Figure 4.24 B and C show a different scenario. The beam is not defocused but deflected until it hits the collimator; a defocusing of the beam is not noticeable. In case C we can also see slight oscillations in the horizontal plane, similar to those in case A. Figure 4.24 D shows the beam profile in case of a fast current change at RQD.A12 ($\tau_1 :< 100$ turns). Initially, the beam evolves as in the previous cases but it is not completely lost. The remaining beam distribution oscillates with time at increasing frequency in both planes, and is progressively lost. The explanation of these different behaviors lies on the type of resonance that leads to the beam loss and the existence of a closed orbit offset at the location of the failing quadrupoles:

- *Case A*: The tune reaches a half-integer resonance. The beam is defocused according to equation 4.4 and the closed orbit is not significantly affected, in spite of the error kick at the quadrupole magnets. The oscillations in the transverse plane have twice the betatron frequency and can be explained by a turn-to-turn unmatching of the optics with respect to the beam distribution, originally matched to the nominal optics (slight non-adiabaticity). The importance of this phenomenon depends on the rate of change of the tune.

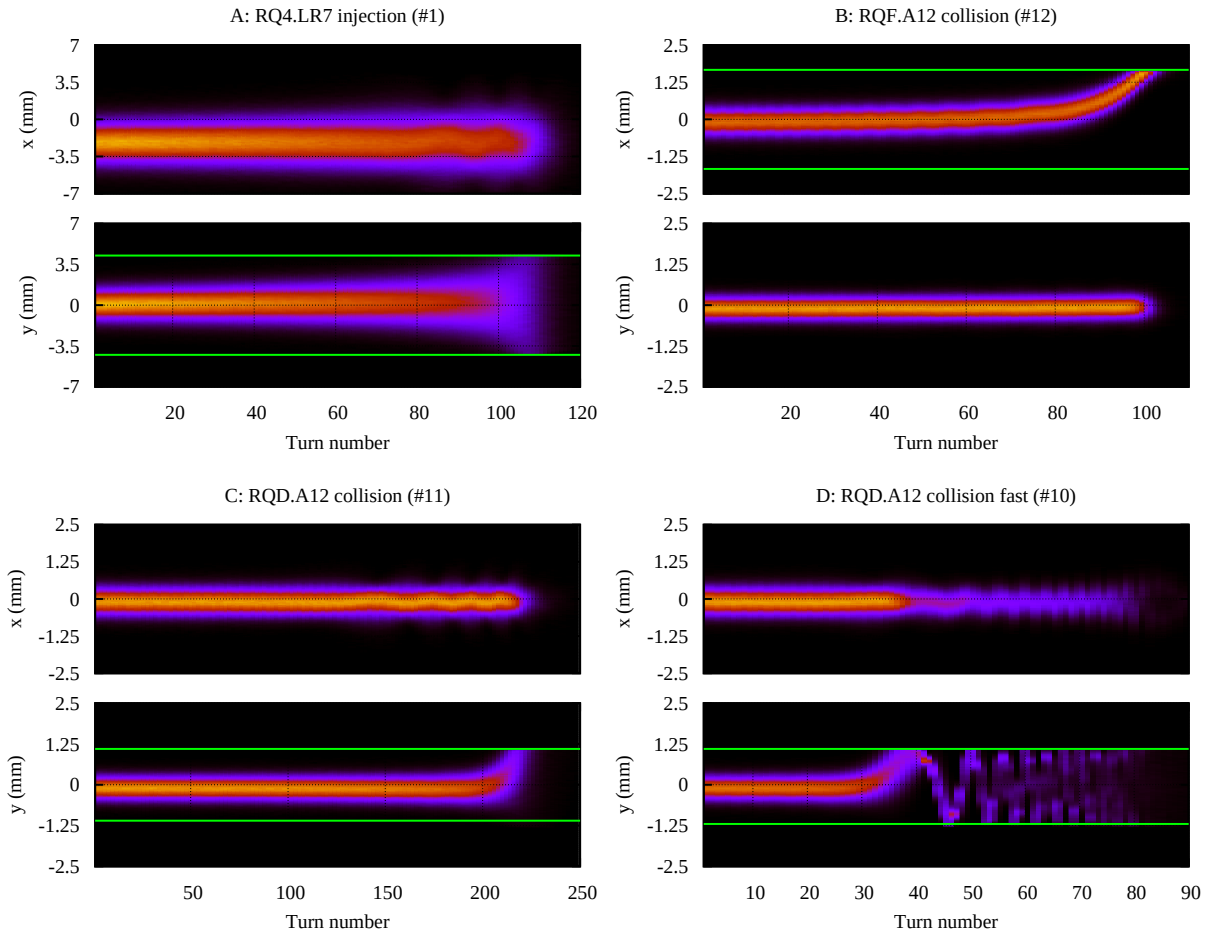

Figure 4.24: Evolution of the beam distribution at TCP.C6L7.B1 for different failure cases. In green the aperture of the collimators where the beam is lost (TCP.C6L7.B1 for the horizontal plane, TCP.D6L7.B1 for the vertical plane).

- *Cases B and C*: The tune reaches an integer resonance and both the beam size and closed orbit are affected. As $Q \rightarrow p,\ p \in \mathbb{N}$, the increase of the closed orbit offset follows basically the evolution of $1/2sin(\pi Q)$ while the increase in the beam size follows $1/2sin(2\pi Q)$. Because $sin(\pi Q)$ approaches zero faster than $sin(2\pi Q)$, the effect on the closed orbit is faster than the increase of the beam size and is responsible for the loss of the beam. Note that although it is a change of the closed orbit offset, the evolution of this change is very different from the change of the closed orbit produced by dipole failures (figure 4.8).
- *Case D*: The working point reaches an integer resonance as in cases B and C, but the change in the tune is fast enough to cross the resonance condition and reestablish stable optics before the whole beam is lost. After the resonance crossing, the remaining particles are not matched to the new optics and the particle distribution oscillates at twice the betatron frequency.

Figure 4.25 shows the beam transverse distribution at TCP.C6L7.B1 at different moments after the start of the current change for three failure cases (1, 11, and 12). For case 1 the distribution flattens due to the defocusing and the losses. After 110 turns the particles are uniformly distributed within the limits set by the collimator aperture. For case 12 (figure 4.25 B), the beam is displaced progressively until it is lost. In this case, an interesting phenomenon happens. The beam size is reduced at this location and the peak particle density increases as the distribution drifts transversely.

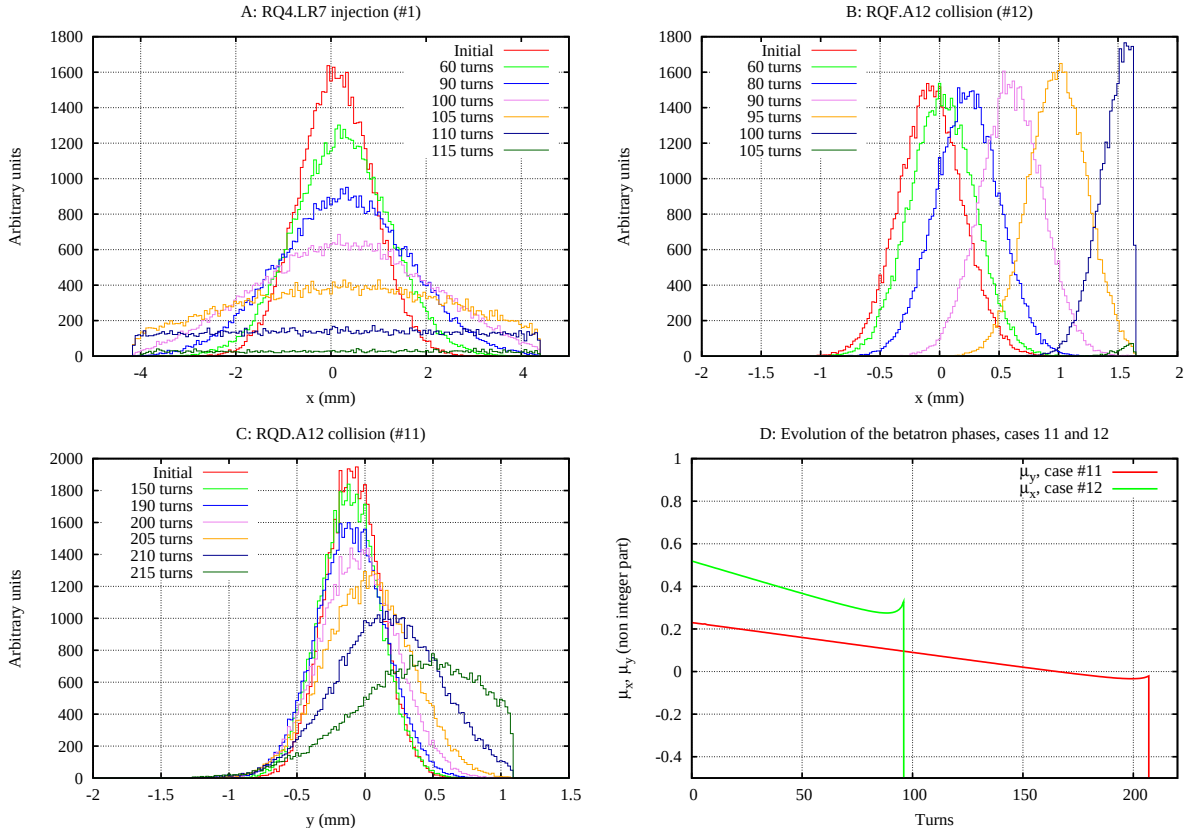

Figure 4.25: Evolution of the beam distribution at TCP.C6L7.B1 for cases 1, 11 and 12. (D) shows the evolution of the betatron phase for cases 11 and 12.

This phenomenon is not observed for case 11 (figure 4.25 C) in which, otherwise, the beam shows the same behavior. This decrease of the beam size in case 12 is due to a sudden increase in the betatron phase at this location from turn 89 (figure 4.25 D). The distribution becomes then unmatched with respect to the previous turn and its transverse size starts changing. The phase-space distribution at TCP.C6L7.B1 stretches from the second to the fourth quadrants and an increase in the value of the betatron phase makes the axis of the phase-space ellipse turn clockwise. The consequence is an initial reduction of the beam size, as observed. Given enough time, the beam size would increase again and oscillate.

4.2.3.2 Evolution of the beam size during resonance crossing

In most cases, the factor that determines the behavior of the beam during a quadrupole failure is the linear resonance that is first reached. If the change of the tune is fast enough, the linear resonances can be crossed without losing all the beam (figure 4.24 D), although the quadrupole failures expected at the LHC are too slow to produce linear resonance crossings. Higher order resonances are also crossed and their influence on the beam size depends on the time-constant of the failure (larger for slower failures) and on the order of the resonance (larger for lower order resonances).

Until now, we have considered the betatron amplitude as a measure of the beam size (the evolution of the beam transverse distribution has been presented for qualitative understanding). However, the beam size can undergo significant changes due to high order phenomena that are not

included in the linear approach. Third order resonance crossings are the most significant non-linear effect in case of quadrupole failures. In order to evaluate the consequences of third order resonance crossings, the width (beam size) and average (beam centroid) of the transverse distribution has been derived at each turn for cases 5 and 6 (figure 4.26).

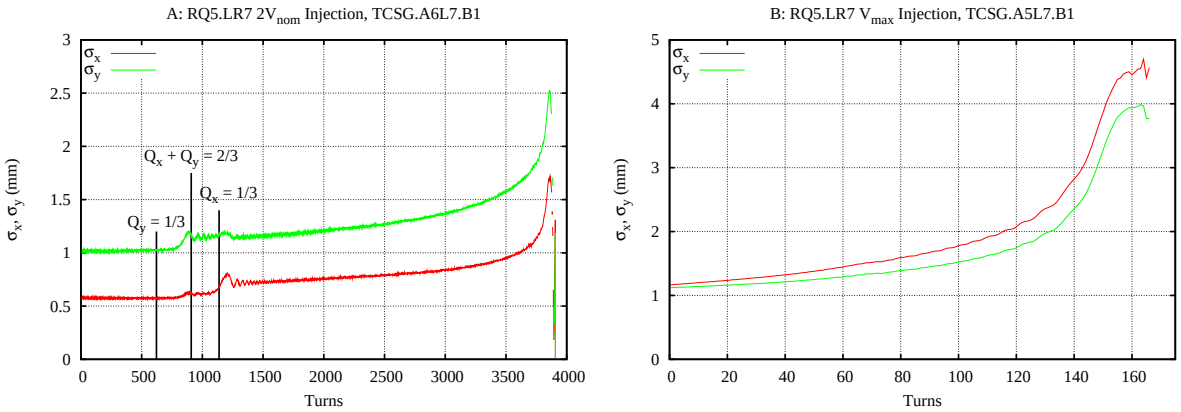

Figure 4.26: Evolution of the beam size at TCSG.A6L7.B1 for case 6 and at TCSG.A5L7.B1 for case 5. The crossing of third order resonances has a clear influence on the beam size for case 6 but not for case 5.

Figure 4.26 shows the evolution of the beam size during the cases 5 and 6, which generate the same changes in the optics at different speeds (for both cases the evolution of the working point is as in case 9, see figure 4.23). The effects of third order resonances are particularly clear in case 6. The beam size experiences a sudden increase when approaching the sum third order resonance, then decays a little due to the losses. The same behavior is repeated in the crossing of the third order resonance in the horizontal plane, which has no particular influence in the vertical beam size (the apparent decrease after the horizontal resonance is generated by the losses of particles with large horizontal amplitudes in skew collimators). After the crossing of the resonance the beam size decreases slightly due to the loss of particles with high betatron amplitudes. The crossing of these resonances, however, does not have any noticeable effect on the beam size for case 5, which is identical to failure 6 but with a much smaller loss time constant. The relevance of non-linear resonance crossings increases with the time constant of the failure and, according to the simulation results, is negligible for failures with loss time constants smaller than about 200 turns.

4.2.3.3 Evolution of the losses

In case of quadrupole failures, the evolution of the losses presents large differences with respect to the losses produced by dipole failures. In most cases, the optics change induced by quadrupole failures produces a sudden change in the beam size when a linear resonance is reached, but the beam remains little affected until then. This results in both a larger loss threshold time and a larger loss rate than in the case of dipole failures with similar time constants. Besides, the crossing of higher order resonances may lead to the loss of a non negligible fraction of the beam before significant losses due to linear effects appear.

Figure 4.27 show the evolution of the losses for four significant failure cases. In all cases most of the losses are generated by resonance conditions (*resonance losses*), although in some cases of slow failures the direct change in the beta beating is responsible for some losses too (*progressive losses*). From the simulation results, the following statements can be made:

- Progressive losses are gradual and do not produce high loss rates. The threshold time to

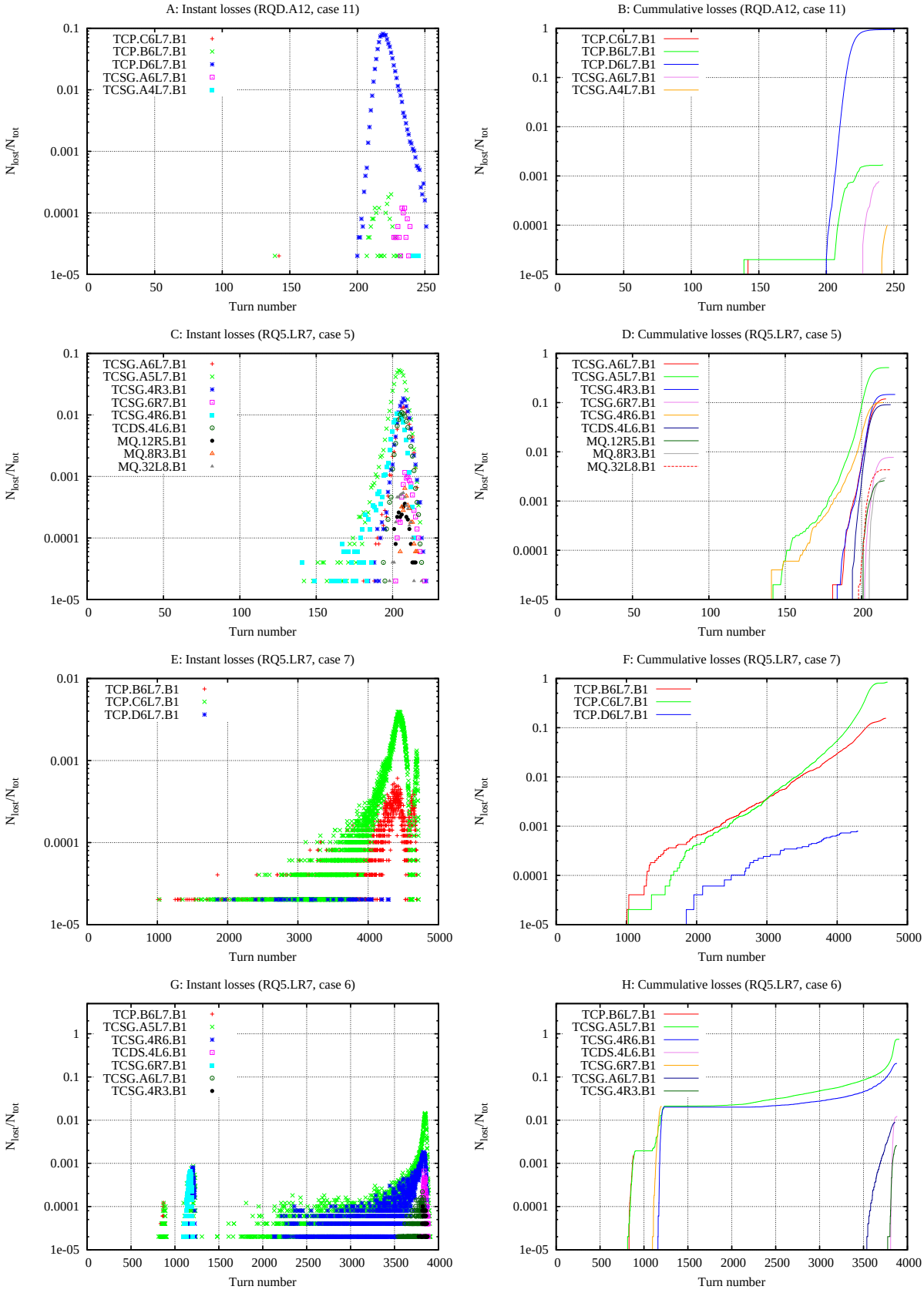

Figure 4.27: Evolution of the beam losses for different failure cases. See section 2.4 for details on the affected elements.

2×10^{-5} of the beam[4] is however shorter with respect to the loss time constant. Progressive losses are more likely to happen in circuits with both focusing and defocusing quadrupoles connected in series because of the smaller change in the tune.

- Resonance losses happen suddenly. If the resonance is not crossed, the threshold time to the simulation resolution with respect to the loss time constant is longer. In any case, the loss rates are higher than for progressive losses.
- The distribution of the losses along the LHC ring depends on the loss time constant and on the nature of the failure. Progressive losses tend to be less distributed than resonance losses.
- Losses due to non-linear resonances are relevant only in case of failures with loss time constants greater than several hundred turns. In some cases losses due to third order resonances may amount up to about 8% of the beam (figure 4.27 G and H, [75]).

4.2.3.4 Influence of the time constant of the failure

In the same way as for dipole failures, we differentiate non-adiabatic from adiabatic changes in the optics. For quadrupole failures, non-adiabatic changes imply the unmatching of the particle distribution from one turn to the next (as in figure 1.4 B and C) and the beam-size oscillates. For slower failures, the changes can be considered adiabatic and the particle distribution adapts gradually to the change in the phase-space ellipse.

Linear current changes with different slopes have been simulated for representative circuits (RQ5.LR7, RQF.A12, RQD.A12). For RQF.A12 and RQD.A12 only current decays have been considered. For RQ5.LR7 both decays and increases of the current have been simulated. These changes do not correspond to any real failure scenario and have been simulated to provide better understanding.

Figures 4.28 and 4.29 show the evolution of the losses at different locations for current decays at RQD.A12 and current increases at RQ5.LR7 with different loss time constants. For fast current decays at RQD.A12 there is no clear loss pattern. This is due to the crossing of first and second order resonances. A large amount of particles is lost during the crossing, but the remaining fraction circulates for some more turns with the stable optics obtained after the crossing. For slower failures, the resonance is not crossed and most of the particles are lost at TCP.D6L7.B1. For the current increases at RQ5.LR7, the losses happen at well determined times. The resonance is approached but not crossed. This happens because of the slower change in the tune with respect to the change in the betatron function. For slower failures progressive losses appear at TCSG.A5L7.B1 reaching up to 10% of the total beam.

Figure 4.30 presents the relative loss threshold times for the failures that were simulated at different speeds. Unlike in the case of dipole failures, the relative loss threshold times tend to increase in the absence of losses due to resonance crossings. This means that the initial losses produced by slower failures arrive proportionally later after the start of the failure. In the presence of resonance crossings we can observe two interesting phenomena:

- The relative loss threshold times for fractions smaller than the corresponding resonance losses drop at the crossing. This is clear for the current increases at RQ5.LR7 with $\tau_1 > 20$ ms for $\tau_{10^{-4}}$, $\tau_1 > 50$ ms for $\tau_{10^{-3}}$ and $\tau_1 > 80$ ms for $\tau_{10^{-2}}$ (figure 4.30 A), evidencing the losses due to the third order resonance crossing. This fact appears clearly also for the current decays at RQD.A12 ($\tau_1 \approx 2$ ms) and RQF.A12 ($\tau_1 \approx 70$ ms).

[4]This corresponds to the simulation resolution of the measurement of losses for 5×10^4 simulated particles

- In case of fast changes in the tune, it can happen that a slower current change leads to smaller loss time constants than slightly faster current changes, particularly for big fractions of the beam. This happens if for the slower change all the beam is lost in the resonance while for the faster one a fraction of the beam survives the crossing. In this case there is a discontinuity in the evolution of the loss threshold tunes, as shown in figure 4.30 C ($\tau_1 \approx 15$ ms) and D ($\tau_1 \approx 4$ ms).

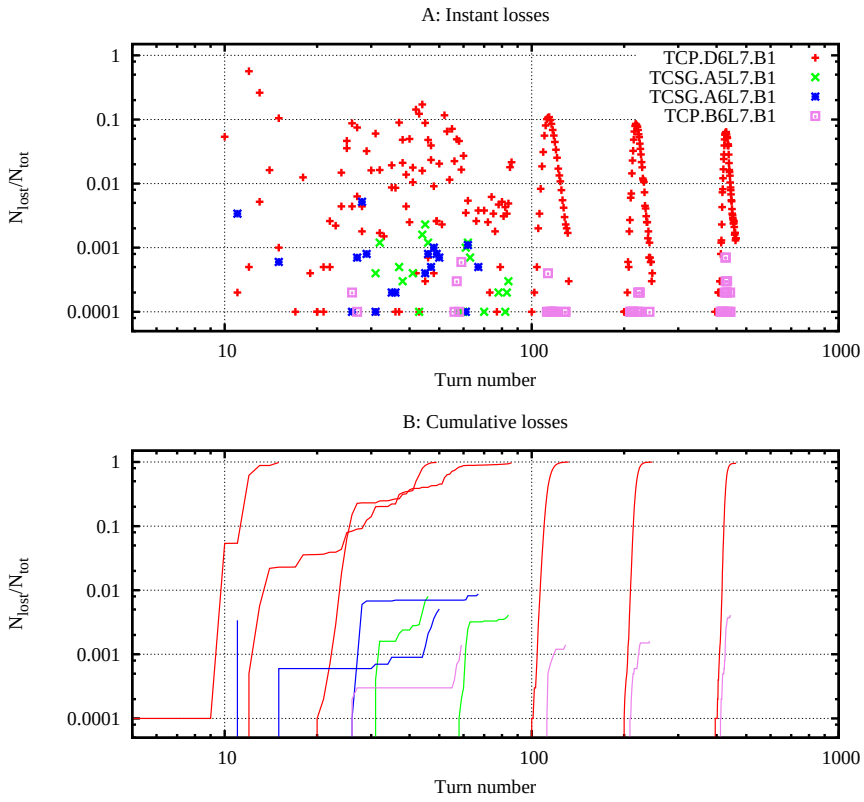

Figure 4.28: Instant and cumulative losses for current decays at RQD.A12 at 7 TeV with different loss time constants. Each simulation corresponds to a set of data (red, green, blue, purple) with a given loss time constant. The current changes have been chosen for convenience and do not correspond to any possible failure scenario and only the locations recording a significant amount of losses are represented.

The maximum loss rates and the number of locations where losses are recorded as a function of the loss time constant are represented in figure 4.31. The maximum loss rates are inversely proportional to the loss time constant of the failure, as one would expect. If a significant fraction of the beam is lost in a resonance crossing, the maximum loss rate decreases slightly (RQD.A12 with $\tau_1 \approx 7$ ms. In the absence of losses due to resonance crossings, the number of loss locations appears to decrease with the loss time constant of the failure. Losses due to resonance crossings may appear in other locations than those that receive most of the losses at the end of the failure, thus increasing the number of locations that record losses. This is the case for the current decay at RQD.A12 with a loss time constant of about 7 ms.

4.2.3.5 Effects of the machine imperfections on the time constant of the losses

The influence of machine imperfections on the losses produced by quadrupole failures is of a different nature than for dipole failures. First, the closed orbit offset implies an additional dipolar error kick

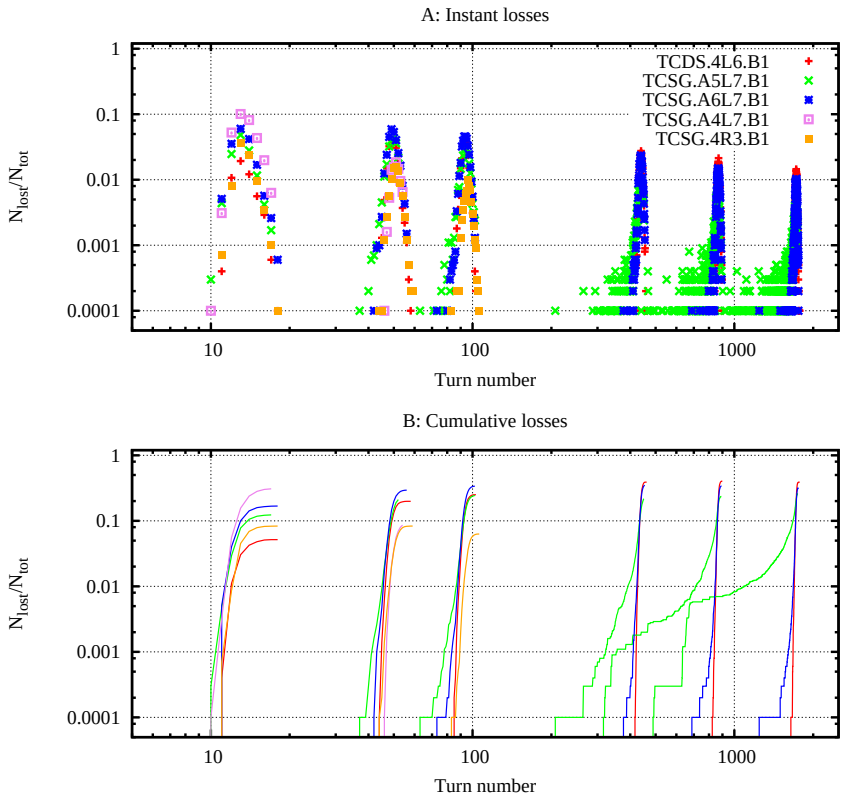

Figure 4.29: Instant and cumulative losses for current increases at RQ5.LR7 at 450 GeV with different loss time constants. Each simulation yields to a set of data (red, green, blue, purple) with a given loss time constant. The current changes have been chosen for convenience and do not correspond to any possible failure scenario and only the locations recording a significant amount of losses are represented.

when a quadrupole fails. Besides, to compensate for the multipolar errors, small quadrupoles and higher order multipoles are used (see section 3.3.0.2). These magnets add higher order fields that may accelerate the loss of particles with large betatron amplitudes when the optics change.

As was done for dipole failures, simulations have been performed using 60 sets of errors with different seeds. 10000 particles were simulated for each error set. The loss threshold times for different fractions of the beam and maximum loss rates have been recorded and are summarized in figure 4.32 for three failure cases of different nature.

For RQ5.LR7 (figure 4.32 A and B), machine imperfections worsen the consequences of the failure, as expected. The influence of the imperfections is however small. The maximum loss rate is increased an average of about 0.5% (maximum of about 1%) and the uncertainty on the loss threshold times is less than 5% of the time constant of the beam for all fractions, and less than 10% of the loss threshold time for the corresponding fraction for the worst case recorded.

For RQD.A12 and RQF.A12 the failures are much more critical in the presence of machine imperfections. The loss time constant changes by more than a factor of two for RQD.A12 and by almost a factor 10 for RQF.A12. The other loss threshold times are also reduced dramatically. The loss threshold rate is more than doubled for RQD.A12 and increases by a factor of about four for RQF.A12. The explanation to this fact is that for the considered current changes, the linear resonances are crossed with an ideal model, while in the presence of machine imperfections all the beam is lost as the resonance is approached. For RQ5.LR7 the resonance is not crossed even with an ideal machine and the influence of machine imperfection is smaller. In both cases, however, the

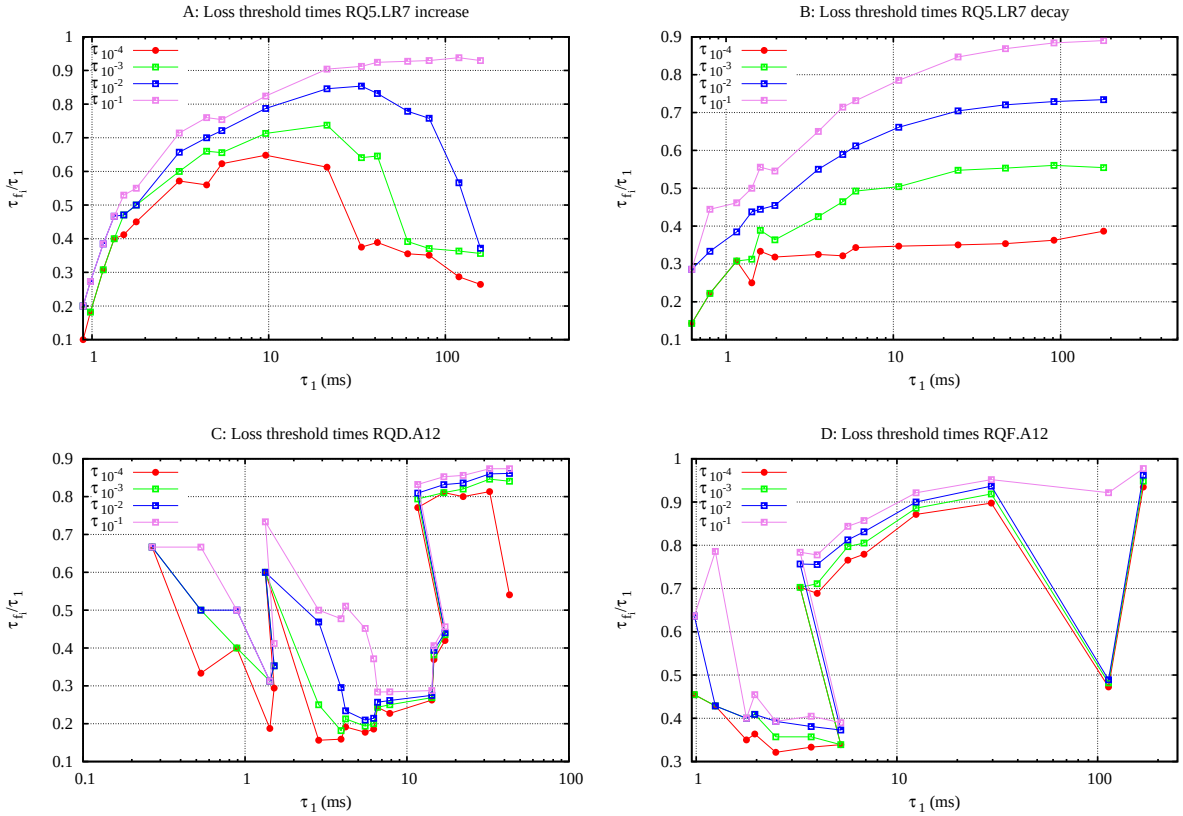

Figure 4.30: Relative loss threshold times for the simulated failures with different time constants. Each set of samples (four points with the same abcissa value) correspond to a simulation of a linear current decay with a different slope. The samples are plotted as a function of their loss time constant.

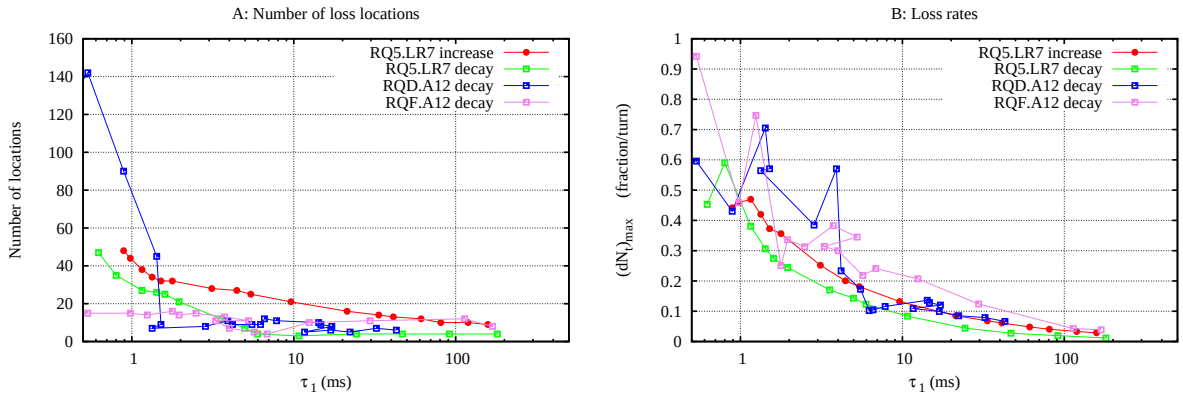

Figure 4.31: Loss rates and number of loss locations for the simulated failures with different time constants.

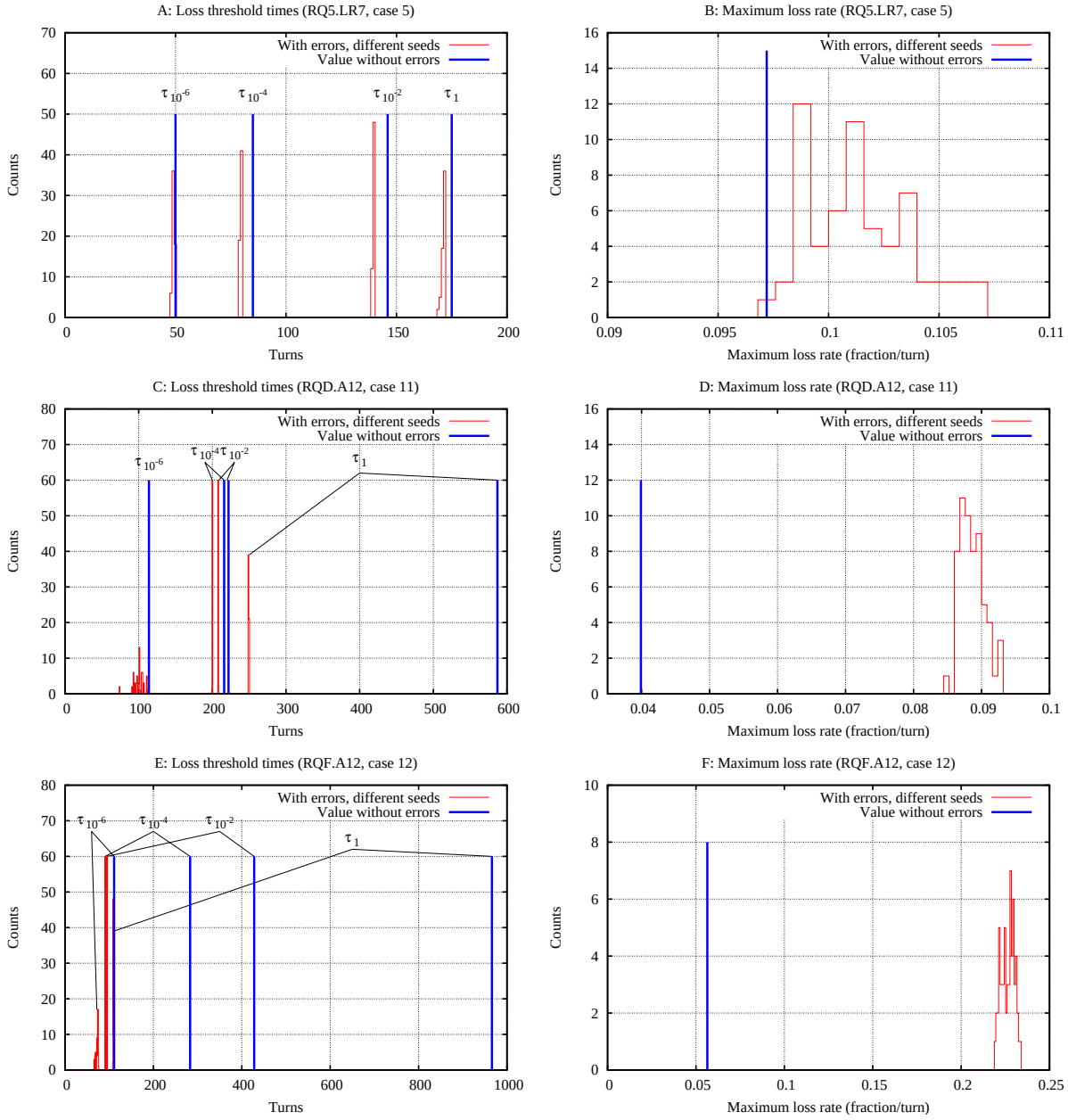

Figure 4.32: Influence of the machine imperfections on the loss threshold times for various fractions of the beam (left) and on the maximum loss rates (right).

uncertainty among different error sets remains below a few percent (maximum of about 10% for $\tau_{10^{-6}}$ for RQD.A12). Note that all the studies of quadrupole failures presented in this document were done with a model including machine imperfections.

Chapter 5

Distribution of the lost particles at the LHC collimators

In the previous chapter we have presented the consequences of magnet failures on the beam itself. The beam losses have been presented, highlighting global loss rates, related to the beam intensity, and local losses, at different locations. In this chapter we focus on the transverse distribution of the lost particles at the collimators.

We recall that only primary losses are recorded. The interest of studying the distribution of the primary impacts of the particles lies in its later use as an input to other simulation codes. Further tracking studies can be done with *sixtrack* [65] to estimate the number of scattered particles lost in the cold aperture. Monte Carlo simulations can be done to study the energy deposition in the collimator jaws. For the LHC collimators, these simulations are done with *FLUKA* [33].

Several patterns of transverse distributions of the lost particles have been observed. Examples of these distributions at injection and collision energy are shown in figure 5.1.

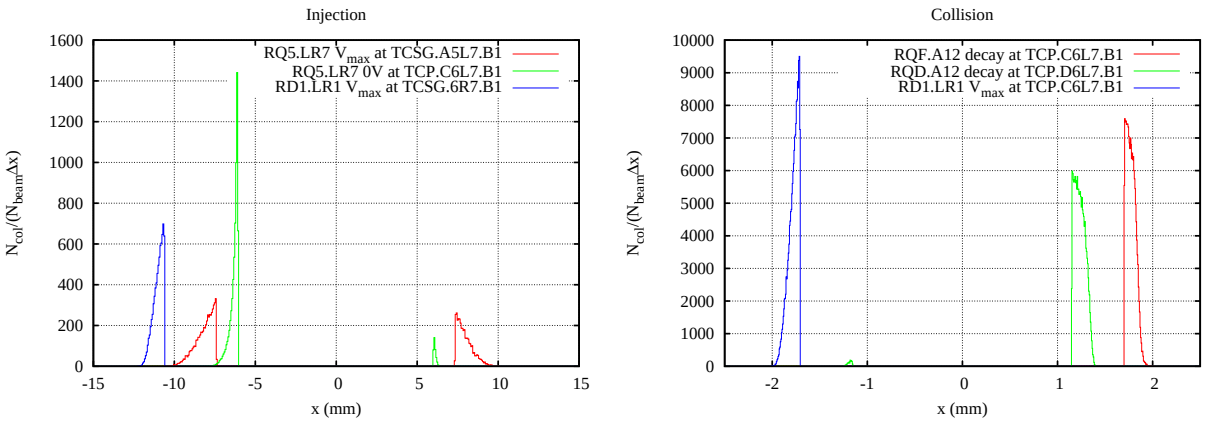

Figure 5.1: Transverse distribution of lost particles at injection and collision energy for different current changes and at different locations. Note the different scale in the horizontal axis. The collimators half-gaps are 7.33, 6.013 and 10.57 mm at injection; 1.668 and 1.178 at collision.

The data presented in figure 5.1 suggest that:

- The distribution at 7 TeV is narrower than at 450 GeV. This is expected as the beam size is also smaller at collision energy.
- Dipole failures produce impacts in only one of the collimator jaws.

- Quadrupole failures may lead to losses in one or the two jaws, depending on the order of the resonance that is reached. Even when losses are recorded in the two jaws, the distribution presents a certain asymmetry. This is due mainly to the effects of the sextupoles. Faster quadrupole failures produce more symmetric distributions in both jaws than slower ones.

These qualitative statements have been confirmed by all the simulations that have been performed so far. In the following, we present a more quantitative study of the distributions in a single jaw, normalized to the total amount of particles in the beam.

5.1 Impact distributions for representative failure cases

The impact parameter (α) represents the transverse offset of a lost particle in a collimator with respect to the edge of the collimator [22]. The distribution of the impact parameter of all the particles hitting a given collimator is referred to as the *impact distribution* at the collimator for a given failure case.

As a failure develops, more and more particles will be lost in the aperture. The time evolution of the primary impact distribution is of interest to determine the available time to dump the beam before the quench or damage levels are reached. Analyzing individually the impact distribution for every single failure case and its evolution with time is not feasible within reasonable time and effort. Instead, we analyze representative cases in order to set up an approximation that can be easily obtained from the simulation data and applied automatically to study any failure case.

The transverse distribution of the lost particles in a collimator is related to the time constant of the losses produced by a magnet failure, as well as to the type and position of the failing magnets. The impact distributions for the failure scenarios listed in table 5.1 have been studied in detail.

Circuit/Magnet	Failure	Mode	Collimator	σ_{col} [mm]	σ_{inj} [mm]	Case
RD1.LR1	$V_{fail} = 0V$	Collision	TCP.C6L7.B1	0.278	1.059	1
RD1.LR1	$V_{fail} = V_{max}$	Injection	TCSG.6R7.B1	0.414	1.577	2
RD2.L2	Quench	Collision	TCSG.4R6.B1	0.502	1.913	3
RD.A34	Energy extraction	Collision	TCSG.6R7.B1	0.414	1.577	4
RQ5.LR7	$V_{fail} = 0V$	Injection	TCP.B6L7.B1	0.232	0.885	5
RQ5.LR7	$V_{fail} = V_{max}$	Injection	TCSG.A5L7.B1	0.289	1.101	6
RQX.R1	Quench	Collision	TCSG.A6L7.B1	0.238	0.908	7

Table 5.1: Simulated circuits, failures and most affected collimator in each case. σ_{col} and σ_{inj} represent the transverse size of the beam at collision and injection respectively, at the location of the collimator.

The impact distribution has been generated for the failure scenarios listed in table 5.1, at different times after the beginning of the failure. For some of these failure cases, the impact has been evaluated at more than one collimator.

5.1.1 Dipole failures

Figure 5.2 shows the impact distribution for the dipole failure cases that were simulated, recorded at the most affected collimators in each case. The width of the impact distribution is strongly dependent on the failure case. In some cases (failure case 2) the relative amount of losses in each collimator is constant with time. It is also possible that the first losses happen at a given collimator, but as the failure develops, more and more particles are lost in another location. For failure case 2 (figures 5.2 C and D) the amount of losses recorded at TCP.C6L7.B1 after 30 turns

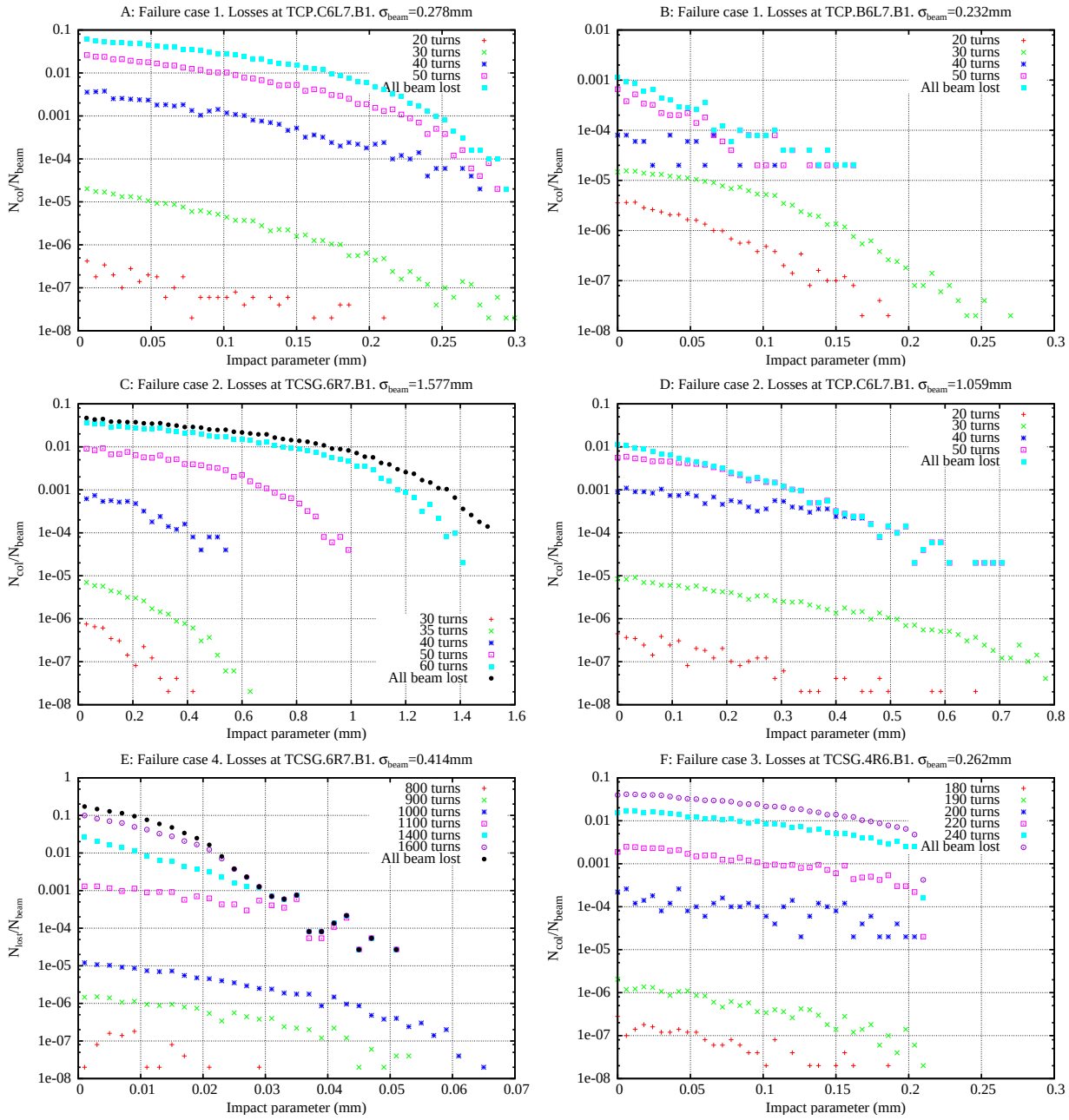

Figure 5.2: Impact distributions after different numbers of turns for each dipole failure. A and B represent losses from the same failure scenario recorded at different collimators, as well as C and D.

is one order of magnitude greater than at TCSG.6R7.B1. If the failure developed completely, the total amount of losses recorded at TCSG.6R7.B1 would be about seven times higher than the losses at TCP.C6L7.B1. A similar figure can be observed for failure case 1 (figures 5.2 A and B).

Another interesting phenomenon can be observed for failure case 3 (figure 5.2 F). The impact distribution is truncated at a depth of about 0.2 mm in the collimator. This happens because the particles with orbit excursions big enough to reach greater impact parameters at TCSG.4R6.B1 are intercepted by the collimators upstream (TCDQA.4R6.B1 and TCDQB.4R6.B1).

Figure 5.3 shows the evolution with time of the total amount of losses recorded in the two

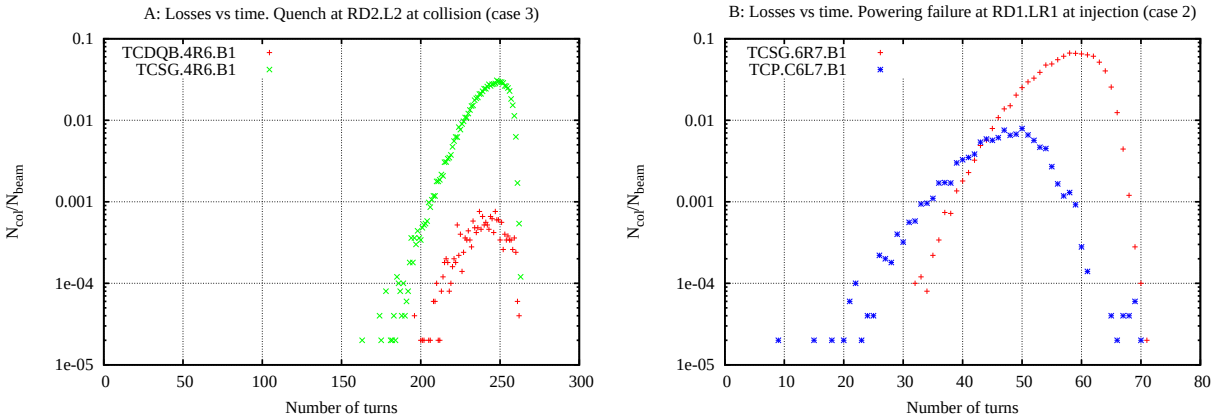

Figure 5.3: Instant losses as a function of the number of turns after the failure starts, recorded in different collimators for two failure scenarios.

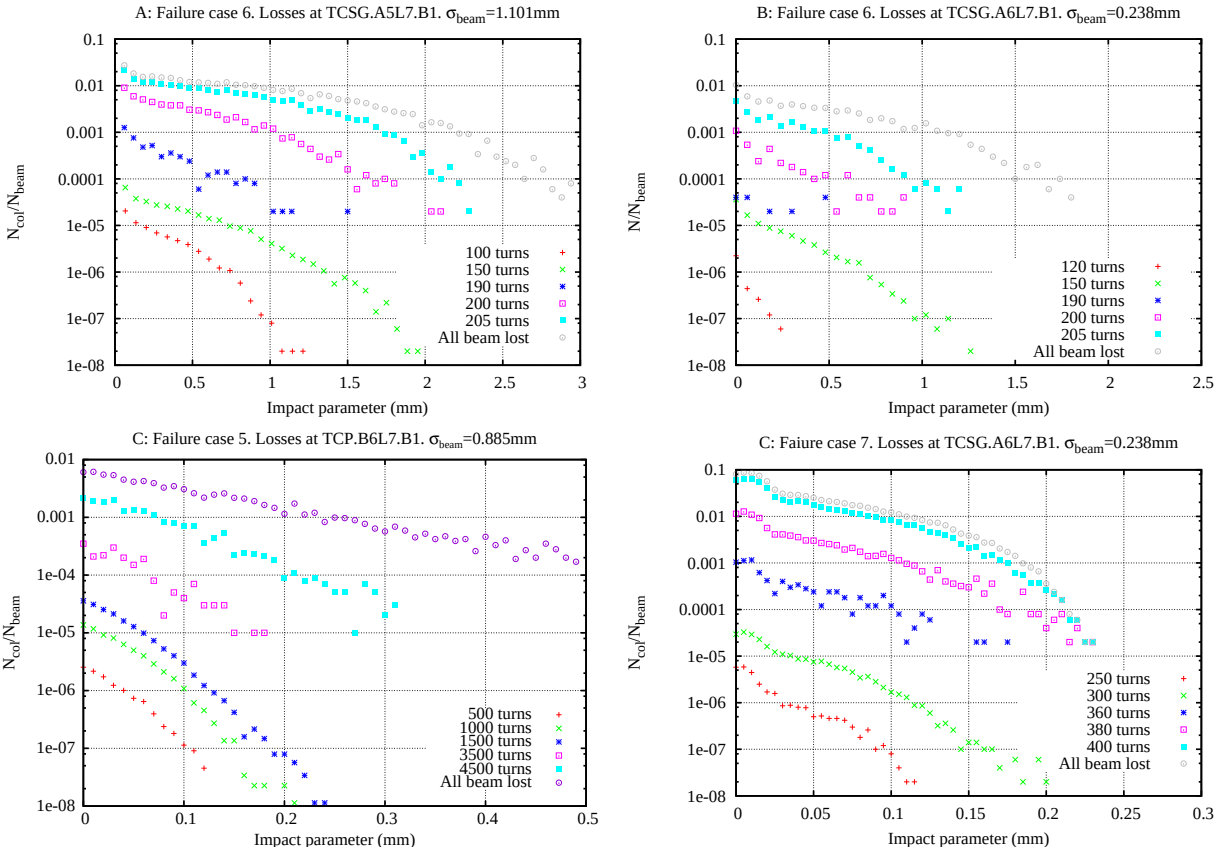

Figure 5.4: Impact distributions after different numbers of turns for each considered quadrupole failure. A and B represent losses from the same failure scenario recorded at different collimators.

particular cases discussed above. The losses at TCSG.4R6.B1 and TCDQB.4R6.B1 (figure 5.3 A) happen at the same time, which is consistent with the data from figure 5.2 F. Figure 5.3 B represents the same picture for failure case 2 (figure 5.2 C and D). In this case, the losses at TCP.C6L7.B1 are recorded first, but most particles would hit TCSG.6R7.B1 if the failure developed completely.

5.1.2 Quadrupole failures

Figure 5.4 shows the impact distribution for the quadrupole failure cases that were simulated, recorded at the most affected collimators in each case. A comparison with figure 5.2 suggests that the shape of the impact distribution in the case of a quadrupole failure is similar than for losses produced by a dipole failure. The amount of losses recorded on the most affected collimator, however, is smaller in the case of quadrupole failures. This is mainly due to two reasons:

- With respect to dipole failures, quadrupole failures produce losses distributed over a larger number of elements.
- Some of the quadrupole failures produce losses on the two collimator jaws, reducing the fraction of losses per jaw.

5.2 Simple fit applicable to every impact distribution

The distributions presented in figures 5.2 and 5.4 show a fast attenuation of the number of particles lost with the impact parameter. To obtain a faster processing of the data for all the failures it is more convenient to approximate the impact distribution with a function whose parameters can be obtained directly from the coordinates of the lost particles. This avoids calculating the distribution every turn, which is a heavy operation in terms of calculation time and memory resources.

With this approach, a reconstruction of the impact distribution can be obtained at any time from only a few stored parameters. In addition, the parameters of the fit function can be evaluated easily as a function of time and provide a mean to to quickly estimate the criticality of an impact.

The data presented in the above figures show linear and parabolic trends in logarithmic scale. The functions $e(x)$, $g(x)$ and $f(x)$ (equation 5.1) have been evaluated as approximations of the probability density functions in three particular failure cases showing impact distributions with different shapes.

$$e(x) = A_e e^{-\frac{x}{\tau_e}} \qquad g(x) = A_g e^{-\frac{x^2}{2\sigma_e{}^2}} \qquad f(x) = A e^{-\frac{x^2}{2\sigma^2}-\frac{x}{\tau}} \tag{5.1}$$

Figure 5.5 A shows a typical impact distribution, which corresponds to failure case 2 after all the beam is lost (figure 5.2 D). Figure 5.5 B shows the impact distribution for the same failure case after 35 turns (figure 5.2 C). In this case, the shape of the distribution in logarithmic scale approaches more to a parabola. Figure 5.5 C shows an impact distribution for failure case 4 after 1400 turns (figure 5.2 E). Here the distribution in logarithmic scale is linear, corresponding to an exponential probability function. It has been found that for an a priori unknown distribution following patterns similar to those presented above, $f(x)$ will provide the best fit. The three functions are normalized so that the integrated probability is equal to one.

The parameters A_g, σ_g, A_e and τ_e from $e(x)$ and $g(x)$ have been obtained directly from the impact parameter of each lost particle using the method of moments (Appendix C). A direct application of this method for $f(x)$ does not yield a good approximation. From figure 5.5 we realize that $g(0)$ underestimates the value of the actual probability density function at $x = 0$ and that $e(0)$ overestimates it for most of the cases. A better fit is obtained by setting

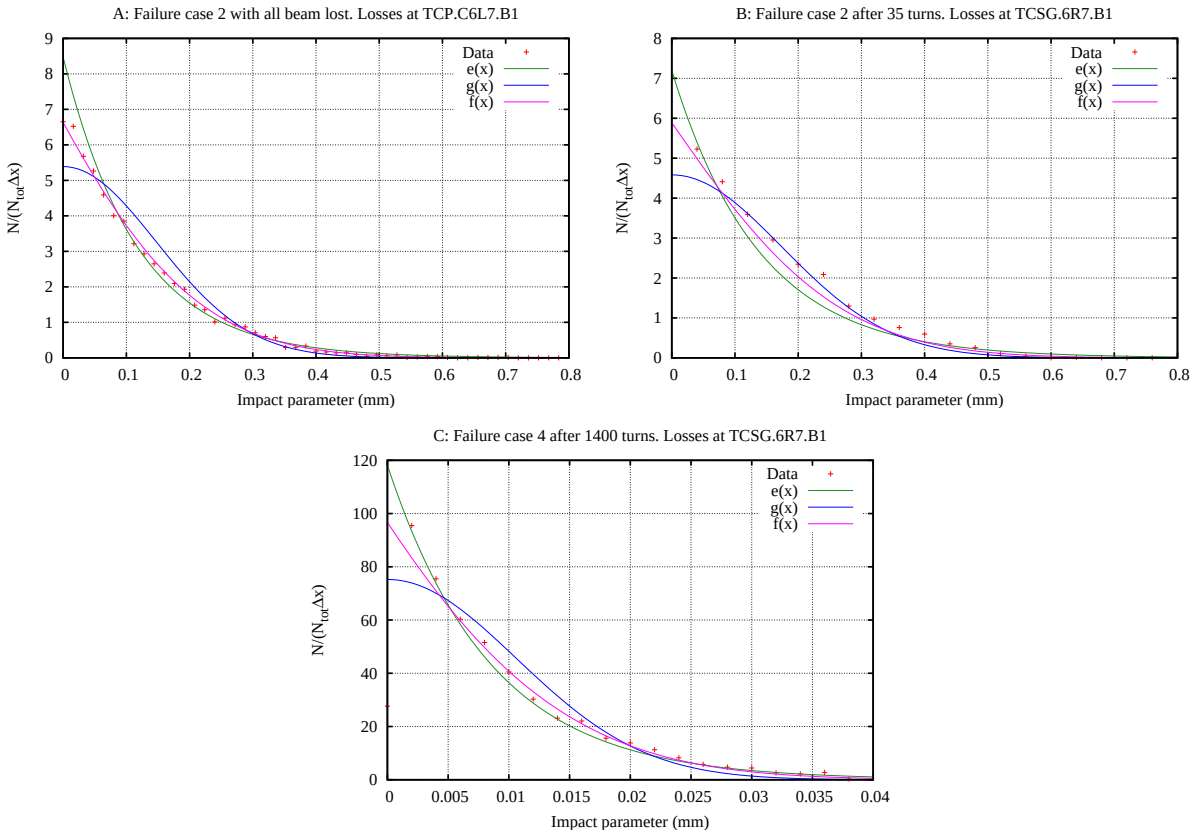

Figure 5.5: Evaluation of the fits obtained with different types of functions for impact distributions with different shapes. Failure case 2 at TCP.C6L7.B1 after all the beam is lost (A). Failure case 2 at TCSG.6R7.B1 after 35 turns (B). Failure case 4 at TCSG.6R7.B1 after 1400 turns (C). The plots are normalized so that the integrated probability is equal to one.

A: Failure case 2 with all beam lost. Losses at TCP.C6L7.B1			
Function	$e(x)$	$g(x)$	$f(x)$
$\frac{\text{RMS of } \Delta y}{f(0)}$	3.26×10^{-2}	5.49×10^{-2}	1.40×10^{-2}

B: Failure case 2 after 35 turns. Losses at TCSG.6R7.B1			
Function	$e(x)$	$g(x)$	$f(x)$
$\frac{\text{RMS of } \Delta y}{f(0)}$	6.04×10^{-2}	3.90×10^{-2}	3.72×10^{-2}

C: Failure case 4 after 1400 turns. Losses at TCSG.6R7.B1			
Function	$e(x)$	$g(x)$	$f(x)$
$\frac{\text{RMS of } \Delta y}{f(0)}$	2.37×10^{-2}	6.92×10^{-2}	3.47×10^{-2}

Table 5.2: Accuracy of the fit for each case of failure studied, corresponding to figure 5.5.

$$A = \frac{A_e + A_g}{2}$$

and then applying the method of moments to obtain σ and τ. Table 5.2 summarizes the accuracy of the fits for each function in each of the three failure cases studied. A is given in mm^{-1}; σ and τ are given in mm.

Figure 5.6 shows the evolution of the parameters A, σ and τ with time for different dipole and quadrupole cases. The evolution of the impact distribution in these cases suggest that for quadrupole failures the distribution becomes wider with time. This is not necessarily the case for dipole failures, for which the impact may become narrower for slow failures.

Figure 5.7 shows the impact distributions as a function of time for some of the cases presented in figures 5.3 and 5.4. These distributions have been reconstructed from the stored values of $A(t)$, $\sigma(t)$ and $\tau(t)$.

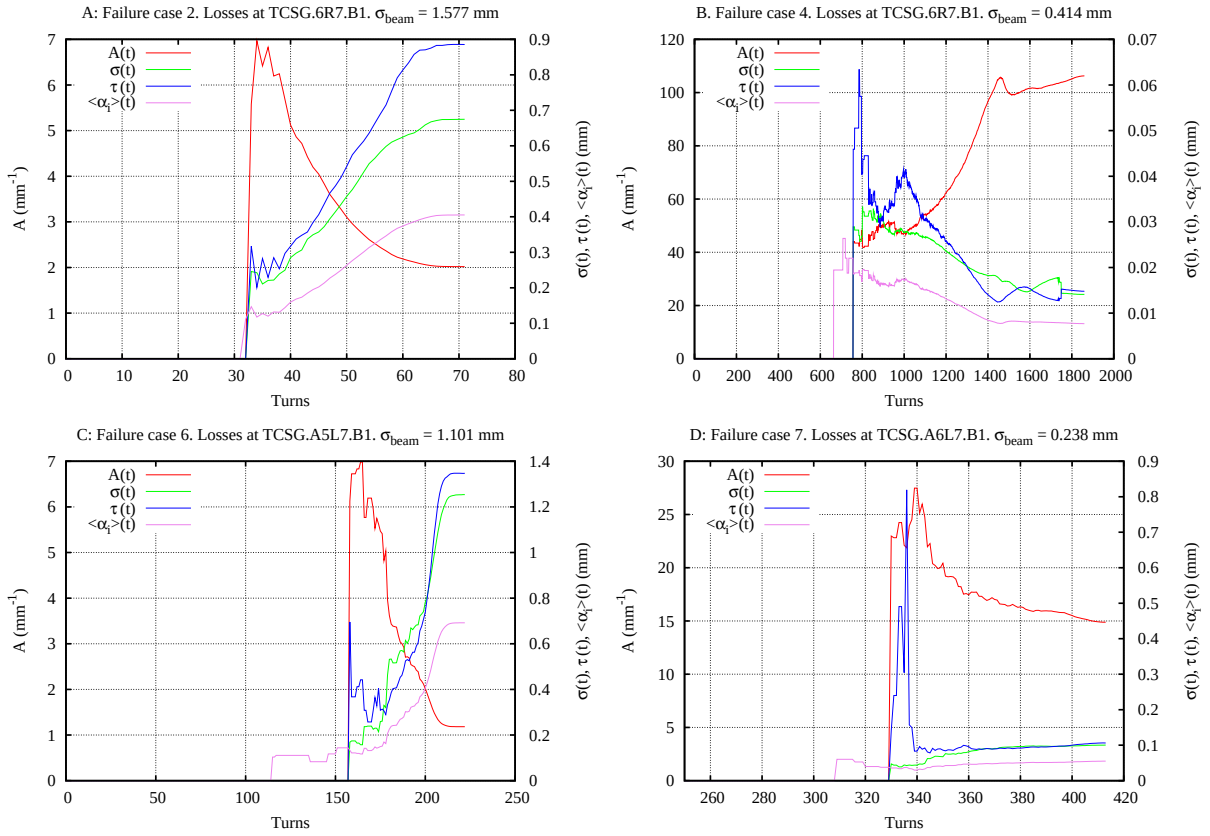

Figure 5.6: Evolution with time of the parameters of the fit function and of the average impact parameter ($\langle\alpha_i\rangle$) for various dipole and quadrupole failure cases.

5.3 Evaluation of the impact distribution

The impact distribution evolves with different shapes, width and time constants depending on the failure that provokes the losses. It is of interest to summarize the criticality of a given impact in a single time-dependent parameter.

Recalling section 2.5.2.3, beam induced damage at the collimators can be of two different natures: melting of the collimator material and deformation of the metallic support, and the

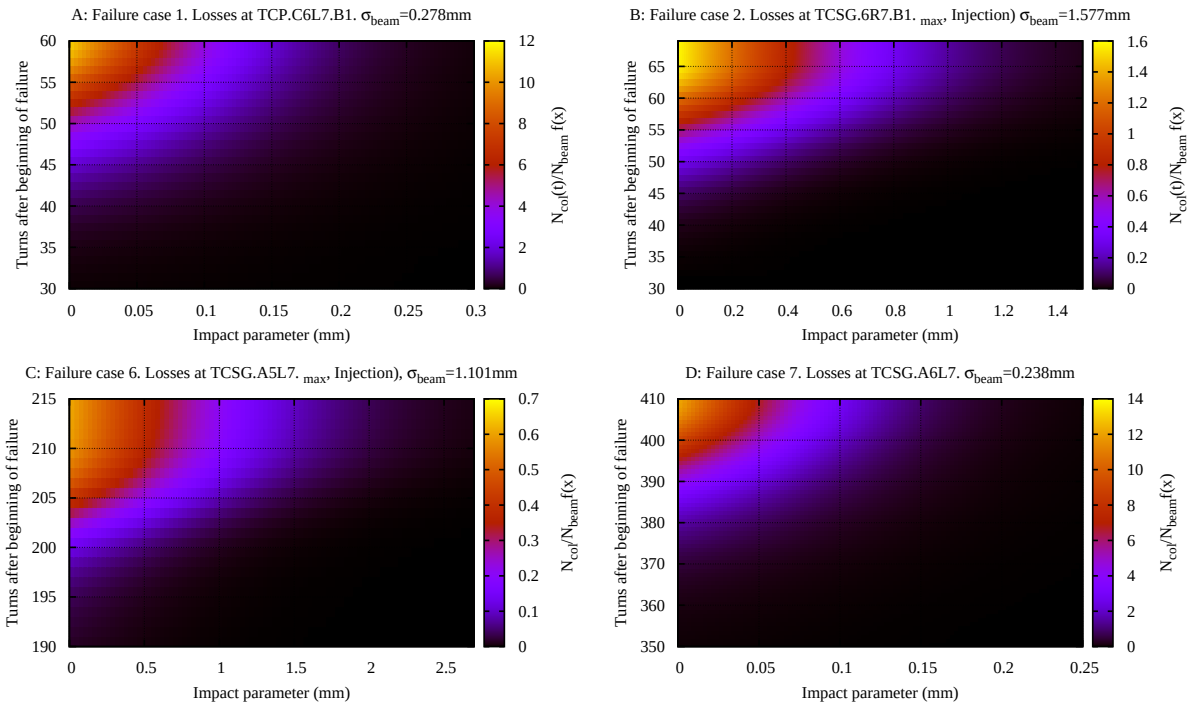

Figure 5.7: Evolution with time of the reconstructed impact distribution for representative failure scenarios.

criticality of an impact with respect to the damage at the collimator depends on the following factors:

- The fraction of the beam that is lost at the collimator jaw (N_{col}/N_{beam}).
- The width and shape of the impact distribution ($f(x)$).
- The evolution with time of the previous two parameters.

In order to summarize these three factors in a single value, the *impact density* is proposed:

$$\xi(x,t) = \frac{N_{col}(t)}{N_{beam}} f(x,t) = A(t)\frac{N_{col}(t)}{N_{beam}} e^{-(\frac{x^2}{2\sigma^2(t)} + \frac{x}{\tau(t)})} \tag{5.2}$$

$\xi(x,t)$ has dimensions of $[\mathrm{L}^{-1}]$ and is given in mm^{-1}. At a given time, the maximum value of $\xi(x,t)$ is $\xi_{max}(t) = \xi(0,t) = A(t)\frac{N(t)}{N_0}$. This value is a good indicator of the criticality of the failure and can be evaluated at every turn. It will be used hereafter to ascertain the degree of concentration of lost particles at a given collimator. We will refer to it as the *maximum impact density*.

In order to compare the impact distributions from different failures at different locations and modes of operation, the parameters A, σ and τ have to be normalized to the beam size (σ_{beam}). This can be useful to study the influence of the type of failure or loss time constant on the impact distribution. The parameters σ and τ are normalized through the division by σ_{beam}. A is normalized by multiplying it by σ_{beam}.

5.4 Influence of the speed of the failure on the width of the impact distribution

The transverse distributions of the losses at the collimators have been evaluated for the cases presented in sections 4.2.2.4 and 4.2.3.4. The maximum impact density after the loss of the whole beam as well as the fraction of the beam lost at the corresponding collimator have been recorded (figure 5.8).

The general trend is that $\xi_{max}(\tau_1)$ increases with the time constant. This means that slower failures produce more concentrated losses. However, this is not always the case, particularly if resonance losses appear somewhere else. For instance, in the case of a current decay in RQF.A12, the most affected collimator is not TCSG.4R6.B1 for loss time constants between 3 and 12 ms. The maximum impact density in this collimator decreases dramatically in this range. For cases where linear resonances are not crossed (MB.A25R1, RQ5.LR7) the maximum impact density always increases with the loss time constant.

The impact densities for the current decays at RQ5.LR7 are one order of magnitude lower than for the other cases. The main reason is the larger beam size at injection. The maximum impact densities normalized to the beam size are only about a factor of two smaller. These plots also suggest that dipole failures produce higher impact densities than quadrupole failures with similar loss time constants. This difference is more pronounced for slow loss time constants.

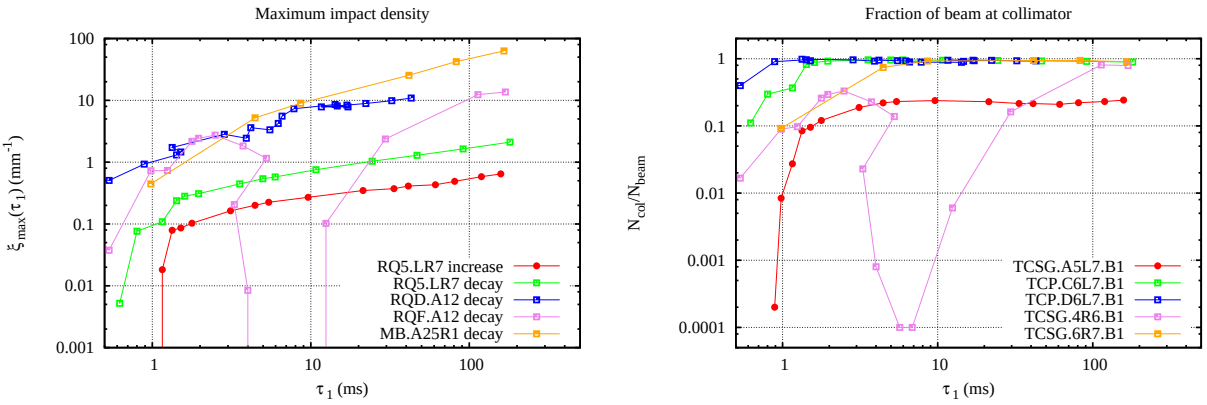

Figure 5.8: Maximum impact density after the loss of all the beam for failures with different loss time constants (left) and fraction of the beam lost at the corresponding collimators (right). Both legends are common to both plots.

Chapter 6

Post-impact tracking and secondary losses

After a beam impact in a collimator, such as those described in the previous chapter, only a small fraction of the beam is absorbed by the collimator itself. Most particles are scattered back into the beam and may circulate for several turns until they are eventually lost. Many of these scattered particles are absorbed by collimators downstream but some escape the collimation system and their energy is deposited in other LHC elements. The particles lost after being scattered at a collimator are referred to as *secondary losses*.

The longitudinal distribution of the scattered particles from a first impact at primary collimators has been studied exhaustively for steady losses during nominal operation [22], [76]. For accidental losses, however, similar studies have not been published so far. The results obtained for steady losses cannot be extrapolated for accidental losses for two main reasons:

- The primary impacts from steady losses happen always in a primary collimator. This is not the case for accidental primary losses, which happen often in a secondary collimator. In this case, the collimation efficiency for these losses is reduced and a larger fraction of particles are expected to escape the collimation system.
- The average impact parameter for steady losses is expected to be less than 5 μm for injection optics and less than 2 μm for collision optics [22]. In case of accidental losses, the average impact parameter can be as high as about 70 μm at collision and 600 μm at injection according to the simulation results presented in the previous chapter.

Dedicated simulations were done with SIXTRACK to estimate the secondary loss patterns after primary impacts with larger impact parameters and for the main phase one collimators (including both primary and secondary collimators).

6.1 Settings for the benchmark simulations

In order to assess the influence of the impact parameter (α) and of the collimator that receives the primary impact on the amount and distribution of the secondary losses, sheet beams were generated at the entrance of each collimator. This configuration is shown in figure 6.1; the sheet beams are 10 μm wide with the particles uniformly distributed in the axis of the collimator. They were generated every 50 μm, centered at α = {5,55,105, ... , 955} μm. In the perpendicular axis, each sheet beam has a Gaussian particle distribution, matched to the optics at the collimator

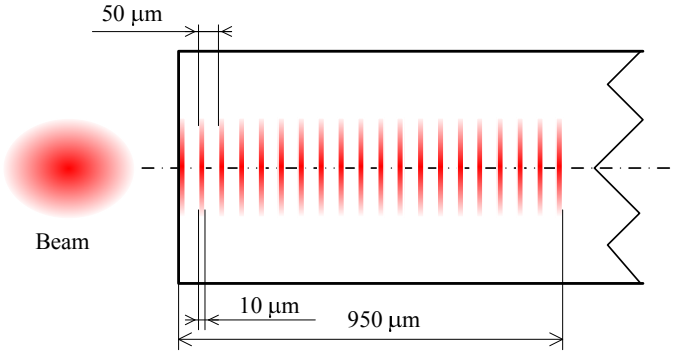

Figure 6.1: Configuration of the initial distributions of particles (sheet beams) generated before each collimator. The collimator representation does not correspond to the collimator real shape and is not to scale.

position. This configuration has been repeated for the nine phase one collimators receiving most of the losses in case of magnet failure, both for collision and injection nominal optics (360 simulated sheet beams in total). The parameters for the benchmark simulations are summarized in table 6.1 and the collimators for which primary impacts were simulated are given in table 6.2. These simulations were done for beam one only. In spite of some slight asymmetries, estimations for beam two can be deduced from the understanding of the results obtained for beam one.

Number of particles per sheet beam	1.6×10^6	
Width of sheet beam	10	μm
Height of sheet beam	σ_i^a	
Minimum offset	5	μm
Maximum offset	955	μm
Number of sheet beams per collimator	20	
Number of collimators^b	9	
Number of simulated scenarios	360	
Total number of jobs	180 000^c	

Table 6.1: Parameters relative to the benchmark simulations.
a: σ_i refers to the size of the beam at the collimator location in the axis parallel to the collimator edge.
c: The maximum number of particles per job in sixtrack is limited to 3200.

Primary	**Secondary**
TCP.D6L7.B1	TCSG.4R6.B1
TCP.C6L7.B1	TCSG.A6L7.B1
TCP.B6L7.B1	TCSG.A5L7.B1
	TCSG.A4L7.B1
	TCSG.A4R7.B1
	TCSG.6R7.B1

Table 6.2: Collimators before which the sheet beams were generated.

6.2 Results

From the benchmark simulations, the efficiency of the collimation system has been estimated as a function of the impact parameter of primary losses and as a function of the collimator that is hit first. Secondary losses may generate quenches before the damage level at the collimators is reached. For this reason, the collimation efficiency has been evaluated separately with respect to normal conducting and superconducting magnets. More attention has been given to the secondary losses in the superconducting magnets. The longitudinal distribution of secondary losses has also been studied. It is important to note that the simulation code does not take into account showers of secondary particles generated in the nuclear interactions inside the collimators. Only scattered protons are recorded as secondary losses. These showers have been considered for other studies for the assessment of the BLM response [77]

6.2.1 Absorption efficiency of the collimation system as a function of the collimator that is hit first

It has been found that the collimator that records the primary impact is the parameter that determines the order of magnitude and location of the secondary losses. More important than the type of collimator (primary or secondary) is its position in the layout of the collimation system. We can classify the collimators in two groups:

- *Isolated collimators*: The last collimators downstream before a group of superconducting elements. They are either outside the cleaning insertion (TCSG.4R6.B1) or the last one of a collimator chain (TCSG.6R7.B1). Only these two isolated collimators were considered for the benchmark simulations, but there are others in the LHC, in particular those for injection protection (TDI).
- *Non-isolated collimators*: They are located inside the cleaning insertions. This implies that there are other collimators downstream that absorb most of the scattered particles.

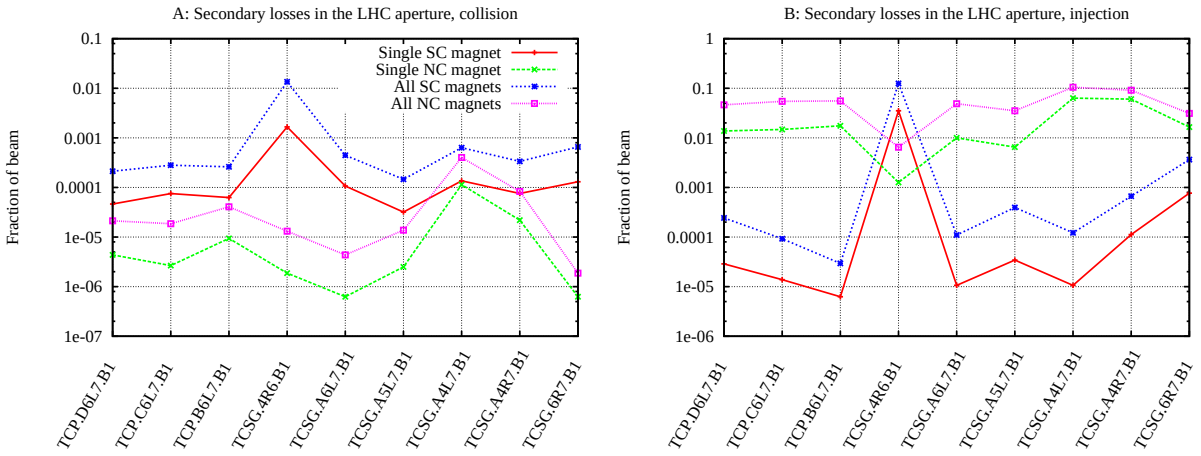

Figure 6.2: Secondary losses in the LHC magnets as a function of the collimator that is hit first, for collision and injection. The legend is common to both plots.

Figure 6.2 shows the fraction of secondary losses at the LHC elements for both collision and injection optics, as a function of the collimator that receives the primary impact. The losses at the most affected magnet and the total amount of losses outside the collimators are given as a summary

of losses that are distributed over a large number of elements. The worst possible impact parameter was chosen for each collimator and the losses at superconducting and normal-conducting magnets are treated separately because of the risk of quench that does not need to be taken into account for normal conducting magnets.

Impacts at isolated collimators produce losses in the superconducting elements orders of magnitude larger than impacts in non-isolated collimators, particularly at injection. The most critical impact happens at TCSG.4R6.B1: in a worst case scenario at collision more than 10^{-3} of the primary losses at TCSG.4R6.B1 could reach a superconducting magnet. For a full impact at TCSG.4R6.B1, this fraction would corresponds to some $5{\times}10^{11}$ protons, one order of magnitude above damage level and about five orders of magnitude above the quench level if the beam was lost completely! At injection the number of protons in a superconducting element would be of the order of 10^{13}, two orders of magnitude above damage level and three orders of magnitude above quench level. For TCSG.6R7.B1 secondary losses are also higher than for the rest of the collimators, particularly at injection.

It is also interesting to note that for non-isolated collimators the fractions of losses at injection and collision in the superconducting elements do not differ much. The losses in the normal conducting elements, however, change by orders of magnitude depending on the energy of the beam. At injection, the secondary losses appear closer to the first impact (see section 6.2.3). This can be explained by a larger scattering angle of the protons escaping the collimator at 450 GeV, as well as a larger aperture of the collimators with respect to the aperture at the magnets. Normal conducting elements, being located within the cleaning insertion, would absorb many of the scattered particles that, at collision, would be absorbed by other collimators.

Tables 6.3 and 6.4 list the LHC magnets that are most affected by secondary losses, as well as an estimation of the amount of secondary losses that they receive. The fraction of secondary losses with respect to the primary losses for superconducting magnets at injection is of the order of 10^{-2} for a primary impact at an isolated collimator, and 10^{-4} or lower for impacts at non-isolated collimators. For normal conducting magnets the fraction of secondary losses is in the order of 10^{-2} or lower for all collimators. At collision, a fraction of secondary losses over 10^{-3} is deposited in one single superconducting element for a primary impact at TCSG.4R6.B1. For primary impacts at any other collimator the order is 10^{-4} or lower. The fraction of secondary losses in the normal conducting magnets at collision is lower than 10^{-4} in any case.

Injection				
Collimator	Magnet (SC)	Secondary losses	Magnet (NC)	Secondary losses
TCSG.4R6.B1	MQY.5R6.B1	$3{\times}10^{-2}$	MBW.B6L7.B1	$1{\times}10^{-3}$
TCP.D6L7.B1	MQM.A7R2.B1	$2{\times}10^{-5}$	MQWA.B5L7.B1	$1{\times}10^{-2}$
TCP.C6L7.B1	DFBAL.5R6.B1[a]	$1{\times}10^{-5}$	MQWA.E5L7.B1	$1{\times}10^{-2}$
TCP.B6L7.B1	MQ.11R7.B1	$6{\times}10^{-6}$	MBW.B6L7.B1	$1{\times}10^{-2}$
TCSG.A5L7.B1	MQM.A7R2.B1	$3{\times}10^{-5}$	MQWA.E4L7.B1	$4{\times}10^{-3}$
TCSG.A6L7.B1	MQ.11R7.B1	$7{\times}10^{-6}$	MQWA.E5L7.B1	$1{\times}10^{-2}$
TCSG.A4L7.B1	MQ.11R7.B1	$9{\times}10^{-6}$	MQWA.A4R7.B1	$6{\times}10^{-2}$
TCSG.A4R7.B1	MCBCV.A5R2.B1	$1{\times}10^{-4}$	MQWA.A4R7.B1	$6{\times}10^{-2}$
TCSG.6R7.B1	MQML.6R8.B1	$1{\times}10^{-2}$	MBW.C6R7.B1	$2{\times}10^{-2}$

Table 6.3: Magnets that are most affected by secondary losses for primary impacts at different collimators. 450 GeV (SC: superconducting. NC: normal conducting).
a: Electrical feed-box. It is a superconducting element but not a magnet.

Collision				
Collimator	Magnet (SC)	Secondary losses	Magnet (NC)	Secondary losses
TCSG.4R6.B1	MB.B10R6.B1	2×10^{-3}	MQWA.A5L7.B1	5×10^{-7}
TCP.D6L7.B1	MQ.11R7.B1	5×10^{-5}	MQWA.A5L7.B1	4×10^{-6}
TCP.C6L7.B1	MB.B9R7.B1	8×10^{-5}	MQWA.A5L7.B1	3×10^{-6}
TCP.B6L7.B1	MQ.11R7.B1	6×10^{-5}	MQWA.A5L7.B1	9×10^{-6}
TCSG.A5L7.B1	MQ.11R7.B1	3×10^{-5}	MQWA.E4R7.B1	2×10^{-6}
TCSG.A6L7.B1	MB.B9R7.B1	1×10^{-4}	MQWA.E4R7.B1	6×10^{-7}
TCSG.A4L7.B1	MQ.11R7.B1	1×10^{-4}	MQWA.D4R7.B1	1×10^{-4}
TCSG.A4R7.B1	MQ.11R7.B1	8×10^{-5}	MQWA.E4R7.B1	2×10^{-5}
TCSG.6R7.B1	MB.B9R7.B1	4×10^{-4}	MQWA.B5L7.B1	6×10^{-7}

Table 6.4: Magnets that are most affected by secondary losses for primary impacts at different collimators. 7 TeV (SC: superconducting. NC: normal conducting).

6.2.2 Absorption efficiency of the collimation system as a function of the impact parameter

Figure 6.3 shows the influence of the impact parameter on the amount of losses that are recorded in the LHC superconducting elements.

For all the non-isolated collimators the efficiency is roughly the same. It decreases with the impact parameter at 7 TeV and remains more or less constant at 450 GeV, apart from a peak of the secondary losses for the smallest impact parameters, which does not appear at 7 Tev. Both at collision and injection, the fraction of particles lost in the superconducting elements for a primary impact in these collimators lies between 10^{-5} and 10^{-4}. At collision, the particles scattered close to the edge of the collimator have smaller amplitudes and a larger probability to escape the collimators downstream. At injection, however, the beam rigidity is much smaller and the probability of the scattered particles to be absorbed in the cleaning insertion is basically independent of the impact parameter (which corresponds to the initial transverse coordinates of the particle). The peaks of secondary losses for small impact parameters are due to a lower absorption rate of the primary losses which is more relevant at 450 GeV (see figure D-1, appendix D).

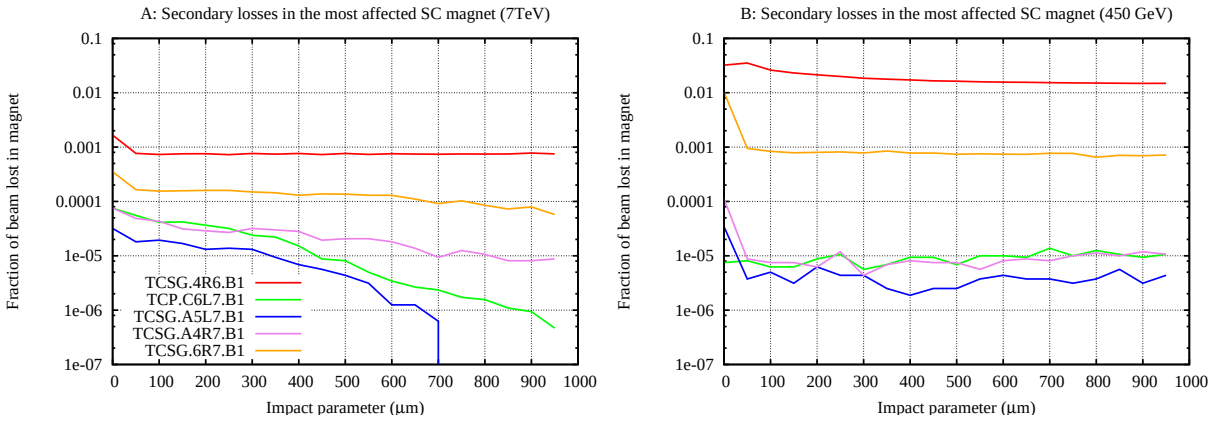

Figure 6.3: Secondary losses in the LHC superconducting elements as a function of the impact parameter for different collimators. The legend is common to both plots.

For the isolated collimators, the fraction of secondary losses in the cold aperture is orders of

magnitude higher than for non-isolated collimators, and does not vary with the impact parameter, apart from a peak of the losses for the smallest impact parameter. Since there are no other collimators before the cold elements, this fact is explained by the fraction of particles that are absorbed for each different initial impact parameter (see figure D-1, appendix D). For isolated collimators, the fraction of losses at the superconducting elements at injection is about one order of magnitude higher than at collision.

6.2.3 Longitudinal distribution of the secondary losses

The longitudinal distribution of secondary losses varies greatly depending on the collimator that receives the primary impact and on the mode of operation. Figure 6.4 shows the longitudinal distribution of the secondary losses in the LHC ring after an initial impact on TCP.C6L7.B1 (non-isolated collimator) and TCSG.4R6.B1 (isolated collimator), for both injection and collision. The corresponding plots for all the simulated cases are given in appendix D.

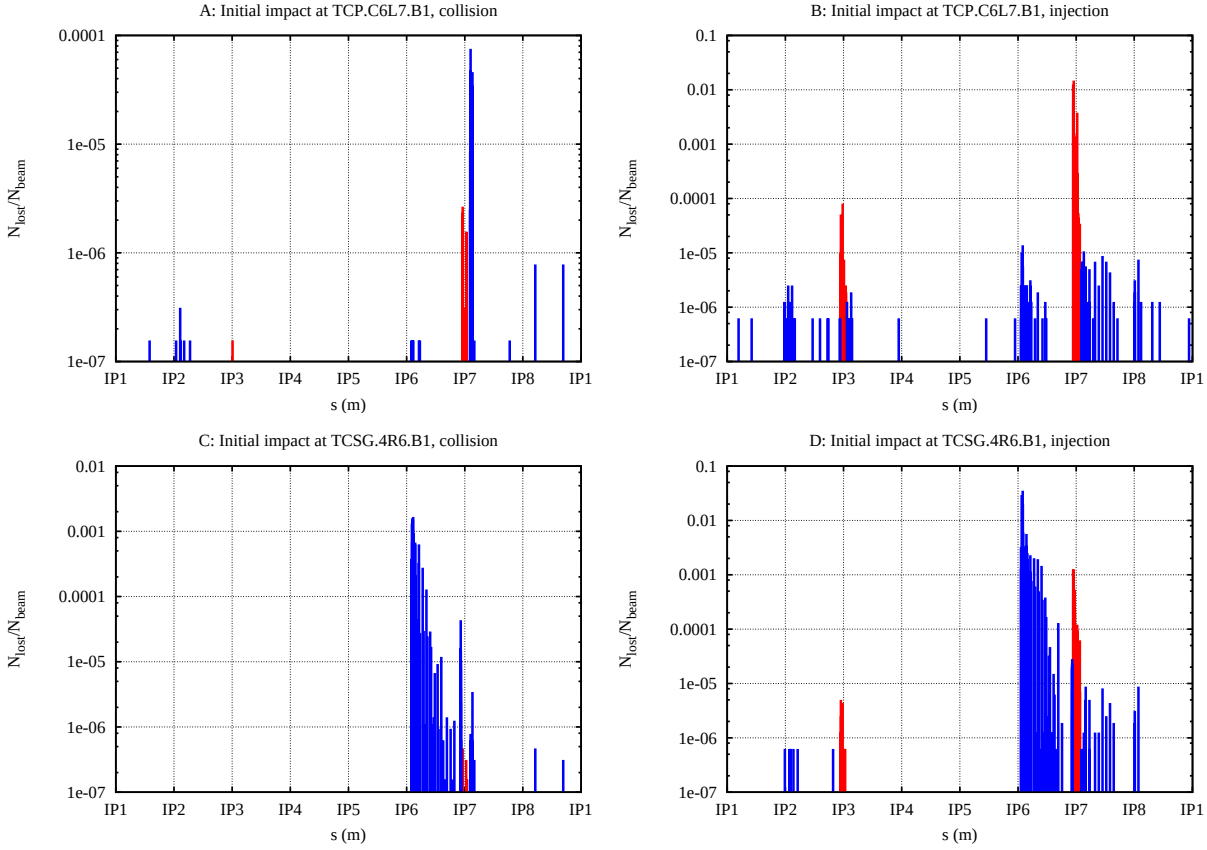

Figure 6.4: Longitudinal distribution of the secondary losses for primary impacts at TCP.C6L7.B1 and TCSG.4R6.B1 at 7 TeV and 450 GeV. Losses at the normal conducting magnets are represented in red. Losses at the super-conducting elements are in blue. The losses were recorded for the impact parameter yielding the worst collimation efficiency (worst case).

At 7 TeV very few secondary losses appear in sectors other than the one following the considered collimator, and they happen mostly in the superconducting elements. They are also less abundant than at injection. This is a consequence of the better efficiency of the collimation system at collision since the ratio between the opening of the collimators and the aperture at other locations is larger than at injection. Therefore, most of the scattered particles that escape their first passage through

the collimation system have a good chance to circulate another turn, and are lost in their second passage through the betatron cleaning insertion. For this reason, the fraction of losses in the LHC aperture at 7 TeV is also about two orders of magnitude smaller than at 450 GeV. At injection, particles are scattered again at other collimators outside the cleaning insertion and lost in the magnets downstream. Particularly, this happens mostly at IR3, the momentum cleaning insertion, as well as at IR2 and IR8, due to the presence of the absorbers for injection protection.

6.3 A method to estimate the quench time constant after a primary impact at a given collimator

By combining the benchmark simulations with the primary impact distributions presented in chapter 5, we can estimate the fraction of losses deposited in a superconducting element from a primary impact at a given collimator as a function of time. This is expressed in equation 6.1,

$$\frac{N_{sc}(t)}{N_{beam}} = \sum_{i=0}^{19} \xi(\alpha_i, t) n(\alpha_i) \Delta\alpha \tag{6.1}$$

where α_i represents the impact parameter from each benchmark simulation, $\xi(\alpha_i, t)$ the primary impact density at the collimator (equation 5.2), $\Delta\alpha$ corresponds to the spacing between consecutive sheet beams in the benchmark simulation and is equal to 50 μm, and $n(\alpha_i)$ is the fraction of scattered particles that reach the superconducting element. $\xi(\alpha_i, t)$ is derived from the MADX tracking, while $n(\alpha_i)$ is obtained from the benchmark simulations. The approximate loss threshold time to a quench can be obtained through the comparison of $N_{sc}(t)$ with the estimated quench threshold.

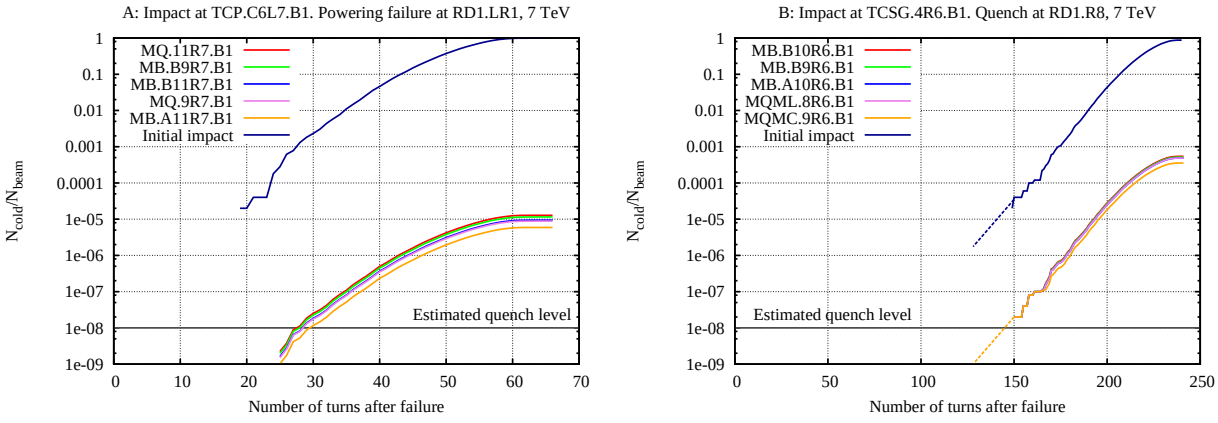

Figure 6.5: Fraction of the beam lost in the most affected super-conducting magnets as a function of time, for an impact at TCP.C6L7.B1 after a short circuit at RD1.LR1 (A) and an impact at TCSG.4R6 after a quench at RD1.R8 (B), both failures at 7 TeV. The dashed lines are extrapolated.

Figure 6.5 shows the result of this calculation for two failure cases at 7 TeV. For a short circuit at RD1.LR1, the most affected collimator is TCP.C6L7.B1. Most of the losses for this failure case concentrate in the 100 μm closest to the collimator edge (5.7 A), and the losses in the magnets follow the evolution of the losses in the collimator a factor of about 10^{-5} lower. In this case, a quench would be generated in the magnets at the beginning of the arc in sector 7-8 about 26 turns after the failure starts developing. For a quench at RD1.R8, the most affected collimator is TCSG.4R6.B1. In this case the secondary losses in the superconducting magnets are about 10^{-3}

of the primary losses and again follow the same evolution. The estimated loss threshold time to quench is less than 150 turns. In both cases, it is noticeable that the quench would happen in several magnets basically at the same time.

It is important to note that using this method to estimate the loss threshold time to a quench involves some approximations that have to be taken into account when considering the resulting data:

- Only secondary losses from the most affected collimator have been considered. This is acceptable in most of the cases since generally, even in the case of relatively distributed losses, more than 90% of the lost particles are recorded in the same collimator (see chapter 7). For very distributed losses the contribution of the primary losses in each location has to be added up.
- The benchmark simulations were done with nominal optics. In case of failure, the optics will be different. This fact is of relevance only if the scattered particles go through the failure (failures at the normal conducting magnets in IR7). For the rest of the failures the majority of the secondary losses are lost at elements close to the primary impact. In these cases, the most affected magnets as well as the order of magnitude of secondary losses are likely to be the same.

Chapter 7

Critical magnet failures at LHC and redundancy of the Machine Protection Systems

The understanding obtained in the previous chapters has been applied to evaluate the criticality of a range of possible failures at the LHC. The data corresponding to these failures have been compared with the reaction times of the protection equipment in order to evaluate the redundancy of the Machine Protection Systems. A summary of these data as well as the evaluation of redundancy are presented in this chapter.

7.1 Simulated failure scenarios

In total, about 160 cases (including failures for both beams) have been simulated based on previous studies [30] and on preliminary simulations. These failures include:

- *Quenches at the superconducting main dipoles in the arc*: Given the number of main superconducting dipoles (1232), quenches are expected to happen at these magnets. Besides, analytical calculations show that the loss time constant is relatively small (in the order of tens of milliseconds). The quench of a single main dipole including the energy extraction for the whole circuit was simulated at each arc with collision energy.
- *Quenches at the superconducting main quadrupoles in the arc*: Quenches at these magnets are also a likely failure although analytical calculations do not suggest that these failures produce fast losses. Quenches of a single main quadrupole including the energy extraction for the whole circuit was simulated for each main quadrupole circuit (focusing and defocusing) at each arc with collision energy.
- *Quenches at the most critical superconducting dipoles in the insertion (D1,D2,D3,D4)*: Quenches of these magnets produce failures that can be even faster than for quenches at the main dipoles.
- *Quenches at the inner triplets*: when operating at 7 TeV, quenches at the inner triplets produce the fastest losses due to quadrupole failures.
- *Powering failures in the insertions*: Powering failures have been simulated for the normal conducting circuits in the insertions (dipole and quadrupole circuits). These failures produce the fastest losses (failures of the normal conducting dipoles (D1) in IR1 and IR5 are the most

critical with circulating beam). Some powering failures of single powered superconducting magnets can lead to fast losses at 450 GeV and have been simulated too.

- *Simultaneous failures of several circuits*: Failures of more than one circuit at the same time have been considered in IR7, where a failure of the transformer may lead to a simultaneous power-off of RD34.LR7, RQ4.LR7 and RQ5.LR7. The results showed that the effects are almost identical to those of the failure of RD34.LR7. This is expected since the loss time constant associated to this failure is about twice faster than for failures of RQ4.LR7 and RQ5.LR7 and, as discussed in chapter 4, quadrupole failures do not produce significant effects until the failure is well developed. The results are not presented hereafter.

Quenches in the arc main dipoles and quadrupoles, quenches in the most critical superconducting magnets in the insertion regions and fast powering failures at the most critical normal conducting circuits in the insertion regions. The parameters for each single circuit and failure are given in appendix B.

Apart from the initial seeds of the particle distribution, most of the simulation settings have been set identically for all the failure cases. The following settings are common to all of the simulations presented in this chapter:

- Two batches of 5×10^4 particles were tracked for each failure case, one corresponding to the whole beam and one corresponding to the outer 0.1% of the transverse Gaussian profile. Thus, the resolution in the measurement of the losses reaches 2×10^{-8}.
- The simulations were limited to a maximum number of 2500 turns, equivalent to about 220 ms. This time is about one order of magnitude greater than the reaction time of the Quench Protection Systems and failures with loss time constants larger than this value are not considered of first order criticality.
- Nominal collision and injection optics settings have been used for the simulations done at each mode of operation. The standard files (LHC optics version 6.500) have been used.
- An ideal model has been used for dipole failures, while imperfections have been included for failures of quadrupoles, according to the results presented in chapter 4. All these failures have been simulated with the same set of errors.
- Only phase 1 collimators have been included, with the aperture settings defined by the mode of operation and centered around the closed orbit at each location.

The definition of the error translating the change in the current depends on the type of failure and circuit. For the failure cases studied, this definition has been done in five different ways:

- *Individually powered magnets*: The relative error is calculated, it is scaled to the strength of the magnet and subtracted from the magnet strength.
- *Normal conducting circuits*: The signs of the strengths of the magnets in the circuit is not the same. Therefore, the relative error is calculated, scaled to the absolute value of the strength and added or subtracted to the strength of each individual magnet depending on its sign.
- *Inner triplets*: The Quench Protection Systems act on the inner triplets as a whole, which means that the relative error is the same for the three quadrupoles in the triplet (only quenches are considered for these circuits). The powering of the magnets is however different and involves three nested power converters. Therefore this relative error is calculated and scaled separately for each power converter. The resulting values are then combined to obtain the value of the change in the current through each magnet.

- *Main dipole and quadrupole circuits in the arc*: Quenches are considered at a single magnet in these circuits. However, the energy extraction system acts simultaneously on all the magnets in the circuit. The relative errors for the quench and the energy extraction are calculated separately and scaled to the strength of the magnets. The error corresponding to the quench is subtracted from the strength of the quenching magnet and the error corresponding to the energy extraction is subtracted from the strengths of all the magnets in the circuit.

7.2 Evaluation of the BLM thresholds based on the time evolution of the losses for the most critical failures

One of the critical settings where the loss time constants and loss rates are important are the values for the thresholds of the Beam Loss Monitors (BLMs). These thresholds define the maximum amount of integrated losses that can be accepted for operation before requesting a beam dump. The losses are sampled over different integration times, for which the thresholds may differ (see section 2.6.3). However, for the early operation of LHC, the threshold values for the integration times lower than 1 s will be set to the same values [78].

The BLM thresholds have to be such that the beam is dumped before the damage level is reached at the collimators. A time margin of 3-4 turns is necessary to allow for the transmission of the beam request signal and the effective dumping of the beam. If the threshold is not low enough, very high loss rates might imply that the damage level is reached in the time gap between the generation of the beam dump request by the BLM system and the actual dump of the beam.

The evolution of the losses with time for the fastest LHC failures has been considered as a worst case scenario to set up the BLM thresholds. These failures correspond to the worst case powering failure at RD1.LR1, both at injection and collision. Figure 7.1 represents the procedure for the evaluation of the threshold. The integrated losses are compared with the damage level, which is reached at time t_{dam}. The threshold for the single-turn losses is obtained from the loss rate four turns before t_{dam}. This margin of four turns is given in order to ensure enough time for the interlock signals to propagate and to the Beam Dumping System to dump the beam properly.

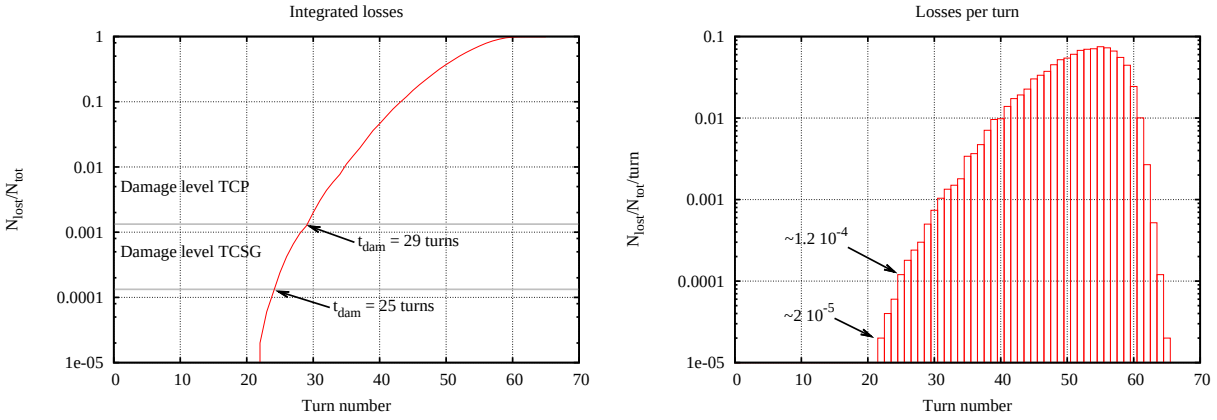

Figure 7.1: Determination of the BLMs thresholds from the evolution of the beam losses with time at 7 TeV. A fast abort of the power converter at RD1.LR1 is considered as the worst case scenario for failures with circulating beam. In order to obtain the thresholds, the integrated losses are compared with the damage level, which is reached at time t_{dam}. The loss rate per turn evaluated four turns before t_{dam} defines the threshold of the BLMs. The margin of four turns is given to leave enough time for the detection systems to react.

The values obtained for the thresholds of the BLMCs, installed downstream from the collimators, are given in table 7.1. The thresholds are different for the different types of collimators due to different damage levels: for a similar impact, more energy is deposited in collimators with longer dimensions. The threshold values have been calculated for primary, secondary and tertiary collimators. The damage levels used are also listed in the table (from [78]).

	450 GeV			7 TeV		
	N_{max}	N_{thres}	N_{thres}/N_{tot}	N_{max}	N_{thres}	N_{thres}/N_{tot}
TCP	6×10^{12}	4×10^{11}	1.3×10^{-3}	4×10^{11}	3.6×10^{10}	1.2×10^{-4}
TCSG	6×10^{11}	3×10^{10}	1×10^{-4}	4×10^{10}	6×10^{9}	2×10^{-5}
TCT	3×10^{9}	1×10^{8}	3×10^{-7}	7×10^{7}	1.2×10^{7}	4×10^{-8}

Table 7.1: Threshold values for the BLMCs for primary, secondary and tertiary collimators. N_{max} corresponds to the estimated damage level. The worst case failure scenario has been assumed to set the thresholds.

The resolution of the BLMs allows detecting losses at the collimator of the order of 5×10^7 and 3×10^6 protons at 450 GeV and 7 TeV respectively. These values are orders of magnitude lower than the required thresholds, confirming the appropriateness of the BLMs to protect the LHC equipment from fast losses produced by circulating beam failures.

7.3 Evaluated quantities for each failure

For each simulated failure global and local quantities were extracted from the output data. Global quantities refer to the effects of the failure on the beam itself or on the LHC as a whole. Local quantities are related to each location where losses are recorded. All the time constants are given in milliseconds.

Global quantities:

- *Number of loss locations (N_{loc})*: The number of locations that record primary losses, with a resolution of 2×10^{-8} of the beam.
- *Maximum loss rate (dN_{max})*: Given per turn and evaluated from the beam intensity taking into account the total amount of losses in the LHC. It is given in fraction of beam per turn.
- *Loss time constant (τ_1)*: The time when the whole beam is lost, given in ms.
- *Loss threshold time to quench (τ_{quench})*: The time at which the first quench would be generated. Evaluated from the primary impact data at the most affected collimator using the method explained in chapter 6. In very few failure cases a very small amount of primary losses have been recorded in the superconducting elements. In these cases the primary losses have been compared directly with the estimated quench threshold.
- *Loss threshold time to damage (τ_{dam})*: Time when the losses at any collimator reach the estimated threshold damage.
- *Loss threshold time to detection (τ_{det})*: Time when the Beam Loss Monitors would generate a beam dump request from losses at any of the BLMCs.

Local quantities, given for the two most affected collimators for each failure case:

- *Amount of losses (F_{lost})*, given as the fraction of the beam that is lost in the collimator. $F_{lost} = N_{lost}/N_{tot}$
- *Maximum impact density (ξ_{max})*, evaluated for the loss of the whole beam.

- *Average impact parameter ($\langle\alpha\rangle$)*, calculated from the impact distribution after the loss of the whole beam and given in mm.
- *Loss threshold time to damage (τ_{dam})* at the collimator, if reached. The values, different for each type of collimator, are given in table 7.1 for primary, secondary and tertiary collimators. For the TCDQ absorbers, the same values as for the secondary collimators have been used.
- *Loss threshold time to detection (τ_{det})* by the BLMs after the collimator, if reached. The detection thresholds have been calculated according to the procedure described in the previous section.
- $\sigma_{impact}/\sigma_{beam}$, the ratio of the size of the impact to the size of the beam at the collimator position.

Besides, for each case, the response capacity of the machine protection dedicated systems or devices are evaluated. These include the Beam Loss Monitors, Quench Protection Systems (for superconducting magnets), Fast Magnet Current Change Monitors (for normal conducting magnets, where installed) and Powering Interlock Controller (for powering failures):

- *Reaction of the Beam Loss Monitors*: the BLMs are supposed to react in time if $\tau_{det-loc} < \tau_{dam-any} - 0.356$, where $\tau_{det-loc}$ stands for the detection time due to the losses at the considered collimator, $\tau_{dam-any}$ is the shortest loss time threshold to damage at a location in the ring and 0.356 corresponds to the time in ms to dump the beam propertly (four turns, with one turn as safety margin).
- *Reaction of the Quench Protection Systems*: The QPS are supposed to react in time if $\tau_{dam} > 15$ ms. This value corresponds to about 11 ms needed by the QPS to trigger the beam dump request plus about 4 ms needed for the transmission of the PIC signal. This evaluation is done only for super-conducting magnets.
- *Reaction of the FMCMs*: For normal conducting circuits in which FMCMs have been installed, the FMCM is supposed to react on time if the damage level has not been reached 0.5 ms after the current decay starts.
- *Reaction of the PIC*: Some powering failures in superconducting circuits have been considered. In this cases the power converters will send a signal to the PIC, which is supposed to be able to request a beam dump in time if the loss threshold time to damage is shorter than 10 ms.

7.4 Results

Considering all the concepts presented above, the obtained quantities for the simulated failure scenarios are presented in this section. The reaction of the BLMs has been evaluated for the BLMCs after the two most affected collimators. If the BLMs are fast enough to react in time at more than one location, the BLM system is intrinsically redundant.

7.4.1 Quenches at the main superconducting dipoles in the arcs

Tables E-1 and E-2 summarize the results of the simulations for quenches of the main dipoles in the arc, for beam 1. Tables E-3 and E-4 list the data for the same failure scenarios for beam 2.

In average the losses produced by these failures are distributed in about seven collimators, although for most cases only one or two collimators receive above 95% of them. The loss time constants vary between 20 and 30 ms and the loss time threshold to damage ranges from about 12

to 19 ms. In all cases the BLM system is able to react in time, although in about two thirds of the cases the beam dump relies on the losses at only one location[1]. The QPS may not react in time for this kind of failures. It is also interesting to note that the size of the impact distribution is about one fourth of the size of the beam at the most affected collimator, and the ξ_{max} ranges between 10 and 20, meaning more concentrated losses and a higher damage risk for the collimators.

7.4.2 Quenches at the main superconducting quadrupoles in the arcs

Tables E-5 and E-6 summarize the results of the simulations for quenches of the main quadrupoles in the arc, for beam 1. Tables E-7 and E-8 list the data for the same failure scenarios for beam 2.

All the loss time constants corresponding to these failures are above 100 ms, and most of them above 200 ms. In some cases only very few losses were recorded before 220 ms (maximum time simulated). Both the BLM System and the QPS are able to request a beam dump in time. The size of the impact is in average about 0.7 times the size of the beam, and the values of ξ_{max} remain below 10 for most cases.

7.4.3 Quenches at the inner triplets

The results for the simulations of quenches at the inner triplets are given in tables E-9 and E-10 for beam 1, and Tables E-11 and E-12 for beam 2.

The loss time constants range from about 20 to 90 ms, and the loss threshold times to damage are comprised between 15 and 70 ms. Both the BLM system and the QPS are fast enough to dump the beam in time. The size of the impact distributions varies significantly for different cases, ranging from less than 5% of the beam size to more than twice its value. Accordingly, the range of the ξ_{max} is also large, from about 2 for large impact distributions (RQX.R5, beam 2) up to more than 100 for the more concentrated impact (RQX.R2, beam 2).

7.4.4 Powering failures of normal conducting quadrupoles in IR3 and IR7 at 450 GeV

The data corresponding to failures of the normal conducting quadrupoles for both beams are summarized in tables E-13, E-14, E-15 and E-16. Only the worst case at injection has is presented for each circuit, since the other failures that were evaluated do not produce fast losses.

The considered failure scenarios produce fast losses, with loss time constants ranging from 9 to 20 ms, while damage would be reached from times as short as 6 ms after the failure starts. For the fastest losses (RQ4.LR3, beam1), the estimation of the BLMs reaction time is about 267 μs, corresponding to 3 turns. This is in the limit of the time needed to dump the beam but for failures of these circuits the extraction of the beam is also ensured by an Fast Magnet Current change Monitor (FMCM), which leads to a beam dump about 0.5 ms after the beginning of the failure. On the other hand, the impact distribution of these losses is large, with an impact size close to the beam size and values of ξ_{max} below unity for most cases. It is also interesting to note that these failures produce very distributed losses: the number of locations recording losses is greater than 10, and in most cases there is more than one collimator that receives an amount of losses larger than 10% of the beam.

[1]This does not take into account the response of other BLMs to showers produced by secondary losses at other locations. This reaction is expected to also produce a beam dump request on time, although further studies would be needed for confirmation.

7.4.5 Failures at the most critical superconducting dipoles in the insertions

Tables E-17, E-18, E-19 and E-20 summarize the data for failures at the most critical superconducting dipoles in the insertions for both beams. Quenches are the failures that produce the fastest losses at these magnets, but for the superconducting D1s at IR2 and IR8 powering failures at injection produce fast losses too. In these cases the Powering Interlock Controller (PIC) reaction has been considered instead of the QPS for the evaluation of redundancy.

These failures lead to a complete loss of the beam in times between 10 and 40 ms, the loss threshold times to damage ranging between 7 and 20 ms. The BLMs would react in time for all cases, although in some cases (RD4.R4, beam 1) they would trigger on detectors located after collimators that would not be the most affected if the failure developed completely. For most quench cases, the QPS do not provide additional protection against these accidental losses, but the PIC does in case of failure of the power converters. The size of the impact distribution at the most affected collimators is about 10 to 50% of the beam size, leading to values of ξ_{max} up to 20 for the most affected collimators.

7.4.6 Most critical normal conducting dipoles in the insertions

Tables E-21, E-22, E-23 and E-24 list the data corresponding to different powering failures for the most critical normal conducting dipoles of the LHC (both beams).

Failures of the normal conducting dipoles are known to produce the fastest losses [8]. For the simulated cases, the loss time constants have values between 4 and 240 ms and damage would be reached only after $\sim$2 ms for the most critical cases (RD1.LR1 and RD1.LR5, worst cases at 7 TeV or 450 GeV). Other considered failures of these magnets, such as a fast abort at 450 GeV (indicated as 0 V in the tables), do not produce such fast losses. Failures at the circuits RD34.LR3 and RD34.LR7 produce fast losses only when operating at 450 GeV. As in the case of the normal conducting quadrupoles, the BLM reaction time is very close to the loss threshold time to damage, and FMCMs are installed to ensure that the beams are extracted on time. The size of the impact for these failures is between 10 and 70% of the beam size for most cases, with values lower than 10% only for the slowest failures. Accordingly, ξ_{max} reaches high values (up to 200) only for failures at RD34.LR3 and RD34.LR7. For faster failures it ranges from 1 to 20.

7.4.7 Summary

Table 7.2 summarizes the data discussed above for the main categories of critical failures, ordered according to the loss threshold time to damage. The values are the average for each failure at a certain number of similar magnets. As expected, the fastest losses are produced by failures of the D1 dipoles at IR1 and IR5, both at 450 GeV or 7 TeV.

At 450 GeV not only powering failures of the normal conducting magnets produce fast losses, but also the worst case failure scenario for the superconducting D1 in IR2 and IR8 could lead to damage in about 14 ms.

At 7 TeV, most fast losses are due to quenches, although the fastest are due to a powering failure of the normal conducting D1. Unlike at 450 GeV, the worst case powering failure at the D3 and D4 normal conducting dipoles in IR3 and IR7 does not produce very fast losses (in average, τ_{dam} = 73.1 ms). Losses due to quenches of the superconducting quadrupoles are not very fast either. In average, τ_{dam} = 34.2 ms for the inner triplets and τ_{dam} = 158.7 ms for the main quadrupoles in the arcs.

450 GeV							
Magnet type	Failure	N_{loc}	dN_{max} (frac./tr)	τ_1 (ms)	τ_{quench} (ms)	τ_{dam} (ms)	τ_{det} (ms)
D1 IR1, IR5	V_{max}	4.5	0.105	4.0	2.3	2.1	1.6
Q4/5 IR3/7	V_{max}	16.8	0.095	12.1	8.7	8.1	6.4
D3/4 IR3/7	V_{max}	3.5	0.018	19.7	9.9	10.5	7.4
D1 IR2, IR8	V_{max}	5.8	0.014	28.3	12.1	14.5	10.6

7 TeV							
Magnet type	Failure	N_{loc}	dN_{max} (frac./tr)	τ_1 (ms)	τ_{quench} (ms)	τ_{dam} (ms)	τ_{det} (ms)
D1 IR1, IR5	V_{max}	7.7	0.080	5.4	1.9	2.4	1.9
D4 IR4,	Quench	8.2	0.052	15.4	9.7	10.3	9.3
D3 IR4,	Quench	6.2	0.050	16.4	10.8	11.0	10.2
D2	Quench	6.9	0.047	17.7	9.8	11.8	10.6
D1 IR2, IR8	Quench	8.0	0.044	18.3	11.4	12.3	10.8
MB	Quench	7.2	0.035	23.1	9.6	15.4	13.5
RQX	Quench	7.5	0.040	48.9	32.0	34.2	30.6
D3/4 IR3/7	V_{max}	3.5	0.002	206.3	69.0	73.1	57.5
MQ	Quench	6.9	0.030	203.2	152.4	158.7	177.8

Table 7.2: Summary of the main quantities related to the losses produced by all the categories of considered failures.

7.5 Evaluation of the redundancy of the LHC Machine Protection Systems

Different types of redundancy have been defined in section 2.6.5. After the study presented above, we assess here each of these types of redundancy for the LHC Machine Protection Systems against failures during operation with circulating beam:

Design redundancy

The systems dedicated to the LHC Machine Protection (Beam and Powering Interlocks, Quench Protection, Beam Loss Monitors, Fast Magnet Current Change Monitors, Beam Dump System, etc.) are redundant by design for their critical parts (basic measurements, generation and transmission of dump signals, etc). The electronics devoted to the generation and transmission of additional data for diagnostics (Post Mortem data) may not be redundant, as they are not critical for the protection of the machine. Obviously, design redundancy is not dependent on the failure case.

Intrinsic measurement redundancy

The BLM system records losses at many different points of the LHC. Therefore, given enough reaction time, it is intrinsically redundant. However, if losses are very localized, it may happen that the dump threshold is reached in time only at one loss location. The reaction time of the BLMs at the two most affected collimators has been compared with the loss threshold time to damage for each failure case. It has been found that in many cases only the monitors located after the most affected collimator react in time, and thus intrinsic redundancy is not ensured for all failure cases. The analysis of the failure cases shows that a redundant behavior of the BLM system does not depend on the type of failure or failing magnet. A combination of the speed of the losses, its

longitudinal distribution and evolution with time at the different loss locations determines which BLMs will react in time.

Inter-system redundancy

Inter-system redundancy is guaranteed only in most but not all of the failure scenarios considered. The type of failures that are not redundantly protected have been determined. We have evaluated the response of the BLM System for all failure cases, the Quench Protection System for quenches, the PIC (power converter standard monitoring) for powering failures in all circuits and the FMCMs instead of the PIC where installed.

The assessment can be summarized for each type of magnet, circuit or failure:

- *Quenches of the main dipoles in the arc*: Only the BLMs react on time in all cases. The QPS do detect the quench, but in about half the cases studied, they do not react fast enough to request a beam dump. In some cases, in-time dump request from the QPS may depend on how the quench itself develops. In the general case, inter-system redundancy is not ensured.
- *Quenches of the main quadrupoles in the arc*: Both the BLM system and the QPS react in time. Inter-system redundancy is ensured.
- *Quenches of the inner triplets*: The situation is the same as for the main quadrupoles in the arc. The BLMs and the QPS react in time, so that redundancy is ensured.
- *Powering failures of the normal conducting quadrupoles in IR3 and IR7 (450 GeV)*: The BLMs react in time in all cases, although the time margin for a worst case failure in RQ4.LR3 (beam 1) is very tight. For these circuits, FMCMs generate a beam dump in time in any case, ensuring inter-system redundancy.
- *Powering failures of the superconducting dipoles in the insertions (450 GeV)*: The BLMs react in time and redundancy is ensured by the PIC. These powering failures are the fastest for superconducting magnets, representing the worst case scenario. Any other failure of a power converter for a superconducting circuit is also redundantly protected against accidental beam losses both by the BLMs and the PIC.
- *Quenches of superconducting dipoles in the insertions*: The BLMs react in time, but in most cases not the QPS. Redundancy is not ensured.
- *Powering failures of normal conducting dipoles in the insertions*: As for the normal conducting quadrupoles, the time margin for the beam dump request is tight for the fastest failures. Redundancy is ensured with FMCMs.

Considering only the reaction of the BLMs, QPS, PIC and FMCMs, redundancy is not ensured for all failure cases. Particularly, protection against many of the dipole quenches relies only on the BLM system, since the QPS reaction time is too long to ensure redundancy. On the other hand, powering failures are treated redundantly in all cases thanks to the PIC and the FMCMs.

Further redundancy in case of quench can be provided by the Fast Beam Current Monitor, which is expected to react in times as short as 1 ms. In this case, the settings for the dump request threshold of this device must also be set taking into account the loss rates and damage thresholds.

Conclusion

The Large Hadron Collider at the European Laboratory for Particle Physics (CERN) requires beams with unprecedented stored energy, two or three orders of magnitude larger than for previous accelerators. Thus, the LHC beams have a destructive potential and Machine Protection Systems are mandatory. In case of magnet failures, the beam is affected and must be extracted before any damage is generated in the accelerator. This doctoral thesis focuses on the effects of magnet failures on the beam and is oriented toward an evaluation of the redundancy of the Machine Protection Systems.

Two types of magnet failures leading to changes in the current at the magnets have been considered: failures at the power converters (exponential current decay) and quenches of superconducting magnets (Gaussian current decay). The magnetic field in the magnets has been supposed to follow the evolution of the current.

In order to study the effects of different types of failures on the beam, tracking with variable magnetic field has been done using MADX. The LHC model used includes machine imperfections and aperture restrictions for an evaluation of the losses, and the tracking procedure yields good results. Primary losses, corresponding to the first hit of the aperture by high amplitude protons, have been recorded using this method. The procedure is however slow and requires a considerable amount of computer resources, which has supposed a limitation to the number and resolution of the simulations that were performed.

The effects on the beam of quadrupole and dipole failures were studied. Dipole failures produce a progressive closed orbit distortion that can be characterized analytically. Beam losses, however, cannot be predicted without simulation tools. Quadrupole failures lead to a change in the optics and the subsequent effects cannot be analyzed analytically. Depending on the failure case, the beam may defocus or drift transversely and the crossing of non-linear resonances may lead to significant beam losses. Contrarily to dipole failures, for quadrupole failures the beam remains mostly unaffected during a certain time, then is suddenly distorted. Both for dipole and quadrupole failures, an increase of the time constant of the failure leads to more localized losses.

Protons lost because of a magnet failure are first intercepted by a collimator. The shape of the distribution of these primary losses at the collimators has been evaluated and the results are similar to those obtained in studies for other accelerators [79]. A fit function has been proposed to approximate the shape of the impact and various quantities have been defined to estimate its criticality (evolution with time, density of impacts). An algorithm based on the method of the moments has been used to obtain these parameters every turn. The influence of the time constant of the failure has also been studied: faster failures produce broader impact distributions on the collimator jaws.

In order to study secondary losses, benchmark simulations including collimation have been done using SIXTRACK. Particles scattered from a primary impact at a collimator were tracked until they were effectively lost. The initial impact parameters at the collimator range up to 950 μm. The percentage of losses absorbed by the collimation system has been evaluated as a function of the

collimator that is hit first and as a function of the impact parameter. In the worst case, a fraction up to 1% of the beam at 7 TeV and 10% at 450 GeV could escape the collimation system. Impacts on isolated collimators produce the highest proportion of secondary losses in the cold aperture. Based on these benchmark simulations and on time dependency of the primary impact, a method to estimate the quench time constant has also been developed.

In total, some 130 magnet failure cases were simulated. At 450 GeV, the fastest failures were generated by worst case powering failures at the D1 in IR1 and IR5 (damage of the collimators reached about 2 ms after the failure). Powering failures at the normal conducting quadrupoles at IR3 and IR7 can lead to damage about 8 ms after the failure while the other possible failures do not reach the damage level before 10 ms after the failure. At 7 TeV, the fastest losses are also produced by powering failures of the D1 at IR1 and IR5, reaching damage level about 2.5 ms after the failure. Quenches of other insertion dipoles can produce damage some 11 ms after the failure, and quenches of the main superconducting dipoles after 15 ms. Damage after a quench at a main superconducting quadrupole does not happen before some 160 ms after the failure.

Three types of redundancy have been defined and evaluated for the LHC Machine Protection Systems. Design redundancy is ensured within the electronic devices that are critical for machine protection. Intrinsic redundancy applies to the BLM system, but it is not ensured from the detection of primary losses in more than 60% of the considered failure cases, particularly when these are very localized (although the response of the BLMs to secondary losses is expected to provide this redundancy). Inter-system redundancy is ensured in all cases by the Fast Beam Current Monitor. However, considering only the BLMs, the QPS, the PIC and the FMCMs, 27% of the failure cases studied are not redundantly protected. These cases correspond all to quenches of superconducting dipoles. The evaluation considers the worst case scenario for the resistive transition and it is believed that for most of the possible quench processes the QPS will still react in time. For the time being there is not enough data to confirm such statement, and the general conclusion from these studies is that for these cases, effective protection is ensured only by the BLM system. Additional protection for these failure cases can be ensured by other devices. In case of need, FMCMs can be added in critical individual magnets. Besides, it is advised that the the Fast Magnet Current Monitor is fully developed and integrated in the Machine Protection Systems to provide full redundancy for every considered failure case.

It is important to note that some significant approximations have been done to obtain the data presented in this work. All of the assumptions concerning the current decays are conservative (an error up to 30% has been observed in comparisons with measured data) and an extra delay may be added to the change in the magnetic field due to eddy currents and saturation effects. In this case the results obtained represent the worst possible situation and a more realistic approach can only yield larger time margins for the Machine Protection Systems to react. The assumption made for the transverse beam profile may have a greater influence. The Gaussian approximation may be too coarse and the distribution of the first losses may be significantly different for a non Gaussian beam profile.

Finally, the outcome of this thesis opens three main directions of further research:

- Detailed studies on the ability of the QPS to react on time for different types of resistive transitions in the superconducting dipoles (training quench, vibration induced quench, beam loss induced quench, etc.)

- Study and timing considerations of the response of the BLM systems to the secondary losses, particularly for the failure cases where intrinsic redundancy of the BLMs is not ensured from their response to the primary losses.

- Further simulations with more realistic input data (better approximation of the current decay in case of quench, transverse beam profile closer to the real one, etc.)

Bibliography

[1] O. Brüning, P. Collier, P. Lebrun, S. Myers, R. Ostojic, J. Poole, and P. Proudlock. LHC design report. Technical report, CERN, June 2004.

[2] http://atlas.web.cern.ch/Atlas/index.html, ATLAS Collaboration.

[3] http://cms.cern.ch/, CMS Collaboration.

[4] http://lhcb.web.cern.ch/lhcb/, LHCb Collaboration.

[5] http://aliceinfo.cern.ch/, ALICE Collaboration.

[6] O. Brüning. Mechanisms for beam losses and their time constants. In *LHC workshop Chamonix XI, Chamonix, France*, 2001.

[7] V. Kain. Studies of equipment failures and beam losses in the LHC. Technical report, CERN, October 2002.

[8] V. Kain. Power converter failure of the normal conducting D1 magnet at experiment insertions IR1 and IR5. LHC project note 322, CERN, Sep 2003.

[9] V. Kain. *Machine Protection and Beam Quality during the LHC Injection Process*. PhD thesis, CERN, 2005.

[10] K. Wille. *The Physics of Particle Accelerators : An Introduction*. Oxford Univ. Press, 2000.

[11] H. Wiedemann. *Particle Accelerator Physics*, volume 1. Springer, 1999.

[12] H. Wiedemann. *Particle Accelerator Physics*, volume 2. Springer, 1999.

[13] L. Rossi. Very high field magnets. In *CAS - CERN Accelerator School on Superconductivity and Cryogenics for Accelerators and Detectors, Erice, Italy*, pages 177–194, May 2002.

[14] N. Bourcey, O. Capatina, V. Parma, A. Poncet, P. Rohmig, L. Serio, B. Skoczen, J. P. Tock, and L. R. Williams. Final design and experimental validation of the thermal performance of the LHC lattice cryostats. In *Cryogenic Engineering Conference, Anchorage, AK, USA*, pages 487–493, September 2003.

[15] C. Hauviller, P. M. Ivanov, A. Poncet, P. Sacr, and P. Trilhe. The electrical distribution feed box for the LHC prototype cell. LHC project report 416, CERN, September 2000.

[16] K. Dahlerup-Petersen, A. Medvedko, A. Erokhin, B. Kazmin, V. Sytchev, and L. Vassiliev. Energy extraction in the CERN Large Hadron Collider : a project overview. In *13th International Pulsed Power Conference and 28th International Conference on Plasma Science, Las Vegas, NV, USA*, pages 1473–1477, June 2001.

[17] K. Dahlerup-Petersen, B. Popov, V. G. Zubko, B. Kazmin, V. Sytchev, and L. Vassiliev. Energy extraction resistors for the main dipole and quadrupole circuits of the LHC. In *7th European Particle Accelerator Conference, Vienna, Austria*, pages 2420–2423, September 2000.

[18] K. Dahlerup-Petersen, R. Denz, J.L. Gómez-Costa, D. Hagedorn, P. Proudlock, F. Rodríguez-Mateos, R. Schmidt, and F. Sonnemann. The protection system for the superconducting elements of the Large Hadron Collider at CERN. LHC project report 283, CERN, April 1999.

[19] F. Bodry and H. Thiesen. LHC inner triplet powering strategy. In *19th IEEE Particle Accelerator Conference, Chicago, IL, USA*, pages 633–636, June 2001.

[20] R. W. Assmann. Collimators and cleaning, could this limit the lhc performance? In *Workshop on LHC performance. Chamonix XII*, Geneva, 2003. CERN.

[21] J. B. Jeanneret, D. Leroy, L. R. Oberli, and T. Trenkler. Quench levels and transient beam losses in LHC magnets. LHC project note 44, CERN, May 1996.

[22] G. Robert-Demolaize. *Design and Performance Optimization of the LHC Collimation System.* PhD thesis, CERN, 2006.

[23] R. W. Assmann, I. S. Baishev, M. Brügger, L. Bruno, H. Burkhardt, G. Burtin, B. Dehning, C. Fischer, B. Goddard, E. Gschwendtner, M. Hayes, J. B. Jeanneret, R. Jung, V. Kain, D. I. Kaltchev, M. Lamont, R. Schmidt, E. B. Vossenberg, E. Weisse, and J. Wenninger. Quench levels and transient beam losses in LHC magnets. LHC project report 599, CERN, July 2002.

[24] L. Bottura et al. LHC main dipoles proposed baseline current ramping. LHC project report 172, CERN, March 1998.

[25] R. Schmidt, R. Assmann, E. Carlier, B. Dehning, R. Denz, B. Goddard, E. B. Holzer, V. Kain, B. Puccio, B. Todd, J. Uythoven, J. Wenninger, and M. Zerlauth. Protection of the CERN Large Hadron Collider. *New Journal of Physics*, November 2006.

[26] R. W. Assmann, F. Schmidt, F. Zimmermann, and M. P. Zorzano-Mier. Equilibrium beam distribution and halo in the LHC. In *10th European Particle Accelerator Conference, Edinburgh, UK*, pages 1326–1329, June 2002.

[27] R. W. Assmann, B. Goddard, E. B. Vossenberg, and E. Weisse. The consequences of abnormal beam dump actions on the LHC collimation system. LHC project note 293, CERN, May 2002.

[28] P. Collier. Objects capable of touching the beams. In *2nd LHC Project Workshop, CERN, Geneva, Switzerland*, pages 285–290, January 2005.

[29] V. Baglin. He leaks in the CERN LHC beam vacuum chambers operating at cryogenic temperatures. *Vacuum*, 81:803–807, February 2007.

[30] A. Gómez Alonso. Most probable failures in LHC magnets and time constants of their effects on the beam. LHC project note 389, CERN, November 2006.

[31] R. Schmidt, R. W. Assmann, H. Burkhardt, E. Carlier, B. Dehning, B. Goddard, J. B. Jeanneret, V. Kain, B. Puccio, and J. Wenninger. Beam loss scenarios and strategies for machine protection at the LHC. In *29th ICFA Advanced Beam Dynamics Workshop on Beam-Halo Dynamics, Diagnostics and Collimation in conjunction with The Beam-Beam Workshop, Montauk, Long Island, New York, USA*, pages 184–187, May 2003.

[32] Wikipedia keyword: fuel efficiency. `http://en.wikipedia.org/wiki/Fuel_efficiency`.

[33] G. Battistoni, F. Cerutti, A. Fasso, A. Ferrari, S. Muraroi, J. Ranft, S. Roesler, and P.R. Sala. The FLUKA code: description and benchmarking. In *Hadronic Shower Simulations Workshop, Batavia, IL, USA*, September 2006.

[34] N. A. Tahir, V. E. Fortov, V. Gryaznov, H. H. Hoffmann Dieter, V. Kain, I. V. Lomonosov, A. R. Piriz, R. Schmidt, A. Shutov, and M. Temporal. The CERN large hadron collider as a tool to study high-energy density matter. *Physical Review Letters*, 94(13):135004/1–4, 2005.

[35] V. Kain, J. Ramillon, R. Schmidt, K.Vorderwinkler, and J.Wenninger. Material damage test with 450 GeV LHC-type beam. In *Particle Accelerator Conference (PAC), Knoxville, USA*, May 2005.

[36] F. Sonnemann R. Schmidt (dir). *Resistive transition and protection of LHC superconducting cables and magnets*. PhD thesis, CERN, 2001.

[37] A. Bertarelli, O. Aberle, R. W. Assmann, S. Calatroni, A. Dallocchio, T. Kurtyka, M. Mayer, R. Perret, S. Redaelli, and G. Robert-Demolaize. Mechanical design for robustness of the LHC collimators. In *21st IEEE Particle Accelerator Conference, Knoxville, TN, USA*, pages 913–915, May 2005.

[38] A. Bertarelli, O. Aberle, R. W. Assmann, A. Dallocchio, T. Kurtyka, M. Mayer, M. Magistris, and M. Santana-Leitner. Permanent deformation of the LHC collimator jaws induced by shock beam impact : an analytical and numerical interpretation. In *10th European Particle Accelerator Conference, Edinburgh, UK*, pages 1801–1803, June 2006.

[39] Y. Kadi, V. Kain, B. Goddard, and R. Schmidt. Attenuation and emittance growth of 450 GeV and 7 TeV proton beams in low-Z absorber elements. In *9th European Particle Accelerator Conference, Lucerne, Switzerland*, pages 581–583, July 2004.

[40] R. Schmidt, N. A. Tahir, D. H. Hoffmann, Y. Kadi, A. Shutov, and A. R. Piriz. Interaction of the CERN Large Hadron Collider (LHC) beam with carbon collimators. In *10th European Particle Accelerator Conference, Edinburgh, UK*, pages 1798–1800, June 2006.

[41] R. Schmidt and J. Wenninger. LHC injection scenarios. LHC project note 287, CERN, Geneva, Mars 2002.

[42] M.Werner, M.Zerlauth, R.Schmidt, V.Kain, and B.Goddard. A fast magnet current change monitor for machine protection in HERA and the LHC, 10th international conference on accelerator and large experimental physics control systems ICALEPCS 2005. In *Europhysiscs conference abstracts*, volume 29J, 2005.

[43] F. Bordry, R. Denz, K. H. Mess, B. Puccio, F. Rodríguez-Mateos, and R. Schmidt. Machine protection for the LHC: Architecture of the beam and powering interlock systems. LHC project report 521, CERN, Geneva, December 2001.

[44] M. Zerlauth. *Powering and Machine Protection of the Superconducting LHC Accelerator*. PhD thesis, CERN, 2004.

[45] R. Schmidt, P. Dahlen, B. Puccio, and M. Zerlauth. The hardware interfaces between warm magnet interlock system, normal conducting magnets and beam interlock system for the LHC ring. Engineering specification LHC-CIW-ES-0001 Ver. 0.1, CERN, Geneva, June 2005.

[46] B. Todd. *A Beam Interlock System for CERN High Energy Accelerators*. PhD thesis, CERN, 2006.

[47] B.Todd, A.Dinius, P.Nouchi, B.Puccio, and R.Schmidt. The architecture, design and realisation of the LHC beam interlock system. In *Europhysiscs conference abstracts*, volume 29J, 2005.

[48] R. Denz. Electronic systems for the protection of superconducting elements in the LHC. LHC project report 879, CERN, Geneva, May 2006.

[49] L. Coull, R. Denz, and D. Hagedorn. High current diffusion type diodes at cryogenic temperatures for the LHC superconducting magnet protection. *Advanced Cryogenics Engineering, A*, 43:371–378. 9 p, August 1997.

[50] C. Dehavay, B. Puccio, R. Schmidt, E. Veyrunes, and M. Zerlauth. From the LHC reference database to the powering interlock system. In *9th International Conference on Accelerator and Large Experimental Physics Control Systems (ICALEPS), Gyeongju, Korea*, pages 395–398, October 2003.

[51] H. Thiesen. Personal communication.

[52] E. B. Holzer et al. Beam loss monitoring system for the LHC. CERN-AB-2006-009, CERN, Sep 2005.

[53] H. Burkhardt B. Jeanneret. On the measurement of the beam losses in the LHC rings. LHC-BLM-ES-0001 rev 2.0, CERN, Geneva, January 2004.

[54] O. R. Jones. LHC beam instrumentation. LHC project report 1028, CERN, Geneva, June 2007.

[55] R.J. Steinhagen and J. Wenninger (dir). *LHC Beam Stability and Feedback Control - Orbit and Energy*. PhD thesis, RWTH Aachen University, Aix-la-Chapelle, 2007. Presented on 22 Jun 2007.

[56] R. Schmidt. Personal communication.

[57] R. Schmidt. Safe LHC parameters generation and transmission (SLPT). LHC-CI-ES-0004 Rev. 0.1, CERN, Geneva, December 2006.

[58] A. Dinius, R. Giachino, J. Gimeno Vicente, P. Nouchi, B. Puccio, R. Schmidt, and J. Wenninger. Beam interlocks for LHC and SPS. In *9th International Conference on Accelerator and Large Experimental Physics Control Systems (ICALEPS), Gyeongju, Korea*, pages 563–566, October 2003.

[59] International Electro technical Commission IEC. Functional safety of electrical-electronic-programmable electronic safety related systems, 1998.

[60] R. Filippini, B. Dehning, G. Guaglio, F. Rodríguez-Mateos, R. Schmidt, B. Todd, J. Uythoven, A. Vergara-Fernández, and M. Zerlauth. Reliability assessment of the LHC machine protection. LHC project report 812, CERN, Geneva, June 2005.

[61] G. Ripken and F. Schmidt. A symplectic six-dimensional thin-lens formalism for tracking. Technical Report CERN-SL-95-12. DESY-95-063, CERN, Geneva, April 1995.

[62] LHC optics web home. http://proj-lhc-optics-web.web.cern.ch/proj-lhc-optics-web/.

[63] *MADX User Guide*. http://mad.web.CERN.ch/mad/uguide.html.

[64] F. Schmidt. SIXTRACK version 1.2: single particle tracking code treating transverse motion with synchrotron oscillations in a symplectic manner; user's reference manual. Technical Report CERN-SL-94-56-AP, CERN, Geneva, September 1994.

[65] G. Robert-Demolaize, R. Assmann, S. Redaelli, and F. Schmidt. A new version of sixtrack with collimation and aperture interface. In *Proceedings of 2005 Particle Accelerator Conference, Knoxville, Tennessee*, July 2005.

[66] C. Bracco. Personal communication.

[67] *LHC Aperture and Commissioning of the Collimation System*, January 2005.

[68] P. Hagen, M. Giovannozzi, J.-P. Koutchouk, T. Risselada, S. Sanfilippo, E. Todesco, and E. Wildner. WISE: An adaptive simulation of the LHC optics. LHC project report 971, CERN, August 2006.

[69] S. Fartoukh and O. Brüning. Field quality specication for the lhc main dipole magnets. Technical Report LHC Project Report 501, CERN, Geneva, October 2001.

[70] S. Fartoukh. Personal communication.

[71] *Tracking tools to evaluate the quench time constants for magnet failures in LHC*, June 2008.

[72] V. Kain. Personal communication.

[73] C. de Almeida Martins. Personal communication.

[74] A. Franchi. *Studies and Measurements of Linear Coupling and Nonlinearities in Hadron Circular Accelerators*. PhD thesis, GSI, Johann Wolfgang Goethe-Universität Frankfurt am Main, August 2007.

[75] A. Gómez Alonso and R. Schmidt. Tracking studies with variable magnetic field to characterize quadrupole failures in LHC. In *22nd Particle Acelerator Conference (PAC), Albuquerque, New Mexico, USA*, July 2007.

[76] E. B. Holzer and B. Dehning. Longitudinal beam loss distribution along the LHC ring. Technical Report LHC Project Report 780, CERN, Geneva, August 2004.

[77] M. Brügger, F. Cerutti, A. Ferrari, M. Magistris, M. Santana-Leitner, and V. Vlachoudis. Fluka simulations for the optimization of the beam loss monitors. Technical Report CERN-AB-Note-2008-038, CERN, Geneva, December 2006.

[78] B. Dehning M. Sapinski. Personal communication.

[79] M. Seidel. *The Proton Collimation System of HERA*. PhD thesis, DESY, Universität Hamburg, June 1994.

[80] Ronald E Walpole, Raymond H Myers, Sharon L Myers, and Keying Ye. *Probability and statistics for engineers and scientists ; 8th ed.* Upper Saddle River, NJ: Pearson, 2007.

Appendix A

Lists of collimators

The collimators used for the simulations are listed in tables A-1, A-2, A-3 and A-4. The settings correspond to the optimal set up of the collimators according to the most recent studies at the time when the failure simulations were started [66].

Name	Angle	Halfgap (mm)	Length (m)	σ_x (μm)	σ_y (μm)	σ_{col} (μm)	n (σ)	β_x (m)	β_y (m)
TDI.4L2.B1	1.571		4.998 4.0	908	603	603	6.8	112.9	49.8
TCP.6L3.B1	0.000	7.848	0.6	981	1026	981	8.0	131.9	144.3
TCSG.5L3.B1	0.000	5.877	1.0	632	1475	632	9.3	54.7	298.1
TCSG.4R3.B1	0.000	4.067	1.0	437	1702	437	9.3	26.2	396.8
TCSG.A5R3.B1	2.981	5.261	1.0	512	1588	566	9.3	35.9	345.3
TCSG.B5R3.B1	0.189	5.896	1.0	577	1513	634	9.3	45.6	313.8
TCDQA.4R6.B1	0.000	14.95	3.0	1869	1077	1869	8.0	478.6	158.2
TCDQB.4R6.B1	0.000	15.12	3.0	1890	1087	1890	8.0	489.4	161.8
TCSG.4R6.B1	0.000	13.39	1.0	1913	1099	1913	7.0	501.5	165.4
TCP.D6L7.B1	1.571	4.263	0.6	1088	748	748	5.7	162.1	76.6
TCP.C6L7.B1	0.000	6.037	0.6	1059	769	1059	5.7	153.7	81.1
TCP.B6L7.B1	2.215	5.044	0.6	1031	791	885	5.7	145.5	85.8
TCSG.A6L7.B1	2.463	6.087	1.0	546	1279	908	6.7	40.9	224.2
TCSG.A5L7.B1	0.710	7.334	1.0	1149	1031	1101	6.7	181.0	145.6
TCSG.A4L7.B1	2.349	6.650	1.0	960	1023	993	6.7	126.2	143.5
TCSG.A4R7.B1	0.808	6.680	1.0	921	1062	997	6.7	116.2	154.5
TCSG.6R7.B1	0.009	10.57	1.0	1577	582	1577	6.7	340.8	46.4
TCTH.4L8.B1	0.000	52.82	1.0	587	592	587	900.0	47.20	48.0

Table A-1: List of phase 1 collimators and collimator settings for beam 1, 450 GeV.

Name	Angle	Halfgap (mm)	Length (m)	σ_x (μm)	σ_y (μm)	σ_{col} (μm)	n (σ)	β_x (m)	β_y (m)
TCTH.4R8.B2	0.000	52.82	1.0	587	592	587	900.0	47.2	48.0
TDI.4R8.B2	1.571	3.879	4.0	892	570	570	6.8	109.0	44.6
TCP.D6R7.B2	1.571	4.168	0.6	1111	731	731	5.7	169.1	73.3
TCP.C6R7.B2	0.000	6.167	0.6	1082	752	1082	5.7	160.4	77.5
TCP.B6R7.B2	2.215	5.043	0.6	1053	774	885	5.7	152.0	82.0
TCSG.A6R7.B2	2.463	6.044	1.0	560	1258	902	6.7	43.0	216.8
TCSG.A5R7.B2	0.710	7.229	1.0	1118	1024	1079	6.7	171.3	143.6
TCSG.A4R7.B2	2.349	6.654	1.0	980	1006	993	6.7	131.5	138.7
TCSG.A4L7.B2	0.808	6.823	1.0	834	1161	1018	6.7	95.4	184.8
TCSG.6L7.B2	0.009	10.07	1.0	1604	572	1603	6.7	352.3	44.7
TCDQA.4L6.B2	0.000	16.00	3.0	2001	1031	2001	8.0	548.5	145.7
TCDQB.4L6.B2	0.000	16.20	3.0	2025	1044	2025	8.0	562.0	149.3
TCSG.4L6.B2	0.000	14.37	1.0	2052	1058	2052	7.0	577.1	153.5
TCP.6R3.B2	0.000	7.889	0.6	986	1020	986	8.0	133.2	142.6
TCSG.5R3.B2	0.000	5.912	1.0	636	1469	636	9.3	55.4	295.7
TCSG.4L3.B2	0.000	4.067	1.0	437	1714	437	9.3	26.2	402.5
TCSG.A5L3.B2	2.981	5.287	1.0	514	1599	568	9.3	36.2	350.4
TCSG.B5L3.B2	0.189	5.929	1.0	580	1524	638	9.3	46.1	318.4

Table A-2: List of phase 1 collimators and collimator settings for beam 2, 450 GeV.

Name	Angle	Halfgap (mm)	Length (m)	σ_x (μm)	σ_y (μm)	σ_{col} (μm)	n (σ)	β_x (m)	β_y (m)
TDI.4L2.B1	1.571	142.410	4.0	238	158	158	900.0	130.0	49.8
TCP.6L3.B1	0.000	3.862	0.6	257	269	257	15.0	131.9	144.3
TCSG.5L3.B1	0.000	2.986	1.0	166	387	166	18.0	54.7	298.1
TCSG.4R3.B1	0.000	2.066	1.0	115	447	115	18.0	26.2	396.8
TCSG.A5R3.B1	2.981	2.672	1.0	134	417	148	18.0	35.9	345.3
TCSG.B5R3.B1	0.189	2.995	1.0	151	397	166	18.0	45.6	313.8
TCDQA.4R6.B1	0.000	3.924	3.0	491	283	491	8.0	478.7	158.9
TCDQB.4R6.B1	0.000	3.968	3.0	496	285	496	8.0	489.5	161.9
TCSG.4R6.B1	0.000	3.766	1.0	502	288	502	7.5	501.6	165.4
TCP.D6L7.B1	1.571	1.178	0.6	285	196	196	6.0	162.1	76.6
TCP.C6L7.B1	0.000	1.668	0.6	278	202	278	6.0	153.7	81.1
TCP.B6L7.B1	2.215	1.394	0.6	270	208	232	6.0	145.5	85.7
TCSG.A6L7.B1	2.463	1.669	1.0	143	336	238	7.0	40.9	224.2
TCSG.A5L7.B1	0.710	2.022	1.0	302	271	289	7.0	181.0	145.6
TCSG.A4L7.B1	2.349	1.824	1.0	252	269	260	7.0	126.3	143.5
TCSG.A4R7.B1	0.808	1.832	1.0	242	279	262	7.0	116.2	154.5
TCSG.6R7.B1	0.009	2.897	1.0	414	153	414	7.0	340.8	46.4
TCTH.4L8.B1	0.000	1.279	1.0	154	155	154	8.3	47.2	48.0

Table A-3: List of phase 1 collimators and collimator settings for beam 1, 7 TeV.

Name	Angle	Halfgap (mm)	Length (m)	σ_x (μm)	σ_y (μm)	σ_{col} (μm)	n (σ)	β_x (m)	β_y (m)
TCTH.4R8.B2	0.000	1.279	1.0	154	155	154	8.3	47.2	48.0
TDI.4R8.B2	1.571	134.730	4.0	234	150	150	900.0	109.0	44.6
TCP.D6R7.B2	1.571	1.152	0.6	292	192	192	6.0	169.1	73.3
TCP.C6R7.B2	0.000	1.704	0.6	284	197	284	6.0	160.4	77.5
TCP.B6R7.B2	2.215	1.393	0.6	276	203	232	6.0	152.0	82.0
TCSG.A6R7.B2	2.463	1.657	1.0	147	330	237	7.0	43.0	216.9
TCSG.A5R7.B2	0.710	1.982	1.0	293	269	283	7.0	171.3	143.6
TCSG.A4R7.B2	2.349	1.825	1.0	257	264	261	7.0	131.5	138.7
TCSG.A4L7.B2	0.808	1.871	1.0	219	305	267	7.0	95.4	184.8
TCSG.6L7.B2	0.009	2.946	1.0	421	150	421	7.0	352.3	44.8
TCDQA.4L6.B2	0.000	4.201	3.0	525	271	525	8.0	548.5	145.8
TCDQB.4L6.B2	0.000	4.252	3.0	532	274	532	8.0	562.0	149.3
TCSG.4L6.B2	0.000	4.040	1.0	539	278	539	7.5	577.1	153.5
TCP.6R3.B2	0.000	3.882	0.6	259	268	259	15.0	133.3	142.6
TCSG.5R3.B2	0.000	3.003	1.0	167	386	167	18.0	55.4	295.7
TCSG.4L3.B2	0.000	2.066	1.0	115	450	115	18.0	26.2	402.6
TCSG.A5L3.B2	2.981	2.685	1.0	135	420	149	18.0	36.2	350.4
TCSG.B5L3.B2	0.189	3.012	1.0	152	400	167	18.0	46.1	318.4

Table A-4: List of phase 1 collimators and collimator settings for beam 2, 7 TeV.

Appendix B

Simulated electrical circuits and failures

The circuits for which failures were simulated are given below. The nominal values are given for operation at 7 TeV.

Circuit	L [H]	R [Ω]	L_f [mH]	R_f [Ω]	R_a [Ω]	C_f1 [mF]	C_f1 [mF]
RD1.LR1	0.174	0.86	2.5	0	0.033	2.0	8.0
RBXWSH.L8	0.400	0.06	3.2	0	0.010	26.4	6.6
QTAF.2202M[a]	0.560	0.52	3.0	0	0.096	5.9	1.5

Table B-1: Parameters for the power converter output filter and inductive load for various circuits, as used in the simulations. Parameter names according to 4.1.
a: Corresponding to an SPS circuit.

Circuit	Magnet type	$N_{magnets}$	R_{tot} (Ω)	$L_{tot}(H)$	τ (s)
RD1.LR1	MBXW	12	0.78	1.740	2.23
RD34.LR3	MBW	12	0.74	2.160	2.90
RQ4.LR3	MQWA	10	0.45	0.280	0.62
RQ5.LR3	MQWA	11	0.45	0.280	0.62
RD1.LR5	MBXW	12	0.79	1.740	2.20
RD34.LR7	MBW	8	0.50	1.440	2.86
RQ4.LR7	MQWA	10	0.42	0.280	0.67
RQ5.LR7	MQWA	10	0.42	0.280	0.66

Table B-2: Normal conducting circuits in the insertions for which failures were simulated.

Circuit	Magnet type	$N_{magnets}$	R_{tot} (Ω)	$L_{tot}(H)$	τ (s)
RB.A12	MB	154	0.001	15.708	16028
RQD.A12	MQ	47	0.001	0.263	263
RQF.A12	MQ	47	0.001	0.263	263
RB.A23	MB	154	0.001	15.708	14437
RQD.A23	MQ	51	0.001	0.286	246
RQF.A23	MQ	51	0.001	0.286	262
RB.A34	MB	154	0.001	15.708	14280
RQD.A34	MQ	51	0.0008	0.286	357
RQF.A34	MQ	51	0.0008	0.286	340
RB.A45	MB	154	0.001	15.708	13778
RQD.A45	MQ	47	0.0008	0.263	313
RQF.A45	MQ	47	0.0009	0.263	302
RB.A56	MB	154	0.001	15.708	15771
RQD.A56	MQ	47	0.0007	0.263	399
RQF.A56	MQ	47	0.0007	0.263	360
RB.A67	MB	154	0.001	15.708	13425
RQD.A67	MQ	51	0.0008	0.286	348
RQF.A67	MQ	51	0.0009	0.286	325
RB.A78	MB	154	0.001	15.708	15103
RQD.A78	MQ	51	0.001	0.286	246
RQF.A78	MQ	51	0.001	0.286	272
RB.A81	MB	154	0.001	15.708	15309
RQD.A81	MQ	47	0.001	0.263	252
RQF.A81	MQ	47	0.001	0.263	250

Table B-3: Superconducting circuits in the arcs for which failures were simulated.

Circuit	Magnet type	$N_{magnets}$	R_{tot} (Ω)	$L_{tot}(H)$	τ (s)
RD2.L1	MBRC	1	0.0009	0.052	56
RQX.L1					
	MQXA	2	0.0005	0.218	426
	MQXB	2	0.0007	0.038	55
	MQXA	1	0.004	0.090	19
RQX.R1					
	MQXA	2	0.0005	0.218	436
	MQXB	2	0.0007	0.038	55
	MQXA	1	0.004	0.090	22
RD2.R1	MBRC	1	0.001	0.052	54
RD2.L2	MBRC	1	0.0008	0.052	65
RQX.L2					
	MQXA	2	0.0007	0.218	311
	MQXB	2	0.001	0.038	38
	MQXA	1	0.008	0.090	10
RD1.L2	MBX	1	0.0006	0.026	43
RQX.R2					
	MQXA	2	0.0007	0.218	320
	MQXB	2	0.001	0.038	38
	MQXA	1	0.002	0.090	50
RD1.R2	MBX	1	0.0006	0.026	44
RD2.R2	MBRC	1	0.0006	0.052	92
RD3.L4	MBRS	2	0.0007	0.052	76
RD4.L4	MBRB	1	0.0006	0.052	82
RD3.R4	MBRS	2	0.0007	0.052	76
RD4.R4	MBRB	1	0.0006	0.052	82
RD2.L5	MBRC	1	0.0009	0.052	56
RQX.L5					
	MQXA	2	0.0005	0.218	427
	MQXB	2	0.0007	0.038	55
	MQXA	1	0.005	0.090	20
RQX.R5					
	MQXA	2	0.0009	0.218	253
	MQXB	2	0.001	0.038	31
	MQXA	1	0.002	0.090	60
RD2.R5	MBRC	1	0.001	0.052	54
RD2.L8	MBRC	1	0.0006	0.052	88
RQX.L8					
	MQXA	2	0.0007	0.218	317
	MQXB	2	0.001	0.038	38
	MQXA	1	0.003	0.090	35
RQX.R8					
	MQXA	2	0.0007	0.218	331
	MQXB	2	0.0009	0.038	41
	MQXA	1	0.0009	0.090	98
RD2.R8	MBRC	1	0.0008	0.052	63

Table B-4: Superconducting circuits in the insertions for which failures were simulated.

Appendix C

Adaptation of the method of the moments for the calculation of A_f, σ and τ

The method of the moments [80] is used to estimate the parameters of a probability density function (pdf) from the values of the random variable distributed according to it. The method is based in equating the moments estimated from samples of the random variable with the unobservable population moments, and then solving those equations for the parameters to be estimated.

If f is the pdf of the distribution, its moments of order n are defined by

$$\mu_n = \int_{-\infty}^{\infty} x^n f(x) dx \tag{C-1}$$

An estimation of the n^{th} moment can also be obtained from the samples of the random variable:

$$\mu_n = \frac{1}{N} \sum_{i=1}^{N} x_i^n \tag{C-2}$$

where N is the total number of samples and x_i the value of each sample.

The calculation of the four first moments for $f(x) = A_f e^{-\frac{x^2}{2\sigma} - \frac{x^2}{\tau}}$ yields, after some algebraic manipulations

$$\mu_0 = \frac{A_f \sqrt{\pi}\sigma}{\sqrt{2}} e^{\frac{\sigma^2}{2\tau^2}} erfc\left(\frac{\sigma}{\sqrt{2}\tau}\right) = 1 \tag{C-3}$$

$$\mu_1 = \sigma^2 \left(A_f - \frac{1}{\tau}\mu_0\right) \tag{C-4}$$

$$\mu_2 = \sigma^2 \left(\mu_0 - \frac{1}{\tau}\mu_1\right) \tag{C-5}$$

$$\mu_3 = \sigma^2 \left(\mu_1 - \frac{1}{\tau}\mu_2\right) \tag{C-6}$$

This recurrent relationship among the moments is very convenient: equations C-4, C-5 and C-6 can be analytically solved for A_f, σ and τ, without having to deal with expressions such as C-3. The resolution yields:

$$A_f = \frac{2\mu_1\mu_2 - \mu_1^3 - \mu_3}{\mu_2^2 - \mu_1\mu_3} \tag{C-7}$$

$$\sigma = \sqrt{\frac{\mu_2^2 - \mu_1\mu_3}{\mu_2 - \mu_1^2}} \tag{C-8}$$

$$\tau = \frac{\mu_2^2 - \mu_1\mu_3}{\mu_1\mu_2 - \mu_3} \tag{C-9}$$

However, it has been found that this estimation tends to underestimate $f(x)$ for small values of x. A better result can be obtained if A_f is set to a convenient value and then σ and τ are calculated from C-4 and C-5.

To find an appropriate value for A_f the method of the moments is applied to $g(x) = A_g^{-\frac{x^2}{2\sigma_g}}$ and $e(x) = A_e^{-\frac{x}{\tau_e}}$. This yields:

$$A_e = \frac{1}{\mu_1} \tag{C-10}$$

$$A_g = \frac{2}{\pi\mu_1} \tag{C-11}$$

and setting $A_f = \frac{A_e + A_g}{2}$ we obtain from C-4 and C-5 the expressions that we used to define the parameters for $f(x)$.

$$A_f = \frac{1}{2\mu_1}\left(1 + \frac{2}{\pi}\right) \tag{C-12}$$

$$\sigma = \sqrt{\frac{2\mu_1^2\left(\mu_1^2 - \mu_2\right)}{\frac{2}{\pi}\mu_1^2 - \left(1 + \frac{2}{\pi}\right)\mu_2}} \tag{C-13}$$

$$\tau = \frac{2\mu_1\left(\mu_1^2 - \mu_2\right)}{2\mu_1^2 - \left(1 + \frac{2}{\pi}\right)\mu_2} \tag{C-14}$$

Appendix D

Additional figures for secondary losses

This appendix contains various figures of data concerning the secondary losses that complete the particular cases that were presented in the corresponding chapter.

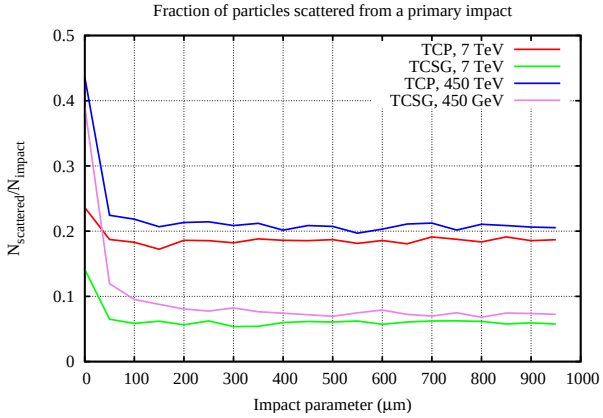

Figure D-1: Fraction of scattered particles for a primary and a secondary collimator at injection and collision energies.

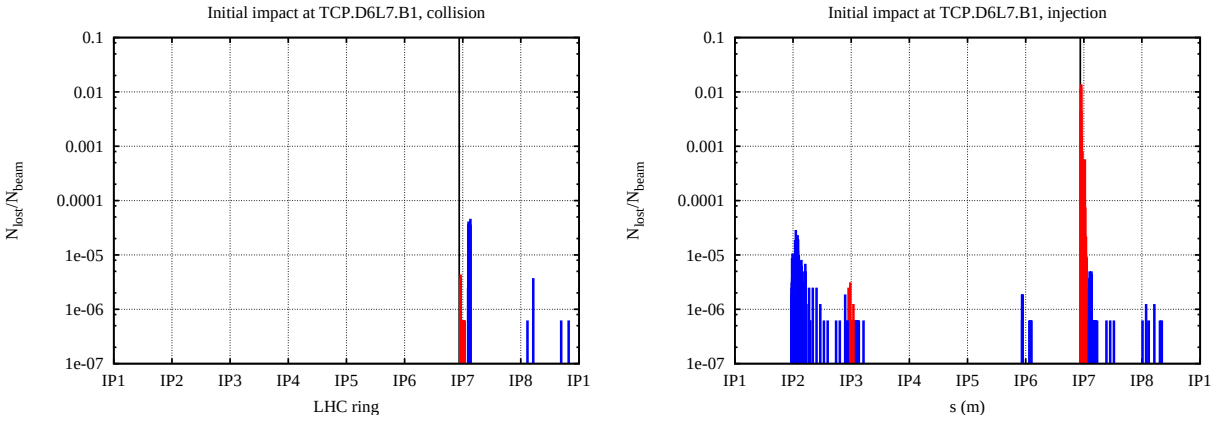

Figure D-2: Longitudinal distribution of the secondary losses after a primary impact at TCP.D6L7.B1.

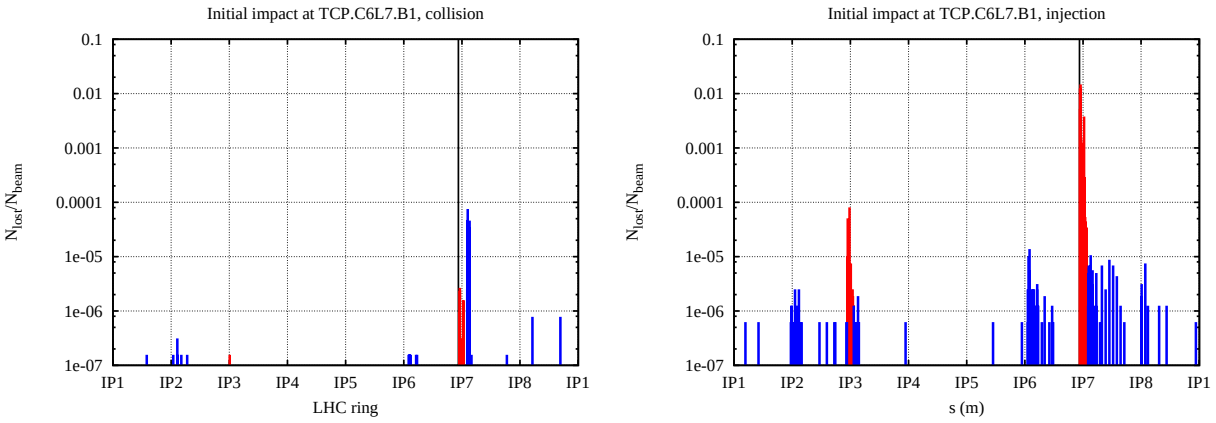

Figure D-3: Longitudinal distribution of the secondary losses after a primary impact at TCP.C6L7.B1.

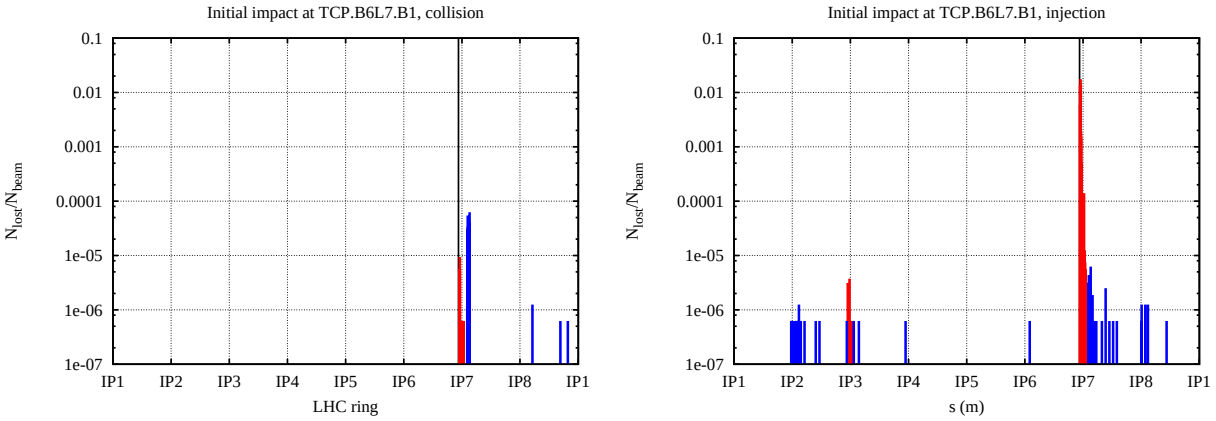

Figure D-4: Longitudinal distribution of the secondary losses after a primary impact at TCP.B6L7.B1.

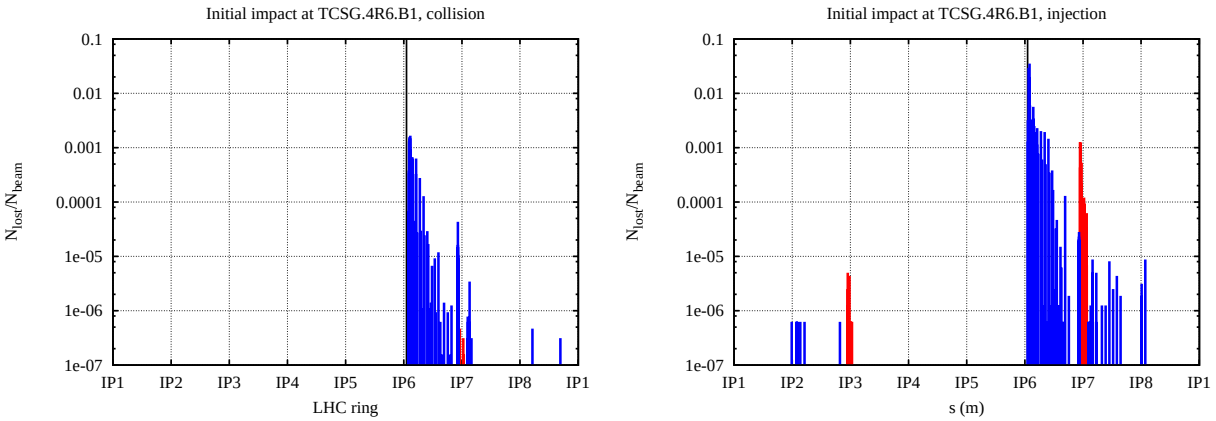

Figure D-5: Longitudinal distribution of the secondary losses after a primary impact at TCSG.4R6.B1.

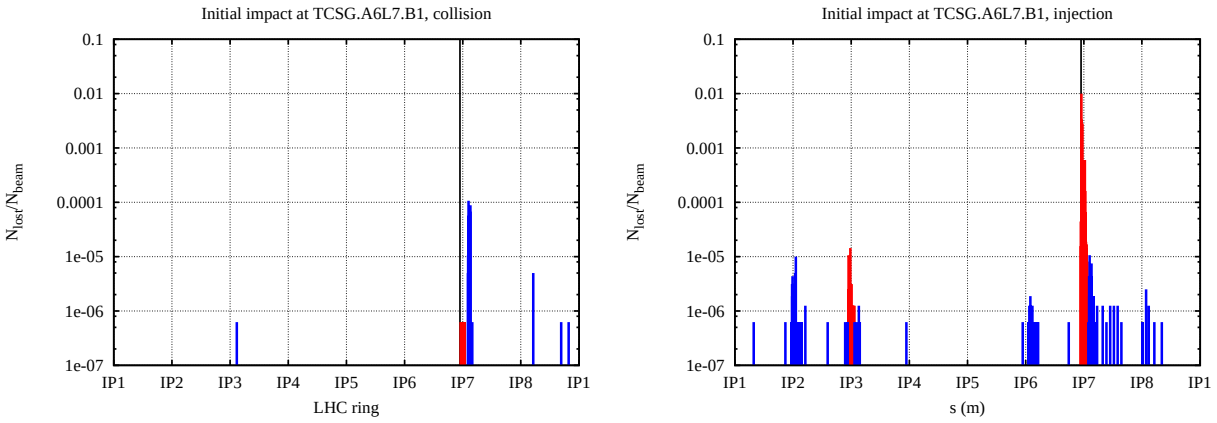

Figure D-6: Longitudinal distribution of the secondary losses after a primary impact at TCSG.A6L7.B1.

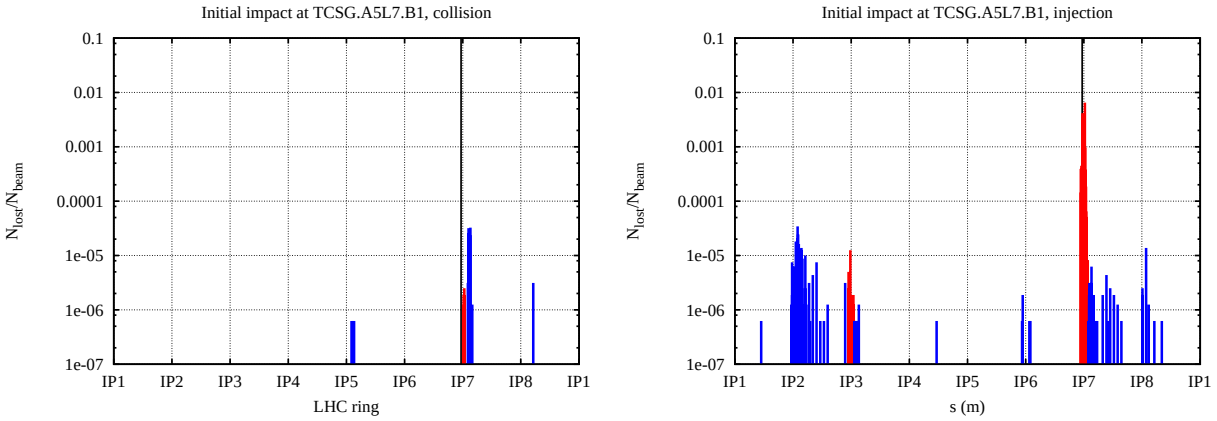

Figure D-7: Longitudinal distribution of the secondary losses after a primary impact at TCSG.A5L7.B1.

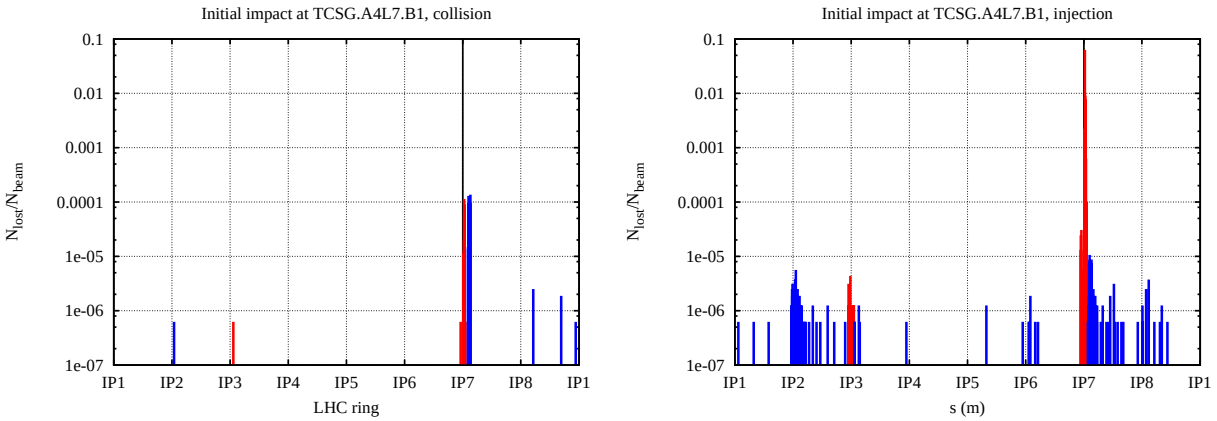

Figure D-8: Longitudinal distribution of the secondary losses after a primary impact at TCSG.A4L7.B1.

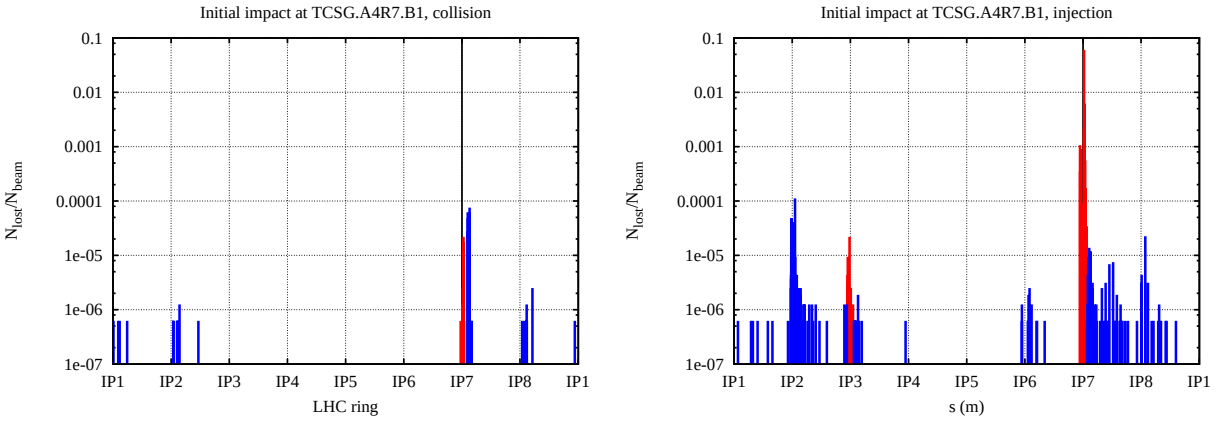

Figure D-9: Longitudinal distribution of the secondary losses after a primary impact at TCSG.A4R7.B1.

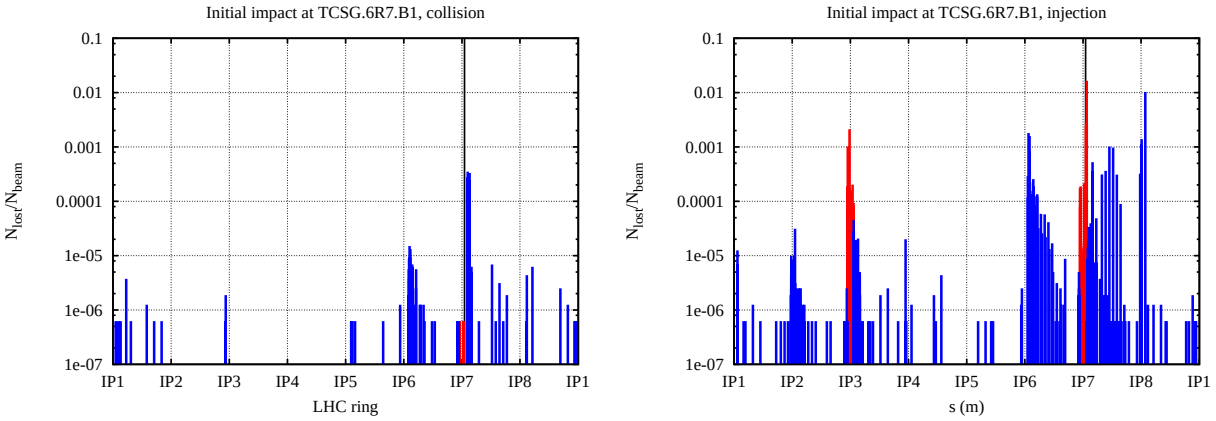

Figure D-10: Longitudinal distribution of the secondary losses after a primary impact at TCSG.6R7.B1.

Appendix E

Simulation output data

The tables on this appendix summarize the results of the simulations for a range of LHC failures. For detailed explanations, see chapter 7.

Global Quantities										
Magnet	Energy	Failure	N_{loc}	dN_{max} (frac./tr)	τ_1 (ms)	τ_{Quench} (ms)	τ_{dam} (ms)	τ_{det} (ms)	BLM	QPS
MB.A25R1	7 TeV	Quench	8	0.029	28.2	9.1	18.3	17.3	YES	YES
MB.A25R2	7 TeV	Quench	6	0.044	21.2	5.1	14.6	13.9	YES	NO
MB.A25R3	7 TeV	Quench	3	0.028	23.8	12.6	15.4	13.6	YES	YES
MB.A25R4	7 TeV	Quench	7	0.038	19.6	11.7	13.1	11.7	YES	NO
MB.A25R5	7 TeV	Quench	12	0.032	26.7	8.2	18.3	16.3	YES	YES
MB.A25R6	7 TeV	Quench	9	0.037	22.1	14.9	14.9	12.1	YES	NO
MB.A25R7	7 TeV	Quench	9	0.026	27.9	15.1	18.3	15.9	YES	YES
MB.A25R8	7 TeV	Quench	7	0.040	18.7	10.4	12.5	10.7	YES	NO

Table E-1: Summary of the global data obtained for the considered failures at the main dipoles in the arc, beam 1.

Local Quantities									
Magnet	Energy	Failure	Collimator	F_{lost}	τ_{det} (ms)	ξ_{max} (mm^{-1})	$\langle\alpha\rangle$ (mm)	$\sigma_{loss}/\sigma_{beam}$	BLM
MB.A25R1	7 TeV	Quench	TCSG.6R7	0.785	17.7	12.68	0.051	0.211	YES
			TCSG.4R6	0.095	21.3	3.41	0.023	0.085	NO
MB.A25R2	7 TeV	Quench	TCSG.6R7	0.999	13.9	11.73	0.070	0.290	YES
			TCP.B6L7	0.001	18.6	0.01	0.020	0.018	NO
MB.A25R3	7 TeV	Quench	TCP.C6L7	0.987	13.6	22.06	0.037	0.257	YES
			TCP.B6L7	0.013	15.2	0.39	0.027	0.023	YES
MB.A25R4	7 TeV	Quench	TCP.C6L7	0.985	11.7	18.50	0.044	0.256	YES
			TCP.B6L7	0.012	13.2	0.35	0.029	0.241	NO
MB.A25R5	7 TeV	Quench	TCSG.4R6	0.793	16.7	9.66	0.067	0.233	YES
			TCSG.A5L7	0.069	17.3	1.65	0.034	0.243	YES
MB.A25R6	7 TeV	Quench	TCSG.A5L7	0.495	12.1	11.92	0.034	0.211	YES
			TCSG.6R7	0.101	14.5	1.77	0.047	0.216	YES
MB.A25R7	7 TeV	Quench	TCP.C6L7	0.666	15.9	17.73	0.031	0.212	YES
			TCSG.A5L7	0.015	20.1	1.09	0.011	0.058	NO
MB.A25R8	7 TeV	Quench	TCP.C6L7	0.989	10.7	17.88	0.045	0.274	YES
			TCP.B6L7	0.011	13.4	0.32	0.028	0.249	NO

Table E-2: Summary of the local data in the two most affected collimators for each case, obtained for the considered failures at the main dipoles in the arc, beam 1.

Global Quantities										
Magnet	Energy	Failure	N_{loc}	dN_{max} (frac./tr)	τ_1 (ms)	τ_{Quench} (ms)	τ_{dam} (ms)	τ_{det} (ms)	BLM	QPS
MB.A25R1	7 TeV	Quench	6	0.042	19.5	4.7	13.4	11.7	YES	NO
MB.A25R2	7 TeV	Quench	3	0.027	24.7	13.1	15.8	13.4	YES	YES
MB.A25R3	7 TeV	Quench	12	0.044	19.1	3.7	13.2	11.9	YES	NO
MB.A25R4	7 TeV	Quench	6	0.031	26.2	7.8	17.0	14.8	YES	YES
MB.A25R5	7 TeV	Quench	6	0.037	19.0	10.6	12.5	10.7	YES	NO
MB.A25R6	7 TeV	Quench	4	0.028	24.5	13.6	16.2	14.0	YES	YES
MB.A25R7	7 TeV	Quench	12	0.044	19.8	4.8	14.0	12.9	YES	NO
MB.A25R8	7 TeV	Quench	6	0.028	28.0	8.6	18.2	15.9	YES	YES

Table E-3: Summary of the global data obtained for the considered failures at the main dipoles in the arc, beam 2.

Local Quantities									
Magnet	Energy	Failure	Collimator	F_{lost}	τ_{det} (ms)	ξ_{max} (mm^{-1})	$\langle\alpha\rangle$ (mm)	$\sigma_{loss}/\sigma_{beam}$	BLM
MB.A25R1	7 TeV	Quench	TCSG.6L7	0.992	12.8	10.51	0.077	0.322	YES
			TCP.C6R7	0.005	11.7	0.18	0.023	0.164	YES
MB.A25R2	7 TeV	Quench	TCP.C6R7	0.989	13.4	21.04	0.038	0.245	YES
			TCP.B6R7	0.011	17.2	0.29	0.030	0.260	NO
MB.A25R3	7 TeV	Quench	TCSG.4L6	0.904	12.4	7.55	0.088	0.348	YES
			TCSG.A5R7	0.028	11.9	0.57	0.040	0.269	YES
MB.A25R4	7 TeV	Quench	TCSG.6L7	0.999	14.8	12.64	0.065	0.260	YES
			TCP.B6R7	0.001	21.9	0.01	0.029	0.172	NO
MB.A25R5	7 TeV	Quench	TCP.C6R7	0.991	10.7	16.88	0.048	0.286	YES
			TCP.B6R7	0.009	13.3	0.22	0.033	0.277	NO
MB.A25R6	7 TeV	Quench	TCP.C6R7	0.990	14.0	20.18	0.040	0.240	YES
			TCP.B6R7	0.010	17.5	0.27	0.029	0.270	NO
MB.A25R7	7 TeV	Quench	TCSG.4L6	0.897	13.3	7.52	0.088	0.347	YES
			TCSG.A5R7	0.032	14.7	0.70	0.037	0.258	NO
MB.A25R8	7 TeV	Quench	TCSG.6L7	0.937	15.9	12.65	0.061	0.246	YES
			TCSG.A5R7	0.042	18.5	0.95	0.036	0.263	NO

Table E-4: Summary of the local data in the two most affected collimators for each case, obtained for the considered failures at the main dipoles in the arc, beam 2.

Global Quantities										
Magnet	Energy	Failure	N_{loc}	dN_{max} (frac./tr)	τ_1 (ms)	τ_{Quench} (ms)	τ_{dam} (ms)	τ_{det} (ms)	BLM	QPS
MQ.24R1	7 TeV	Quench	9	0.001	> 250	164.4	198.6	164.5	YES	YES
MQ.24R2	7 TeV	Quench	5	0.028	217.2	185.3	183.1	174.8	YES	YES
MQ.24R3	7 TeV	Quench	10	0.001	> 250	171.8	170.3	168.7	YES	YES
MQ.24R4	7 TeV	Quench	3	0.001	> 250	170.6	199.6	179.6	YES	YES
MQ.24R5	7 TeV	Quench	8	0.042	231.2	168.2	168.4	164.2	YES	YES
MQ.24R6	7 TeV	Quench	5	0.025	216.4	191.3	192.7	182.7	YES	YES
MQ.24R7	7 TeV	Quench	5	0.034	231.1	167.4	169.8	164.3	YES	YES
MQ.24R8	7 TeV	Quench	3	0.025	216.7	163.0	182.3	163.0	YES	YES
MQ.25R1	7 TeV	Quench	10	0.037	216.4	182.1	187.5	168.6	YES	YES
MQ.25R2	7 TeV	Quench	8	0.002	> 250	169.7	167.5	162.1	YES	YES
MQ.25R3	7 TeV	Quench	3	0.022	216.5	168.7	187.1	168.7	YES	YES
MQ.25R4	7 TeV	Quench	9	0.003	> 250	167.9	167.2	163.0	YES	YES
MQ.25R5	7 TeV	Quench	11	0.023	216.3	196.2	192.3	174.2	YES	YES
MQ.25R6	7 TeV	Quench	8	0.043	228.6	167.3	168.4	164.1	YES	YES
MQ.25R7	7 TeV	Quench	3	0.028	216.5	165.7	183.8	165.7	YES	YES
MQ.25R8	7 TeV	Quench	9	0.037	229.3	165.8	167.2	162.2	YES	YES

Table E-5: Summary of the global data obtained for the considered failures at the main quadrupoles in the arc, beam 1.

Local Quantities									
Magnet	Energy	Failure	Collimator	F_{lost}	τ_{det} (ms)	ξ_{max} (mm^{-1})	$\langle\alpha\rangle$ (mm)	$\sigma_{loss}/\sigma_{beam}$	BLM
MQ.24R1	7 TeV	Quench	TCSG.A4L7	0.001	171.1	-	-	-	YES
			TCSG.A4R7	0.001	170.5	-	0.924	-	YES
MQ.24R2	7 TeV	Quench	TCSG.6R7	0.999	174.8	4.01	0.201	0.735	YES
			TCSG.A5L7	0.001	214.0	-	0.026	-	NO
MQ.24R3	7 TeV	Quench	TCP.D6L7	0.002	216.6	0.20	0.010	0.096	NO
			TCSG.A6L7	0.001	193.6	-	0.034	-	YES
MQ.24R4	7 TeV	Quench	TCP.C6L7	0.043	179.6	1.22	0.029	0.193	YES
			TCP.B6L7	0.002	204.2	0.03	0.025	0.180	NO
MQ.24R5	7 TeV	Quench	TCSG.A4R7	0.555	171.6	3.39	0.132	0.936	YES
			TCSG.A4L7	0.326	171.2	2.61	0.104	0.838	YES
MQ.24R6	7 TeV	Quench	TCSG.A5L7	0.979	182.7	3.29	0.220	1.32	YES
			TCTH.4L8	0.016	∼210	0.46	0.029	0.392	NO
MQ.24R7	7 TeV	Quench	TCP.D6L7	0.961	185.7	12.63	0.058	0.576	NO
			TCP.B6L7	0.027	167.4	0.42	0.051	0.512	YES
MQ.24R8	7 TeV	Quench	TCP.C6L7	0.996	163.0	6.96	0.121	0.684	YES
			TCP.B6L7	0.005	190.7	0.11	0.032	0.307	NO
MQ.25R1	7 TeV	Quench	TCSG.4R6	0.502	181.6	4.28	0.096	0.281	YES
			TCDQA.4R6	0.261	206.1	1.50	0.143	0.559	NO
MQ.25R2	7 TeV	Quench	TCSG.A4R7	0.016	201.2	0.26	0.050	0.370	NO
			TCP.C6L7	0.010	162.1	0.52	0.015	0.086	YES
MQ.25R3	7 TeV	Quench	TCP.C6L7	0.971	168.7	6.41	0.122	0.651	YES
			TCP.B6L7	0.018	178.3	0.29	0.049	0.472	YES
MQ.25R4	7 TeV	Quench	TCSG.A4R7	0.027	170.5	0.35	0.063	0.468	YES
			TCSG.A4L7	0.017	170.2	0.25	0.056	0.436	YES
MQ.25R5	7 TeV	Quench	TCSG.4R6	0.465	183.3	3.71	0.103	0.258	YES
			TCDQA.4R6	0.304	206.0	1.35	0.184	0.716	NO
MQ.25R6	7 TeV	Quench	TCSG.A4R7	0.519	171.0	2.59	0.161	1.81	YES
			TCSG.A4L7	0.346	169.1	2.79	0.097	0.822	YES
MQ.25R7	7 TeV	Quench	TCP.C6L7	0.997	165.7	8.19	0.100	0.813	YES
			TCP.B6L7	0.004	188.7	0.08	0.033	0.332	NO
MQ.25R8	7 TeV	Quench	TCP.D6L7	0.930	189.0	10.63	0.058	0.561	NO
			TCP.B6L7	0.033	165.7	0.47	0.058	0.571	YES

Table E-6: Summary of the local data in the two most affected collimators for each case, obtained for the considered failures at the main quadrupoles in the arc, beam 1.

Global Quantities										
Magnet	Energy	Failure	N_{loc}	dN_{max} (frac./tr)	τ_1 (ms)	τ_{Quench} (ms)	τ_{dam} (ms)	τ_{det} (ms)	BLM	QPS
MQ.24R1	7 TeV	Quench	3	0.038	216.4	183.4	199.7	168.7	YES	YES
MQ.24R2	7 TeV	Quench	7	0.002	$>$ 250	172.2	197.8	171.2	YES	YES
MQ.24R3	7 TeV	Quench	15	0.041	217.2	178.9	192.2	178.4	YES	YES
MQ.24R4	7 TeV	Quench	4	0.002	$>$ 250	172.2	192.3	168.4	YES	YES
MQ.24R5	7 TeV	Quench	3	0.049	101.3	89.0	92.8	89.0	YES	YES
MQ.24R6	7 TeV	Quench	9	0.058	110.4	103.2	103.4	102.0	YES	YES
MQ.24R7	7 TeV	Quench	12	0.051	102.2	94.7	93.7	92.3	YES	YES
MQ.24R8	7 TeV	Quench	11	0.061	110.3	103.9	104.4	103.2	YES	YES
MQ.25R1	7 TeV	Quench	9	0.003	$>$ 250	206.1	207.7	184.5	YES	YES
MQ.25R2	7 TeV	Quench	3	0.024	216.0	154.6	178.7	154.6	YES	YES
MQ.25R3	7 TeV	Quench	7	0.009	$>$ 250	197.8	200.3	166.7	YES	YES
MQ.25R4	7 TeV	Quench	3	0.034	216.6	169.3	188.8	174.8	YES	YES
MQ.25R5	7 TeV	Quench	13	0.056	108.0	100.7	100.7	99.6	YES	YES
MQ.25R6	7 TeV	Quench	7	0.054	102.6	95.1	96.1	94.6	YES	YES
MQ.25R7	7 TeV	Quench	5	0.050	105.1	94.3	97.5	94.2	YES	YES
MQ.25R8	7 TeV	Quench	3	0.052	101.6	94.3	93.3	91.8	YES	YES

Table E-7: Summary of the global data obtained for the considered failures at the main quadrupoles in the arc, beam 2.

Local Quantities									
Magnet	Energy	Failure	Collimator	F_{lost}	τ_{det} (ms)	ξ_{max} (mm^{-1})	$\langle\alpha\rangle$ (mm)	$\sigma_{loss}/\sigma_{beam}$	BLM
MQ.24R1	7 TeV	Quench	TCSG.6L7	0.111	168.7	0.01	8.3	0	YES
			TCP.B6R7	0.000	-	-	-	-	NO
MQ.24R2	7 TeV	Quench	TCP.D6R7	0.079	171.2	5.50	0.006	0.046	YES
			TCP.B6R7	0.005	173.3	0.12	0.027	0.239	YES
MQ.24R3	7 TeV	Quench	TCSG.4L6	0.546	184.8	4.01	0.111	0.253	YES
			TCDQA.4L6	0.102	210.4	0.70	0.117	0.207	NO
MQ.24R4	7 TeV	Quench	TCP.D6R7	0.046	168.4	7.64	0.005	0.037	YES
			TCP.D6R7	0.057	181.1	3.85	0.012	0.124	YES
MQ.24R5	7 TeV	Quench	TCP.B6R7	0.008	94.3	0.12	0.047	0.498	NO
			TCP.C6R7	0.993	89.0	6.89	0.120	0.637	YES
MQ.24R6	7 TeV	Quench	TCP.D6R7	0.967	104.0	10.00	0.079	0.641	NO
			TCSG.A4L7.	0.016	102.0	0.21	0.058	0.436	YES
MQ.24R7	7 TeV	Quench	TCSG.4L6	0.449	93.2	3.16	0.122	0.288	YES
			TCDQA.4L6	0.241	95.1	1.06	0.189	0.483	NO
MQ.24R8	7 TeV	Quench	TCSG.A4L7	0.616	104.0	3.15	0.162	1.01	NO
			TCSG.A4R7	0.333	104.3	2.59	0.102	0.797	NO
MQ.25R1	7 TeV	Quench	TCP.D6R7	0.033	210.0	1.05	0.026	0.257	NO
			TCSG.A4L7	0.013	200.4	0.22	0.048	0.369	YES
MQ.25R2	7 TeV	Quench	TCP.C6R7	0.997	154.6	8.04	0.104	0.791	YES
			TCP.B6R7	0.004	190.3	0.07	0.033	0.327	NO
MQ.25R3	7 TeV	Quench	TCSG.A4L7	0.131	166.7	1.09	0.083	0.621	YES
			TCSG.A4R7	0.001	218.4	0.03	0.043	0.250	NO
MQ.25R4	7 TeV	Quench	TCP.C6R7	0.994	174.8	8.60	0.095	0.778	YES
			TCP.B6R7	0.007	196.4	0.15	0.036	0.316	NO
MQ25R5	7 TeV	Quench	TCSG.A6R7	0.838	99.6	4.30	0.142	0.776	YES
			TCP.D6R7	0.049	101.5	3.45	0.012	0.088	NO
MQ25R6	7 TeV	Quench	TCP.C6R7	0.994	95.3	6.47	0.135	0.616	YES
			TCP.B6R7	0.003	97.0	0.06	0.046	0.419	NO
MQ25R7	7 TeV	Quench	TCP.D6R7	0.994	94.2	11.18	0.067	0.603	YES
			TCP.B6R7	0.006	98.0	0.08	0.054	0.505	NO
MQ25R8	7 TeV	Quench	TCSG.6L7	1.000	91.8	4.13	0.203	0.627	YES
			-	-	-	-	-	-	-

Table E-8: Summary of the local data in the two most affected collimators for each case, obtained for the considered failures at the main quadrupoles in the arc, beam 2.

Global Quantities										
Magnet	Energy	Failure	N_{loc}	dN_{max} (frac./tr)	τ_1 (ms)	τ_{Quench} (ms)	τ_{dam} (ms)	τ_{det} (ms)	BLM	QPS
RQX.L1	7 TeV	Quench	11	0.036	31.2	19.8	22.6	21.9	YES	YES
RQX.L2	7 TeV	Quench	8	0.009	71.5	43.7	47.6	41.4	YES	YES
RQX.L5	7 TeV	Quench	6	0.035	24.7	14.6	17.0	15.5	YES	YES
RQX.L8	7 TeV	Quench	8	0.013	61.3	37.6	41.8	40.1	YES	YES
RQX.R1	7 TeV	Quench	12	0.043	28.7	20.3	22.0	19.0	YES	YES
RQX.R2	7 TeV	Quench	5	0.008	84.0	55.8	55.4	47.4	YES	YES
RQX.R5	7 TeV	Quench	7	0.030	27.7	17.0	19.1	17.0	YES	YES
RQX.R8	7 TeV	Quench	6	0.016	49.6	31.9	33.4	29.4	YES	YES

Table E-9: Summary of the global data obtained for the considered failures at the most critical insertion quadrupoles, beam 1.

Local Quantities									
Magnet	Energy	Failure	Collimator	F_{lost}	τ_{det} (ms)	ξ_{max} (mm^{-1})	$\langle\alpha\rangle$ (mm)	$\sigma_{loss}/\sigma_{beam}$	BLM
RQX.L1	7 TeV	Quench	TCSG.A4L7	0.999	21.9	7.70	0.103	0.816	YES
			TCSG.A4R7	0.001	23.0	0.00	0.012	0.00	NO
RQX.L2	7 TeV	Quench	TCP.D6L7.	0.841	41.4	64.31	0.007	0.049	YES
			TCP.B6L7	0.055	44.1	1.98	0.023	0.187	YES
RQX.L5	7 TeV	Quench	TCP.C6L7	0.998	15.5	13.73	0.059	0.371	YES
			TCP.B6L7	0.003	19.2	0.07	0.027	0.246	NO
RQX.L8	7 TeV	Quench	TCSG.4R6	0.910	40.1	18.12	0.034	0.107	YES
			TCSG.A4L7	0.065	41.0	2.35	0.022	0.162	YES
RQX.R1	7 TeV	Quench	TCSG.A4R7	0.396	19.0	6.18	0.052	0.368	YES
			TCSG.A6L7	0.283	21.7	5.62	0.041	0.300	NO
RQX.R2	7 TeV	Quench	TCP.D6L7	0.999	47.4	44.76	0.009	0.080	YES
			TCP.B6L7	0.001	63.6	0.02	0.023	0.176	NO
RQX.R5	7 TeV	Quench	TCP.C6L7	0.992	17.0	15.26	0.053	0.334	YES
			TCSG.A4R7	0.008	18.9	0.12	0.051	0.387	NO
RQX.R8	7 TeV	Quench	TCSG.4R6	0.650	32.9	12.56	0.042	0.132	YES
			TCSG.A5L7	0.175	29.4	3.19	0.045	0.313	YES

Table E-10: Summary of the local data in the two most affected collimators for each case, obtained for the considered failures at the most critical insertion quadrupoles, beam 1.

Global Quantities										
Magnet	Energy	Failure	N_{loc}	dN_{max} (frac./tr)	τ_1 (ms)	τ_{Quench} (ms)	τ_{dam} (ms)	τ_{det} (ms)	BLM	QPS
RQX.L1	7 TeV	Quench	9	0.101	26.3	22.3	22.8	20.7	YES	YES
RQX.L2	7 TeV	Quench	5	0.030	91.5	59.4	65.8	58.2	YES	YES
RQX.L5	7 TeV	Quench	9	0.096	26.4	22.3	22.8	21.9	YES	YES
RQX.L8	7 TeV	Quench	3	0.015	48.1	29.7	30.8	26.9	YES	YES
RQX.R1	7 TeV	Quench	13	0.099	27.4	23.3	23.1	22.5	YES	YES
RQX.R2	7 TeV	Quench	6	0.008	91.4	51.2	59.3	50.6	YES	YES
RQX.R5	7 TeV	Quench	9	0.086	27.3	21.1	22.7	21.0	YES	YES
RQX.R8	7 TeV	Quench	3	0.010	64.6	41.9	40.4	35.8	YES	YES

Table E-11: Summary of the global data obtained for the considered failures at the most critical insertion quadrupoles, beam 2.

Local Quantities									
Magnet	Energy	Failure	Collimator	F_{lost}	τ_{det} (ms)	ξ_{max} (mm^{-1})	$\langle\alpha\rangle$ (mm)	$\sigma_{loss}/\sigma_{beam}$	BLM
RQX.L1	7 TeV	Quench	TCSG.A4L7	0.505	20.7	2.29	0.182	1.23	YES
			TCSG.A4R7	0.445	22.4	1.54	0.238	1.78	NO
RQX.L2	7 TeV	Quench	TCP.B6R7	0.873	58.2	7.58	0.094	0.968	YES
			TCP.C6R7	0.102	86.9	0.56	0.148	1.01	NO
RQX.L5	7 TeV	Quench	TCP.D6R7	0.926	21.9	4.37	0.163	1.22	YES
			TCP.B6R7	0.060	22.0	0.55	0.088	0.789	YES
RQX.L8	7 TeV	Quench	TCP.C6R7	0.987	26.9	55.87	0.014	0.057	YES
			TCP.B6R7	0.014	34.1	1.35	0.008	0.066	NO
RQX.R1	7 TeV	Quench	TCSG.6L7	0.980	22.5	2.07	0.395	1.63	YES
			TCP.B6R7	0.012	25.1	0.15	0.067	0.655	NO
RQX.R2	7 TeV	Quench	TCP.D6R7	0.970	50.6	109.34	0.005	0.035	YES
			TCP.B6R7	0.026	53.8	0.90	0.022	0.176	YES
RQX.R5	7 TeV	Quench	TCP.C6R7	0.901	21.0	2.27	0.325	2.47	YES
			TCP.B6R7	0.022	22.2	0.21	0.081	0.785	YES
RQX.R8	7 TeV	Quench	TCP.C6R7	0.976	35.8	62.90	0.013	0.062	YES
			TCP.B6R7	0.025	42.1	0.77	0.026	0.226	NO

Table E-12: Summary of the local data in the two most affected collimators for each case, obtained for the considered failures at the most critical insertion quadrupoles, beam 2.

Global Quantities										
Magnet	Energy	Failure	N_{loc}	dN_{max} (frac./tr)	τ_1 (ms)	τ_{Quench} (ms)	τ_{dam} (ms)	τ_{det} (ms)	BLM	FMCM
RQ4.LR3	450 GeV	V_{max}	23	0.131	8.9	6.1	6.4	6.0	YES	YES
RQ4.LR7	450 GeV	V_{max}	20	0.117	7.9	5.8	5.7	4.9	YES	YES
RQ5.LR3	450 GeV	V_{max}	11	0.106	10.3	7.2	7.4	5.7	YES	YES
RQ5.LR7	450 GeV	V_{max}	31	0.129	10.5	7.5	7.9	6.3	YES	YES

Table E-13: Summary of the global data obtained for the considered failures at the most critical insertion dipoles, beam 2.

Local Quantities									
Magnet	Energy	Failure	Collimator	F_{lost}	τ_{det} (ms)	ξ_{max} (mm^{-1})	$\langle\alpha\rangle$ (mm)	$\sigma_{loss}/\sigma_{beam}$	BLM
RQ4.LR3	450 GeV	V_{max}	TDI.4L2	0.401	6.4	0.68	0.482	1.35	NO
			TCTV.4L2.	0.282	6.1	0.25	0.931	1.62	NO
RQ4.LR7	450 GeV	V_{max}	TDI.4L2	0.377	6.0	0.48	0.636	1.89	NO
			TCP.D6L7	0.310	4.9	0.85	0.302	0.686	YES
RQ5.LR3	450 GeV	V_{max}	TCP.D6L7	0.289	6.3	0.62	0.383	0.965	YES
			TCSG.A5L7	0.273	5.7	0.34	0.647	1.05	YES
RQ5.LR7	450 GeV	V_{max}	TCSG.A5L7	0.448	6.3	0.46	0.798	1.28	YES
			TCSG.4R3	0.176	7.9	0.40	0.356	1.43	NO

Table E-14: Summary of the local data in the two most affected collimators for each case, obtained for the considered failures at the most critical insertion dipoles, beam 2.

Global Quantities										
Magnet	Energy	Failure	N_{loc}	dN_{max} (frac./tr)	τ_1 (ms)	τ_{Quench} (ms)	τ_{dam} (ms)	τ_{det} (ms)	BLM	FMCM
RQ4.LR3	450 GeV	V_{max}	15	0.033	20.2	14.7	10.5	6.9	YES	YES
RQ4.LR7	450 GeV	V_{max}	14	0.051	18.4	10.8	11.9	9.8	YES	YES
RQ5.LR3	450 GeV	V_{max}	10	0.102	10.9	8.3	7.6	6.2	YES	YES
RQ5.LR7	450 GeV	V_{max}	11	0.093	9.7	9.2	7.1	5.5	YES	YES

Table E-15: Summary of the global data obtained for the considered failures at the most critical insertion dipoles, beam 2.

Local Quantities									
Magnet	Energy	Failure	Collimator	F_{lost}	τ_{det} (ms)	ξ_{max} (mm^{-1})	$\langle\alpha\rangle$ (mm)	$\sigma_{loss}/\sigma_{beam}$	BLM
RQ4.LR3	450 GeV	V_{max}	TCP.D6R7	0.297	6.9	2.28	0.112	0.182	YES
			TCSG.4L6	0.226	13.8	0.21	0.901	0.625	NO
RQ4.LR7	450 GeV	V_{max}	TCSG.4L6	0.662	9.8	0.63	0.864	0.765	YES
			TCDQA.4L6	0.221	14.5	0.16	1.19	0.882	NO
RQ5.LR3	450 GeV	V_{max}	TCSG.6L7	0.999	6.2	0.71	1.21	1.10	YES
			TCSG.A5R7	0.001	10.2	0.00	0.306	0.352	NO
RQ5.LR7	450 GeV	V_{max}	TCP.C6R7	0.985	5.5	1.21	0.669	1.08	YES
			TCP.B6R7.	0.010	7.3	0.03	0.226	0.491	NO

Table E-16: Summary of the local data in the two most affected collimators for each case, obtained for the considered failures at the most critical insertion dipoles, beam 2.

Global Quantities										
Magnet	Energy	Failure	N_{loc}	dN_{max}	τ_1	τ_{Quench}	τ_{dam}	τ_{det}	BLM	QPS/PIC
RD1.L2	7 TeV	Quench	6	0.046	15.8	8.7	10.4	9.0	YES	NO
RD1.L2	450 GeV	V_{max}	3	0.015	21.7	9.4	11.2	7.7	YES	YES
RD1.L8	7 TeV	Quench	11	0.052	17.4	11.8	11.7	10.7	YES	NO
RD1.L8	450 GeV	V_{max}	9	0.016	25.0	10.8	12.7	9.8	YES	YES
RD1.R2	7 TeV	Quench	6	0.036	19.5	11.0	12.8	11.3	YES	NO
RD1.R2	450 GeV	V_{max}	3	0.011	30.2	10.2	15.6	10.6	YES	YES
RD1.R8	7 TeV	Quench	12	0.040	21.4	14.6	14.6	13.3	YES	NO
RD1.R8	450 GeV	V_{max}	8	0.011	37.8	15.8	19.2	14.5	YES	YES
RD2.L1	7 TeV	Quench	8	0.064	11.4	6.8	7.8	6.8	YES	NO
RD2.L2	7 TeV	Quench	12	0.037	23.3	16.6	16.4	15.5	YES	YES
RD2.L5	7 TeV	Quench	7	0.072	10.4	6.1	6.9	6.1	YES	NO
RD2.L8	7 TeV	Quench	6	0.035	23.7	7.2	15.5	14.8	YES	YES
RD2.R1	7 TeV	Quench	6	0.048	14.9	8.7	10.0	8.8	YES	NO
RD2.R2	7 TeV	Quench	6	0.039	21.4	14.8	14.5	13.7	YES	NO
RD2.R5	7 TeV	Quench	4	0.051	14.2	8.1	9.3	8.3	YES	NO
RD2.R8	7 TeV	Quench	3	0.034	19.9	11.6	13.2	11.6	YES	NO
RD3.L4	7 TeV	Quench	3	0.051	14.2	8.4	9.4	8.5	YES	NO
RD3.R4	7 TeV	Quench	6	0.047	17.4	11.8	11.7	10.9	YES	NO
RD4.L4	7 TeV	Quench	5	0.059	12.3	7.1	8.2	7.1	YES	NO
RD4.R4	7 TeV	Quench	13	0.044	18.2	12.6	12.5	11.3	YES	NO

Table E-17: Summary of the global data obtained for the considered failures at the most critical insertion dipoles, beam 1.

Local Quantities									
Magnet	Energy	Failure	Collimator	F_{lost}	τ_{det} (ms)	ξ_{max} (mm^{-1})	$\langle\alpha\rangle$ (mm)	$\sigma_{loss}/\sigma_{beam}$	BLM
RD1.L2	7 TeV	Quench	TCP.C6L7	0.991	9.0	15.39	0.053	0.331	YES
			TCP.B6L7	0.010	10.7	0.25	0.032	0.270	NO
RD1.L2	450 GeV	V_{max}	TCP.C6L7	0.975	7.7	8.59	0.093	0.183	YES
			TCP.B6L7	0.026	10.9	0.15	0.137	0.309	NO
RD1.L8	7 TeV	Quench	TCSG.4R6	0.776	10.8	7.84	0.081	0.256	YES
			TCSG.A5L7	0.051	11.1	1.03	0.040	0.295	YES
RD1.L8	450 GeV	V_{max}	TCSG.4R6	0.922	9.8	3.67	0.184	0.127	YES
			TCSG.A5L7	0.077	10.5	0.25	0.166	0.301	YES
RD1.R2	7 TeV	Quench	TCP.C6L7	0.990	11.3	18.16	0.045	0.269	YES
			TCP.B6L7	0.011	13.5	0.31	0.028	0.255	NO
RD1.R2	450 GeV	V_{max}	TCP.C6L7	0.971	10.6	10.79	0.074	0.110	YES
			TCP.B6L7	0.030	14.9	0.19	0.125	0.273	YES
RD1.R8	7 TeV	Quench	TCSG.4R6	0.877	13.3	8.55	0.076	0.250	YES
			TCSG.A5L7	0.056	13.8	1.16	0.040	0.281	YES
RD1.R8	450 GeV	V_{max}	TCSG.4R6	0.895	14.5	4.41	0.132	0.086	YES
			TCSG.A5L7	0.066	17.4	0.36	0.152	0.256	YES
RD2.L1	7 TeV	Quench	TCP.C6L7	0.505	6.8	6.42	0.064	0.415	YES
			TCP.B6L7	0.009	7.5	0.21	0.034	0.306	NO
RD2.L2	7 TeV	Quench	TCSG.4R6	0.843	15.5	4.42	0.075	0.255	YES
			TCSG.A5L7	0.025	15.7	0.56	0.037	0.250	YES
RD2.L5	7 TeV	Quench	TCP.C6L7	0.992	6.1	11.66	0.070	0.444	YES
			TCP.B6L7	0.009	6.9	0.21	0.034	0.288	NO
RD2.L8	7 TeV	Quench	TCSG.6R7	0.999	14.8	12.69	0.065	0.269	YES
			TCP.B6L7	0.001	16.2	0.00	0.029	0.00	NO
RD2.R1	7 TeV	Quench	TCP.C6L7	0.992	8.8	14.91	0.054	0.336	YES
			TCP.B6L7	0.009	10.4	0.21	0.034	0.302	NO
RD2.R2	7 TeV	Quench	TCSG.6R7	0.999	13.7	5.95	0.069	0.287	YES
			TCP.B6L7	0.001	17.6	0.01	0.023	0.217	NO
RD2.R5	7 TeV	Quench	TCP.C6L7	0.990	8.3	14.50	0.056	0.351	YES
			TCP.B6L7	0.011	9.8	0.24	0.036	0.313	NO
RD2.R8	7 TeV	Quench	TCP.C6L7	0.988	11.6	18.33	0.044	0.262	YES
			TCP.B6L7	0.013	13.4	0.34	0.031	0.266	NO
RD3.L4	7 TeV	Quench	TCP.C6L7	0.990	8.5	14.55	0.056	0.349	YES
			TCP.B6L7	0.011	10.1	0.26	0.032	0.270	NO
RD3.R4	7 TeV	Quench	TCSG.6R7	0.999	10.9	10.03	0.082	0.468	YES
			TCP.B6L7	0.001	13.5	0.03	0.024	0.152	NO
RD4.L4	7 TeV	Quench	TCP.C6L7	0.991	7.1	12.99	0.062	0.405	YES
			TCP.B6L7	0.010	8.5	0.23	0.036	0.137	NO
RD4.R4	7 TeV	Quench	TCSG.4R6	0.458	12.0	5.80	0.065	0.263	NO
			TCSG.6R7	0.378	11.4	6.21	0.050	0.372	NO

Table E-18: Summary of the local data in the two most affected collimators for each case, obtained for the considered failures at the most critical insertion dipoles, beam 1.

Global Quantities										
Magnet	Energy	Failure	N_{loc}	dN_{max}	τ_1	τ_{Quench}	τ_{dam}	τ_{det}	BLM	QPS/PIC
RD1.L2	7 TeV	Quench	12	0.041	21.1	14.5	14.6	12.4	YES	NO
RD1.L2	450 GeV	V_{max}	8	0.011	38.0	15.9	19.2	14.7	YES	YES
RD1.L8	7 TeV	Quench	3	0.037	19.0	10.3	12.2	10.6	YES	NO
RD1.L8	450 GeV	V_{max}	3	0.011	30.7	15.5	15.8	10.9	YES	YES
RD1.R2	7 TeV	Quench	12	0.051	17.3	11.9	11.9	10.9	YES	NO
RD1.R2	450 GeV	V_{max}	9	0.018	23.0	9.8	11.7	9.0	YES	YES
RD1.R8	7 TeV	Quench	2	0.046	15.4	8.3	10.1	8.5	YES	NO
RD1.R8	450 GeV	V_{max}	3	0.017	20.0	9.1	10.5	7.4	YES	YES
RD2.L1	7 TeV	Quench	4	0.050	14.2	8.1	9.3	8.2	YES	NO
RD2.L2	7 TeV	Quench	3	0.033	20.0	10.6	13.0	10.9	YES	NO
RD2.L5	7 TeV	Quench	9	0.044	16.1	9.0	10.4	9.1	YES	NO
RD2.L8	7 TeV	Quench	12	0.035	23.5	7.2	16.2	14.5	YES	YES
RD2.R1	7 TeV	Quench	5	0.067	10.8	6.2	6.9	6.2	YES	NO
RD2.R2	7 TeV	Quench	6	0.034	23.4	15.7	15.3	13.6	YES	YES
RD2.R5	7 TeV	Quench	13	0.076	11.7	6.9	8.1	7.1	YES	NO
RD2.R8	7 TeV	Quench	6	0.027	24.1	13.4	15.5	13.9	YES	YES
RD3.L4	7 TeV	Quench	11	0.048	18.3	12.6	12.7	11.7	YES	NO
RD3.R4	7 TeV	Quench	5	0.054	15.8	10.4	10.1	9.5	YES	NO
RD4.L4	7 TeV	Quench	9	0.040	17.8	10.3	11.7	10.5	YES	NO
RD4.R4	7 TeV	Quench	6	0.065	13.4	8.9	8.8	8.4	YES	NO

Table E-19: Summary of the global data obtained for the considered failures at the most critical insertion dipoles, beam 2.

Local Quantities									
Magnet	Energy	Failure	Collimator	F_{lost}	τ_{det} (ms)	ξ_{max} (mm^{-1})	$\langle\alpha\rangle$ (mm)	$\sigma_{loss}/\sigma_{beam}$	BLM
RD1.L2	7 TeV	Quench	TCSG.4L6	0.776	13.7	7.64	0.083	0.341	YES
			TCSG.A5R7	0.116	12.4	1.55	0.038	0.271	YES
RD1.L2	450 GeV	V_{max}	TCSG.4L6	0.869	14.7	4.00	0.138	0.093	YES
			TCSG.A5R7	0.131	16.8	0.46	0.150	0.266	YES
RD1.L8	7 TeV	Quench	TCP.C6R7	0.992	10.6	17.70	0.046	0.274	YES
			TCP.B6R7	0.009	12.9	0.24	0.031	0.256	NO
RD1.L8	450 GeV	V_{max}	TCP.C6R7	0.964	10.9	9.82	0.080	0.173	YES
			TCP.B6R7	0.037	14.7	0.25	0.121	0.263	YES
RD1.R2	7 TeV	Quench	TCSG.4L6	0.763	11.4	6.98	0.090	0.342	YES
			TCSG.A4R7	0.004	12.2	0.09	0.033	0.263	NO
RD1.R2	450 GeV	V_{max}	TCSG.4L6	0.908	9.0	3.26	0.202	0.146	YES
			TCSG.A5R7	0.092	10.5	0.29	0.185	0.333	YES
RD1.R8	7 TeV	Quench	TCP.C6R7	0.993	8.5	15.45	0.053	0.317	YES
			TCP.B6R7	0.008	10.7	0.21	0.031	0.264	NO
RD1.R8	450 GeV	V_{max}	TCP.C6R7	0.971	7.4	6.87	0.116	0.159	YES
			TCP.B6R7	0.030	9.7	0.18	0.129	0.291	YES
RD2.L1	7 TeV	Quench	TCP.C6R7	0.993	8.2	14.38	0.056	0.348	YES
			TCP.B6R7	0.008	9.9	0.18	0.033	0.282	NO
RD2.L2	7 TeV	Quench	TCP.C6R7	0.992	10.9	18.47	0.044	0.259	YES
			TCP.B6R7	0.009	13.7	0.24	0.030	0.275	NO
RD2.L5	7 TeV	Quench	TCP.C6R7	0.985	9.1	15.96	0.051	0.308	YES
			TCP.B6R7	0.008	11.2	0.21	0.029	0.259	NO
RD2.L8	7 TeV	Quench	TCSG.4L6	0.622	15.2	6.57	0.078	0.254	YES
			TCSG.A5R7	0.200	14.5	4.23	0.0036	0.253	YES
RD2.R1	7 TeV	Quench	TCP.C6R7	0.995	6.2	11.93	0.068	0.435	YES
			TCP.B6R7	0.006	7.7	0.14	0.035	0.298	NO
RD2.R2	7 TeV	Quench	TCSG.6L7	0.999	13.6	12.46	0.066	0.266	YES
			TCSG.A5R7	0.001	18.3	0.00	0.048	0.301	NO
RD2.R5	7 TeV	Quench	TCSG.4L6	0.700	8.4	5.45	0.095	0.308	NO
			TCP.C6R7	0.194	7.1	4.14	0.038	0.259	YES
RD2.R8	7 TeV	Quench	TCP.C6R7	0.989	13.9	20.78	0.039	0.242	YES
			TCP.B6R7	0.009	16.9	0.23	0.030	0.275	NO
RD3.L4	7 TeV	Quench	TCSG.4L6	0.817	11.9	6.95	0.088	0.334	YES
			TCSG.A5R7	0.087	11.7	1.74	0.041	0.276	YES
RD3.R4	7 TeV	Quench	TCSG.6L7	0.999	9.5	9.29	0.088	0.482	YES
			TCSG.A5R7	0.001	12.1	0.02	0.035	0.266	NO
RD4.L4	7 TeV	Quench	TCP.C6R7	0.788	10.5	15.38	0.042	0.253	YES
			TCSG.4L6	0.154	14.8	2.68	0.047	0.152	NO
RD4.R4	7 TeV	Quench	TCSG.6L7	0.999	8.4	8.69	0.094	0.499	YES
			TCP.B6R7	0.001	12.3	0.01	0.017	0.053	NO

Table E-20: Summary of the local data in the two most affected collimators for each case, obtained for the considered failures at the most critical insertion dipoles, beam 2.

Global Quantities										
Magnet	Energy	Failure	N_{loc}	dN_{max} (frac./tr)	τ_1 (ms)	τ_{Quench} (ms)	τ_{dam} (ms)	τ_{det} (ms)	BLM	FMCM
RD1.LR1	450 GeV	0 V	4	0.005	91.5	48.6	49.7	35.9	YES	YES
RD1.LR1	7 TeV	V_{max}	7	0.075	5.7	2.1	2.5	2.1	NO	YES
RD1.LR1	450 GeV	V_{max}	5	0.105	4.2	2.3	2.2	1.8	YES	YES
RD1.LR5	450 GeV	0 V	4	0.004	90.5	38.0	40.9	32.6	YES	YES
RD1.LR5	7 TeV	V_{max}	6	0.090	4.7	1.7	2.2	1.7	YES	YES
RD1.LR5	450 GeV	V_{max}	6	0.108	4.0	2.1	2.0	1.6	YES	YES
RD34.LR3	7 TeV	V_{max}	3	0.003	133.9	48.8	50.6	40.2	YES	YES
RD34.LR3	450 GeV	V_{max}	3	0.022	14.8	7.1	7.9	5.5	YES	YES
RD34.LR7	7 TeV	V_{max}	5	0.002	202.8	91.3	95.9	75.7	YES	YES
RD34.LR7	450 GeV	V_{max}	5	0.018	23.1	14.2	12.8	9.0	YES	YES

Table E-21: Summary of the global data obtained for the considered failures at the most critical normal conducting dipoles in the insertions, beam 1.

Local Quantities									
Magnet	Energy	Failure	Collimator	F_{lost}	τ_{det} (ms)	ξ_{max} (mm^{-1})	$\langle\alpha\rangle$ (mm)	$\sigma_{loss}/\sigma_{beam}$	BLM
RD1.LR1	450 GeV	0 V	TCSG.6R7	0.990	46.4	12.50	0.066	0.068	YES
			TCP.B6L7	0.010	46.8	0.21	0.071	0.151	YES
RD1.LR1	7 TeV	V_{max}	TCP.C6L7	0.993	2.1	11.38	0.071	0.451	NO
			TCP.B6L7	0.007	3.1	0.17	0.034	0.331	NO
RD1.LR1	450 GeV	V_{max}	TCSG.6R7	0.803	1.8	1.32	0.501	0.527	YES
			TCP.C6L7	0.192	1.8	1.01	0.161	0.268	YES
RD1.LR5	450 GeV	0 V	TCSG.6R7	0.998	32.6	12.28	0.066	0.069	YES
			TCP.B6L7	0.003	63.8	0.02	0.079	0.162	NO
RD1.LR5	7 TeV	V_{max}	TCP.C6L7	0.994	1.7	10.26	0.079	0.708	YES
			TCP.B6L7	0.007	2.5	0.16	0.035	0.307	NO
RD1.LR5	450 GeV	V_{max}	TCSG.6R7	0.999	1.6	1.31	0.617	0.690	YES
			TCP.C6L7	0.001	2.5	0.01	0.125	0.260	NO
RD34.LR3	7 TeV	V_{max}	TCP.C6L7	0.983	40.2	130.82	0.008	0.071	YES
			TCP.B6L7	0.015	47.0	2.57	0.017	0.144	NO
RD34.LR3	450 GeV	V_{max}	TCP.C6L7	0.981	5.5	5.52	0.152	0.151	YES
			TCP.B6L7	0.020	7.8	0.10	0.147	0.332	YES
RD34.LR7	7 TeV	V_{max}	TCSG.4R6.	0.098	111.4	84.79	0.006	0.017	NO
			TCP.C6L7	0.006	75.7	0.67	0.007	0.046	YES
RD34.LR7	450 GeV	V_{max}	TCP.C6L7	0.213	9.0	2.23	0.078	0.145	YES
			TCSG.4R6	0.761	14.2	3.07	0.167	0.146	NO

Table E-22: Summary of the local data in the two most affected collimators for each case, obtained for the considered failures at the most critical normal conducting dipoles in the insertions, beam 1.

Global Quantities										
Magnet	Energy	Failure	N_{loc}	dN_{max} (frac./tr)	τ_1 (ms)	τ_{Quench} (ms)	τ_{dam} (ms)	τ_{det} (ms)	BLM	FMCM
RD1.LR1	450 GeV	0 V	3	0.004	89.8	45.2	47.6	33.0	YES	YES
RD1.LR1	7 TeV	V_{max}	5	0.083	5.1	1.7	2.2	1.7	YES	YES
RD1.LR1	450 GeV	V_{max}	4	0.097	4.1	3.2	2.2	1.6	YES	YES
RD1.LR5	450 GeV	0 V	3	0.004	77.6	36.1	38.4	26.2	YES	YES
RD1.LR5	7 TeV	V_{max}	13	0.071	6.2	2.0	2.8	2.2	YES	YES
RD1.LR5	450 GeV	V_{max}	3	0.110	3.8	1.4	2.0	1.4	YES	YES
RD34.LR3	7 TeV	V_{max}	3	0.001	143.7	52.5	55.0	43.2	YES	YES
RD34.LR3	450 GeV	V_{max}	3	0.019	16.6	7.7	8.6	6.1	YES	YES
RD34.LR7	7 TeV	V_{max}	3	0.002	238.5	83.2	90.7	70.8	YES	YES
RD34.LR7	450 GeV	V_{max}	3	0.013	24.5	10.6	12.5	8.9	YES	YES

Table E-23: Summary of the global data obtained for the considered failures at the most critical insertion dipoles, beam 2.

Local Quantities									
Magnet	Energy	Failure	Collimator	F_{lost}	τ_{det} (ms)	ξ_{max} (mm^{-1})	$\langle\alpha\rangle$ (mm)	$\sigma_{loss}/\sigma_{beam}$	BLM
RD1.LR1	450 GeV	0 V	TCP.C6R7	0.635	33.0	13.16	0.039	0.067	YES
			TCP.B6R7	0.037	41.7	0.35	0.083	0.178	YES
RD1.LR1	7 TeV	V_{max}	TCP.C6R7	0.995	1.7	10.51	0.077	0.485	YES
			TCP.B6R7	0.006	2.5	0.12	0.037	0.332	NO
RD1.LR1	450 GeV	V_{max}	TCP.C6R7	0.965	1.6	2.13	0.368	0.617	YES
			TCSG.6L7	0.025	2.7	0.14	0.151	0.205	NO
RD1.LR5	450 GeV	0 V	TCP.C6R7	0.941	26.2	19.71	0.044	0.065	YES
			TCP.B6R7	0.050	34.6	0.57	0.071	0.151	YES
RD1.LR5	7 TeV	V_{max}	TCP.C6R7	0.544	2.2	8.92	0.050	0.320	YES
			TCSG.4L6	0.372	3.2	3.47	0.088	0.261	NO
RD1.LR5	450 GeV	V_{max}	TCP.C6R7	0.991	1.4	1.96	0.410	0.636	YES
			TCP.B6R7	0.010	2.1	0.05	0.170	0.429	NO
RD34.LR3	450 GeV	V_{max}	TCP.C6R7	0.830	43.2	7.05	0.010	0.056	YES
			TCP.B6R7	0.007	49.8	0.24	0.018	0.148	YES
RD34.LR3	7 TeV	V_{max}	TCP.C6R7	0.972	6.1	6.53	0.118	0.160	YES
			TCP.B6R7	0.029	8.4	0.15	0.152	0.330	NO
RD34.LR7	7 TeV	V_{max}	TCP.C6R7	0.949	70.8	202.26	0.004	0.024	YES
			TCP.B6R7	0.045	79.1	2.75	0.013	0.108	YES
RD34.LR7	450 GeV	V_{max}	TCP.C6R7	0.961	8.9	9.89	0.080	0.111	YES
			TCP.B6R7	0.039	11.3	0.25	0.131	0.280	YES

Table E-24: Summary of the local data in the two most affected collimators for each case, obtained for the considered failures at the most critical insertion dipoles, beam 2.